Developing new tools to identify novel factors that contribute to bacterial cell mechanics

—by—

George Kuri Auer

A dissertation submitted in partial fulfillment

of the requirements for the degree of

Doctor of Philosophy

(Biomedical Engineering)

at the

UNIVERSITY OF WISCONSIN-MADISON

2016

Date of Final Oral Examination: February 25th, 2016

This dissertation is approved by the following members of the Final Oral Committee:

Douglas B. Weibel, Associate Professor, Biochemistry and Biomedical Engineering

Shaoqin Gong, Professor, Biomedical Engineering, BIONATES

Joseph P. Dillard, Professor, Medical Microbiology and Immunology

Jue D. Wang, Associate Professor, Bacteriology

Kalin Vestigian, Assistant Professor, Bacteriology and Systems Biology

Table of Contents

Acknowledgements

I have learned many things throughout my Graduate career, and although at times the work was challenging and the hours were long I would not change a moment. I would like to thank all of the members of the Weibel lab who have come and gone throughout the years, especially Manohary Rajendram, Lars Renner, Hannah Tuson, Mathew Copeland, and Piercen Oliver.

I would especially like to thank Hannah Tuson for her endless help throughout the years, from our work on CLAMP to taking the time to edit papers. I would like to thank Piercen Oliver for his collaboration on Proteus, we tried many things, and when nothing else worked we made something that did. I would like to thank Lars Renner, he is a true and great friend. Finally, Manohary Rajendram for the endless hours of work producing mutants, troubleshooting experiments, ideas, input, and just all around expertise in anything and everything.

I have been fortunate to have terrific collaborators, especially Dr. KC Huang who was with me at the beginning of my Graduate career and has been with me until the end. Furthermore, I would like to thank all of my committee members for their help, insight, guidance and critique. I am truly and honestly grateful.

I am grateful for the friendship of Laura Vanderploeg, and her willingness to adopt my orphaned plants. We have had many great conversations and I hope to have many more in the future.

I would finally like to thank my advisor Doug Weibel, for all of his help throughout the years, the encouragement, the patience, the yogurt, and if he holds true to his promise…

a snake skin vest. I am grateful that he took a chance on me, and I know that I have become a better person and a better scientist because of him.

Finally, like she did for me in her thesis I would like to thank my partner in life and in the lab Manohary Rajendram. I always said if I got nothing else out of my time in Graduate school at least I get you, and that was worth every moment. We have been many places together and I know we will go to many more.

I am also truly grateful to my entire family for their endless encouragement and prayers, which have supported me throughout my graduate career. I wouldn't be who I am today without them, and I hope that I have made them all proud. Thank you….

Developing new tools to identify novel factors that contribute to bacterial cell mechanics

George Kuri Auer

Under the supervision of Douglas B. Weibel

Department of Biochemistry

University of Wisconsin-Madison, Madison WI

In plant, fungal and bacterial cells, the cell wall determines cell shape and provides mechanical stability against the large pressure differentials that reach into the tens of atmospheres. Perturbations in the construction and underlying architecture of the cell wall cause physical abnormalities in bacterial shape, a loss of mechanical integrity, and subsequent cell lysis resulting from membrane rupture. The typical cell envelope of Gram–negative bacteria is composed of four distinct components, the lipopolysaccharides, the outer membrane, the peptidoglycan, and the inner membrane. In contrast the cell envelop of Gram–positive bacteria is composed of three distinct components, the wall teichoic and lipoteichoic acids, the peptidoglycan, and the inner membrane. In both Gram–negative and Gram–positive bacteria, peptidoglycan is known to play a major role in maintaining mechanical integrity of the bacterial cell. And although much is currently known about the underlying structure and

construction of peptidoglycan, an infusion of more accessible methods and a better understanding of the spatial, temporal, and genetic modulators of bacterial mechanics could truly kick start our understanding of mechanical regulation across species. This dissertation describes the development and application of three unique methods/tools that are able to 1) quantitatively measure a bacteria's longitudinal stiffness, 2) screen for genetic modulators of bacterial stiffness, and 3) measure the bending rigidity of bacteria. First, using our CLAMP methodology to measure longitudinal stiffness, we discovered that Gram–negative and Gram–positive rod shaped bacteria have similar cell wall mechanical properties. We also found that that the bacterial cytoskeletal protein MreB does not impact longitudinal stiffness in *Escherichia coli*. Second, using our GRABS methodology, a high throughput screening method to discern genetic modulators of bacterial stiffness, we identified non-essential genes capable of modulating stiffness in *E. coli*. We found an extremely diverse range of cellular functions able to influence bacterial stiffness. As expected, genes related to cell wall and membrane biogenesis still had the greatest impact on bacterial stiffness. Additionally, by correlating our data to a previously published chemical screen we identified that the proton ionophore, CCCP, is generally able to increase cell stiffness. Finally, using a microfluidic-bending device, to measure bending rigidity, we discovered that swarming bacteria transition from short stiff rods, to highly flexible filaments. We found that this transition increases sensitivity of single cells to changes in the osmotic environment and

to cell wall targeting antibiotics. We determined that the change in bending rigidity, osmotic and antibiotic sensitivity stem from a decrease in peptidoglycan thickness of swarming bacteria.

Chapter 1

MechanoMicroBiology

Adapted from

George K. Auer and Douglas B. Weibel

Manuscript in preparation

Abstract

In bacterial cells, the cell wall determines cell shape and provides mechanical stability against the large pressure differentials that reach into the tens of atmospheres. Perturbations in the construction and underlying architecture of the cell wall cause physical abnormalities in bacterial shape, a loss of mechanical integrity, and subsequent cell lysis resulting from membrane rupture. The typical cell wall of Gram–negative bacteria is composed of four distinct material layers, the lipopolysaccharides, the outer membrane, the peptidoglycan, and the inner membrane. In contrast the cell wall of Gram–positive bacteria is composed of three distinct layers, the wall teichoic and lipoteichoic acids, the peptidoglycan, and the inner membrane. In both Gram–negative and Gram–positive bacteria the peptidoglycan layer plays a major role in mechanical integrity of the cell. However it is becoming clear that perhaps the peptidoglycan is not the sole component found in bacteria that can contribute to the mechanical properties of the cell. In this review we will summarize the known contributions from each of the distinct material layers in Gram–positive and Gram–negative bacteria, as well as individual proteins that are known to directly alter the mechanical properties of the cell.

Introduction

Bacteria inhabit a plethora of different environments where they experience a wide range of physical and chemical stresses. For example, bacteria are constantly under pressure arising from the mismatch in the intracellular and extracellular concentration of solutes. Sudden shifts in the osmotic environment expose bacterial cells to osmotic pressures (turgor) that reach 20 atmospheres (1). To survive, bacteria have evolved cell walls that mechanically resist turgor pressure and osmoregulatory machinery that senses changes in osmotic pressure and transports solutes in/out of cells. In the current model of bacterial mechanics, the polymeric meshwork surrounding cells—referred to as the peptidoglycan—provides the majority of cellular mechanical properties. The peptidoglycan is a macromolecular cellular 'exoskeleton' that stabilizes the cell membranes from catastrophic defects and loss of structural integrity. Additional structural elements have recently been uncovered indicating that the peptidoglycan may be just one element of a more complete set of macromolecular materials—such as the bacterial homolog, MreB of eukaryotic actin—that the cell uses to control mechanics (2, 3). Several simplistic new tools were described recently that enable studies of bacterial mechanics at the single cell level (2, 4, 5) and that provide a proteome/genome-wide view of mechanomicrobiology.

Compared to microbes, eukaryotic cell mechanics have been studied for a very long time. Eukaryotic studies have provided insight into the progression of human

diseases (6-9) in which changes in cellular mechanics can be important (8, 9). For example, the infection of red blood cells by the parasite *Plasmodium falciparum,* which is responsible for most of the mortality caused by malaria (10), causes a ten-fold increase in the stiffness of infected red blood cells (6), reduces the flow of blood, and eventually leads to a loss of microcirculation. Additionally, changes in cell mechanics are linked to a wide range of human health conditions and diseases, including: asthma, osteoporosis, cancer, glaucoma, and osteoarthritis (9).

The study of eukaryotic cell mechanics has provided insight into the importance of control over cell mechanics in normal cellular function. Likewise, the study of bacteria may uncover roles for cell mechanics linked to bacterial cellular function as well as applications to the infection of eukaryotic hosts. Further, the widespread drug resistance of bacteria to antibiotics may benefit from studies in this area, in which a more detailed understanding of bacterial mechanics will uncover new therapeutic targets and insight into the mechanisms of resistance of clinical antibiotics.

Mechanical characteristics of bacterial cells

The mechanical properties of cells are most frequently described by the Young's modulus and bending rigidity (2-4, 11-15). Below we provide a brief overview of these terms.

Young's modulus. The stiffness of a material can be defined by its Young's modulus (or tensile elasticity), which is characterized by the relationship between the applied stress on the material (force per unit area) and the resulting strain (fractional change in length). This relationship is typically linear—i.e., the ratio of stress to strain is a constant value—and the Young's modulus is defined by the slope of the stress/strain curve in the linear region. The Young's modulus is measured in units of Pa ($N\ m^2$). If a physical load is applied to material in the linear region the material will deform, however removal of the load will return the material to its pre-load state. Stress applied to a material outside of the linear regime results in the permanent and irreversible deformation of a material (i.e., hysteresis).

Bending rigidity or flexural rigidity. Bending rigidity (units of $N\ m^2$) is the resistance of a material to bending under a load and represents the product of the Young's modulus and the second moment of inertia. In bacteria, the second moment of inertia is equivalent to $\pi r^3 h$, where r is the radius of a bacterial cell, and h is the thickness of the mechanically relevant material being studied; typically this is the peptidoglycan layer in the cell wall (~30-nm thick in gram–positive bacteria and ~4-nm thick in gram–negative bacteria). Importantly, the bending rigidity can provide insight into cellular elements that are oriented perpendicular (3, 16) to the long axis of bacterial cells, provide mechanical support, and may be difficult to interrogate by other measurements (2). The

bending rigidity can also be used as a secondary means of determining the Young's modulus.

Mechanical contributions of common components of the bacterial cell wall

Bacteria can be broadly classified into gram–negative and gram–positive based on the presence of an outer membrane. An outer membrane is only present in gram–negative bacteria and in addition to phospholipids, contains a significant concentration of lipopolysaccharides (LPS). Gram–positive bacteria do not have an outer membrane nor LPS, however they contain wall techoic acids (WTA) and lipoteichoic acids (LTA) that are polysaccharides covalently attached to the peptidoglycan or inserted into the cytoplasmic membrane, respectively. We summarize the structure and mechanical function of these classes of materials below.

Lipopolysaccharides (LPS) of gram–negative bacteria

The LPS is expressed by most gram–negative bacteria, plays an important role in the function and structural integrity of the outer lipid membrane, and is linked to the pathology of certain bacteria in humans (17). The LPS is located in the outer leaflet of the outer membrane, and is a large molecule (>100 KDa) (18) containing a lipid moiety attached to a long-chain polysaccharide. LPS molecules can be conceptually broken down into 3 distinct parts: 1) lipid A, which is the physical anchor between the LPS and

the outer lipid membrane; 2) the inner and outer core; and 3) a hydrophilic O-antigen. Lipid A is a unique chemical moiety containing 6 saturated fatty acyl chains, rather than the 2-4 fatty acyl chains characteristic of prokaryotic membrane lipids (19), and is only found in the LPS of gram-negative bacteria. The hydrophobic acyl chains in Lipid A pack tightly together to aid in stabilization of the outer membrane (20). The inner core of the LPS is highly conserved among bacterial species (17) and typically consists of 3-deoxy-D-manno-octulosonic acid (Kdo) and heptose sugars. Except in *Neisseria meningitides* (21), Lipid A and at least one Kdo (from the inner LPS core) are necessary for cell viability in LPS producing bacteria. In contrast, the remaining two sections of the molecule are not essential for cell viability and display a low degree of conservation among bacterial species (17). The O-antigen has a range of lengths (17, 19) and the molecule is linked to the potential virulence of pathogenic strains (22). Truncations in LPS produce physical aberrations in the morphology of bacterial colonies. Wild-type bacterial cells that contain intact LPS are referred to as "smooth", as their outer cell morphology is continuous and defect-free. Bacterial cells that have lost the O-antigen are classified as "rough" mutants; cells that have lost both the outer core and the O-antigen are classified as "deep-rough" mutants and appear to have a rough membrane morphology as determined by electron microscopy (23). LPS mutant cells are more permeable to small molecules than wild-type cells (24) and have increased susceptibility to environmental stress (25).

Molecules of LPS are negatively charged and electrostatically repel other LPS molecules (19), leading to physical separation between the molecules and a subsequent increase in membrane permeability. To overcome electrostatic repulsion and increase stability, LPS molecules typically bind tightly to divalent cations such as Ca^{2+} or Mg^{2+}. Amro et al. (26) used AFM to monitor the effect of divalent cations on LPS and membrane architecture and found that after the removal of divalent cations by EDTA treatment, 40-50% of the LPS was lost from the outer membrane (26). Providing possible insight into this observation, Clifton et al. (27) used an asymmetric membrane bilayer, composed of phosphatidylcholine as the inner leaflet and deep-rough mutant LPS as the outer leaflet to demonstrate that after the removal of divalent cations from LPS it flips between the outer and inner leaflets of the bilayer. Flipping of LPS molecules between the leaflets minimizes the repulsive electrostatic forces that would arise between adjacent LPS molecules (27), however in vivo these repulsive forces may drive the release of LPS from the outer membrane into the extracellular environment (26).

Support for the relationship between the stability of the LPS layer and its contribution to membrane permeability is clear, however there is a noticeable absence of quantitative studies linking LPS to gram–negative bacteria stiffness. The state-of-the-art on the mechanical role of the LPS layer is based on in vitro measurements of membrane rigidity, membrane fluidity, and the viscoelastic properties of the LPS in lipid vesicles or model membrane bilayers.

Bacterial membrane lipids form a stable lamellar phase bilayer in which the hydrophilic portion of the molecules are aligned at the water interface and the hydrophobic portion is sequestered away from water forming and forms a stable network from the packing between acyl chains. Similar to membrane lipids, isolated LPS or lipid A can form stable lamellar phases consisting of bilayers and multilayers in aqueous solution (28, 29). LPS-containing membranes are stabilized by the presence of divalent cations, which increase the ordering and rigidity of multilamellar LPS layers (29, 30). Addition of Ca^{2+} to a "deep-rough" LPS monolayer, containing only lipid A and 2 Kdo sugars, resulted in the formation of a physically cross-linked elastic gel (31). Furthermore, increasing the polysaccharide length of the LPS enabled this formation in the absence of Ca^{2+}—possibly due to increased hydrogen bonding—and resulted in additional lateral compression of the LPS monolayer (31, 32). These in vitro studies support the concept that the stability of the LPS layer is influenced by the polysaccharide chain length and that the LPS is stabilized through the presence of divalent cations. Additional in vivo studies will illuminate the mechanical response of the LPS to changing environmental conditions (33) and its role in outer membrane homeostasis (23, 34).

Glycopolymers of gram–positive bacteria

Wall teichoic acids (WTAs). WTAs are abundant glycopolymers attached to the peptidoglycan layer in gram–positive bacteria and account for ~50% of the weight of the cell wall (35). WTAs are non-essential in gram-positive bacteria and their function(s) remains unknown (36). WTA consists of 2 primary structural features: 1) the dissacharide linkage that connects WTAs to the peptidoglycan; and 2) a primary polymeric chain that is typically composed of glycerol phosphate or ribitol phosphate repeats that can be 20-40 units in length (37). The linkage unit is highly conserved among bacterial species (38) and consists of *N*–acetylmannosamine–*N*–acetylglucosamine–1–phosphate linked to the peptidoglycan through a phosphodiester bond attached to the *N*–acetylmuramyl residue (39). The polymeric backbone of the WTA main chain is negatively charged due to the presence of phosphate, however WTA is generally zwitterionic due to the presence of positively charged D–alanine residues that decorate the backbone (40). By altering the groups attached to the WTA backbone, cells are able to modulate antibiotic susceptibility and improve their survival (37). Additionally, the presence of WTAs is crucial for maintaining wild–type cell wall structure and cell shape. For example, deletion of WTAs in *Bacillus subtilis* causes changes in cell morphology (36) and peptidoglycan thickness (41). *B. subtilis* WTAs are also important for the correct function of proteins involved in cell elongation (36, 42); in

spherical *Staphylococcus aureus* cells, WTAs appear to be promiscuous and play roles in both cell elongation and cell division (41).

Although little is presently known about the mechanical contribution of WTAs in gram–positive bacteria, a hypothesis is that this family of molecules influences cell morphology and peptidoglycan thickness in ways that affect the mechanical properties of the cell. In support of this hypothesis, the density of *S. aureus* peptidoglycan increased in the absence of WTAs and was explained as arising from the loss of electrostatic repulsion between neighboring WTA molecules (43).

Lipoteichoic acids (LTA). In addition to WTAs, gram–positive bacteria contain a second family of glycopolymer referred to as lipoteichoic acids (LTAs), which extends from the inner membrane into the extracellular space that immediately surrounds the cell. LTA molecules consist of two distinct structural components: 1) a lipid anchor that is used to attach LTA to the inner membrane of all gram–positive bacteria; and 2) the main polymeric chain composed of alditolphosphate-containing or glycosyl-phosphate-containing monomers (44). LTA is generally considered essential for cell viability and plays a role in construction and placement of the peptidoglycan layer and in cellular integrity (41). For example, LTAs in the rod-shaped bacterium *B. subtilis* is involved in cell division (42). A suppressor mutation in GdpP, a cyclic di-AMP phosphodiesterase in *S. aureus* enables the deletion of LTA, and causes an increase in peptidoglycan cross-

linking (45). Although no direct measurements of cell mechanics were made, this result may indicate that LTA plays a functional role in cell mechanics and can be compensated by increasing the stiffness of the peptidoglycan layer.

Similar to WTA, LTA is negatively charged and can become zwitterionic by the decoration of the main polymeric chain with positively charged D-Ala units. Incorporation of D-Ala into LTA provides cells with several adaptive advantages, including improved host cell adhesion and invasion and resistance to cationic antimicrobial peptides (44). In *S. aureus,* LTA is highly modified with D–Ala (46); a loss of D–Ala decorations caused no visible change in *S. aureus* cell shape, however transmission electron microscopy images demonstrated an increase in peptidoglycan thickness, concave membrane topology, and an elevated frequency of cell lysis. D–alanylation of *S. aureus* LTA is essential for cell viability in the absence of WTA (41). In contrast, the loss of D–alanylation of LTA in *Streptococcus agalactiae* did not produce changes in cell morphology or peptidoglycan thickness; it instead reduced cell wall rigidity by 20-fold (47). The importance of D-alanylated LTA for these phenotypes is not understood presently, however it is clearly connected to cell wall architecture and cell mechanics.

Isolated LTAs are able to forms monolayers in the absence of membrane phospholipids, but however these structures are relatively unstable (48). Mixing LTAs with the gram–positive lipid dipalmitoyldiphosphatidylglycerol—a phospholipid

found in the membranes of gram–positive bacteria—produces a monolayer with increased membrane stability and rigidity (48). LTA is also stabilized in phospholipid vesicles containing diacylglycerol and phosphatidylglycerol (49). These studies illustrate that the membrane may act as a scaffold to stabilize the LTA layer in gram–positive bacteria (50).

Peptidoglycan

The peptidoglycan is a cross-linked polymeric meshwork that encapsulates bacterial cells (with the exception of Mycoplasma and Ureaplasma (51)) and has historically been considered an important factor for cellular mechanical properties. The peptidoglycan thickness varies in gram–negative (2.5 – 6.5-nm thick when fully hydrated) and gram–positive bacteria (19 – 33-nm thick when fully hydrated) (52-56). Although varying in thickness, the peptidoglycan of gram–negative and gram–positive bacteria shares a similar structure consisting of glycans and amino acids.

The glycan backbone of peptidoglycan is highly conserved across bacteria and consists of alternating *N*–acetylglucosamine (GlcNAc) and *N*–acetylmuramic acid (MurNAc) monomers linked by a β–1,4 glycosidic bond (52). A 'stem peptide' is attached to the C-3 hydroxyl group of each MurNAc monomer. In gram–negative bacteria, the most common stem peptide consists the 5-amino acid sequence: L–Ala–D–Glu–*meso*–diaminopimelic acid (*meso*–DAP)–D–Ala–D–Ala. This basic 5-unit peptide

structure is shared by some gram-positive bacteria, but also shows exception that the *meso*–DAP monomer at position 3 in the peptide can be replaced by L–Lys (57).

The basic polymer 'mesh' network that surrounds gram-negative and gram-positive bacteria is built through cross-linking of the stem peptides. In gram-negative bacteria, adjacent peptides are directly cross-linked to produce the more abundant 3-4 linkage between position 3 (*meso*-DAP) and position 4 (D-Ala) (58) or a 3-3 linkage (59, 60). In gram–positive bacteria, adjacent peptides are cross–linked directly (61, 62) or alternatively are cross-linked using an inner peptide bridge (62) to produce 2–4 or 3–4 linkages (52). The inner peptide bridge may be 1 to 7 peptides in length and consist of various amino acids (52).

Peptidoglycan can be comprised of greater than 50 individual types (63) of peptidoglycan subunits (or muropeptides) that are characterized as either monomeric (zero cross-link), dimeric (one cross-link), or trimeric (two cross-links) depending on the number of cross-links to a single peptide stem (64). The relative abundance of peptide cross-links in peptidoglycan can predict the stiffness of the material (64, 65); a high degree of crosslinking indicates a stiff layer. Although peptidoglycan is a strong material the resulting cross-linked peptidoglycan structure is not highly ordered and the macromolecular structure is porous (43, 66-68). In gram–negative bacteria, the stem peptides are aligned along the long axis of the cell and glycans are ordered circumferentially around the cell (53), which is hypothesized to impart directional (e.g.,

anisotropic) mechanical properties. This organization enables the peptide bonds to swell and shrink with changes in turgor pressure, while the relatively rigid glycan chains remain comparatively immobile (69). Due in part to the thickness of the peptidoglycan layer in gram–positive bacteria, the orientation of the stem peptides and the glycan strands relative to the axis of the cell remains generally unknown. However, the recent application of solid-state NMR to study isolated peptidoglycan may provide insight into its orientation (70). There have been several proposed models of peptidoglycan orientation and growth in gram-positive bacteria (71-73), including a model similar to the structure in gram–negative bacteria.

The Young's modulus of peptidoglycan has been measured in wild-type gram–negative and gram–positive bacteria (13, 14, 74-76). A recent understanding of the roles of the different pencillin-binding proteins (PBPs) in peptidoglycan synthesis (77) and new analytical tools for rapidly determining peptidoglycan structure (e.g., crosslinking and glycan length), such as UPLC-MS (78) is enabling studies to quantitatively investigate how changing peptidoglycan structure affects its stiffness. Recent reports have discovered that increasing glycan strand length and increasing cross-linking increases the mechanical properties of bacterial cells (79-81). For example 4 enzymes with essential glucosaminidase activity in *S. aureus* are responsible for hydrolysis of the bonds linking the GlcNAc and MurNAc (81). Loss of their glucosaminidase activity increases glycan strand chain length, which in turn increases the number of cross-links

per strand and leads to an increase in cell stiffness (81). Altering the glycan chain length has been proposed as a mechanism to increase the stiffness of peptidoglycan when cross-linking is reduced (82). The *S. aureus* enzyme PBP4 is non-essential for cell growth and performs secondary transpeptidation, or cross-linking of peptide stems, to produce highly cross-linked peptidoglycan (80). Deletion of PBP4 is deleted, reduces cell stiffness by 2- to 4-fold (80). In comparison, the antibiotic lysostaphin can cleave all the cross-linking in *S. aureus* and reduce cell stiffness by ~10-fold (79). Our current understanding of peptidoglycan is that it plays a key mechanical role in cells, however it is difficult to ignore that this material interacts with other layers of the cell wall (e.g., membranes) through protein such as Lpp (see below) that can influence cell stiffness.

The lipid membrane

Bacterial membranes are three-dimensional, supramolecular structures that encapsulate cells. Gram-positive bacteria contain a single inner phospholipid bilayer; gram-negative bacteria contain two lipid bilayers. These membranes primarily consist of three families of phospholipids: phosphatidylethanolamine (70-80% of total lipids) phosphatidlyglycerol (20-25% of total lipids), and cardiolipin (5-10% of total lipids) (31). Bacterial membranes can contain a mixture of phospholipids, proteins, lipopolysaccharides and lipoteichoic acids. We do not review the role of membrane proteins in influencing cell stiffness, although there is evidence that membrane proteins

such as OmpA (83) and Tol-Pal (83) interact with multiple layers of the cell wall and may influence cell mechanics (84, 85). We list known examples of proteins (not integral membrane proteins) that alter cell mechanics, below, however there are likely to be many more candidate proteins waiting to be identified and characterized.

Three primary forces hold the membrane together: 1) electrostatic interactions between oppositely charged polar lipid head groups; 2) hydrophobic forces causing the non-polar portions of the lipid to aggregate together rather than dissolve in water; and 3) van der Waals forces between the neighboring fatty acyl chains. Changes in the horizontal spacing of lipids reduces phospholipid interactions, decreases membrane rigidity, and increases membrane fluidity (86).

Similar to the peptidoglycan, changes in membrane thickness can affect bending rigidity of the lipid membrane (87). Bending rigidity is dependent on the square of the bilayer thickness and an approximate bending energy is ~20 K_BT (88, 89). The introduction of double bonds in acyl chains (i.e., incorporating unsaturated lipids) alters the geometry of the acyl chain, making it shorter and wider, reduces the packing order of the acyl chains in the membrane, and reduces the rigidity of lipid bilayers (90). The presence of two or more cis-double bonds in the fatty acyl chain alters their packing and results in a membrane with a 2-fold decrease in rupture tension and an ~2-5-fold increase in water permeability (91). Vesicles consisting of an *E. coli* lipid extract are ~50% less stiff than those containing dioleoyl phosphatidylglycerol alone (92), which

highlights the effect of lipid diversity in the mechanical properties of the bacterial membrane.

Mechanical contribution of proteins in bacteria

Few proteins have been reported to alter the mechanical properties of bacterial cells. Proteins that fit into this category influence cell mechanics through interactions with cell wall components. However, this is still a new area of study in which additional studies can broaden our understanding of the mechanisms by which proteins affect cell mechanics and the function this has on cells.

MreB

In many rod-shaped gram–negative and gram–positive bacteria, insertion of new peptidoglycan is coordinated by the bacterial actin cytoskeleton homolog, MreB (93). MreB monomers polymerize into short filaments that rotate approximately perpendicular to the long axis of cells (94); *E. coli* MreB is positioned in contact with the cytoplasmic membrane through an N-terminal amphipathic helix (95). MreB has been hypothesized to localize a complex containing proteins that perform peptidoglycan synthesis and degradation to regions of the cell wall that exhibits negative curvature (96, 97). The directed motion of MreB in these regions of the cell is correlated with peptidoglycan assembly and enables cells to maintain a rod-shape (97). Inhibiting MreB

function causes cells to change gradually in shape from a rod to a sphere (98) due to the undirected and mislocalized insertion of peptidoglycan throughout cells (97).

Several measurements have been performed to determine the contribution of MreB to bacterial cell mechanics. Depolymerization of MreB in *E. coli* cells followed by applying a bending stress demonstrated that these cells had a 30% decrease in bending rigidity compared to wild-type cells (3). Using a compressive force to measures the longitudinal stiffness of cells, no change in stiffness was observed after depolymerizing MreB (2); these results were attributed to the timescale of MreB attachment to the cell wall. Specifically, to affect the longitudinal stiffness, MreB would need to remain attached to the cell membrane for a time scale that is incompatible with the known properties and dynamics of this protein: MreB filaments turnover rapidly, detach from the cell wall, diffuse, and reattach to the cell wall to coordinate peptidoglycan growth (99).

Lpp

Lpp (also referred to as Braun's lipoprotein) is the most abundant lipoprotein in *E. coli* and is located in the inner leaflet of the outer membrane (100). Lpp is present in gram-negative bacteria, but is typically only found in enteric and endosymbiont bacteria as a way to adapt to high-osmolarity environments (84). Lpp is the only known lipoprotein to be covalently attached to the peptidoglycan layer, stitching the outer membrane and

the peptidoglycan together. ~30% of the $5x10^5$ copies of Lpp in each cell are attached to the *meso*–DAP residue in the peptide stem of peptidoglycan (100). Loss of Lpp from cells increases formation of membrane vesicles and decreases membrane integrity (101). In *E. coli*, loss of Lpp reduces the effective rigidity of cells by 42% and decreases the viscosity of the membrane bilayer, which may make cells more deformable to external forces (102).

Techniques to measure the mechanical properties of bacterial cells

The small physical dimensions of bacteria (several μm) present a challenge for measuring their mechanical properties. Early studies of the mechanical properties of bacteria took advantage of tensile testing (a bulk-material technique) to measure the properties of mesoscopic 'threads' consisting of ~10^{10} *B. subtilis* cells and secreted extracellular polymers. Using a needle dipped into a suspension of cells, the authors 'pulled' 60 μm-diameter threads that were large enough to be mounted on a tensile testing instrument, and measured a Young's modulus of 10 MPa (14). This value represents a composite material of cells and extracellular polymers. Most bacteria are unable to form these types of structures—in fact, the strain used in the original report was a *B. subtilis* mutant —and limits this technique for making mechanical measurements of bacteria. Several other techniques have been developed to measure the mechanical properties of bacterial cells, including: microfluidic-based assays,

optical-trapping, polymer-based and atomic force microscopy (AFM). We discuss the application of some of these techniques below:

Atomic force microscopy. AFM is a technique that that has been used to measure the mechanical properties and surface topography of bacteria at nanometer resolution. Briefly, AFM consists of a piezoelectric scanner, laser diode, photodetector, electrical feedback system, and cantilever with a mounted probing tip (103) (the geometry, surface chemistry, and mechanical properties of the tip vary depending on the application). The Young's modulus of a bacterial cell or sample derived from bacteria can be determined by measuring force-distance curves in which the deflection of a cantilever (with an applied load) is measured as a function of the y-displacement of the piezo scanner (104). The force-distance curve is often fit with a Hertz model that assumes a bacterium is an isotropic and linear elastic solid (13). However, not all samples exhibit these idealized properties, and several different models may be required to extract the salient mechanical data (13). Due to the heterogeneity of bacterial samples, peak force tapping AFM is an imaging mode that is being used with increasing frequency as it enables quantitative mapping of the mechanical properties across an entire cell surface (66, 105). AFM is a powerful technique that has provided many insights into the mechanical properties of cells, many of which have been highlighted in previous sections of this review.

Microfluidic-based assays. Microfluidic structures have physical dimensions that can match individual or small groups of cells, and provide unique capabilities for measuring cell mechanics, including: Young's modulus, bending rigidity, and turgor pressure. A microfluidic system for measuring cell bending rigidity was reported in which bacteria are filamented inside of channels positioned so that the majority of the volume of the cell is oriented within a main flow channel (4). The flow of fluid through the central channel bends cells; measuring cell deflection and fitting to a mechanical model enables the determination of bending rigidity. This approach was used to measure the bending rigidity of gram-negative (5×10^{-20} N m^2) and gram-positive bacteria (2.4×10^{-19} N m^2), and extract values of Young's modulus of 30 MPa, and 20 MPa, respectively (4). A shortcoming of this approach is the need to perform all steps of the experiment—including cell growth—in the device. A recent report demonstrates how modifications to this approach improves the ability to prepare cells externally and load (and reload) them, which increases experimental throughput.

Another approach to measuring cell mechanical properties is based on transverse compression. Measuring the rate of change in the radius of curvature of *E. coli* cells under compression was used to extract a Young's modulus value for cells (106). Briefly, cells were placed within a microfluidic device composed of a glass coverslip patterned with 0.8-0.9 μm tall micropillars, composed of positive photoresist, that were positioned

below a PDMS layer that had a height controlled by air pressure. The micropillars ensured that only moderate deformation of the cells (diameter, ~1 μm) occurred. This approach led to measurements of Young's modulus of 22 MPa and a turgor pressure of 140 KPa (~1.4 atm) for *E. coli* cells. Under compression, a concentration of mechanical stress occurred at the periphery of cells and caused membrane blebbing.

Extrusion loading microfluidic techniques have not yet been used to measure specific numerical values for Young's modulus, bending rigidity, or turgor pressure, however they provide a compelling alternative to micropipette based methods, which have been used to study the mechanical properties of neutrophils (107). Extrusion loading microfluidic systems consist of tapered channels; the channel width at the entrance is 1.4 μm and tapers to a width of 250 nm at the exit (16). In one configuration, 12 tapered channels are aligned in parallel and each one applies a load ranging from 0.0037 MPa - 0.045 MPa. It is possible to monitor qualitative changes in bacterial stiffness based on the distance a cell is forced into the tapered channel by the applied load. Using this microfluidic system, Sun et al. (16) qualitatively demonstrated that gram–negative cells (e.g., *E. coli*) were less stiff than gram–positive cells (e.g., *B. subtilis*) (16), an observation that has been previously been reported in the literature (2, 4).

Agarose embedment. We were able to extract the Young's modulus for cell walls of gram-negative (*E. coli* ~100 MPa, *P. aeruginosa* ~150 MPa*)* and gram-positive (*B.*

subtilis~150 MPa) bacteria (2). Briefly, by using microscopy-based growth of single cells embedded in agarose hydrogels of tunable mechanical stiffness we are able to observe a decrease in relative cellular elongation with increasing gel stiffness. Using a finite-element model of the growth of an elastic shell we were able to determine the Young's modulus. We have since determined that the growth of bacteria in agarose can also be monitored by optical density measurements in a plate reader. This has enabled us to screen the non-essential genes of *E. coli* for modulators of cell stiffness, opening up an entirely new world of mechanomicrobiology.

Conclusions

While a great deal is known about the general stiffness properties of bacteria, there still remains much to be discovered. This topic seems well suited for collaborations between microbiologists, biochemists, and engineers as it will require: 1) the development of more approachable techniques for the determination of mechanical properties; 2) elucidating the mechanisms that bacteria use in order to modulate their mechanics; and 3) determination of the role of bacterial mechanics and their importance in cell survival. The work described in this thesis addresses several of these questions on a more fundamental level. Chapter 2 describes the development and validation of a simple methodology for measuring the longitudinal stiffness of the cell wall using embedment in agarose. Chapter 3 describes the development of a high throughput

screening platform that was used to identify novel stiffness-modulating proteins in *E. coli*. This chapter also describes a major role for PBP1b, known to perform cell wall synthesis at the division site, in maintaining bacterial stiffness in vivo and the enzymatic activities that are required. Chapter 4 describes the mechanical changes associated with swarming, a specialized form of surface motility accompanied by a drastic morphological change, in the bacteria *Proteus mirabilis* and *Vibrio parahaemolyticus* and the consequences for survival. Chapter 5 and the appendix summarize and give perspective on the data described herein and suggests avenues for further study.

References

1. Reuter M, *et al.* (2014) Mechanosensitive channels and bacterial cell wall integrity: does life end with a bang or a whimper? *J R Soc Interface* 11(91):20130850.

2. Tuson HH, *et al.* (2012) Measuring the stiffness of bacterial cells from growth rates in hydrogels of tunable elasticity. *Mol Microbiol* 84(5):874-891.

3. Wang S, Arellano-Santoyo H, Combs PA, & Shaevitz JW (2010) Actin-like cytoskeleton filaments contribute to cell mechanics in bacteria. *Proc Natl Acad Sci U S A* 107(20):9182-9185.

4. Amir A, Babaeipour F, McIntosh DB, Nelson DR, & Jun S (2014) Bending forces plastically deform growing bacterial cell walls. *Proc Natl Acad Sci U S A* 111(16):5778-5783.

5. Louise Meyer R, *et al.* (2010) Immobilisation of living bacteria for AFM imaging under physiological conditions. *Ultramicroscopy* 110(11):1349-1357.

6. Suresh S, *et al.* (2005) Connections between single-cell biomechanics and human disease states: gastrointestinal cancer and malaria. *Acta Biomater* 1(1):15-30.

7. Suwanarusk R, *et al.* (2004) The deformability of red blood cells parasitized by Plasmodium falciparum and P. vivax. *J Infect Dis* 189(2):190-194.

8. Boal DH (2002) *Mechanics of the cell* (Cambridge University Press, Cambridge ; New York) pp xiv, 406 pages.

9. Rodriguez ML, McGarry PJ, & Sniadecki NJ (2013) Review on cell mechanics: experimental and modeling approaches. *Appl Mech Rev* 65(6).

10. Olliaro P (2008) Editorial commentary: mortality associated with severe *Plasmodium falciparum* malaria increases with age. *Clin Infect Dis* 47(2):158-160.

11. Cerf A, Cau JC, Vieu C, & Dague E (2009) Nanomechanical properties of dead or alive single-patterned bacteria. *Langmuir* 25(10):5731-5736.

12. Chen YY, *et al.* (2009) Surface rigidity change of *Escherichia coli* after filamentous bacteriophage infection. *Langmuir* 25(8):4607-4614.

13. Gaboriaud F, Bailet S, Dague E, & Jorand F (2005) Surface structure and nanomechanical properties of *Shewanella putrefaciens* bacteria at two pH values (4 and 10) determined by atomic force microscopy. *J Bacteriol* 187(11):3864-3868.

14. Thwaites JJ & Mendelson NH (1985) Biomechanics of bacterial walls: studies of bacterial thread made from *Bacillus subtilis*. *Proc Natl Acad Sci U S A* 82(7):2163-2167.

15. Yao X, Jericho M, Pink D, & Beveridge T (1999) Thickness and elasticity of gram-negative murein sacculi measured by atomic force microscopy. *J Bacteriol* 181(22):6865-6875.

16. Sun X, Weinlandt WD, Patel H, Wu M, & Hernandez CJ (2014) A microfluidic platform for profiling biomechanical properties of bacteria. *Lab Chip* 14(14):2491-2498.

17. Erridge C, Bennett-Guerrero E, & Poxton IR (2002) Structure and function of lipopolysaccharides. *Microbes Infect* 4(8):837-851.

18. Lameire N & Mehta RL (2000) *Complications of dialysis* (M. Dekker, New York) pp xiv, 877 pages.

19. Delcour AH (2009) Outer membrane permeability and antibiotic resistance. *Biochim Biophys Acta* 1794(5):808-816.

20. Yu Z, Qin W, Lin J, Fang S, & Qiu J (2015) Antibacterial mechanisms of polymyxin and bacterial resistance. *Biomed Res Int* 2015:679109.

21. Steeghs L, *et al.* (1998) Meningitis bacterium is viable without endotoxin. *Nature* 392(6675):449-450.

22. Lerouge I & Vanderleyden J (2002) O-antigen structural variation: mechanisms and possible roles in animal/plant-microbe interactions. *FEMS Microbiol Rev* 26(1):17-47.

23. Smit J, Kamio Y, & Nikaido H (1975) Outer membrane of *Salmonella typhimurium*: chemical analysis and freeze-fracture studies with lipopolysaccharide mutants. *J Bacteriol* 124(2):942-958.

24. Yethon JA, Heinrichs DE, Monteiro MA, Perry MB, & Whitfield C (1998) Involvement of *waaY*, *waaQ*, and *waaP* in the modification of *Escherichia coli* lipopolysaccharide and their role in the formation of a stable outer membrane. *J Biol Chem* 273(41):26310-26316.

25. Linkevicius M, Anderssen JM, Sandegren L, & Andersson DI (2016) Fitness of *Escherichia coli* mutants with reduced susceptibility to tigecycline. *J Antimicrob Chemother*.

26. Amro NA, *et al.* (2000) High-resolution atomic force microscopy studies of the *Escherichia coli* outer membrane: Structural basis for permeability. *Langmuir* 16(6):2789-2796.

27. Clifton LA, *et al.* (2015) Effect of divalent cation removal on the structure of gram-negative bacterial outer membrane models. *Langmuir* 31(1):404-412.

28. Labischinski H, *et al.* (1985) High state of order of isolated bacterial lipopolysaccharide and its possible contribution to the permeation barrier property of the outer membrane. *J Bacteriol* 162(1):9-20.

29. Naumann D, Schultz C, Sabisch A, Kastowsky M, & Labischinski H (1989) New insights into the phase behavior of a complex anionic amphiphile: architecture and dynamics of bacterial deep rough lipopolysaccharide membranes as seen by FTIR, X-Ray, and molecular modeling techniques. *J Mol Struct* 214:213-246.

30. Le Brun AP, *et al.* (2013) Structural characterization of a model gram-negative bacterial surface using lipopolysaccharides from rough strains of *Escherichia coli*. *Biomacromolecules* 14(6):2014-2022.

31. Herrmann M, Schneck E, Gutsmann T, Brandenburg K, & Tanaka M (2015) Bacterial lipopolysaccharides form physically cross-linked, two-dimensional gels in the presence of divalent cations. *Soft Matter* 11(30):6037-6044.

32. Ivanov IE, *et al.* (2011) Relating the physical properties of *Pseudomonas aeruginosa* lipopolysaccharides to virulence by atomic force microscopy. *J Bacteriol* 193(5):1259-1266.

33. Gaboriaud F, *et al.* (2006) Multiscale dynamics of the cell envelope of *Shewanella putrefaciens* as a response to pH change. *Colloid Surface B* 52(2):108-116.

34. Kamio Y & Nikaido H (1976) Outer membrane of *Salmonella typhimurium*: accessibility of phospholipid head groups to phospholipase c and cyanogen bromide activated dextran in the external medium. *Biochemistry-Us* 15(12):2561-2570.

35. Brown S, Santa Maria JP, Jr., & Walker S (2013) Wall teichoic acids of gram-positive bacteria. *Annu Rev Microbiol* 67:313-336.

36. D'Elia MA, Millar KE, Beveridge TJ, & Brown ED (2006) Wall teichoic acid polymers are dispensable for cell viability in Bacillus subtilis. *J Bacteriol* 188(23):8313-8316.

37. Swoboda JG, Campbell J, Meredith TC, & Walker S (2010) Wall teichoic acid function, biosynthesis, and inhibition. *Chembiochem* 11(1):35-45.

38. Araki Y & Ito E (1989) Linkage units in cell walls of gram-positive bacteria. *Crit Rev Microbiol* 17(2):121-135.

39. Hancock IC (1997) Bacterial cell surface carbohydrates: structure and assembly. *Biochem Soc Trans* 25(1):183-187.

40. Weidenmaier C & Peschel A (2008) Teichoic acids and related cell-wall glycopolymers in Gram-positive physiology and host interactions. *Nat Rev Microbiol* 6(4):276-287.

41. Santa Maria JP, Jr., *et al.* (2014) Compound-gene interaction mapping reveals distinct roles for *Staphylococcus aureus* teichoic acids. *Proc Natl Acad Sci U S A* 111(34):12510-12515.

42. Schirner K, Marles-Wright J, Lewis RJ, & Errington J (2009) Distinct and essential morphogenic functions for wall- and lipo-teichoic acids in *Bacillus subtilis*. *Embo J* 28(7):830-842.

43. Marquis RE (1973) Immersion refractometry of isolated bacterial cell walls. *J Bacteriol* 116(3):1273-1279.

44. Percy MG & Grundling A (2014) Lipoteichoic acid synthesis and function in gram-positive bacteria. *Annu Rev Microbiol* 68:81-100.

45. Corrigan RM, Abbott JC, Burhenne H, Kaever V, & Grundling A (2011) c-di-AMP is a new second messenger in *Staphylococcus aureus* with a role in controlling cell size and envelope stress. *Plos Pathog* 7(9):e1002217.

46. Oku Y, *et al.* (2009) Pleiotropic roles of polyglycerolphosphate synthase of lipoteichoic acid in growth of *Staphylococcus aureus* cells. *J Bacteriol* 191(1):141-151.

47. Saar-Dover R, *et al.* (2012) D-alanylation of lipoteichoic acids confers resistance to cationic peptides in group B streptococcus by increasing the cell wall density. *Plos Pathog* 8(9):e1002891.

48. Gutberlet T, Markwitz S, Labischinski H, & Bradaczek H (1991) Monolayer investigations on the bacterial amphiphile lipoteichoic acid and on lipoteichoic acid dipalmitoyl-phosphatidylglycerol mixtures. *Makromol Chem-M Symp* 46:283-287.

49. Gutberlet T, Frank J, Bradaczek H, & Fischer W (1997) Effect of lipoteichoic acid on thermotropic membrane properties. *J Bacteriol* 179(9):2879-2883.

50. Labischinski H, Naumann D, & Fischer W (1991) Small and medium-angle X-ray analysis of bacterial lipoteichoic acid phase structure. *Eur J Biochem* 202(3):1269-1274.

51. Razin S, Yogev D, & Naot Y (1998) Molecular biology and pathogenicity of mycoplasmas. *Microbiol Mol Biol Rev* 62(4):1094-1156.

52. Vollmer W (2007) Structure and biosynthesis of the murein (peptidoglycan) sacculus. *Periplasm*:198-213.

53. Gan L, Chen S, & Jensen GJ (2008) Molecular organization of Gram-negative peptidoglycan. *Proc Natl Acad Sci U S A* 105(48):18953-18957.

54. Beeby M, Gumbart JC, Roux B, & Jensen GJ (2013) Architecture and assembly of the Gram-positive cell wall. *Mol Microbiol* 88(4):664-672.

55. Matias VR & Beveridge TJ (2005) Cryo-electron microscopy reveals native polymeric cell wall structure in *Bacillus subtilis* 168 and the existence of a periplasmic space. *Mol Microbiol* 56(1):240-251.

56. Matias VR & Beveridge TJ (2006) Native cell wall organization shown by cryo-electron microscopy confirms the existence of a periplasmic space in *Staphylococcus aureus*. *J Bacteriol* 188(3):1011-1021.

57. Vollmer W, Blanot D, & de Pedro MA (2008) Peptidoglycan structure and architecture. *FEMS Microbiol Rev* 32(2):149-167.

58. Ghosh AS, Chowdhury C, & Nelson DE (2008) Physiological functions of D-alanine carboxypeptidases in *Escherichia coli*. *Trends Microbiol* 16(7):309-317.

59. Lavollay M, *et al.* (2008) The peptidoglycan of stationary-phase *Mycobacterium tuberculosis* predominantly contains cross-links generated by L,D-transpeptidation. *J Bacteriol* 190(12):4360-4366.

60. Peltier J, *et al.* (2011) *Clostridium difficile* has an original peptidoglycan structure with a high level of N-acetylglucosamine deacetylation and mainly 3-3 cross-links. *J Biol Chem* 286(33):29053-29062.

61. Atrih A, Bacher G, Allmaier G, Williamson MP, & Foster SJ (1999) Analysis of peptidoglycan structure from vegetative cells of *Bacillus subtilis* 168 and role of PBP 5 in peptidoglycan maturation. *J Bacteriol* 181(13):3956-3966.

62. Navarre WW & Schneewind O (1999) Surface proteins of gram-positive bacteria and mechanisms of their targeting to the cell wall envelope. *Microbiol Mol Biol R* 63(1):174-229.

63. Vollmer W & Bertsche U (2008) Murein (peptidoglycan) structure, architecture and biosynthesis in *Escherichia coli*. *Biochim Biophys Acta* 1778(9):1714-1734.

64. Desmarais SM, De Pedro MA, Cava F, & Huang KC (2013) Peptidoglycan at its peaks: how chromatographic analyses can reveal bacterial cell wall structure and assembly. *Mol Microbiol* 89(1):1-13.

65. Glauner B (1988) Separation and quantification of muropeptides with high-performance liquid chromatography. *Anal Biochem* 172(2):451-464.

66. Dover RS, Bitler A, Shimoni E, Trieu-Cuot P, & Shai Y (2015) Multiparametric AFM reveals turgor-responsive net-like peptidoglycan architecture in live streptococci. *Nat Commun* 6:7193.

67. Turner RD, Hurd AF, Cadby A, Hobbs JK, & Foster SJ (2013) Cell wall elongation mode in Gram-negative bacteria is determined by peptidoglycan architecture. *Nat Commun* 4:1496.

68. Gumbart JC, Beeby M, Jensen GJ, & Roux B (2014) *Escherichia coli* peptidoglycan structure and mechanics as predicted by atomic-scale simulations. *Plos Comput Biol* 10(2):e1003475.

69. van den Bogaart G, Hermans N, Krasnikov V, & Poolman B (2007) Protein mobility and diffusive barriers in Escherichia coli: consequences of osmotic stress. *Mol Microbiol* 64(3):858-871.

70. Kim SJ, Chang J, & Singh M (2015) Peptidoglycan architecture of Gram-positive bacteria by solid-state NMR. *Biochim Biophys Acta* 1848(1 Pt B):350-362.

71. Ghuysen JM (1989) The rigid matrix of bacterial-cell walls - a citation classic commentary on the use of bacteriolytic enzymes in determination of wall structure and their role in cell-metabolism. *Cc/Agr Biol Environ* (25):20.

72. Hayhurst EJ, Kailas L, Hobbs JK, & Foster SJ (2008) Cell wall peptidoglycan architecture in *Bacillus subtilis*. *Proc Natl Acad Sci U S A* 105(38):14603-14608.

73. Vollmer W & Holtje JV (2001) Morphogenesis of Escherichia coli. *Curr Opin Microbiol* 4(6):625-633.

74. Pelling AE, Li Y, Shi W, & Gimzewski JK (2005) Nanoscale visualization and characterization of *Myxococcus xanthus* cells with atomic force microscopy. *Proc Natl Acad Sci U S A* 102(18):6484-6489.

75. Schar-Zammaretti P & Ubbink J (2003) The cell wall of lactic acid bacteria: surface constituents and macromolecular conformations. *Biophys J* 85(6):4076-4092.

76. Thwaites JJ, Surana UC, & Jones AM (1991) Mechanical properties of *Bacillus subtilis* cell walls: effects of ions and lysozyme. *J Bacteriol* 173(1):204-210.

77. Sauvage E, Kerff F, Terrak M, Ayala JA, & Charlier P (2008) The penicillin-binding proteins: structure and role in peptidoglycan biosynthesis. *FEMS Microbiol Rev* 32(2):234-258.

78. Kuhner D, Stahl M, Demircioglu DD, & Bertsche U (2014) From cells to muropeptide structures in 24 h: peptidoglycan mapping by UPLC-MS. *Sci Rep* 4:7494.

79. Francius G, Domenech O, Mingeot-Leclercq MP, & Dufrene YF (2008) Direct observation of *Staphylococcus aureus* cell wall digestion by lysostaphin. *J Bacteriol* 190(24):7904-7909.

80. Loskill P, *et al.* (2014) Reduction of the peptidoglycan crosslinking causes a decrease in stiffness of the *Staphylococcus aureus* cell envelope. *Biophys J* 107(5):1082-1089.

81. Wheeler R, *et al.* (2015) Bacterial Cell Enlargement Requires Control of Cell Wall Stiffness Mediated by Peptidoglycan Hydrolases. *MBio* 6(4):e00660.

82. Vollmer W & Holtje JV (2004) The architecture of the murein (peptidoglycan) in gram-negative bacteria: vertical scaffold or horizontal layer(s)? *J Bacteriol* 186(18):5978-5987.

83. Schwechheimer C & Kuehn MJ (2015) Outer-membrane vesicles from Gram-negative bacteria: biogenesis and functions. *Nat Rev Microbiol* 13(10):605-619.

84. Yeh YC, Comolli LR, Downing KH, Shapiro L, & McAdams HH (2010) The caulobacter Tol-Pal complex is essential for outer membrane integrity and the positioning of a polar localization factor. *J Bacteriol* 192(19):4847-4858.

85. Clavel T, Germon P, Vianney A, Portalier R, & Lazzaroni JC (1998) TolB protein of *Escherichia coli* K-12 interacts with the outer membrane peptidoglycan-associated proteins Pal, Lpp and OmpA. *Mol Microbiol* 29(1):359-367.

86. Vance DE & Vance JE (2008) *Biochemistry of lipids, lipoproteins and membranes* (Elsevier, Amsterdam ; Boston) Fifth edition. Ed pp xii, 631 pages, 638 unnumbered pages of plates.

87. Purushothaman S, Cicuta P, Ces O, & Brooks NJ (2015) Influence of High Pressure on the Bending Rigidity of Model Membranes. *J Phys Chem B* 119(30):9805-9810.

88. Bermudez H, Hammer DA, & Discher DE (2004) Effect of bilayer thickness on membrane bending rigidity. *Langmuir* 20(3):540-543.

89. Phillips R, Ursell T, Wiggins P, & Sens P (2009) Emerging roles for lipids in shaping membrane-protein function. *Nature* 459(7245):379-385.

90. Russell NJ & Nichols DS (1999) Polyunsaturated fatty acids in marine bacteria--a dogma rewritten. *Microbiology* 145 (Pt 4):767-779.

91. Olbrich K, Rawicz W, Needham D, & Evans E (2000) Water permeability and mechanical strength of polyunsaturated lipid bilayers. *Biophys J* 79(1):321-327.

92. White GF, Racher KI, Lipski A, Hallett FR, & Wood JM (2000) Physical properties of liposomes and proteoliposomes prepared from *Escherichia coli* polar lipids. *Biochim Biophys Acta* 1468(1-2):175-186.

93. Jones LJ, Carballido-Lopez R, & Errington J (2001) Control of cell shape in bacteria: helical, actin-like filaments in *Bacillus subtilis*. *Cell* 104(6):913-922.

94. White CL & Gober JW (2012) MreB: pilot or passenger of cell wall synthesis? *Trends Microbiol* 20(2):74-79.

95. Salje J, van den Ent F, de Boer P, & Lowe J (2011) Direct membrane binding by bacterial actin MreB. *Mol Cell* 43(3):478-487.

96. Renner LD, Eswaramoorthy P, Ramamurthi KS, & Weibel DB (2013) Studying biomolecule localization by engineering bacterial cell wall curvature. *Plos One* 8(12):e84143.

97. Ursell TS, *et al.* (2014) Rod-like bacterial shape is maintained by feedback between cell curvature and cytoskeletal localization. *Proc Natl Acad Sci U S A* 111(11):E1025-1034.

98. Bean GJ, *et al.* (2009) A22 disrupts the bacterial actin cytoskeleton by directly binding and inducing a low-affinity state in MreB. *Biochemistry-Us* 48(22):4852-4857.

99. Defeu Soufo HJ, *et al.* (2010) Bacterial translation elongation factor EF-Tu interacts and colocalizes with actin-like MreB protein. *Proc Natl Acad Sci U S A* 107(7):3163-3168.

100. Cowles CE, Li Y, Semmelhack MF, Cristea IM, & Silhavy TJ (2011) The free and bound forms of Lpp occupy distinct subcellular locations in *Escherichia coli*. *Mol Microbiol* 79(5):1168-1181.

101. Cascales E, Bernadac A, Gavioli M, Lazzaroni JC, & Lloubes R (2002) Pal lipoprotein of *Escherichia coli* plays a major role in outer membrane integrity. *J Bacteriol* 184(3):754-759.

102. Vadillo-Rodriguez V, Schooling SR, & Dutcher JR (2009) In situ characterization of differences in the viscoelastic response of individual gram-negative and gram-positive bacterial cells. *J Bacteriol* 191(17):5518-5525.

103. Binnig G, Quate CF, & Gerber C (1986) Atomic force microscope. *Phys Rev Lett* 56(9):930-933.

104. Dufrene YF (2002) Atomic force microscopy, a powerful tool in microbiology. *J Bacteriol* 184(19):5205-5213.

105. Deng Y, Sun M, & Shaevitz JW (2011) Direct measurement of cell wall stress stiffening and turgor pressure in live bacterial cells. *Phys Rev Lett* 107(15):158101.

106. Si F, Li B, Margolin W, & Sun SX (2015) Bacterial growth and form under mechanical compression. *Sci Rep* 5:11367.

107. Needham D & Hochmuth RM (1992) A sensitive measure of surface stress in the resting neutrophil. *Biophys J* 61(6):1664-1670.

Chapter 2

Measuring the stiffness of bacterial cells from growth rates in hydrogels of tunable elasticity

Adapted from

George K. Auer^, Hannah H. Tuson^, Lars D. Renner, Mariko Hasebe, Carolina Tropini, Max Salick, Wendy C. Crone, Ajay Gopinathan, Kerwyn Casey Huang, Douglas B. Weibel, *Molecular Microbiology* (2012) 84: 874 – 891

^Equal contributions

G.K.A. and H.H.T. designed and conducted experiments, analysed data and wrote paper. L.D.R, M.H., and M.S. conducted experiments. C.T. conducted experiments and analysed data. W.C.C. provided equipment. A.G. performed simulations. K.C.H. and D.B.W. designed experiments and wrote paper.

Abstract

Although bacterial cells are known to experience large forces from osmotic pressure differences and their local microenvironment, quantitative measurements of the mechanical properties of *growing* bacterial cells have been limited. We provide an experimental approach and theoretical framework for measuring the mechanical properties of live bacteria. We encapsulated bacteria in agarose with a user-defined stiffness, measured the growth rate of individual cells, and fit data to a thin-shell mechanical model to extract the effective longitudinal Young's modulus, a measure of stiffness, of the cell envelope of *Escherichia coli* MG1655 (50-150 MPa), *Bacillus subtilis* BB11 (100-200 MPa), and *Pseudomonas aeruginosa* PAO1 (100-200 MPa). Our data provide estimates of cell wall stiffness similar to values obtained via the more labor-intensive and expensive technique of atomic force microscopy. To address physiological perturbations that produce changes in cellular mechanical properties, we tested the effect of A22-induced MreB depolymerization on the stiffness of *E. coli* MG1655. The effective longitudinal Young's modulus was not significantly affected by A22 treatment at short time scales, supporting a model in which the interactions between MreB and the cell wall persist on the same time scale as growth. Our technique therefore enables the rapid determination of how changes in genotype and biochemistry affect the mechanical properties of the bacterial envelope.

Introduction

The bacterial cell wall is a rigid network surrounding the cytoplasmic membrane that is required for cellular integrity and the maintenance of cell shape in virtually all eubacteria. The cell wall is composed of peptidoglycan, a macromolecule consisting of polysaccharides cross-linked by peptide bonds, and bears the stress of turgor pressures as high as 25 atmospheres to protect bacteria from osmotic shock and mechanical stress (1, 2). The cell wall is hydrated (~85% of the mass is bound water (3)), stiff, viscoelastic, and is the primary load-bearing material in both Gram-negative and Gram-positive bacteria (4, 5).

Peptidoglycan synthesis, remodeling, and regulation are central to bacterial physiology, with cell shape and size directly involved in a variety of critical functions including division, cell motility, cellular differentiation, and immunity. A growing body of evidence suggests that cytoskeletal proteins control the spatial organization of peptidoglycan growth in replicating bacteria and participate in regulating the size and shape of cells. Electron cryotomography has revealed a common peptidoglycan ultrastructure in isolated, intact cell walls (sacculi) from *Escherichia coli* and *Caulobacter crescentus* with a single, 2 to 4-nm-thick layer of glycan strands that are preferentially oriented circumferentially around the cylindrical cell body (6). In *Bacillus subtilis*, there is evidence that the glycan strands form cables that have an orientation similar to that in *E. coli* and *C. crescentus* (7). Theoretical models have provided a framework for inferring the molecular stiffness of the peptide crosslinks from macroscopic measurements of the

peptidoglycan Young's modulus (8) and determining the consequent effects on cell shape (9, 10).

Although peptidoglycan is widely conserved in bacteria, our understanding of its physical properties is limited to studies from a small number of model organisms, and it is unclear how pertinent these characteristics are across bacteria. The stiffness of a material can be described by the tensile elasticity or Young's modulus (E), which is measured in units of Pa (N m^{-2}) and represents the ratio between the applied stress on the material (force per unit area) and the resulting strain (fractional change in length). The Young's modulus is analogous to the force constant describing the restoring force exerted by a stretched spring: for a block of material of length L, the force F required to cause a fractional length change $\Delta L/L_0$ is $F = EA\Delta L/L_0$, where A is the area of the face onto which the force is applied. In principle, the Young's modulus can vary depending on the direction of the applied force; our analysis focuses on the modulus in the direction of growth: that is, along the long axis of the cell. For a thin shell similar to the cell wall of a rod-shaped bacterium in which the cross-sectional face is an annulus of width d, the force required for extension in the longitudinal direction increases linearly with d. A Gram-positive cell with a thicker wall (and thus a greater cross-sectional area) will require a larger force for its extension than a Gram-negative cell with a thinner wall. As a result, a Gram-positive cell will extend less at a given stress (such as turgor pressure) if the Young's modulus of the wall is the same as a Gram-negative cell.

Representing the elastic properties of a material as a single value of the Young's modulus assumes a linear response (force linearly proportional to extension); a nonlinear response can be translated into a range of values of the Young's modulus.

Tensile strength measurements and atomic force microscopy (AFM) are two methods that have been used to measure the Young's modulus for intact peptidoglycan fragments and for both live and dead bacterial cells. Using tensile strength measurements, Thwaites and Mendelson studied extruded filaments of cells from *B. subtilis* strain FJ7 (Δ*lyt*) and determined that the Young's modulus of the cells (E_{cell}) was ~30 MPa (Table 1) (11-13). Although this method is conceptually straightforward, an obvious disadvantage is that most bacterial strains do not form mesoscopic threads and hence are not compatible with this technique.

In a typical AFM experiment, cells are immobilized on a surface and imaged using contact- or tapping-mode AFM. Force curves are measured at various locations on the cell surface and are fit to a model of cell mechanics to extract the Young's modulus. AFM has been used to measure E_{cell} for several Gram-positive and Gram-negative bacteria using force spectroscopy or force-volume mode measurements, although reported values vary by several orders of magnitude, even for a single species (Table 1). Despite the quantitative nature of AFM, several technical challenges remain, most notably: 1) modulus measurements are typically restricted to a small area of the cell surface, which can lead to large standard deviations (14); 2) local deformations of

the cell wall may be larger than the diameter of the probe (15); 3) meticulous sample preparation, measurements, and data analysis are required; and 4) the cost, throughput, and availability of these instruments in microbiology labs is generally prohibitive. Therefore, a technique for the rapid screening of strains, mutants, or environmental conditions that influence the mechanical properties of the cell wall *in vivo* will be critical for expanding the exploration of mechanical properties initiated by AFM studies.

Here we report a new technique for measuring the mechanical properties of bacterial cells *in vivo* that we refer to as **C**ell **L**ength **A**nalysis of **M**echanical **P**roperties (CLAMP). This methodology represents a first step in developing a high-throughput capability for measuring bacterial cell stiffness in a species-independent manner. As the cell envelope is a complex structure consisting of multiple materials, we refer to this stiffness as an effective Young's modulus (E_{cell}). CLAMP combines quantitative analysis of time-lapse imaging and biophysical modeling to enable the determination of E_{cell} using standard equipment found in microbiology labs. We encapsulated bacterial cells in layers of agarose with a user-defined stiffness (E_{gel}), determined the initial growth rates of individual cells in hydrogels of varying stiffness using phase-contrast optical microscopy, and fit the data to three-dimensional finite-element simulations to determine E_{cell}. The synthesis of biophysical theory and experiment has previously been successful in elucidating the mechanisms by which bacteria determine and maintain

their shape (9, 10); here we employed modeling to establish a framework for interpreting CLAMP-derived imaging data.

We used CLAMP to measure and compare E_{cell} for *E. coli* MG1655, *Pseudomonas aeruginosa* PAO1, and *B. subtilis* BB11. Despite the differences in cell wall thickness among these species, our results suggest that the Young's moduli of the cell envelopes are similar, indicating that these species may share a common network architecture. We also found that depolymerization of MreB using the small molecule A22 did not significantly affect the longitudinal stiffness of *E. coli* cells, illustrating the utility of CLAMP in the study of how physiological perturbations affect the mechanical properties of bacterial cells. CLAMP therefore provides an integrated experimental and computational platform that enables fundamental studies of the bacterial cell wall. We envision that this paradigm will become the foundation for physical studies of living cells.

Materials and Methods

Preparation of agarose prepolymer. Stock solutions of 5% and 8% w/v UltraPure agarose (Invitrogen Corporation, Carlsbad, CA, USA) were prepared by dissolving agarose in 100 mL of Luria Bertani (LB) medium consisting of tryptone (1% w/v), yeast extract (0.5% w/v), and sodium chloride (1% w/v). The stock solution was autoclaved and stored at 100 °C on a heated magnetic stirrer. Working solutions were prepared by mixing LB prewarmed to 65 °C with the required volume of the agarose stock solution. We prepared 1-5% (w/v) agarose working solutions from the 5% w/v agarose stock and 6-8% (w/v) agarose working solutions from the 8% agarose stock. The gels were visually homogeneous, with no particulates or deformations observed under high magnification.

Growth of bacterial strains. Individual liquid cultures of *E. coli* MG1655 and *P. aeruginosa* PAO1 were prepared by diluting overnight cultures 1:100 into fresh LB. Liquid cultures of *B. subtilis* BB11 were prepared by diluting an overnight culture 1:100 into fresh LB containing 1 mM IPTG and 2 μg mL^{-1} phleomycin. Liquid cultures of *E. coli* FB76 (16) were prepared by diluting an overnight culture 1:100 into fresh LB containing 25 μg mL^{-1} chloramphenicol. All cultures were grown in a shaker at 37 °C with shaking to an absorbance of 0.6 (λ = 600 nm).

Microfluidic flow chamber growth measurements. Cells were grown to an absorbance of 0.1 (λ = 600 nm) in LB, diluted 1:100, and loaded into an ONIX Microfluidic Plate (CellASIC Corporation, Hayward, CA, USA). *B. subtilis* BB11 was grown supplemented with 1 mM IPTG and 2 μg mL^{-1} phleomycin. Cells were imaged for 30 min at 30 s intervals using a Nikon Eclipse Ti-E inverted microscope running μManager and equipped with a Nikon Plan Apo 100X objective (numerical aperture of 1.4). To measure whether a change in growth rate occurred when *E. coli* MG1655 cells were treated with A22, cells were seeded into the ONIX chip at an absorbance of 0.001 (λ = 600 nm); after 30 min the media was switched to LB supplemented with 10 μg mL^{-1} A22, and imaging was continued for an additional 30 min.

Cell length measurements were obtained using MicrobeTracker (17); fractional extension growth curves and fits were performed using custom MATLAB (The MathWorks, Natick, MA, USA) code. Growth curves that showed unusually large length variation in a single 30 s time step were rejected as a result of probable noise in MicrobeTracker length fitting. Cells that did not grow more than ~2% in the first 5 min were also discarded. Growth curves were fit to the exponential function $A \exp(at)$.

Preparation of polydimethylsiloxane (PDMS) chambers. PDMS elastomer (Dow Corning, Midland, MI, USA) was prepared at a ratio of 10:1 base:curing agent. We used

a spincoater (Laurell Technology Corporation, North Wales, PA, USA) to coat #1.5 glass cover slips with a 250-μm thick layer of PDMS prepolymer. The PDMS was polymerized by incubating the cover slips for 8-10 h at 65 °C. To prepare a chamber for defining the geometry of the agarose gel, we used a scalpel to cut a square 15 mm x 15 mm opening in the center of the PDMS layer; the height of the chamber was 250 μm.

Encapsulation of live bacterial cells in agarose gels. An aliquot (17 mL) of a log-phase liquid bacterial culture was centrifuged for 5 min at 3000 × *g*. We resuspended the resulting cell pellet in 12 mL LB and centrifuged again for 5 min at 3000 × *g*. The resulting cell pellet was resuspended in 200 μL LB and used for cell encapsulation experiments. Immediately before each experiment, a stock solution of the agarose prepolymer was prepared as described above; from the stock solution, we prepared 10-mL working solutions of agarose and incubated them at 65 °C for 5 min to equilibrate. For epifluorescence imaging of strain FB76, the agarose stock solution was made using 1X phosphate-buffered saline rather than LB to reduce background fluorescence. We incubated the working solutions in a 37 °C water bath for 1 min prior to the addition of cells. The bacterial cell suspension (200 μL) was incubated at 37 °C for 2 min and added to the working solution. Two hundred microliters of the cell/agarose suspension was poured into a PDMS chamber that was pre-warmed to 42 °C on a plate heater to ensure that higher-percentage agarose gels did not polymerize instantly. A glass cover slip was

pressed against the surface of the PDMS jig and excess molten agarose was forced out, resulting in a 250-μm thick agarose pad. The gel was incubated on the plate heater for 1 min and then removed and gelled at 25 °C. The top glass cover slip was removed from the chamber, the gel was overlaid with LB, the bottom cover slip containing the gel was positioned on the stage of an inverted microscope, and the cells were imaged.

Imaging cells. We measured the growth rates of cells encapsulated in agarose gels using phase optics on a TE2000-E+PFS inverted microscope (Nikon, Tokyo, Japan) equipped with a heated stage (Tokai hit, Fujinomiya, Japan), an objective heater (Bioptechs, Butler, PA, USA), and a CoolSNAP DV2 camera (Photometrics, Munich, Germany). The objective heater and heated stage were held at 37 °C. We used a Nikon PlanApo 60X oil objective to capture a field of view containing multiple well-separated cells. We imaged cells at focal planes that were ~50 μm below the surface of the gel to ensure that cells: 1) were completely encapsulated in agarose and were located far enough from the gel edge to avoid mechanical effects from the edge of the agarose; 2) exchanged gas rapidly, which enabled strictly aerobic bacteria such as *B. subtilis* to grow; and 3) were kept in a region of the gel at a constant temperature. We acquired phase-contrast images at 1-min intervals over 30 min.

Data analysis. We analyzed time-lapse images using MATLAB 2010b (The MathWorks, Inc., Natick, MA, USA) script MicrobeTracker (17) and determined the length of individual cells as a function of time. We manually discarded data from cells that were egregiously out-of-plane at any stage and growth curves in which errors in cell outline detection led to large, unphysiological jumps in extension. Moreover, small errors in cell-length measurements due to out-of-plane growth would not affect our analysis of the *relative* cell length increase $\Delta L/L_0$, since any out-of-plane correction will affect ΔL and L_0 proportionately. The MicrobeTracker parameter file is provided in Table 2. Average growth curves were determined from measurements of 17-51 cells from each species at each agarose concentration.

Measuring the Young's modulus of agarose gels (E_{gel}). Agarose gels (1-8% w/v) were prepared immediately prior to tensile testing and stored in ddH_2O to keep them hydrated; they were prepared as described above without encapsulated cells. Gels were cast in a custom-fabricated mold to comply with the specifications of ASTM D 638-03 type IV samples with a gage length of 44.5 mm (18). We used an Instron Model 5548 MicroTester (Instron, Norwood, MA, USA) equipped with a 10-N load cell and custom self-aligning grips to measure the tensile properties of the gels. For each concentration, we measured the mechanical properties of 3 to 9 agarose gels by elongating them at a rate of 10 mm min^{-1} until fracture. Tests were conducted in ambient conditions. Sample

cross sections were measured with calipers, and cross head displacement was used to measure extension. E_{gel} was determined by calculating the slope of the linear region of the stress vs. strain response (Figure 1, 2).

Rate of growth of E. coli cells on agarose surfaces. To determine whether cell contact with agarose influenced cell growth, we measured the growth rate of *E. coli* MG1655 on gel surfaces. Cells were cultured and prepared as described above, and a 5-μL aliquot was transferred onto the surfaces of 1%, 3%, and 5% w/v agarose gels. We inverted the gels onto a glass cover slip and imaged cell growth at 1-min intervals for 60 min at 37 °C. The elongation rate was determined using MicrobeTracker, and the doubling time was determined from data for individual cells; average growth curves were essentially independent of gel stiffness (Figure 3).

Metabolic activity of bacteria encapsulated in agarose gels. We used the redox indicator 5-cyano-2,3-ditolyltetrazolium chloride (CTC) to measure the metabolic activity of *E. coli* MG1655 cells encapsulated in gels (5% w/v) in which the mechanical resistance of the gel to cell growth was large. Following encapsulation, the gels were overlaid with 200 μL LB and incubated at 37 °C. After 0, 30, 60, and 90 min of incubation, we removed the LB from the gel surface and overlaid a solution of 25 mM CTC on top of the agarose. We incubated for 30 min to allow the CTC to diffuse through

the gel, after which the equilibrium concentration of CTC in the gel was 50 μM. We then imaged cells using epifluorescence microscopy ($\lambda_{excitation}$ = 484 nm; $\lambda_{emission}$ = 620 nm) on a Nikon TE2000 inverted microscope using an Andor iXon EMCCD (Belfast, Northern Ireland). As a negative control, we killed *E. coli* MG1655 cells by exposing them to 80% ethanol for 15 min, added CTC to a final concentration of 50 μM, incubated for 30 min, transferred the cells to an agarose pad, and imaged using phase contrast and epifluorescence microscopy. CTC did not label these cells (Figure 4).

Effect of A22 on the mechanical properties of E. coli cells. We determined the effect of MreB depolymerization on *E. coli* MG1655 stiffness by adding S-(3,4-dichlorobenzyl)isothiourea (A22) to the agarose during cell encapsulation; the compound was synthesized according to published procedures and recrystallized three times (19). Cells and agarose working solutions were prepared as described, except that during the preparation of the agarose working solution, A22 was added to the LB to a final concentration in the gel of 10 μg mL^{-1}. The encapsulation of cells in agarose containing A22 caused rapid delocalization of MreB (Figure 5).

Computational methods. Using the finite-element analysis software COMSOL 4.2 (COMSOL, Inc., Burlington, MA, USA), we represented a cell as a thin cylindrical shell with hemispherical endcaps. The thickness of the shell was 30 nm, and the cylinder had

a radius of 0.5 mm and a length of 4 mm for *E. coli* and *P. aeruginosa* or 8 mm for *B. subtilis*. For *E. coli* and *P. aeruginosa*, E_{cell} was scaled by a factor of 4/30 to mimic the surface modulus of a shell with thickness 4 nm. We set the Young's modulus of the endcaps to 1000 MPa to focus on the elongation of the cylindrical region. The surrounding gel was a cylindrical volume 50 mm in length along the long axis of the cell and 20 mm in diameter along the other two dimensions. E_{gel} was varied according to the gel moduli in Figure 1, while E_{cell} was varied from 10 to 250 MPa. Most rigid polymers have a Poisson ratio between 0.3 and 0.5 (20), thus we assumed a Poisson ratio of n = 0.4 for all 3D simulations; the precise value of n has little effect on our results. To mimic elongation of the cylindrical body, the rest length of the cylinder was increased by 1%. After the cell and gel relaxed to a new mechanical equilibrium, the length of the cell was measured to compute the relative extension $\Delta L/L_0$.

Results

Experimental system for measuring cell elongation in hydrogels. We designed our experimental system (Figure 6) to be a quantitative, reproducible assay that is capable of medium- or high-throughput analysis of cell stiffness. This approach is technically straight-forward, incorporates components found in most biological labs, and consists of an extendable platform that accommodates the assaying of cellular mechanical properties in a wide variety of bacteria and other organisms, including yeast and fungi. We used agarose as the polymer for encapsulating bacteria for several reasons, including: 1) it is biocompatible and has been used previously to encapsulate a variety of cell types, including bacteria (21-23); 2) it is chemically and mechanically stable and may be polymerized with user-defined stiffness spanning the kPa to MPa regime (Figs. 1, 2); 3) it is relatively transparent to the diffusion of ions, small molecules, secondary metabolites, metabolic waste, and gases, which is an important feature for maintaining normal cell growth; 4) it hydrates encapsulated cells, a critical factor impacting measurements of E_{cell} by AFM (Table 1); and 5) bacteria in contact with agarose continue to grow (Figure 3).

We encapsulated cells in agarose layers and measured their growth using phase-contrast microscopy and automated image analysis (Figure 6). In a typical experiment we adjusted the imaging focal plane of the microscope so that it extended ~50 μm into the agarose from the top of the gel, thus avoiding issues of gas diffusion that could

affect the growth of aerobic bacteria. We only measured and analyzed the growth of bacterial cells that were separated by more than 5 μm from their closest neighbors to avoid mechanical interactions mediated by gel compression. For each species, we imaged the growth of ~30 cells at each concentration of agarose every 1 min for 30 min, a time-frame selected based on their typical division times in liquid media. To increase the number of cells appearing in focus at each time point, we found that the gel could be optically sectioned by moving the *z*-axis of the gel in 500-nm increments and imaging cells in 10 different focal planes (Figure 6).

Our initial experiments focused on *E. coli*, *B. subtilis*, and *P. aeruginosa* because the mechanical properties of the bacterial cell wall have been most frequently examined in these organisms (Table 1). We systematically analyzed the growth of cells encapsulated in 1-8% (w/v) agarose gels. To characterize the mechanical properties of these gels, we measured E_{gel} for various agarose concentrations (infused with LB media, but without cells) using tensile testing with an Instron MicroTester. The modulus increased linearly with the agarose concentration over two orders of magnitude, with $E_{gel} \approx 60$ kPa for a 1% gel and 1500 kPa for an 8% gel (Figure 1).

We found that cells elongated linearly in agarose gels at early time points. Relative cell elongation (the change in cell length divided by the initial cell length, $\Delta L/L_0$) reached saturation slowly when cells were encapsulated in gels of low E_{gel} and more rapidly as E_{gel} was increased (Figure 7). To ascertain whether the cells were still

viable once cell length plateaued, we queried the metabolic state of encapsulated *E. coli* cells using the redox indicator 5-cyano 2,3-ditolyltetrazolium chloride. Encapsulated cells elongated only slightly in 90 min, but nevertheless remained metabolically active (Figure 4). To ascertain whether cellular uptake of small molecules was affected by gel strength, we measured the diffusion of fluorescein through 1% and 5% agarose gels. The mean distance of fluorescein diffusion in these gels was within the standard deviation of the measurements (Figure 8), and thus we concluded that the decrease in growth rate for encapsulated cells was not due to nutrient diffusion. We therefore inferred that growth inhibition at increasing E_{gel} can be attributed to the compressive force imparted by the agarose, which resists the extension of the bacterial cell wall.

Analytical model of elongation in an elastic hydrogel. To provide a framework for interpreting our data on cell growth in elastic gels, we first present a simple one-dimensional model of an elastic rod-shaped bacterial cell that predicts the qualitative growth dynamics in our experiments. We modeled the cell wall as a connected chain of n_0 springs, each with spring constant k and relaxed length l_r; we use lowercase l to denote the length of a single spring and uppercase L to denote the length of the cell (Figure 9A). Each spring represents a longitudinally oriented peptide crosslink within the cell wall. For a cell wall with thickness d and radius r, k is related to the longitudinal Young's modulus E_{cell} via the relation $k = 2\pi r d E_{cell}/l_r$. Since the springs are arranged in

series, their combined mechanical response to an applied force is equivalent to that of a single spring with a smaller effective spring constant $K_0 = k/n_0$ and longer relaxed length $L_{0r} = n_0 l_r$. Before the cell is embedded in the gel, the only longitudinal force across the wall arises from turgor pressure P acting on the cell ends, which extends the combined length of the springs to a total length L_0. Assuming that the cell is at mechanical equilibrium, each spring extends to a length l_0 and force balance dictates that $P = K_0(L_0 - L_{0r})$ where $L_0 = n_0 l_0$.

Once the cell is embedded in a gel, we assume that the major forces in the gel are compressive along the longitudinal axis due to cell growth. Thus, we represent the surrounding material as a spring with force constant K_g and model cell growth by inserting material to reach a new length of n springs ($n > n_0$) so that the cell will extend to length $L = nl$ (Figure 9B). The length of each spring after growth (l) is a function of K_g and n and is less than the expected length l_0 that would occur in liquid, due to the restoring force of the gel as the cell attempts to displace the gel. Equivalently, one can think of the gel as relieving some of the force due to turgor pressure, which then reduces the extension of the springs. We can estimate K_g from E_{gel} by assuming that the force is evenly distributed within the gel over a length scale l that is similar to the micron size of the cell, such that $K_g \approx E_{gel} l$. For $E_{gel} = 1$ MPa and $l = 1$ mm, the equivalent spring constant is $K_g = 1000$ pN nm^{-1}. Balancing the force due to turgor pressure with the forces due to gel compression and cell extension,

$$P = K_g(L - L_0) + \frac{k}{n}(L - nl_o^r). \quad (1)$$

For the case $L = L_0$ and $n = n_0$, Eq. 1 gives $P = k(l_0 - l_0^r)$, which allows us to eliminate the variable P from the relative elongation of the cell. By balancing the compressive force of the gel with the expansion force of the cell due to growth (Figure 9B), we find that

$$K_g(L - L_0) = k(l_0 - l). \quad (2)$$

To compare theory and experiment, we solved for the fractional extension in our model

$$\frac{\Delta L}{L_0} = \frac{\eta\xi}{\eta + 1 + \xi}, \quad (3)$$

where $\Delta L = L\text{-}L_0$, $h = \Delta n/n_0$ is the fractional insertion, and $x = k/n_0K_g$ is the ratio of the cellular and gel spring constants. Pressure does not appear on the right-hand side of Eq. 3, which is in agreement with a key prediction of our model: that the fractional extension ($\Delta L/L_0$) should be independent of turgor pressure, which contributes equally to ΔL and to L_0 and hence cancels from the ratio. $\Delta L/L_0$ has a sigmoidal shape as a function of h that is qualitatively similar to our experimental measurements in Figure 7, with a growth saturation crossover point at $h = 1+x$ (Figure 9C). Our model predicts that some growth will occur even at high gel stiffness because there is initially little energy cost to compress the gel. Indeed, we observe that the growth rate of *E. coli* cells decreases but remains nonzero even in 5% agarose gels with a stiffness of ~1 MPa (Figure 7E).

Although our model does not depend on where the new material is inserted in the cell wall, connecting the fractional insertion and the insertion rate over time requires assumptions regarding the dependence of insertion on applied force. The external force from gel compression can stall the peptidoglycan synthesis machinery if a certain amount of extension is required, for example to make room for newly inserted material. However, stall effects will be less important at early time points after encapsulation since little gel compression will have taken place. Moreover, if the force applied by the peptidoglycan synthesis machinery during insertion is large enough compared with the force of gel compression such that stalling can be ignored, then insertion will be unaffected by the confinement of the cells in the gel and the relative insertion h will be approximately linear in time.

As cells continue to insert peptidoglycan, the resulting network will become increasingly compressed, and the cell length will saturate at $L_{max} = L_0(1+x)$; as the cell approaches this length, the gel compression increases to the point that the addition of new material results mostly in compression of the old material rather than elongation and further compression of the gel. In this scenario, our model predicts that the maximal relative extension $(L_{max}-L_0)/L_0$ will scale inversely with the gel modulus (proportional to $1/K_g$), independent of initial length.

A number of testable predictions follow immediately from Eq. 3. First, assuming that the gel stiffness K_g is a function only of the cross-sectional dimensions of the cell

and hence is independent of n_0, the fractional increases in length and initial elongation rate should depend directly on the initial cell length (which is proportional to n_0); since longer cells require more compression of the gel to achieve a given fractional elongation, they will grow more slowly and saturate at a shorter fractional extension. Second, $\Delta L/L_0$ should be invariant to an equal scaling of k and K_g, and thus two cells that differ in stiffness by the ratio k_1/k_2 should grow similarly if embedded in hydrogels with the same ratio of stiffness. The cell stiffness may change either by constructing peptidoglycan with a different architecture or by varying the thickness of the cell wall; we expect that for the same Young's modulus, the stiffness will increase linearly with the thickness. Using a relaxed peptide length l_r = 1 nm, Figure 9C illustrates several predicted growth curves as a function of h for different values of the initial cell length (n_0) and the longitudinal Young's moduli of the cell and the gel. The curves representing the same cell in gels of different stiffness (green) are qualitatively similar to the growth curves in Figure 7F, with a decrease in growth as the gel stiffness increases.

Our theory predicts the growth kinetics of cells with a given value of the surface modulus dE_{cell} (cell wall thickness multiplied by the Young's modulus) since the energy of the cell depends only on this product (24). Thus, for testing an uncharacterized bacterium with CLAMP, a determination of the longitudinal Young's modulus obtained from growth kinetics similar to Figure 9 requires an independent estimate of the cell

wall thickness. Recent cryo-electron microscopy measurements have placed the cell wall thickness of the Gram-negative bacteria *E. coli* and *C. crescentus* at 2 to 4 nm (6), suggesting that this may be a reasonable estimate for many Gram-negative cells. The thickness of the cell wall of the Gram-positive bacterium *B. subtilis* has been estimated at ~30 nm (13, 25, 26).

The initial elongation rate near $h = 0$ calculated from Eq. 3 is predicted to also depend on k, n_0, and K_g and can be modeled by

$$\left.\frac{d\left(\Delta L / L_0\right)}{d\eta}\right|_{\eta=0} = \frac{\xi}{1+\xi}. \tag{4}$$

Using Eq. 4, we produced a set of curves representing the growth of 4-mm cells with a wall thickness of 4 nm, a radius of 500 nm, and different Young's moduli that can be directly compared with our experimental data in Figure 7. To compare to experimental values, we measured the growth rate of *E. coli* cells in liquid in a microfluidic flow chamber (doubling time 23.7 ± 3.5 min, see Experimental Procedures and Figure 10A), which we assume closely mimics an unencapsulated growth environment and establishes the time scale for the synthesis and insertion of a given amount of material. The blue circles in Figure 9D are experimental measurements derived from a linear fit to the first 5 min of *E. coli* MG1655 cell growth data at each agarose concentration in Figure 7, normalized to the microfluidic chamber growth rate. Our experimental

measurements fall between the curves representing cells with longitudinal Young's moduli of 20 to 75 MPa, with the data at larger agarose concentrations falling between 50 and 75 MPa (Figure 9D). The range of possible Young's modulus values that are consistent with our data could represent a nonlinear response of the cell wall, or systematic experimental measurement errors. Nevertheless, the qualitative agreement between our model predictions and experimental measurements suggests that our model accurately represents the mechanical perturbations to the cell caused by gels of known stiffness, and provides an estimate for the stiffness of the cell wall.

Finite-element modeling of the bacterial cell wall as a thin shell. Although our one-dimensional model accurately predicts the qualitative behavior of bacterial cells encapsulated in gels, a quantitative determination of the Young's modulus of the cell requires an accurate three-dimensional model of the cell geometry. To illustrate this point, there are two regions of the gel that have different responses depending on the initial cell length: the gel longitudinally compresses parallel to the long axis of the cell next to the endcaps, but also stretches adjacent to the cell body. The former compression is independent of L_0, but the latter stretching should scale with $1/L_0$, similar to the spring constant of the cell. Thus, to quantitatively predict the elastic properties of the cell, it was necessary to account for the geometric details of gel compression.

We modeled the cell envelope as a cylindrical thin shell with hemispherical end-caps whose deformation energy arises from bending, stretching, and turgor forces. The gel is represented as a collection of connected small volumes with an isotropic Young's modulus whose compression energy was computed using a finite-element method (27). We simulated growth by increasing the relaxed length of the cylindrical portion of the cell by a fraction f, thereby increasing the energy of the cell due to longitudinal compression, and allowed the cell to relax mechanically by displacing the surrounding gel (see *Computational methods* in Experimental Procedures). We assumed that during the early stages of growth in which $\Delta L \approx 0$, the insertion of new material is unlikely to be

inhibited by the surrounding gel; therefore, we focused only on the cell deformation for small f and constant insertion rate, such that the fractional insertion h is linear in time t.

Based on estimates from our one-dimensional model, we computed the strain after 1% elongation in cell walls with an initial length of 4 μm, E_{cell} = 250 MPa, and cell wall thickness d = 4 nm embedded in a gel with E_{gel} = 56 kPa (Figure 11A). The strain is clearly localized to a region of the gel within a few microns of the cell body (Figure 11A), validating both our selection of individual cells for analysis that were >5 μm from other cells encapsulated in the hydrogel and our estimate of K_g in our one-dimensional model. Next, we determined the relative rate of elongation of the embedded cell $d(\Delta L/L_0)/dh$ after 1% insertion as a function of E_{gel} for cells with various values of E_{cell} (Figure 11B). To compare to experimental values, we normalized our measurements of the initial fractional elongation rate to the experimental time scale required for 1% insertion determined from the growth rate in a microfluidic flow chamber (Figure 10A). To address the stiffness of Gram-positive cells, we also computed the gel stresses (Figure 11C) and relative rate of elongation (Figure 11D) for a cell wall with thickness 30 nm and length 8 mm. The increase in thickness more than offsets the decrease in effective stiffness due to increased cell length, leading to faster fractional elongation for a given gel modulus. In Figure 11B, D, the qualitative behavior is similar to the predictions of our one-dimensional model in which cell elongation increases with increasing E_{cell} and decreasing E_{gel}. The data in Figure 11B, D can thus be considered a

set of standard curves to which experimental measurements of the initial elongation rate can be fit to determine the most likely longitudinal Young's modulus of a given species within the assumptions of our model.

CLAMP predicts similar Young's moduli for different bacterial species. Growth curves for individual cells of *E. coli* MG1655 (Figure 7), *P. aeruginosa* PAO1 (Figure 12A), and *B. subtilis* BB11 (Figure 12B) grown in agarose with different values of E_{gel} fit well to the functional form

$$\frac{L(t) - L_0}{L_0} = \frac{At}{t_{1/2} + t}, \tag{5}$$

which is similar to the predicted behavior in our one-dimensional model (Eq. 3). We observed a similar degree of heterogeneity in the growth kinetics of individual cells encapsulated in gels and growing in microfluidic flow cells (Figure 7, 10). In each case the single-cell growth curves were reasonably smooth and enabled us to extract the average initial growth rates in each gel and compare them to the predictions of our three-dimensional simulations (Figure 11). To do so, we also measured the doubling times in liquid of *P. aeruginosa* PAO1 cells (31.8 ± 5.3 min, Figure 10C) and *B. subtilis* BB11 (28.8 ± 7.1 min, Figure 10D). Given the similarities between *P. aeruginosa* and *E. coli* (23.7 ± 3.5 min) doubling times and gel-encapsulated growth curves (Figure 7F, 12A), if we assume a similar wall thickness, our simulations predict similar values of the

longitudinal Young's modulus for both species (50-150 MPa for *E. coli* and 100-200 MPa for *P. aeruginosa*, Figure 11B).

Our models predict that growth should be more inhibited for longer cells at the same gel stiffness. To test this prediction we used *B. subtilis* strain BB11 in which a single copy of *ftsZ*, a gene that encodes an essential division protein, is placed under IPTG-control at the chromosomal locus; these cells form filaments in the absence of IPTG. We removed IPTG and incubated *B. subtilis* BB11 to promote modest filamentation, then measured the growth of cells encapsulated in 1% to 8% agarose gels. We binned cells based whether their starting length was shorter than 9 μm or longer than 12 μm, and analyzed their growth rates. As predicted, cell elongation was more inhibited for longer cells in gels of a given agarose concentration (Figure 13). For gels at low agarose concentrations, *B. subtilis* BB11 growth curves exhibited an upward curvature at longer time scales. This increase in growth rate may arise from the tearing of the gel at high strains (~15%, Figure 2). Regardless, this behavior is unlikely to skew our determination of cell stiffness, since we use only data from the first five minutes of encapsulated growth—when strain in the gel is still within the linear, elastic regime (Figure 2)—to calculate the initial growth rate. Assuming a cell wall thickness of 30 nm, our simulations predict that the longitudinal Young's modulus of *B. subtilis* BB11 cells is ~100-200 MPa (Figure 11D).

Quantifying the role of MreB in cell mechanics. To demonstrate the utility of CLAMP for determining whether a change in stiffness occurs after a physiological perturbation, we focused on the role of the cytoskeleton in determining the stiffness of *E. coli* cells. MreB, a prokaryotic homolog of eukaryotic actin, is essential for maintaining a rod-like shape in bacteria such as *E. coli*, *B. subtilis*, and *P. aeruginosa* (28-30). MreB is thought to form oligomers or short filaments that are depolymerized by the small molecule inhibitor S-(3,4-dichlorobenzyl)isothiourea (A22) (31-33). Using optical trapping, it was recently shown that the flexural (bending) rigidity of *E. coli* cells is reversibly reduced approximately two-fold by A22 treatment (34). This reduction in bending rigidity supports a model in which MreB is bound to the cell wall through the inner membrane and thereby influences the bending modulus of cells.

We used CLAMP to explore a different mechanical perturbation, in which the extension of the cell wall during *growth* is balanced by gel compression. Any significant contribution of MreB to the longitudinal stiffness of the cell would require it to remain bound to the cell wall on time scales significantly longer than growth; however, fluorescence recovery after photobleaching experiments of MreB filaments indicate rapid turnover (35). We used CLAMP to test the relationship between A22-induced disassembly of MreB filaments *in vivo* and longitudinal cell stiffness. We first measured the doubling time in a microfluidic flow chamber of *E. coli* MG1655 cells in LB containing A22 (10 μg mL^{-1}) to establish its effect on growth rate in the absence of

mechanical stress. We found that inhibition of MreB by A22 did not affect the growth rate of *E. coli* MG1655 cells within the error of our growth rate measurements (22.3 ± 4.1 min, Figure 10C), and there was no noticeable change in the growth of individual cells upon A22 addition (Figure 14A). We then encapsulated *E. coli* MG1655 cells in agarose gels of varying stiffness containing 10 μg mL^{-1} A22 and immediately measured cell elongation at 1-min intervals (Figure 14B). MreB was depolymerized by the time we started imaging (Figure 5), and cells maintained their rod shape during the 30-min imaging time frame. Our measurements of agarose-embedded cells indicated that A22 treatment caused only a slight reduction in the initial fractional elongation rate (Figure 14C) that was well within the error bars of our measurements, in quantitative agreement with the maintenance of growth rate of unencapsulated cells; we note that A22 treatment did cause a more dramatic ~30-50% reduction in the fractional elongation after 30 minutes (Figure 14B). These data suggest that MreB alone has no affect on the longitudinal stiffness of actively growing *E. coli* cells, though growth in the absence of MreB may reduce cell wall stiffness.

We realized that if MreB altered the longitudinal stiffness of the cell wall during growth, A22 treatment should reduce the amount of extensive force the cell is able to produce to displace the gel. For cells growing in agarose after sufficiently long time scales, treatment with A22 would then rapidly reduce cell length due to the force exerted on the cell by compression of the gel. Six minutes after encapsulating *E. coli*

MG1655 cells within a 3% w/v agarose gel, we added a solution of A22 to the surface of the gel that after diffusion would produce a final A22 concentration of 10 mg mL^{-1} within the gel, which is larger than the concentration required for MreB depolymerization. We imaged the cells throughout this procedure and found no detectable reduction in the length or growth rate of the cells after A22 treatment (Figure 14D). Taken together, these observations indicate that MreB does not affect the longitudinal Young's modulus of the cell envelope during growth, and that MreB is bound to the cell wall in an unstressed state such that its depolymerization does not alter the mechanical equilibrium between cell wall extension and turgor forces.

Discussion

Here we describe an integrated computational and experimental approach for measuring the longitudinal stiffness of live, intact bacteria (Figure 6). Cell growth was inhibited by encapsulation in stiff agarose gels (Figure 7) in which the cells remained metabolically active (Figure 4). Previous studies have demonstrated the long-term survival of bacterial cells encapsulated in rigid materials (36, 37), with one study showing that cells of *Azospirillum brasilense* and *Pseudomonas fluorescens* are viable even after 14 years of encapsulation in alginate (38). We used CLAMP to determine E_{cell} for the rod-shaped bacteria *E. coli*, *B. subtilis*, and *P. aeruginosa* (Figure 11) and thereby laid the groundwork for studying a wide range of other bacteria. Our simple, one-dimensional biophysical model for the elongation of rod-shaped cells embedded in gels predicts all of the qualitative features of our experiments (Figure 9), and our three-dimensional finite-element simulations make possible quantitative comparisons with experimental data (Figure 11).

Our measurements indicate a range of Young's modulus values for *E. coli* cells that is 3- to 5-fold higher than some AFM measurements of isolated cell walls (5, 39), though the large spread of AFM data for *E. coli* in the literature suggests that these measurements are extremely sensitive to environmental conditions. In contrast to many AFM measurements, our measurements specifically address the stiffness of live, growing cells, which may be different from isolated cell walls; for instance, the outer

membrane of Gram-negative cells may also contribute to stiffness such that our measurements actually probe the combined stiffness of the cell envelope. It is also possible that the high values of E_{cell} that we have inferred are inflated due to incomplete polymerization of the gel around the cell (leading us to assume a higher gel modulus around the cell than is actually the case). While this point is difficult to address experimentally, it should not significantly affect our ability to measure relative changes in stiffness due to perturbations such as A22 treatment as long as the polymerization reaches similar levels of completeness at all gel concentrations. In fact, independent of the model used to infer cellular stiffness, our method can be utilized to determine the ratio of the stiffness of two strains of the same species or in media containing antibiotics or other biologically active small molecules by simply comparing fractional elongation rates.

Using the inhibitor A22 to rapidly depolymerize MreB, we demonstrated that MreB likely does not affect the longitudinal stiffness of the *E. coli* cell wall during growth; MreB disassembly had little affect on either the unecapsulated growth rate (Figure 10B) or the encapsulated growth rate (Figure 14) relative to untreated cells. These results demonstrate the quantitative nature of our methodology: despite cell-to-cell variation in single cell growth rates, we observed the same A22-independence of growth rates in microfluidic flow chambers and in agarose gels across a wide range of values of stiffness. We note that our data does not contradict previous observations of

MreB increasing the bending rigidity of *E. coli* cells (34), which predict that a similar reduction in stiffness should be observed if forces unrelated to growth are exerted to shorten or elongate A22-treated cells. Instead, our observations probed a different scenario, that of growth-related elongation due to cell wall insertion. The impact of MreB on bending stiffness but not longitudinal stiffness during elongation requires MreB to form rigid polymers whose dynamics are comparable with cell wall insertion. Indeed, recent studies have shown that MreB rotates in a circumferential direction driven by cell wall synthesis (40), and that MreB is only transiently attached to the cell wall and does not stretch as it mediates cell wall insertion, but rather unbinds and moves along the cell wall to the next position of cell wall assembly. CLAMP studies of A22 treatment of other bacterial species may help elucidate the relationship between MreB dynamics and cell wall insertion.

Our analysis has assumed linear springs; although we cannot rule out nonlinear effects resulting from forces due to turgor pressure or gel compression, our method for longitudinal Young's modulus determination utilizes growth data only from the first few minutes after encapsulation, during which gel compression is small. Although our model does not enable us to distinguish between stiffness arising from the thickness of the cell wall versus stiffness resulting from a material with a larger Young's modulus (Figure 9C), our methodology generates a direct estimate for the cellular stiffness of a living bacterium. The reasonable agreement between the cellular Young's modulus

determined by our measurements (Figure 11B, D) and data from AFM experiments on isolated sacculi (Table 1) indicates that the cell wall is the major contributor to stiffness, as has been previously hypothesized. Given that the cell wall thicknesses of various Gram-negative bacteria are hypothesized to be similar (6), our observation that the growth of encapsulated Gram-negative cells of *E. coli* and *P. aeruginosa* is slowed at a similar value of E_{gel} (Figure 7, 12) suggests that Gram-negative peptidoglycan is a material with common mechanical properties across species. This characteristic of peptidoglycan has important consequences for molecular-level modeling of the organization of Gram-negative peptidoglycan, and obviates the need for species-specific parameters representing peptide crosslink stiffness (9, 10, 34).

There are a number of advantages to our technique. CLAMP is rapid, conceptually simple, easy to implement, and employs materials that are found in most biological laboratories. The development of a computational model for analyzing the growth kinetics of new bacteria is rapid and depends only on the initial shape of the cell and a model for the location of newly inserted cell wall precursors. In addition to rod-shaped bacteria, cells with other shapes can also be analyzed with CLAMP. Since agarose is compatible with the encapsulation of a variety of other organisms, it should be possible to extend this technique to the measurement of yeast (41), fungi (42), and Archaea (43). In principle, other biologically compatible hydrogels can be used as long as they are sufficiently stiff and are physically unchanged in the presence of ions and

biomolecules secreted by encapsulated bacteria. Although experimentally untested, it should be possible to measure E_{cell} for different species simultaneously by mixing them together in the same gel, as long as the cells can be cultured in a single medium and have distinguishing features such as species-specific fluorescence or different cell morphologies.

Several aspects of this technique can be improved. CLAMP requires measurable cell growth over the time scale of an experiment, which places limitations on the time scale for determining the Young's moduli of slow-growing bacteria. At present the technique lacks the resolution of force-volume and force-spectroscopy AFM measurements, though this may be a result of heterogeneity in growth dynamics between cells. Here we have reported the growth rate of cells in agarose gels that vary by 1% (w/v) concentration changes; it is possible to make gels reproducibly that vary by smaller increments. The resolution of CLAMP may be improved by measuring cell growth at smaller increments of gel concentration, possibly increasing the accuracy of determining the growth-inhibiting gel concentration. CLAMP is ultimately limited by the resolution of optical microscopy, which makes it difficult to detect very small changes in cell length. One approach for improving the resolution is to incorporate fluorescent nanoparticles into the gel as tracers before polymerization and employ traction-force microscopy to measure the displacement of the particles by the cells (44, 45).

There are a variety of interesting structural questions that CLAMP is particularly well suited to probe in bacteria. For example, CLAMP will enable studies of the mechanical properties of bacterial cells in the context of antimicrobial technologies. β-lactams are the most successful family of antibiotics to date, targeting the enzymes that assemble and remodel the peptidoglycan. These small molecules are suicide inhibitors of the penicillin-binding proteins that play a role in peptidoglycan synthesis during cell replication (46). Inhibition of the penicillin-binding proteins produces defects in the cell wall and leads to changes in cell shape and size and eventually to lysis (47, 48). Although the β-lactams have been mainstays in the arsenal of antimicrobial compounds since the 1940s, the resistance of bacteria to these compounds has slowly reduced their impact in the treatment of infections. New families of small molecules that inhibit the assembly and reorganization of the cell wall await discovery (49-53); an important step in the development of these compounds is a quantitative, mechanistic understanding of the effect of small molecules on the mechanical properties of the cell wall and their attenuation of cell wall assembly and remodeling (53-55). Given our success in assaying the mechanical effects of A22-mediated MreB disassembly (Figure 14), CLAMP provides a framework upon which a high-throughput technique may be developed to identify new targets and small molecules that disrupt cell wall assembly and ultimately pathogenesis.

Our work demonstrates how CLAMP can be used to build quantitative relationships between physiological changes and the mechanical properties of the bacterial cell envelope. Deriving physical parameters such as the Young's modulus can have significant impact on our understanding of how cells interact with each other and the surrounding microenvironment, how cells grow and divide, and the common features of cell-envelope synthesis across different species. In concert with fluorescent labeling, it may also provide insight into the role of intracellular spatiotemporal organization within the cell on the assembly of the cell wall. We anticipate that CLAMP will be particularly useful to microbiologists because it opens a window into viewing the mechanical properties of microbial cell walls, a characteristic that makes this technique particularly useful for building connections among genetics, biochemistry, and bacterial cell shape.

Acknowledgements

We thank Gaurav Misra for helpful conversations, Tom Record for use of a vapor pressure osmometer and Ben Knowles for assistance with its use, Piet de Boer for *E. coli* strain FB76, and Rut Carballido-Lopez for *B. subtilis* strain BB11. We acknowledge the Aspen Center for Physics and NSF grant 1066293. H.H.T. acknowledges support from an NIH National Research Service Award (T32 GM07215). C.T. acknowledges support from a Stanford Graduate Fellowship and the Bruce and Elizabeth Dunlevie Bio-X Stanford Interdisciplinary Graduate Fellowship. K.C.H. acknowledges support from a National Institutes of Health K25 award (5K25 GM075000) and an NIH Director's New Innovator award (DP2OD006466). K.C.H. and A.G. acknowledge support from NSF grant EF-1038697. A.G. acknowledges support from the James S. McDonnell Foundation. D.B.W. acknowledges support from DuPont, the Alfred P. Sloan Foundation, and an NIH Director's New Innovator award (DP2OD008735).

Figure 1. Linear relationship between agarose concentration and Young's modulus of agarose gels (E_{gel}).

Agarose samples ($n \geq 3$ for each concentration) were elongated at 10 mm min^{-1} until fracture. Error bars represent the standard deviation of the mean values. The equation describing the linear fit (dotted line) is $y = 216x - 176$, where y is measured in kPa and x is measured as a percentage from 0 to 100.

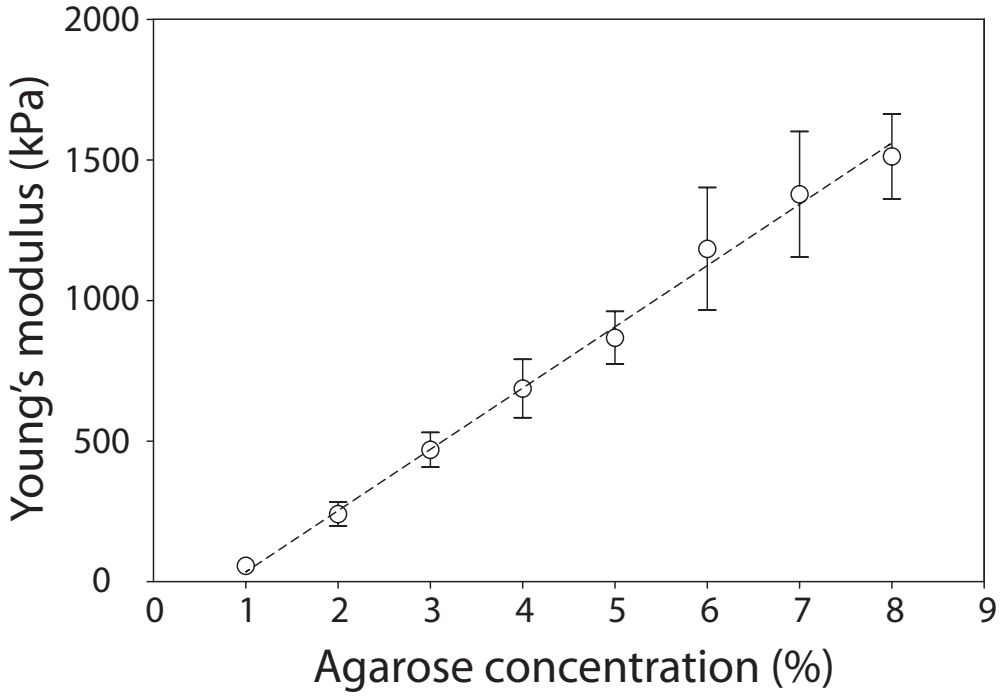
2000
1500
1000
500
0
Young's modulus (kPa)
0
1
2
3
4
5
6
7
8
9
Agarose concentration (%)

Figure 1

Figure 2. Agarose gel response to stretching is linear up to strains of 10-15%.

Agarose samples were elongated using an Instron MicroTester as described in the *Experimental Procedures*. Plots of individual stress-strain curves for agarose gels of increasing stiffness (1-8% w/v) are shown. The stress-strain curves remain linear until the point of fracture.

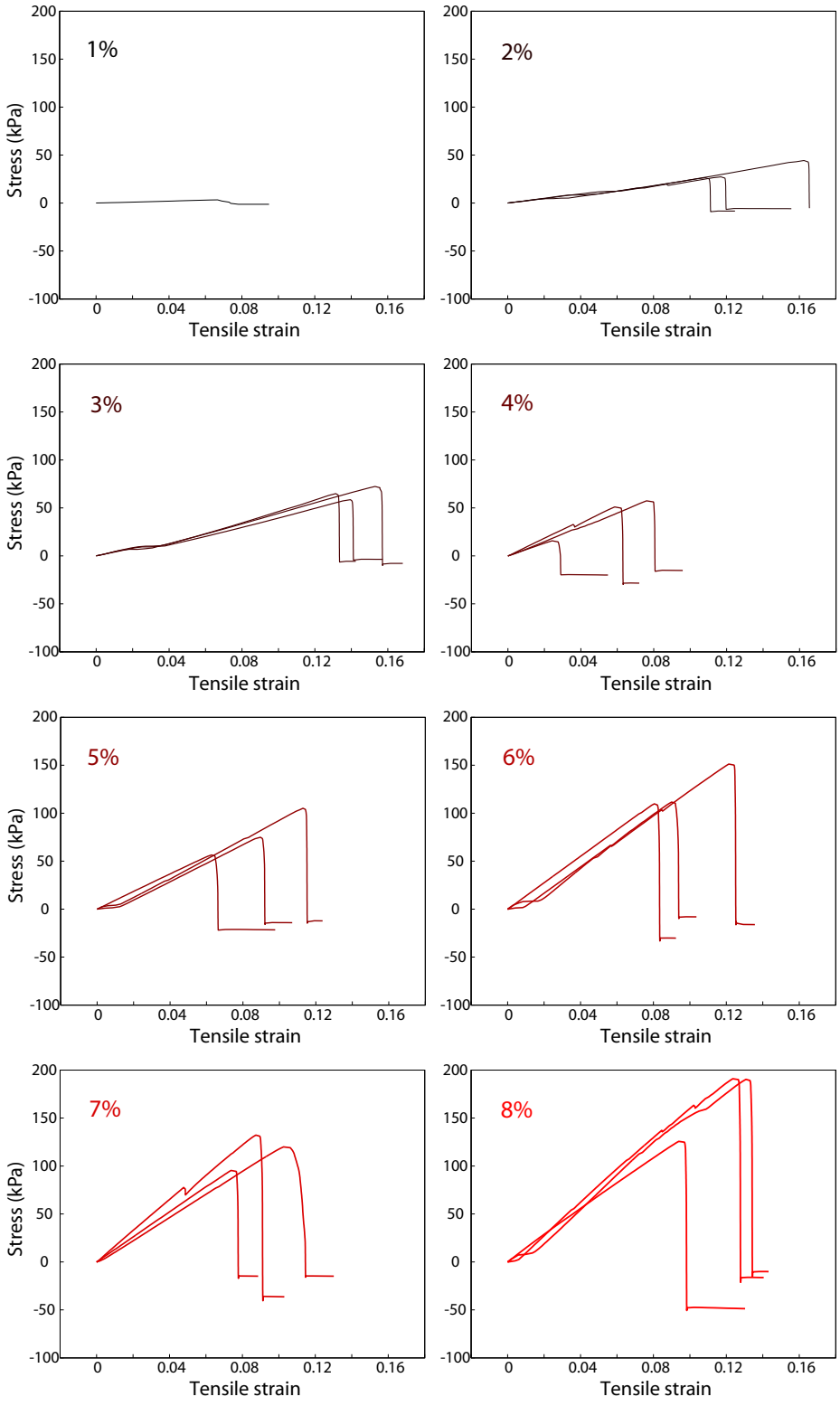
1%
2%
3%
4%
5%
6%
7%
8%
Stress (kPa)
Tensile strain
200
150
100
50
0
-50
-100
0
0.04
0.08
0.12
0.16

Figure 2

Figure 3. Relative elongation of *E. coli* MG1655 cells on the surface of 1% (56 kPa), 3% (468 kPa), and 5% w/v (867 kPa) agarose gels.

Images were taken at 1-min intervals using phase contrast microscopy, and the lengths of individual cells ($n > 30$ cells per agarose concentration) were monitored until division occurred. Increasing the stiffness of the agarose had minimal effect on cells growing on the surface. Shaded regions indicate one standard deviation above and below the mean growth curves.

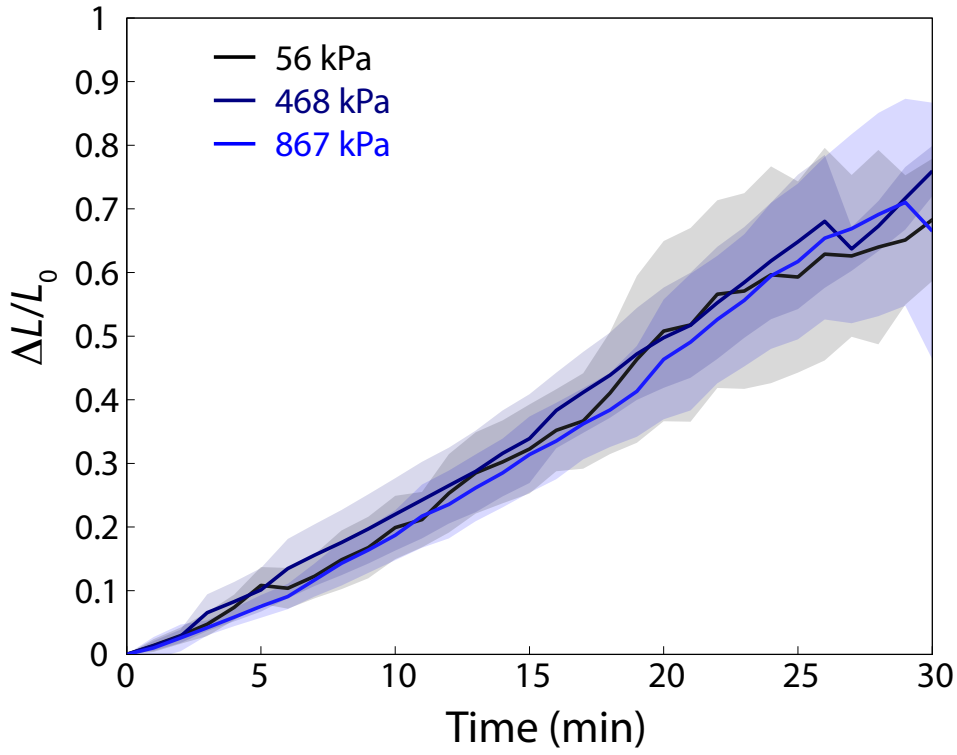
56 kPa
468 kPa
867 kPa
$\Delta L/L_0$
Time (min)
0
0.1
0.2
0.3
0.4
0.5
0.6
0.7
0.8
0.9
1
0
5
10
15
20
25
30

Figure 3

Figure 4. Cells remain metabolically active following encapsulation and incubation in agarose gels, even when the polymer resists cell growth.

E. coli MG1655 cells were imaged after ethanol treatment (control) or after 0, 30, 60, or 90 min of encapsulation in agarose. High levels of 5-cyano 2,3-ditolyl tetrazolium chloride (CTC) fluorescence denote cells that are metabolically active.

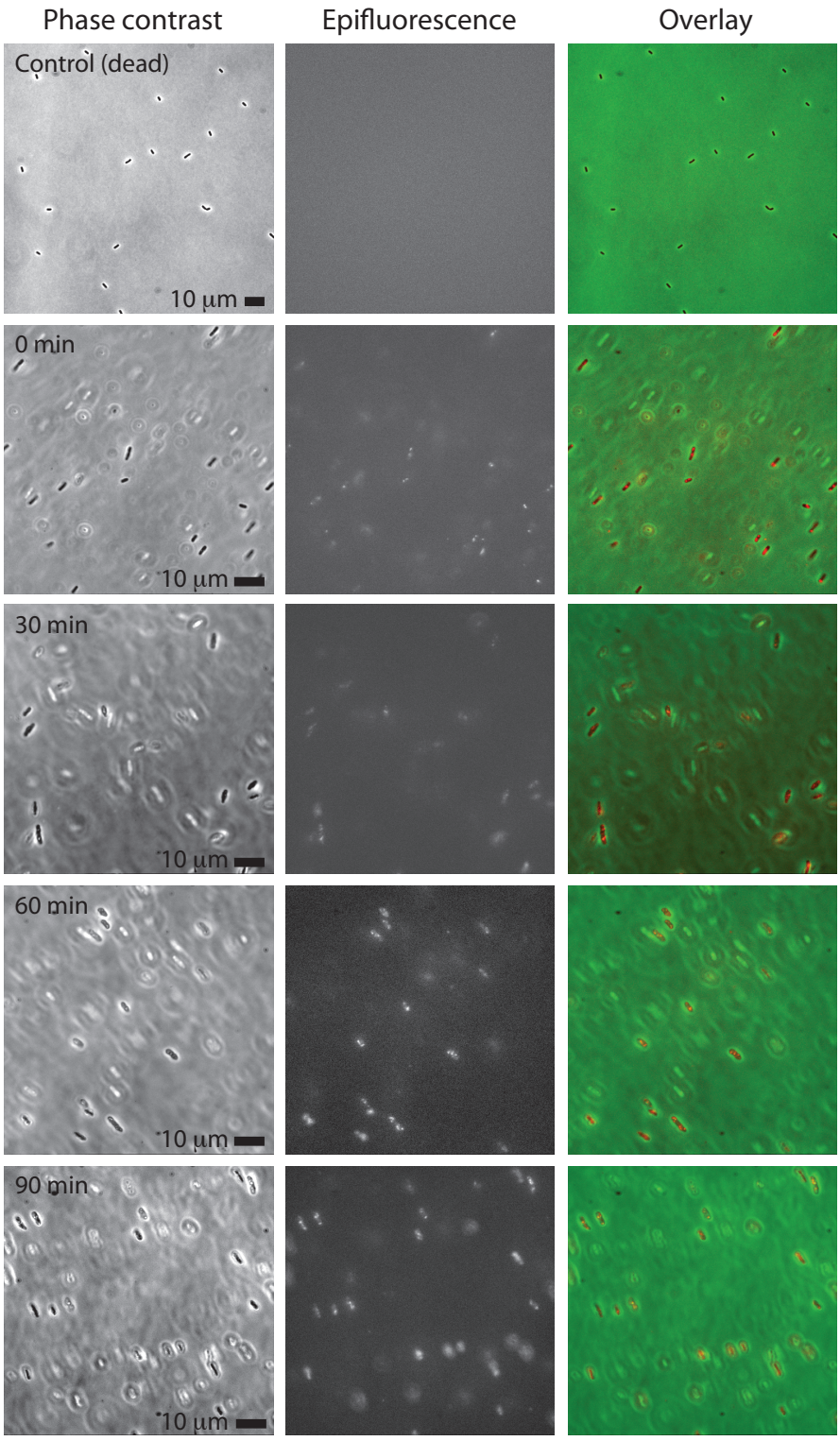
Phase contrast
Epifluorescence
Overlay
Control (dead)
10 µm
0 min
10 µm
30 min
10 µm
60 min
10 µm
90 min
10 µm

Figure 4

Figure 5. A22 depolymerizes MreB in agarose-encapsulated cells.

E. coli FB76 cells expressing a complementing chromosomally integrated MreB-RFP fusion (56)) were prepared as described in *Experimental Procedures*. Shown are 10 cells encapsulated in 5% agarose in phosphate-buffered saline without (left two columns) or with (right two columns) 10 μg mL^{-1} A22; after being in the presence of A22 for 2 min images were captured by brightfield and epifluorescence microscopy. RFP fluorescence is shown in red and phase-contrast image in green. Untreated cells have RFP puncta throughout the cell, while A22-treated cells have either diffuse fluorescence, indicating MreB depolymerization, or the only puncta are localized to the poles or the septum.

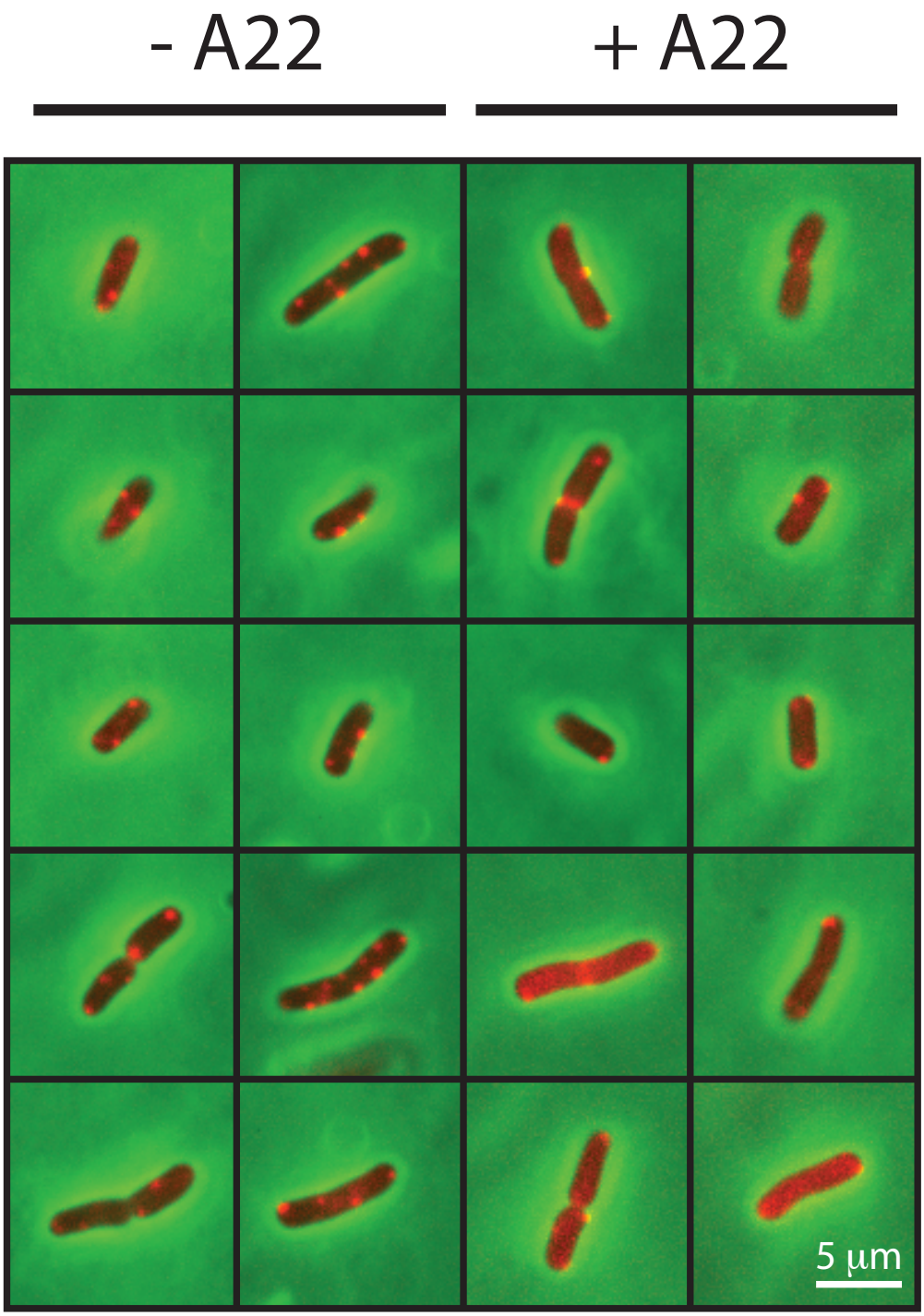

Figure 5

Figure 6. Methodology for encapsulating bacterial cells in agarose gels and measuring their growth.

A) Cells are mixed with a warm agarose solution, poured into a polydimethylsiloxane (PDMS) chamber, and gelled. The resulting agarose slab (15 mm on an edge, 250 μm tall) is mounted on a heated stage and imaged with phase contrast microscopy.

B) Cells are imaged in multiple focal planes (*z*-stack) at 1-min intervals to increase the number of cells for analysis. The cell length, *L*, is determined over time using image analysis scripts.

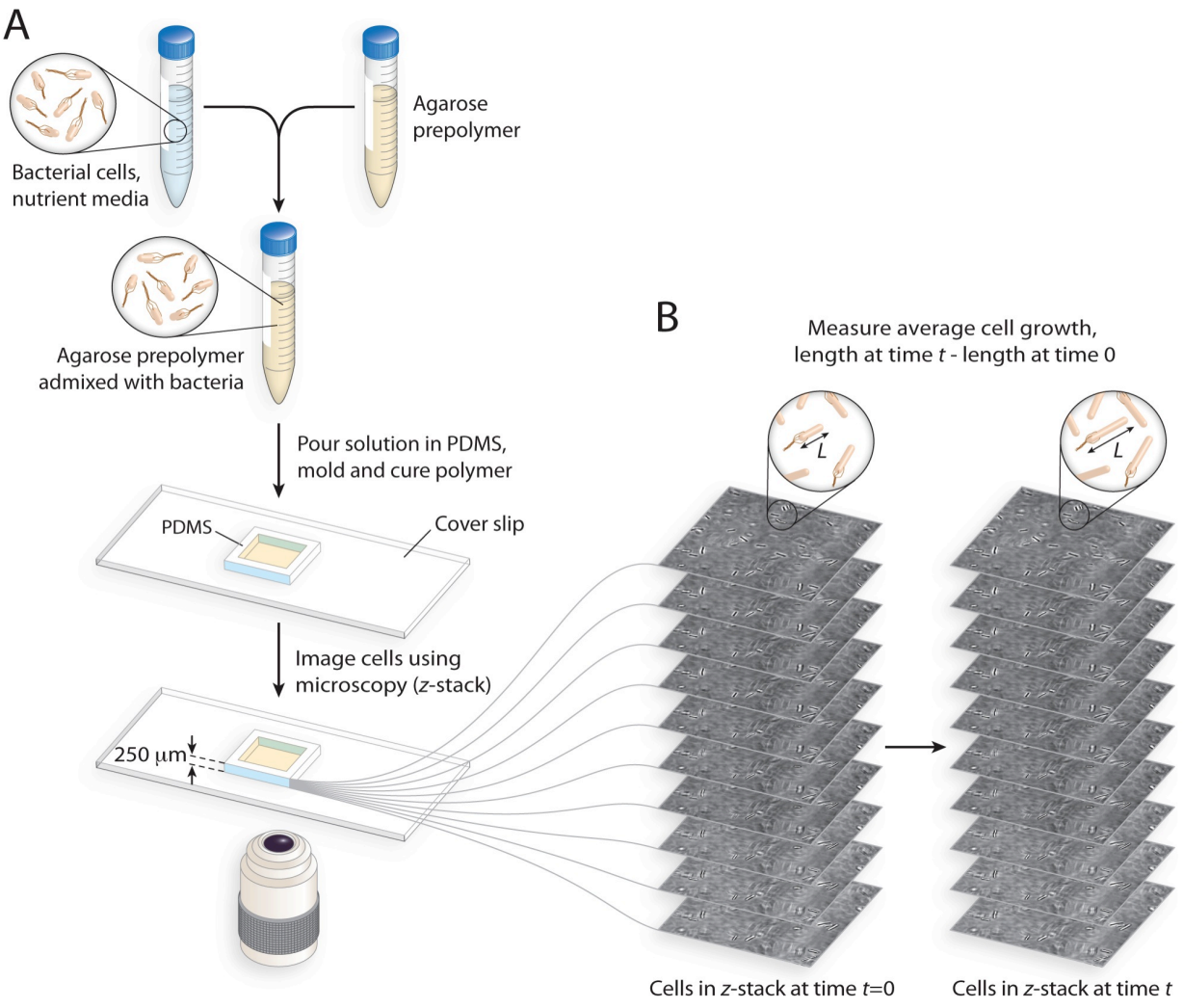
A
Bacterial cells,
nutrient media
Agarose
prepolymer
Agarose prepolymer
admixed with bacteria
Pour solution in PDMS,
mold and cure polymer
PDMS
Cover slip
Image cells using
microscopy (z-stack)
250 µm
B
Measure average cell growth,
length at time t - length at time 0
L
L
Cells in z-stack at time t=0
Cells in z-stack at time t

Figure 6

Figure 7. Growth of *E. coli* MG1655 cells saturates when cells are embedded in stiff agarose gels.

A-E) Growth curves of individual cells embedded in 1-5% agarose gels ($n > 26$ cells for each agarose concentration). Solid thick lines represent the average growth curve of all cells at a given agarose concentration, while shaded areas indicate one standard deviation above and below the mean growth curves.

F) Compilation of average growth data from (A-E) at all agarose concentrations. Dashed lines are fits to Eq. 5 of the average growth during the first 20 min (black to green gradient denotes increasing agarose concentration and therefore increasing gel stiffness).

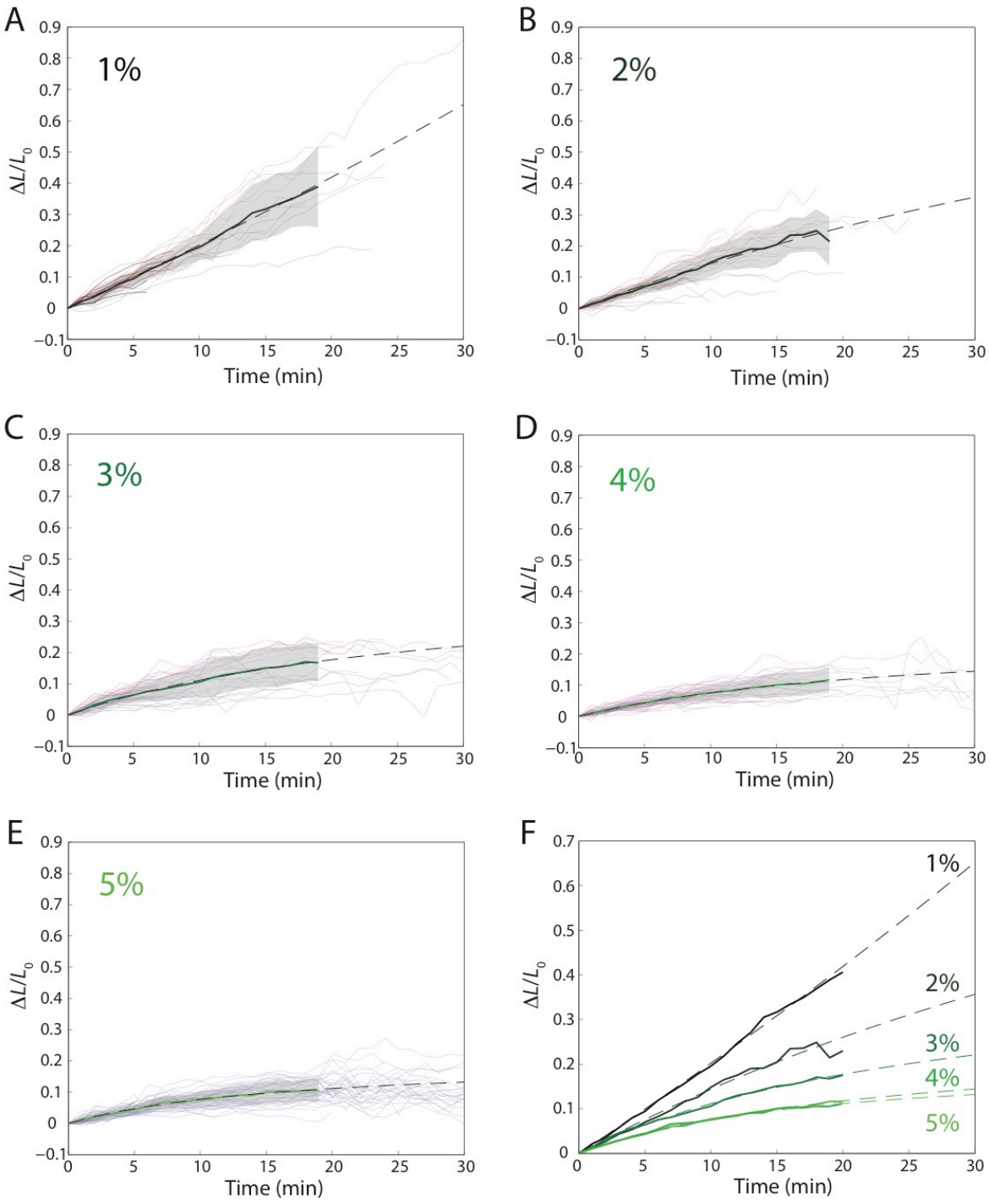

Figure 7

Figure 8. Diffusion of fluorescein is not significantly different in agarose gels of different stiffnesses.

Fluorescein (100 mM) was added to a hole in the center of a 1 or 5% agarose gel and the gel was photographed every 10 minutes for 2 hours. The distance travelled by the dye was measured at each time point. Thick lines represent the mean of three independent experiments (thin lines); shaded regions represent one standard deviation above and below the mean.

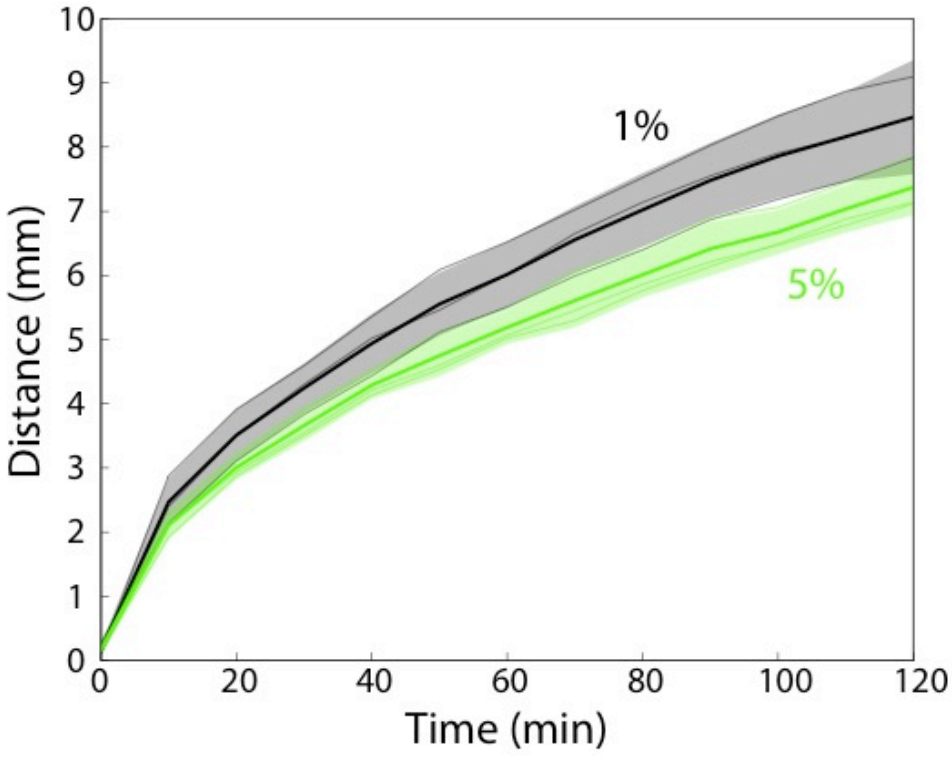

Figure 8

Figure 9. Gel inhibition of cell growth predicted by a one-dimensional spring model.

A) A rod-shaped bacterial cell is modeled as a connected line of n_0 springs each with spring constant k and relaxed spring length l_r, with pressure P exerting a force on the cell ends (red rectangles) that extends the length of the springs to l_0. Initially, the turgor ($\mathbf{F}_P$) and spring extension forces ($\mathbf{F}_{cw}$) are balanced. A multi-layer cell wall with thickness d is modeled as multiple lines of springs.

B) As the agarose-encapsulated cell grows to a length of n springs in a gel modeled by a spring constant K_g, full elongation (light red rectangles) is inhibited by the restoring force of the gel ($\mathbf{F}_{gel}$). The newly inserted vertex and spring appear brown and in bold, respectively.

C) Relative elongation $\Delta L/L_0$ as a function of the fractional insertion $h = \Delta n/n_0$ for different values of the stiffness ratio $x = kd/n_0K_g$. Cell growth becomes increasingly inhibited as the gel modulus K_g increases (black to green gradient of curves, with E_{cell} = 100 MPa, d = 4 nm, n_0 = 4000). For a fixed gel modulus of 800 kPa, the growth is more inhibited for longer cells (n_0 = 10,000, red curve) and less inhibited for stiffer cells (E_{cell} = 125 MPa, blue curve) or thicker cell walls (d = 30 nm, purple curve).

D) Predictions of initial growth rate $d(\Delta L/L_0)/dh$ for different values of the cell modulus E_{cell} based on our one-dimensional model. Our experimental measurements of initial growth rate for *E. coli* MG1655 cells (blue circles) fall between 20-75 MPa. Error bars indicate one standard deviation about the mean. The dashed line is a fit to Eq. 4.

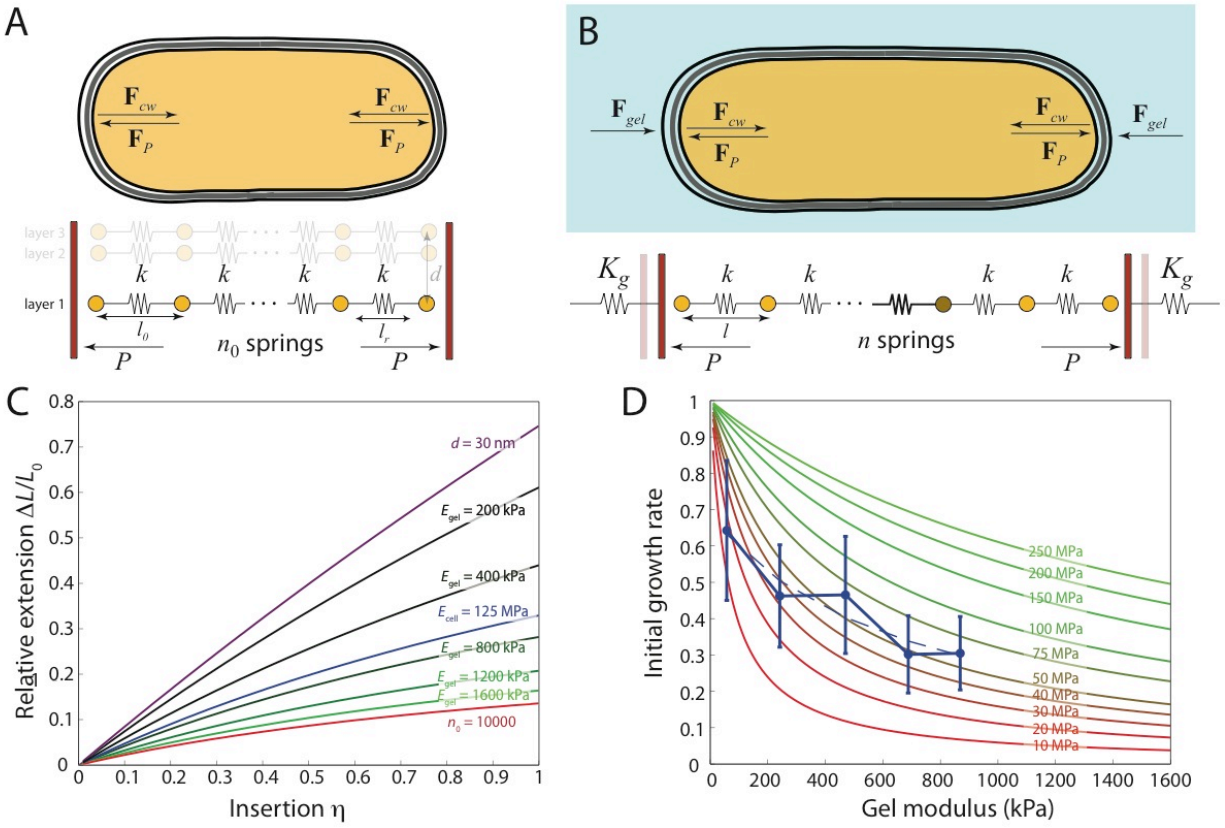
A
B
C
D
layer 3
layer 2
layer 1
n0 springs
n springs
Relative extension ΔL/L0
Insertion η
d = 30 nm
Egel = 200 kPa
Egel = 400 kPa
Ecell = 125 MPa
Egel = 800 kPa
Egel = 1200 kPa
Egel = 1600 kPa
n0 = 10000
Initial growth rate
Gel modulus (kPa)
250 MPa
200 MPa
150 MPa
100 MPa
75 MPa
50 MPa
40 MPa
30 MPa
20 MPa
10 MPa

Figure 9

Figure 10. Microfluidic flow chamber measurements of growth rates in liquid. Cell growth in an ONIX Microfluidic Plate was measured for 30 min at 30 s intervals. Thin lines represent the growth of individual cells. Thick lines represent fits to the experimental data for DL/L_0+1 with the exponential function A exp(at).

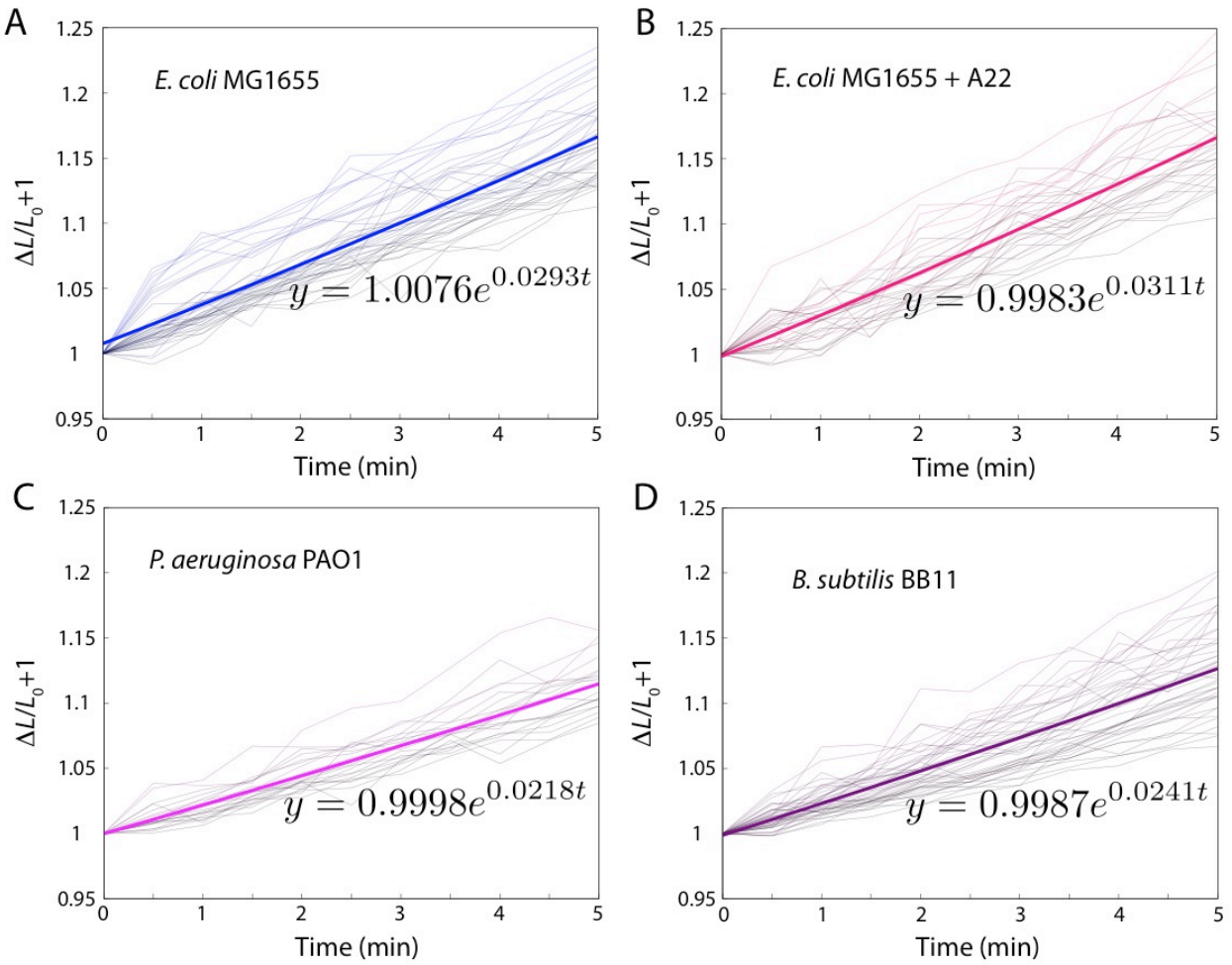
A
E. coli MG1655
$y = 1.0076e^{0.0293t}$
B
E. coli MG1655 + A22
$y = 0.9983e^{0.0311t}$
C
P. aeruginosa PAO1
$y = 0.9998e^{0.0218t}$
D
B. subtilis BB11
$y = 0.9987e^{0.0241t}$
ΔL/L0+1
Time (min)

Figure 10

Fig. 11. Estimation of cellular mechanical properties based on three-dimensional simulations of growth.

A,C) Three-dimensional finite element simulations of the mechanical equilibrium of a rod-shaped bacterium with a radius of 0.5 μm, cell wall thickness of 4 nm (A) or 30 nm (C), and Young's modulus E_{cell} = 250 MPa, embedded in a gel with E_{gel} = 56 kPa. Strains in the gel along the longitudinal axis of the cell (heat map) are depicted for cells with initial lengths of 4 μm (A) or 8 μm (C) after 1% growth of the cylindrical, mid-cell region.

B) Initial fractional extension rate $d(\Delta L/L_0)/dh$ from simulations of cells with different Young's moduli, initial length 4 μm, and envelope thickness 4 nm, after insertion of h = 1% new material. Close agreement between simulations and experimental measurements of initial fractional extension rates for *E. coli* MG1655 cells (blue) and *P. aeruginosa* PAO1 cells (magenta) predicts that $E_{cell} \approx$ 50-150 MPa for *E. coli* and 100-200 MPa for *P. aeruginosa*. Error bars indicate one standard deviation about the mean; dashed lines are fits to Eq. 4.

D) Initial fractional extension rate $d(\Delta L/L_0)/dh$ from simulations of cells with different Young's moduli, initial length 8 μm, and envelope thickness 30 nm, after insertion of h = 1% new material. Close agreement between simulations and experimental measurements of initial fractional extension rates for *B. subtilis* BB11 cells

(purple) predicts that $E_{cell} \approx$ 100-200 MPa. Error bars indicate one standard deviation about the mean; dashed lines are fits to Eq. 4.

Experimental data in (B,D) is shown slightly offset for comparison with simulation data.

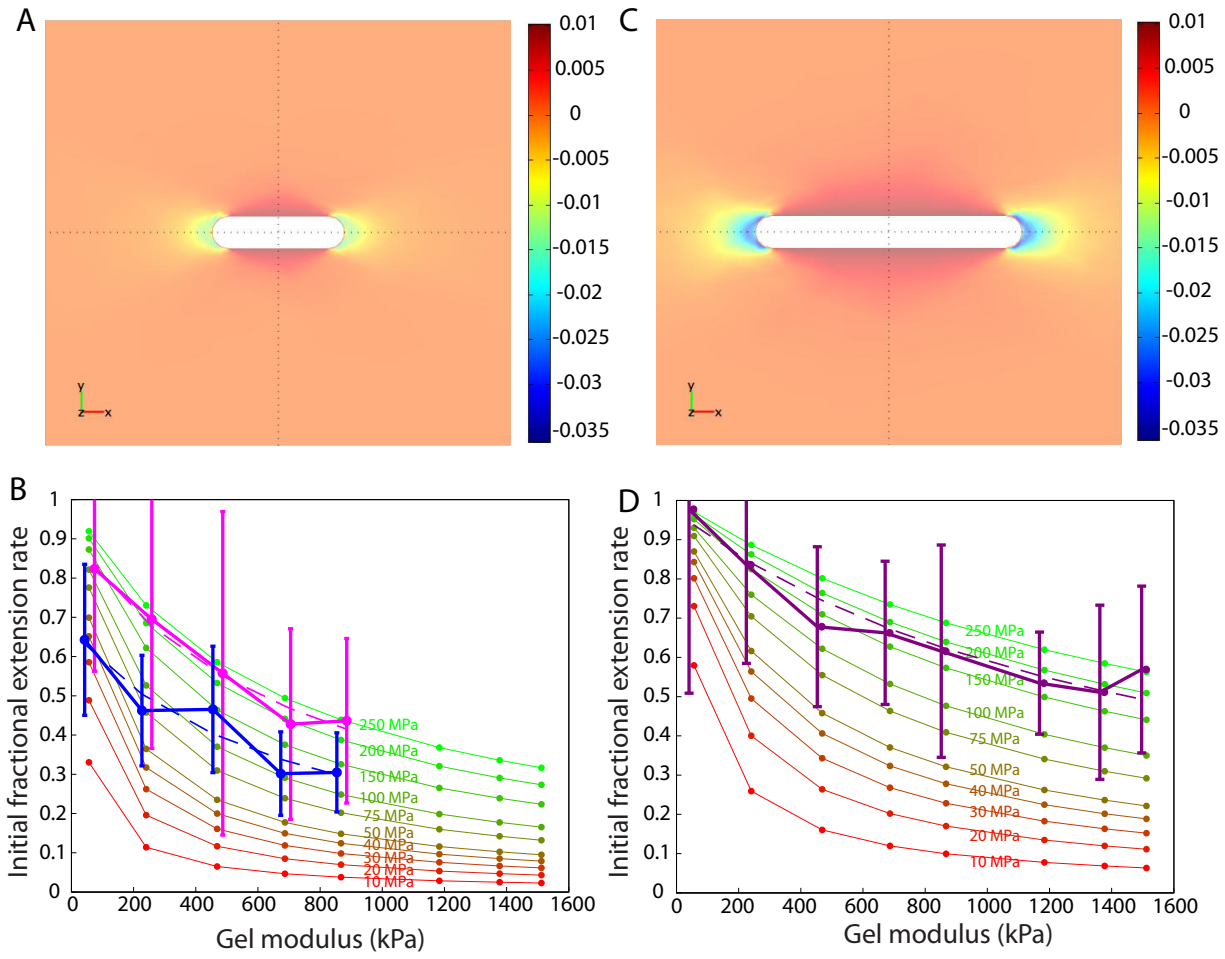
A
0.01
0.005
0
-0.005
-0.01
-0.015
-0.02
-0.025
-0.03
-0.035
C
0.01
0.005
0
-0.005
-0.01
-0.015
-0.02
-0.025
-0.03
-0.035
B
Initial fractional extension rate
Gel modulus (kPa)
250 MPa
200 MPa
150 MPa
100 MPa
75 MPa
50 MPa
40 MPa
30 MPa
20 MPa
10 MPa
D
Initial fractional extension rate
Gel modulus (kPa)
250 MPa
200 MPa
150 MPa
100 MPa
75 MPa
50 MPa
40 MPa
30 MPa
20 MPa
10 MPa

Figure 11

Figure 12. Gram-negative and Gram-positive species both exhibit growth inhibition upon encapsulation.

Average growth curves (solid lines) of (A) *P. aeruginosa* PAO1 and (B) *B. subtilis* BB11 cells embedded in agarose gels of various stiffnesses ($n > 27$ cells of *P. aeruginosa* PAO1 and $n > 17$ cells of *B. subtilis* BB11 for all agarose concentrations; black to green gradient denotes increasing agarose concentration and therefore increasing gel stiffness). Dashed lines are fits to Eq. 5 of growth during the first 20 min. Shaded regions indicate one standard deviation above and below the mean growth curves.

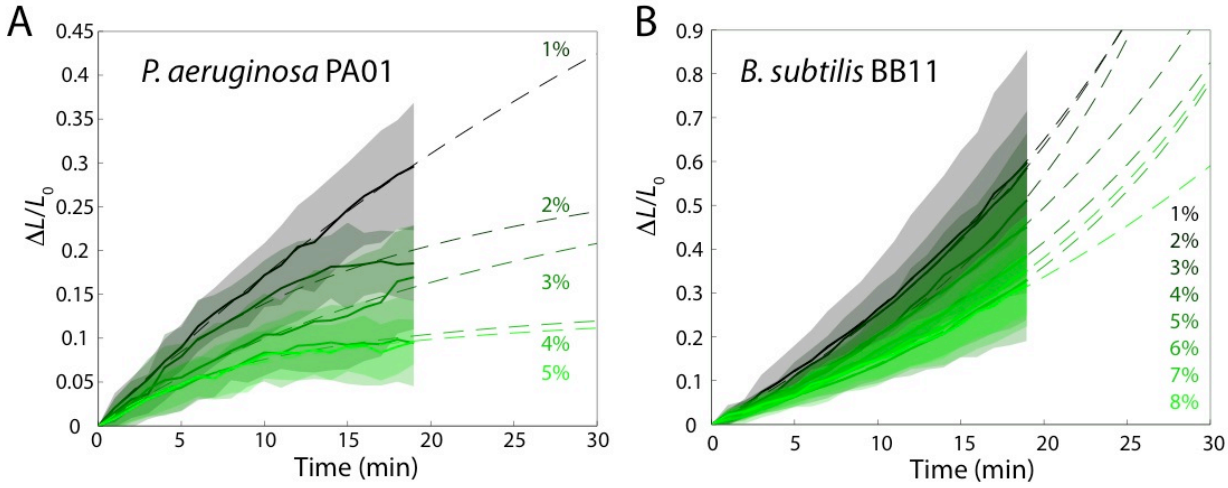
A
P. aeruginosa PA01
1%
2%
3%
4%
5%
ΔL/L0
Time (min)
B
B. subtilis BB11
1%
2%
3%
4%
5%
6%
7%
8%
ΔL/L0
Time (min)

Figure 12

Figure 13. Shorter cells elongate more when encapsulated in agarose.

Average growth curves (dashed lines) for *B. subtilis* BB11 cells embedded in 1-8% agarose gels (black to green gradient denotes increasing agarose concentration and therefore increasing gel stiffness). Solid lines are sigmoidal fits to growth during the first 20 minutes. Shown in (A) are average growth curves over the subset of cells with initial length less than 9 mm, while (B) depicts the growth of cells longer than 12 mm (n = 5-24 and 2-16 cells, respectively, across gel concentrations).

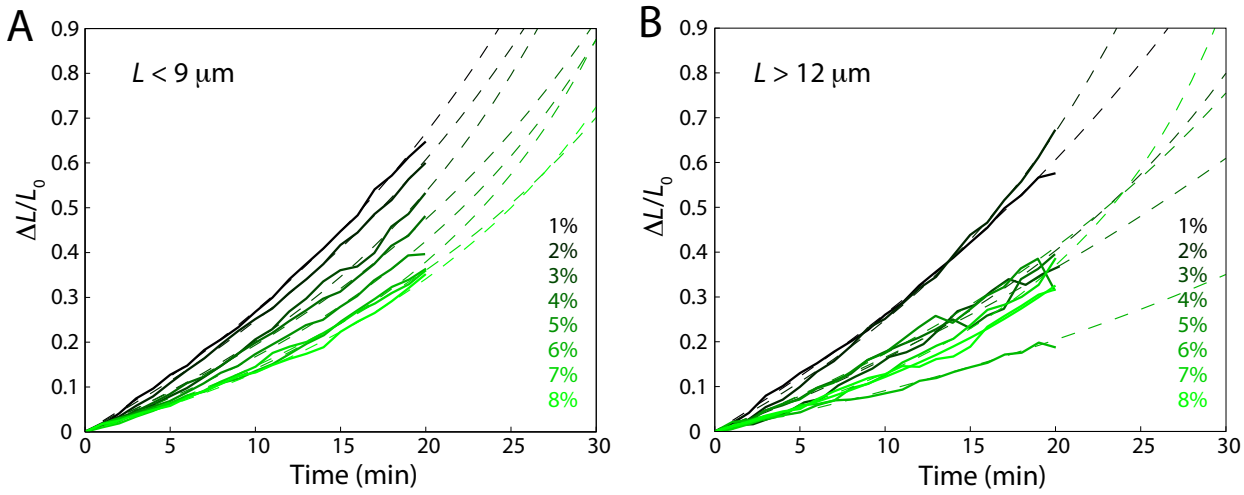

Figure 13

Figure 14. A22 treatment does not reduce the longitudinal stiffness of growing *E. coli* cells.

A) Growth rate of individual *E. coli* cells (n = 13) in a microfluidic flow chamber is not affected by A22 treatment at t = 0.

B) Average growth curves (solid lines) for cells embedded in 1-5% agarose gels (n > 24 cells for each agarose concentration); black to green gradient denotes increasing agarose concentration and therefore increasing gel stiffness. Dashed lines are fits to Eq. 5 of growth during the first 20 min.

C) The average initial fractional extension rate during the first 5 min of growth is shown for cells with (pink) and without (blue) A22 as a function of increasing agarose stiffness. Liquid growth rate without A22 was used to normalize both curves. Error bars represent one standard deviation above and below the mean. Dashed lines represent fits to Eq. 4.

D) Average growth curve (solid line) for cells embedded in a 3% agarose gel (n > 9). A22 was added to the gel after 6 minutes of growth.

Shaded regions in (B) and (D) indicate one standard deviation above and below the mean growth curves.

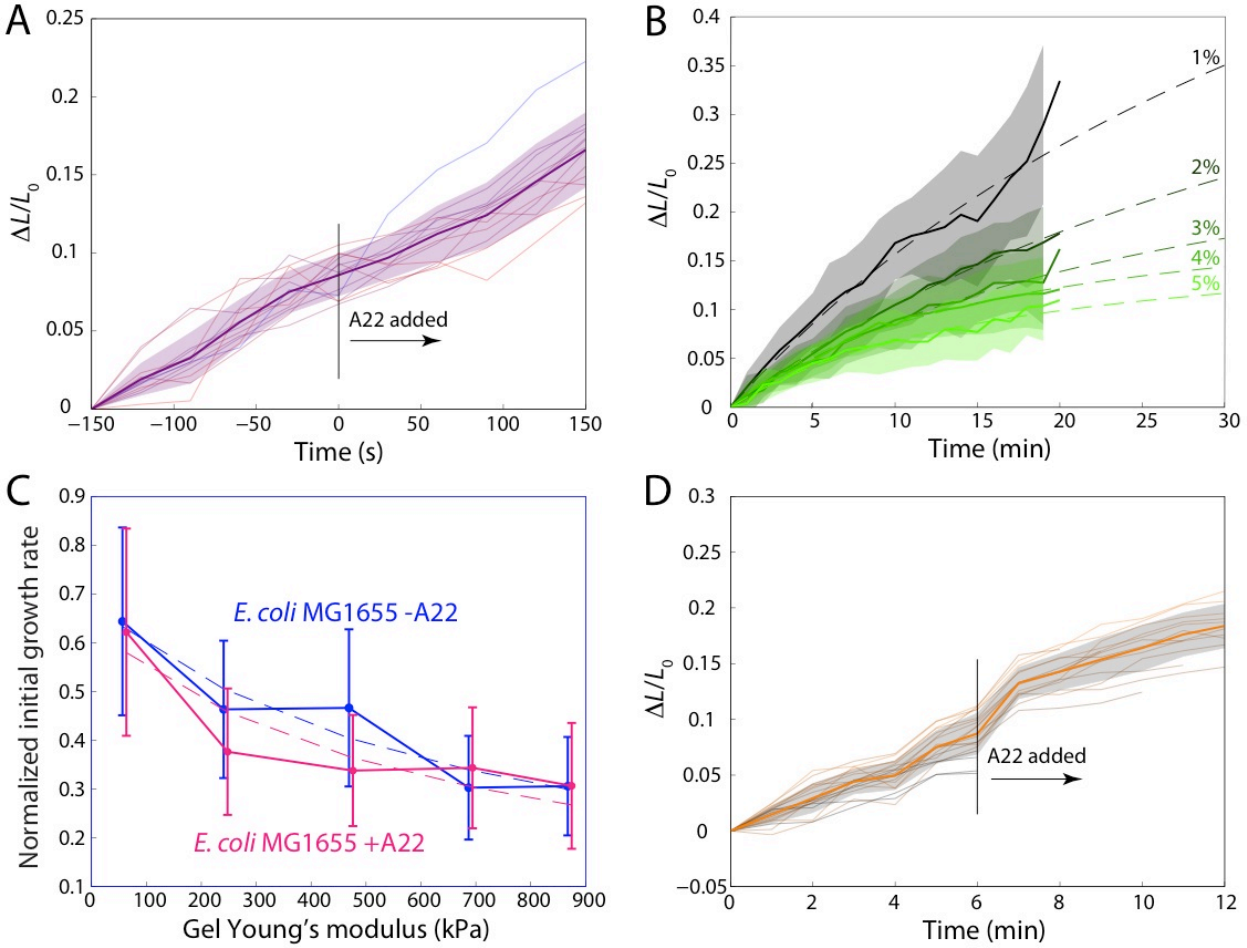
A
B
C
D
ΔL/L0
Time (s)
A22 added
Time (min)
1%
2%
3%
4%
5%
Normalized initial growth rate
E. coli MG1655 -A22
E. coli MG1655 +A22
Gel Young's modulus (kPa)

Figure 14

Table 1. Young's modulus measurements for Gram-negative (white) and Gram-positive (gray) bacteria. COS, chitooligosaccharide; EDTA, ethylenediaminetetraacetic acid. Full species designations are *Escherichia coli*, *Sphingomonas paucimobilis*, *Shewanella putrefaciens*, *Staphylococcus aureus*, *Bacillus subtilis*, and *Brevibacterium casei*.

Organism	Strain	*E* (MPa)	Conditions	Reference
E. coli	AB264	25	Isolated sacculi	Yao 1999
E. coli	JM109	12.8	Whole cells	Abu-Lail 2006
E. coli	JM109	0.12	Whole cells	Chen 2009
E. coli	JM109	0.05	Whole cells+EDTA	Chen 2009
E. coli	DH5a	2-3	Whole cells (live)	Cerf 2009
E. coli	DH5a	6	Whole cells (dead)	Cerf 2009
E. coli	NCTC 9001	221	Whole cells	Eaton 2008
E. coli	NCTC 9001	182	Whole cells+COS	Eaton 2008
E. coli	BE100	32	Whole cells	Deng 2011
E. coli	ATCC 9637	2.6	Whole cells	Perry 2009
S. paucimobilis	—	0.05	Whole cells	Penegar 1999
S. paucimobilis	—	0.08	Whole cells+Cu(II)	Penegar 1999
S. putrefaciens	CN32	0.21	Ph4; force spec mode	Gaboriaud 2005
S. putrefaciens	CN32	0.04	Ph10; force spec mode	Gaboriaud 2005
S. putrefaciens	CN32	69-98	Force vol mode	Gaboriaud 2008
S. aureus	NCTC 8532	95	Whole cells	Eaton 2008
S. aureus	NCTC 8532	88	Whole cells+COS	Eaton 2008
S. aureus	ATCC 25923	1.8	Whole cells	Francius 2008
S. aureus	ATCC 25923	0.2	Post-lysostaphin	Francius 2008
S. aureus	ATCC 25923	0.57	Whole cells	Perry 2009
B. subtilis	FJ7	10-30	Bacterial filament	Thwaites
B. casei	—	769	Whole cells	Kumar 2009

Table 2. MicrobeTracker parameters for analyzing the growth of bacterial cells encapsulated in agarose gels. The script was optimized for *E. coli* MG1655 cells at a resolution of 0.064 mm pixel^{-1}.

Category	Parameter	Value
Algorithm	-	4
Pixel-based parameters	areaMin	140
	areaMax	1000
	ThresFactorM	1.2
	edgemode	2
	edgeSigmaL	0.1
	valleythres2	0.001
Constraint parameters	cellwidth	10
	wspringconst	0.2
	rigidity	1
	rigidityRangeB	5
	attrCoeff	0.1
	repCoeff	0.3
Fitting parameters	fitMaxIter	500
Joining and splitting	splitThreshold	0.4

References

1. Holtje JV (1998) Growth of the stress-bearing and shape-maintaining murein sacculus of Escherichia coli. *Microbiol Mol Biol Rev* 62(1):181-203.

2. Vollmer W & Bertsche U (2008) Murein (peptidoglycan) structure, architecture and biosynthesis in *Escherichia coli*. *Biochim Biophys Acta* 1778(9):1714-1734.

3. Hobot JA, Carlemalm E, Villiger W, & Kellenberger E (1984) Periplasmic gel: New concept resulting from the reinvestigation of bacterial cell envelope ultrastructure by new methods. *J Bacteriol* 160(1):143-152.

4. Xu W, *et al.* (1996) Modeling and measuring the elastic properties of an archaeal surface, the sheath of *Methanospirillum hungatei*, and the implication for methane production. *J Bacteriol* 178(11):3106-3112.

5. Yao X, Jericho M, Pink D, & Beveridge T (1999) Thickness and elasticity of gram-negative murein sacculi measured by atomic force microscopy. *J Bacteriol* 181(22):6865-6875.

6. Gan L, Chen S, & Jensen GJ (2008) Molecular organization of Gram-negative peptidoglycan. *Proc Natl Acad Sci USA* 105(48):18953-18957.

7. Hayhurst EJ, Kailas L, Hobbs JK, & Foster SJ (2008) Cell wall peptidoglycan architecture in *Bacillus subtilis*. *Proc Natl Acad Sci USA* 105(38):14603-14608.

8. Boulbitch A, Quinn B, & Pink D (2000) Elasticity of the rod-shaped Gram-negative Eubacteria. *Phys Rev Lett* 85(24):5246-5249.

9. Furchtgott L, Wingreen NS, & Huang KC (2011) Mechanisms for maintaining cell shape in rod-shaped Gram-negative bacteria. *Mol Microbiol* 81(2):340-353.

10. Huang KC, Mukhopadhyay R, Wen B, Gitai Z, & Wingreen NS (2008) Cell shape and cell-wall organization in Gram-negative bacteria. *Proc Natl Acad Sci USA* 105(49):19282-19287.

11. Thwaites JJ & Mendelson NH (1989) Mechanical properties of peptidoglycan as determined from bacterial thread. *Int J Biol Macromol* 11(4):201-206.

12. Thwaites JJ & Mendelson NH (1991) Mechanical behavior of bacterial cell walls. *Adv Microb Physiol* 32:173-222.

13. Thwaites JJ & Surana UC (1991) Mechanical properties of *Bacillus subtilis* cell walls: Effects of removing residual culture medium. *J Bacteriol* 173(1):197-203.

14. Abu-Lail NI & Camesano TA (2006) The effect of solvent polarity on the molecular surface properties and adhesion of *Escherichia coli*. *Colloids Surf B Biointerfaces* 51(1):62-70.

15. Vadillo-Rodriguez V, Beveridge TJ, & Dutcher JR (2008) Surface viscoelasticity of individual Gram-negative bacterial cells measured using atomic force microscopy. *J Bacteriol* 190(12):4225-4232.

16. Bendezú FO, Hale CA, Bernhardt TG, & de Boer PAJ (2009) RodZ (YfgA) is required for proper assembly of the MreB actin cytoskeleton and cell shape in *E. coli*. *EMBO J* 28(3):193-204.

17. Sliusarenko O, Heinritz J, Emonet T, & Jacobs-Wagner C (2011) High-throughput, subpixel precision analysis of bacterial morphogenesis and intracellular spatio-temporal dynamics. *Mol Microbiol* 80(3):612-627.

18. ASTM (2003) Annual Book of ASTM Standards. in *Standard test method for tensile properties of plastics* (ASTM International, West Conshohocken, PA), pp 50-64.

19. Iwai N, *et al.* (2004) Structure-activity relationship of S-benzylisothiourea derivatives to induce spherical cells in *Escherichia coli*. *Biosci Biotechnol Biochem* 68(11):2265-2269.

20. Simmons G & Wang H (1971) *Single crystal elastic constants and calculated aggregate properties: A handbook* (M.I.T. Press, Cambridge, Mass.,) 2d Ed pp xv, 370 p.

21. Eun Y-J, Utada AS, Copeland MF, Takeuchi S, & Weibel DB (2011) Encapsulating bacteria in agarose microparticles using microfluidics for high-throughput cell analysis and isolation. *ACS Chem Biol* 6(3):260-266.

22. Katsuragi T, Tanaka S, Nagahiro S, & Tani Y (2000) Gel microdroplet technique leaving microorganisms alive for sorting by flow cytometry. *J Microbiol Meth* 42(1):81-86.

23. Zengler K, *et al.* (2002) Cultivating the uncultured. *Proc Natl Acad Sci USA* 99(24):15681-15686.

24. Minc N, Boudaoud A, & Chang F (2009) Mechanical forces of fission yeast growth. *Curr Biol* 19(13):1096-1101.

25. Matias VRF & Beveridge TJ (2005) Cryo-electron microscopy reveals native polymeric cell wall structure in *Bacillus subtilis* 168 and the existence of a periplasmic space. *Mol Microbiol* 56(1):240-251.

26. Matias VRF & Beveridge TJ (2008) Lipoteichoic acid is a major component of the *Bacillus subtilis* periplasm. *J Bacteriol* 190(22):7414-7418.

27. Zienkewicz OC (2005) *The finite element method for solid and structural mechanics* (Butterworth-Heinemann) 6th Ed.

28. Carballido-Lopez R & Formstone A (2007) Shape determination in *Bacillus subtilis*. *Curr Opin Microbiol* 10(6):611-616.

29. Gitai Z, Dye N, & Shapiro L (2004) An actin-like gene can determine cell polarity in bacteria. *Proc Natl Acad Sci USA* 101(23):8643-8648.

30. Kruse T, Bork-Jensen J, & Gerdes K (2005) The morphogenetic MreBCD proteins of *Escherichia coli* form an essential membrane-bound complex. *Mol Microbiol* 55(1):78-89.

31. Bean GJ, *et al.* (2009) A22 disrupts the bacterial actin cytoskeleton by directly binding and inducing a low-affinity state in MreB. *Biochemistry-Us* 48(22):4852-4857.

32. Gitai Z, Dye NA, Reisenauer A, Wachi M, & Shapiro L (2005) MreB actin-mediated segregation of a specific region of a bacterial chromosome. *Cell* 120(3):329-341.

33. Iwai N, Nagai K, & Wachi M (2002) Novel S-benzylisothiourea compound that induces spherical cells in *Escherichia* coli probably by acting on a rod-shape-determining protein(s) other than penicillin-binding protein 2. *Biosci Biotechnol Biochem* 66(12):2658-2662.

34. Wang S, Arellano-Santoyo H, Combs PA, & Shaevitz JW (2010) Actin-like cytoskeleton filaments contribute to cell mechanics in bacteria. *Proc Natl Acad Sci USA* 107(20):9182-9185.

35. Defeu Soufo HJ, *et al.* (2010) Bacterial translation elongation factor EF-Tu interacts and colocalizes with actin-like MreB protein. *Proc Natl Acad Sci USA* 107(7):3163-3168.

36. Young C-C, Rekha PD, Lai W-A, & Arun AB (2006) Encapsulation of plant growth-promoting bacteria in alginate beads enriched with humic acid. *Biotechnol Bioeng* 95(1):76-83.

37. Flemming CA, Leung KT, Lee H, Trevors JT, & Greer CW (1994) Survival of *lux-lac*-marked biosurfactant-producing *Pseudomonas aeruginosa* UG2L in soil monitored by nonselective plating and PCR. *Appl Environ Microb* 60(5):1606-1613.

38. Bashan Y & Gonzalez L (1999) Long-term survival of the plant-growth-promoting bacteria *Azospirillum brasilense* and *Pseudomonas fluorescens* in dry alginate inoculant. *Appl Microbiol Biotechnol* 51(2):262-266.

39. Deng Y, Sun M, & Shaevitz JW (2011) Direct measurement of cell wall stress stiffening and turgor pressure in live bacterial cells. *Phys Rev Lett* 107(15).

40. van Teeffelen S, *et al.* (2011) The bacterial actin MreB rotates, and rotation depends on cell-wall assembly. *Proc Natl Acad Sci USA* 108(38):15822-15827.

41. Gift EA, Park HJ, Paradis GA, Demain AL, & Weaver JC (1996) FACS-based isolation of slowly growing cells: Double encapsulation of yeast in gel microdrops. *Nat Biotechnol* 14(7):884-887.

42. Jain R, Saxena J, & Sharma V (2010) The evaluation of free and encapsulated *Aspergillus awamori* for phosphate solubilization in fermentation and soil-plant system. *Appl Soil Ecol* 46(1):90-94.

43. Ben-Dov E, Kramarsky-Winter E, & Kushmaro A (2009) An in situ method for cultivating microorganisms using a double encapsulation technique. *FEMS Microbiol Ecol* 68(3):363-371.

44. Sabass B, Gardel ML, Waterman CM, & Schwarz US (2008) High resolution traction force microscopy based on experimental and computational advances. *Biophys J* 94(1):207-220.

45. Wang JH-C & Lin J-S (2007) Cell traction force and measurement methods. *Biomechanics and Modeling in Mechanobiology* 6(6):361-371.

46. Popham DL & Young KD (2003) Role of penicillin-binding proteins in bacterial cell morphogenesis. *Curr Opin Microbiol* 6(6):594-599.

47. Nilsen T, Ghosh AS, Goldberg MB, & Young KD (2004) Branching sites and morphological abnormalities behave as ectopic poles in shape-defective *Escherichia coli*. *Mol Microbiol* 52(4):1045-1054.

48. Varma A & Young KD (2004) FtsZ collaborates with penicillin binding proteins to generate bacterial cell shape in *Escherichia coli*. *J Bacteriol* 186(20):6768-6774.

49. Gross BJ, Swoboda JG, & Walker S (2008) A strategy to discover inhibitors of O-linked glycosylation. *J Am Chem Soc* 130(2):440-441.

50. Ha S, Gross B, & Walker S (2001) *E. coli* MurG: A paradigm for a superfamily of glycosyltransferases. *Curr Drug Targets Infect Disord* 1(2):201-213.

51. Lange RP, Locher HH, Wyss PC, & Then RL (2007) The targets of currently used antibacterial agents: Lessons for drug discovery. *Curr Pharm Des* 13(30):3140-3154.

52. Silver LL (2003) Novel inhibitors of bacterial cell wall synthesis. *Curr Opin Microbiol* 6(5):431-438.

53. van Dam V, Olrichs N, & Breukink E (2009) Specific labeling of peptidoglycan precursors as a tool for bacterial cell wall studies. *Chembiochem* 10(4):617-624.

54. Vollmer W (2006) The prokaryotic cytoskeleton: A putative target for inhibitors and antibiotics? *Appl Microbiol Biotechnol* 73(1):37-47.

55. Vollmer W, Blanot D, & de Pedro MA (2008) Peptidoglycan structure and architecture. *FEMS Microbiol Rev* 32(2):149-167.

56. Bendezú FO, Hale CA, Bernhardt TG, & de Boer PAJ (2009) RodZ (YfgA) is required for proper assembly of the MreB actin cytoskeleton and cell shape in *E. coli*. *EMBO J* 28(3):193-204.

Chapter 3

Mechanical genomics: high-throughput identification of bacterial cell-stiffness modulators

Adapted from

George K. Auer, Timothy K. Lee^, Manohary Rajendram^, Spencer Cesar, Amanda Miguel, Kerwyn Casey Huang, and Douglas B. Weibel, *In press Cell Systems*

^Equal contributions

G.K.A., K.C.H., and D.B.W. conceived of the methodology. G.K.A, T.K.L., M.R., K.C.H., and D.B.W. designed experiments. M.R constructed mutants and plasmids associated with this study. T.K.L. analyzed data, performed analysis of mutant morphologies, and built chemical genomics correlations. S.C. and A.M. performed UPLC experiments. G.K.A., M.R., T.K.L., S.C., A.M., K.C.H., and D.B.W. interpreted data. G.K.A., T.K.L., M.R., K.C.H., and D.B.W. wrote the manuscript.

Abstract

Bacteria must maintain mechanical integrity to withstand the large osmotic pressure differential across the cell envelope; although many antibiotics disrupt this integrity, the proteins that modulate and contribute to cellular mechanics remain unidentified. Here, we describe a rapid, straightforward method for identifying cell-stiffness changes through optical absorbance-based measurements of the growth of cells embedded in hydrogels. We applied this technique to a genome-wide collection of ~4000 *Escherichia coli* mutants and identified 46 genes whose deletion substantially changed embedded growth. These genes have a diverse range of functions, highlighting surprising connections to cell mechanics. Using a microfluidic-based bending assay as a complementary measurement of Young's modulus, we confirmed that changes in optical density during agarose-embedded growth correspond to alterations in cell stiffness. Our measurements indicate that while some proteins involved in cell-envelope assembly are also involved in cell-stiffness determination, even proteins with extensive functional redundancy exhibited widely varying stiffness defects when deleted. For the cell-wall synthesis enzyme PBP1b, the hit from our screen with the largest decrease in stiffness, we determined that its glycosyltransferase activity is responsible for modulating cell stiffness. Correlating our genome-wide data with published chemical screens revealed that reduced membrane potential generally increases cell stiffness.

Taken together, this methodology lays the groundwork for systematic studies of bacterial mechanoregulation.

Introduction

In plant, fungal, and bacterial cells, the cell wall determines cell shape and provides mechanical stability by stretching to counter expansion due to large osmotic pressure differentials (turgor) on the order of atmospheres (1). Perturbations to the cell wall can result in the loss of mechanical integrity and subsequent lysis due to membrane rupture (1, 2). Remarkably, the roles that individual proteins play in cell mechanics are still unknown even in bacteria, in part due to the large number of genes whose functions still remain experimentally undetermined (>2000 of the ~4300 genes in *Escherichia coli* K12 strains) (3). Additionally, bacteria possess multiple systems to maintain essential cellular processes that may make sets of proteins appear redundant; measurements of novel phenotypes such as cell stiffness can reveal the specific role(s) of these individual proteins (4). A methodology for identifying proteins that modulate bacterial cell mechanics may provide fundamental insights into the biochemical, biophysical, and cell-biological aspects of cell growth, and also empower applications such as target identification for combination antibiotic therapy. Moreover, findings may have general significance for the growth and survival of any cell within a stiff extracellular environment, such as within a tumor.

There are several techniques available for directly measuring cell mechanics, including atomic force microscopy (5), tensile testing (6), and optical trapping (7). However, these methods generally involve meticulous sample preparation and data

analysis, equipment cost and availability can be prohibitive, and data can be difficult to interpret in the context of cellular growth. We previously reported a strategy using single-cell tracking of cell growth to extract a composite Young's modulus of bacterial cells embedded in agarose gels of varying stiffness; the gels provide mechanical resistance to cell elongation (8). However, all of these strategies, including our previous work (8), have limited throughput and hence are not suitable for large-scale analyses. Thus, it remains unknown to what extent chemical and genetic perturbations can modulate cell stiffness, and whether cell stiffness is linked primarily to a specific cellular process or is a global emergent property of cell growth and metabolism.

Most mechanical properties of bacterial cells have been attributed to the peptidoglycan cell wall, which is a macromolecular network consisting of polysaccharides cross-linked by short peptides and is essential for resisting expansion due to turgor pressure (1). Enzymatic degradation of the peptidoglycan produces cells with altered shapes that are sensitive to osmotic shifts (9). The genes involved in peptidoglycan assembly code for a family of enzymes known as the penicillin binding proteins (PBPs) that have been the subject of detailed biochemical analyses (10) and are obvious candidate cell-stiffness modulators. However, it is unknown whether perturbations to any part of the cell-wall synthesis and turnover machinery impact cellular mechanics; chemical inhibition of an essential PBP does not impact peptidoglycan composition even at doses that alter cell shape and decrease growth rate

(11). The only protein in *E. coli* that has been identified to affect cellular mechanics is the actin homolog MreB, which orchestrates the spatial organization of PBPs and thereby drives rod-shape determination. Depolymerization of MreB using the small molecule A22 (12) results in an immediate decrease in the bending stiffness of cells (7), illustrating that changes to cell stiffness can be due to changes that are not connected to the composition of the cell envelope. Genetic perturbations to the membrane-biogenesis machinery can lead to more frequent lysis (13), which is generally accompanied by mechanical failure of the membranes and cell wall. However, previous studies measured changes in cellular properties that were not directly attributable to altered cell stiffness (13, 14), thus it remains undetermined whether envelope perturbations generally disrupt cell mechanics.

Here, we describe a mechanical genomics assay, General Regulators Affecting Bacterial Stiffness (GRABS), that enables comparisons of the growth rates of cells in liquid medium and cells embedded in agarose gels from measurements of light absorption in 96-well or 384-well plates. By normalizing the growth of cells embedded in agarose to cell growth in liquid, our methodology accounts for non-mechanical changes in the growth of mutants. Thus, cell growth in agarose gels directly reflects the effects of mechanical constraints of the polymer environment isolated from the general metabolic effects of a mutation, and mimics a frequently encountered environmental context for cells from all kingdoms that grow in molecule- or material-rich

environments (e.g., polymers, soil, sediment). By screening the Keio collection of non-essential gene deletions in *E. coli* (15), we identified 46 candidate proteins with diverse functions extending beyond cell-envelope assembly that affect cell stiffness, and validated the mechanical role of a subset of these proteins using a microfluidic bending assay. By correlating our GRABS scores with chemical-genomics data (14), we successfully predicted chemicals and/or environmental conditions that increased or decreased cell stiffness, illustrating the discovery power of meta-analyses of genomics data. Perturbations to cell-wall synthesis had a wide range of effects; for example, while deletion of PBP1b or inactivation of its glycosyltransferase domain had the greatest impact on cell stiffness across our screen, deletion of PBP1a had little effect, despite its redundancy with PBP1b for growth-rate and cell-shape determination. Taken together, our methodology enables the rapid evaluation of how chemical perturbations or genetic disruptions, from single amino-acid changes to whole-gene deletions, alter the mechanical properties of cells, suggesting that our methodology is suitable for a wide range of future applications investigating the connections between cell stiffness and biochemistry.

Materials and Methods

Strain and plasmid construction. Table 1 lists the strains and plasmids used in this study for cloning. Primers are described in Table 2. Screening was performed using the Keio collection of non-essential single-gene deletion mutants (15). We used allele exchange to individually delete genes in frame in *E. coli* MG1655 without leaving a scar on the chromosome after excision (16).

Growth of bacterial cultures for screening. Individual 2-mL cultures were inoculated from a freezer stock and grown overnight in lysogeny broth (LB) at 37 °C with shaking until saturation (~16 h). For this initial overnight culture, Keio mutants were grown in the presence of 30 mg/mL kanamycin for selection of the Keio mutant. Strains containing plasmid pBAD33 c280 or plasmid pAM238/pSK12 were grown overnight in 30 mg/mL chloramphenicol or 30 mg/mL spectinomycin, respectively.

Preparation of GRABS 96-well plates. The absorbance values (λ = 600 nm) of 1:10 dilutions in LB of saturated overnight cultures of 48 strains grown in tubes were determined using a spectrophotometer (Amersham Biosciences, Buckinghamshire, UK). Cells were spun down at 800 x *g* for 10 min, the supernatants were removed, and the pellets were resuspended in 1 mL LB to a final density of 0.32 × optical density (OD). To prepare for agarose encapsulation, 48 microstirrers (V&P Scientific, San Diego, CA,

USA) were sterilized with 70% ethanol and placed into individual wells in columns 1-6 of a 96-well microplate (Thermo Scientific Nunc, Waltham, MA, USA). The microplate was covered with a lid and sterilized with ultraviolet light for 20 min. After sterilization, the microplate was placed onto our custom magnetic surface composed of two magnets (BZ0Z02-N52; KJ Magnetics, Pipersville, PA, USA) mounted in plastic casing, and a new sterile microplate was inverted on top. The two plates were turned over and placed onto the magnetic surface to draw the microstirrers into the new sterile plate. Finally, a sterile lid was placed onto the new microplate, which was transferred to a 50 °C hotplate to warm the plate and magnets for at least 20 min prior to the addition of agarose. This warming step ensured that the agarose remained in solution after being added to the plate.

Agarose was prepared as a solution of 1% w/v UltraPure agarose (Invitrogen Corporation, Carlsbad, CA, USA) in 20 mL LB. The solution was heated in a microwave until the agarose dissolved completely and the solution was visually homogeneous. The hot agarose solution was placed in a 65 °C water bath for 30 s while air bubbles rose to the surface. To prepare the final plate for growth-curve measurements, we maintained the microplate at 50 °C and pipetted 150 mL LB into the wells in columns 7-12 (these wells lacked magnets) and let the LB warm for >20 min. Using a positive displacement pipette (Eppendorf, Hamburg, Germany), we added 150 mL of agarose prepolymer from a 2.5-mL tip into each well that contained a magnetic stirrer. Antibiotics were

added as necessary and the cultures were mixed with magnetic stirrers for ~10 s. The microplate was transferred to a second hotplate set to 37 °C and cooled for 15-20 s. We aliquoted 5 mL of each cell suspension using a multichannel pipette into one well with LB and one well with agarose prepolymer to yield an OD ~0.01 and mixed the resulting cultures with magnetic stirrers for ~10 s.

We then took the microplate off the hotplate, removed the microplate lid, and rapidly applied the magnetic lid to extract the stirrers out of the wells. We removed the magnetic lid and quickly popped any bubbles on the surface of the agarose gel with a sterile pipette tip to ensure that the gel surface was smooth to enable accurate absorbance readings. The lid was again placed on the microplate, which was incubated at room temperature for 5 min while the agarose solidified. The lid was removed and the plate was sealed with a transparent polymer film (Excel Scientific, Victorville, CA, USA). To reduce condensation on the film, we made ~0.25-0.5 cm cuts with a razor blade sterilized with 70% ethanol on opposite sides of each well near its edge. Finally, we placed the microplate into a preheated 37 °C M1000 plate reader (Tecan, Mannedorf, Switzerland) and acquired growth curves at 37 °C by measuring absorbance at 595 nm. The orbital and linear shaking durations were 30 s and 15 s, respectively, and the shaking amplitude was 2 mm. Readings were taken for 16 h at 1-min intervals. The Tecan M1000 plate reader was driven using i-control v. 1.9.17.0 (Tecan), which was used to collect and export data for further analysis.

GRABS measurements in variable agarose concentrations. *E. coli* BW25113 was inoculated from a freezer stock into 2 mL LB and grown overnight at 37 °C in a shaking incubator. We measured the absorbance (λ = 600 nm) of a 1:10 dilution in LB of the overnight culture and calculated the volume of culture needed for resuspension in 1 mL of fresh medium for a final absorbance of 2. This volume of cells was spun down at 800 x *g* for 10 min, the supernatant was removed, and the pellet was resuspended in 1 mL LB. The cells were stored at 37 °C until use (within 5 min).

A stock solution of 5% (w/v) agarose was prepared by dissolving UltraPure agarose into 65 mL LB and placing the solution in a 70 °C water bath. Twenty-milliliter working solutions of 0.25-5% (w/v) agarose were prepared in 50-mL conical tubes by diluting the appropriate volume of 5% (w/v) agarose in preheated LB. These solutions were also placed into the 70 °C water bath. Using a positive displacement pipette, 2 mL of the agarose working solutions were aliquoted into individual preheated glass test tubes and kept at 65 °C in a water bath. Individual tubes were subsequently removed from the 70 °C water bath and allowed to cool in a 37 °C water bath for ~20 s. Ten microliters of the cell suspension were added to each test tube, yielding a final cell density in solution of 0.01 (λ = 600 nm), and the tube was vigorously shaken to ensure homogenous incorporation of the cells into the agarose solution. Using a positive displacement pipette, 150 μL of the agarose cell solution were pipetted into a 96-well

microplate in replicate ($n \geq 3$). This process was repeated for each agarose concentration. We also monitored growth in liquid LB in order to determine the percent inhibition of each gel compared to liquid. The liquid control was prepared at room temperature with the same cell suspension used for the agarose growth curves. The plate was placed on the bench at room temperature for ~3 min in order to allow the agarose wells to solidify. Growth was monitored with a plate reader.

GRABS data analysis. Growth data were collected over 16 h for Keio mutants in both agarose and liquid medium. To reduce the growth curve to a scalar value, we first normalized the growth data in liquid and agarose by subtracting the minimum OD reading (in agarose and liquid) for each mutant. Next, we averaged the 10 min of growth before the 8 h time point, which is approximately when BW25113 cells begin to enter stationary phase in liquid medium (Figure 1). Cells tend to reach saturation at later time points when embedded in agarose (Figure 1), and thus our mechanical phenotype is sensitive to the time point of measurement; t = 8 h was selected because it provided the largest dynamic range of values (Figure 1). We then determined a percent growth value for each mutant compared to wildtype. The GRABS score is a relative percentage of wild-type OD, calculated as $((OD_{mutant,agarose}/OD_{WT,agarose}) - (OD_{mutant,liquid}/OD_{WT,liquid}))$. A positive growth value indicates an increase in GRABS score, and a negative growth score indicates a decrease in GRABS score. Note that this GRABS

score is a measure of cell mechanics that is complementary, but not identical, to the Young's modulus. For our screen in kanamycin, we normalized all mutant data to an average of several wild-type growth curves in liquid and agarose. In our secondary screen in LB, we used the wild-type control on each plate to normalize the data.

Analysis of cell morphology. To estimate the average cell morphology across the Keio collection, images from the National BioResource Project were segmented with a custom MATLAB software package (17). At least 100 cells were included in the calculation of average cell width and length for each Keio mutant.

Correlation with chemical-genomics data. To compare GRABS scores against colony growth data from a variety of chemical conditions, we calculated the Pearson correlation coefficient between the GRABS scores for all tested mutants and the S-scores for the equivalent mutants in the chemical condition from Ref. (14). The significance of the correlation for each condition was estimated by comparing the correlation score against the correlation of 1000 random permutations of S-scores.

Complementation and deletion assays for GRABS hits and PBP1b mutants. Keio-complementation and wild-type control strains were streaked out from freezer stock onto LB agar plates with appropriate antibiotics to obtain individual colonies.

Individual colonies were inoculated into 2 mL LB with appropriate antibiotics and grown overnight at 37 °C. Saturated overnight cultures were diluted 1:100 into 2 mL fresh LB (without antibiotics) and grown to an absorbance of ~0.6 (λ = 600 nm). Microplates were prepared as described above. For complementation assays, antibiotics were not added to microplate wells so as to not influence the growth of the cells. Five microliters of a 2.5 mM arabinose stock solution were added to the wells containing strains with plasmid pBAD33 c280; the final arabinose gel concentration was 0.08 mM. Strains with wildtype or mutant PBP1b under the control of isopropyl β-D-1-thiogalactopyranoside were not induced; the basal level of expression from the *lac* operon was sufficient for full complementation of the stiffness defect (Figure 2A). Growth curves were compared to curves for the appropriate empty vector/native PBP1b controls to confirm recovery or loss of cell stiffness when the proteins were expressed in *trans*.

E. coli MG1655 mutants (Δ*mrcB*, Δ*mrcA*, Δ*lpoB*, Δ*lpoA*, Δ*hscA*, and Δ*hfq*) were streaked out from freezer stocks onto LB agar plates to obtain individual colonies. Individual colonies were inoculated into 2 mL LB and grown overnight at 37 °C. Wild-type and mutant strains were screened for stiffness changes as described above and compared to the corresponding BW25113 mutants.

Confirmation of chemical effectors of GRABS measurements. *E. coli* BW25113 and 45 additional Keio strains were grown overnight from freezer stock until saturation, in the appropriate antibiotic. Carbonyl cyanide *m*-chlorophenyl hydrazone (CCCP, Sigma-Aldrich) stock was prepared by dissolving CCCP into dimethyl sulfoxide (DMSO) (Sigma-Aldrich, St. Louis, MO, USA). CCCP was diluted into 1 mL LB to yield a 64 mg/mL working solution. The GRABS plate and cells were prepared as described above. During preparation of the GRABS plate, 5 μL CCCP were added to each well. The final concentrations of CCCP and DMSO in the plate were 2 mg/mL and ~0.1%, respectively. Appropriate DMSO-only controls were performed to confirm that DMSO did not affect the GRABS score. The percent growth values were determined as described, using the BW25113 (DMSO+) and (CCCP+) wells to normalize data from the mutants.

Microscopy-based stiffness measurements. Single-cell measurements of encapsulated cell growth were performed in 1-4% (w/v) agarose as described previously (8). Briefly, bacteria were grown in liquid LB without antibiotics to an absorbance (l = 600 nm) of ~0.6. Cells were diluted 1:100 and spotted onto 2% agarose pads. Elongation was monitored on a Nikon Eclipse Ti inverted microscope (Nikon, Tokyo, Japan) equipped with a heated stage (Okolab, Pozzuoli, Italy) and objective heater (Bioptechs, Butler, PA, USA) at 37 °C. Images were collected over a 30-min period at 1-min intervals using a

CoolSNAP HQ2 camera (Photometrics, Munich, Germany). Cell length was measured for each mutant and wild-type strain using MicrobeTracker (18). Length measurements were halted after cells divided. We calculated the fractional elongation over time for each mutant, averaged over all single cells (8).

Microfluidic-based stiffness measurements. Keio mutants and wild-type strains were transformed with a plasmid (pDB192) containing *sulA* under an isopropyl β-D-1-thiogalactopyranoside-inducible promoter. The strains were grown overnight in 2 mL LB containing 30 mg/mL kanamycin and 50 mg/mL ampicillin. We fabricated and applied a microfluidic device to the determination of cellular bending rigidity and Young's modulus as described previously (19). As an alternative means of causing cells to filament, we applied 1 mg/mL aztreonam (MP Biomedicals, CA, USA) . Deflection of cells under fluid flow was monitored on a Zeiss Axiovert 100 microscope (Zeiss, Oberkochen, Germany) equipped with a 60X oil objective. Images were collected with an Andor iXon 3 EMCCD (Andor, Belfast, UK) using μManager v. 1.4.16 (20). Deflection of the cells was determined using a custom Igor Pro (WaveMetrics Inc.) image analysis algorithm.

To account for changes in the diameter of mutant cells compared to wild-type cells after filamentation, we collected static images on a Nikon Eclipse Ti inverted microscope equipped with a 60X oil objective (Nikon) using a CoolSNAP HQ2 camera

(Photometrics). Cell width was measured using MicrobeTracker (18). These measurements were used to calculate the Young's modulus from the flexural rigidity, in which the moment of inertia (I) of a cross-section is dependent on cell radius (r) and thickness of the cell wall (h) according to $I = \pi r^3 h$.

Cell death in 1% agarose and liquid. The GRABS assay for Keio mutants and wild-type strains was carried out as described above. One hundred and fifty microliters of liquid LB and agarose (prior to gelling) were pipetted out of the 96-well plate and transferred to an 8-well LAB-TEK II chambered coverglass #1.5 (Nunc, NY, USA). The agarose was allowed to solidify at room temperature. LAB-TEK II chambers were placed into a 37 °C incubator with shaking for 8 h, at which point the GRABS score was determined. After 8 h, cells were removed from the 37 °C incubator and labeled via the LIVE/DEAD BacLight Viability Kit (L7007, Invitrogen) at room temperature. For staining of cells grown in liquid, cells were diluted 1:20 in fresh LB and stained in the dark for 20 min according to the manufacturer's guidelines. For staining of cells grown in agarose, 25 mL of a stock solution (100 mL component A (1.67 mM SYTO 9, 1.67 mM Propidium iodide) + 1.5 mL component B (1.67 mM SYTO 9, 18.3 mM Propidium iodide)) were pipetted onto the agarose surface and allowed to diffused through the gel in the dark for 30 min. Cells were imaged with epifluoresence using a Nikon Ti inverted

microscope equipped with a CoolSNAP HQ2 camera (Photometrics) and a 100X oil objective (Nikon).

Purification of sacculi and ultra performance liquid chromatography (UPLC) of peptidoglycan composition. Overnight cultures of *E. coli* BW25113 or Keio strains were diluted 1:100 in LB and grown at 37 °C to an OD_{600} of 0.7. The cultures were then harvested by centrifugation at 5,000 × *g* for 10 min at room temperature and resuspended in 3 mL LB. Cell suspensions were lysed by boiling in sodium dodecyl sulfate, and insoluble material was collected by several rounds of ultracentrifugation at 400,000 × *g* for 20 min at room temperature. Samples were prepared for UPLC as previously described (21) and injected onto a Waters H Class UPLC system equipped with a BEH C18 1.7-μm column (Waters, MA, USA), using elution conditions previously described (22). Peaks were quantified and identified as particular muropeptide species using the software package Chromanalysis (23), from which the crosslinking density and strand length were calculated (24, 25).

Shape of agarose-embedded cells. The GRABS assay for Keio mutants and wild-type strains was carried out as previously described. One hundred and fifty milliliters of agarose (prior to gelling) were pipetted out of the 96-well plate and transferred to an 8-well LAB-TEK II chambered coverglass #1.5 w/cover (Nunc, NY, USA). The agarose was

allowed to solidify at room temperature. LAB-TEK II chambers were placed into a 37 °C incubator with shaking for 8 h (at which point the GRABS score is typically determined). After 8 h, cells were removed from the incubator and labeled with FM 4-64 FX (Invitrogen). For staining, 25 μL of a 100 mg/mL stock were pipetted onto the surface of the agarose and allowed to diffuse through the gel, in the dark, for 30 min. Cells were imaged using phase contrast and epifluoresence microscopy.

Cell density versus OD measured by plate reader. A saturated overnight culture of *E. coli* BW25113 was diluted 1:100 into 60 mL of fresh LB and grown in a 37 °C incubator with shaking until an absorbance of 3.0 (λ = 600 nm). We calculated the volume of the culture needed for resuspension in 200 mL of fresh LB medium for a final absorbance of 248 OD. This volume of cells was spun down at 800 × *g* for 10 min, the supernatant was removed, and the pellet was resuspended in fresh LB media. A 2-fold dilution series was made from 240 OD to 0.007 OD. Five microliters of diluted culture were inoculated into agarose for a final cell density in the plate of 8 OD-0.0004 OD. The OD (λ = 595 nm) was measured immediately using a M200 PRO plate reader (Tecan).

Measurement of SOS using a promoter-fusion assay. To measure SOS induction we used the plasmids pUA66-*sulA* promoter-GFP (p*SulA*-GFP) and the empty vector control pUA66-GFP (pUA66) transformed in the Keio parent strain *E.coli* BW25113 and

the Keio strains (Δ*mrcB*, Δ*lpoB*, Δ*hscA*, Δ*hfq*, Δ*iscA*, Δ*recA*). Three biological replicates of wildtype cells and Keio strains containing p*SulA*-GFP and pUA66 were inoculated from a plate of overnight cultures in LB and grown at 37 °C in an incubator with shaking. The GRABS assay was carried out as described above. As a positive control to test the effects of inducing the SOS response, norfloxacin was added at three times the minimum inhibitory concentration (30 ng/mL) to wild-type cells grown in liquid and embedded in agarose. OD was measured at λ = 595 nm and GFP fluorescence was measured with excitation at 485 nm and emission at 515 nm using a Tecan M200 PRO plate reader at 10 min intervals for 8 h.

Analysis of SOS induction was performed by first normalizing the data to fluorescence intensity per cell for p*SulA*-GFP and pUA66 at each time point (t) using the ratio (fluorescence intensity(t)/optical density(t)). We corrected for basal GFP expression by subtracting normalized fluorescence values of pUA66 from p*sulA*-GFP at each time point: (p*SulA*-GFP$_{\text{normalized}}$(t) – pUA66$_{\text{normalized}}$(t)). 3 biological replicates were averaged at each time point. We subtracted average fluorescence values at t = 0 from each subsequent time point to monitor changes in SOS induction for 1% agarose and liquid.

Results

A high-throughput screen for genes that affect bacterial cell mechanics. To address the dearth of knowledge regarding the modulators of bacterial cell stiffness, we sought to develop a comprehensive, reproducible, and high-throughput methodology for quantifying the effects of genetic and chemical perturbations on cellular mechanics. We previously developed a methodology for determining bacterial cell stiffness using microscopy-based growth of single cells embedded in agarose hydrogels of tunable mechanical stiffness (8). We observed a decrease in bacterial growth as we increased gel stiffness, which enabled us to estimate Young's modulus of the cell wall using a finite-element model of the growth of an elastic shell (8). This method for determining cell stiffness, while quantitative and robust, is not amenable to high-throughput measurements at a genomic scale. We hypothesized that decreases in the growth of bacteria embedded in agarose could be measured optically using a standard microplate reader to measure light scattering. This strategy would enable rapid screens of a diverse collection of mutants, including genome-wide knockout libraries, for changes that specifically affect growth embedded in agarose.

To test this approach, we embedded cells of the Keio collection wild-type parent strain *E. coli* BW25113 in agarose gels (0.25% to 5%) that were infused with lysogeny broth (LB) and solidified in a 96-well plate (Experimental Procedures). We measured light scattering using a microplate reader (Figure 3A). As in our single-cell assay of cell

stiffness (8), we observed a monotonic decrease in the optical density (OD) (Figure 3A) and the maximum growth rate of wild-type cells as the concentration of agarose increased (Figure 3B). Based on these data, we inferred that a 1% (Young's modulus 56 kPa) agarose gel is reasonable for detecting changes in cell growth, as wild-type cells growing in agarose had an OD decrease of ~80% relative to liquid medium (Figure 3B; determined at 8 h, which is approximately when wild-type cells enter stationary phase in liquid medium). The OD of cultures embedded in 1% agarose was linearly correlated with cell density over a broad range (Figure 4). Gels with agarose concentrations below 1% are not suitable for our purposes because the pores have dimensions close to the diameter of cells (26).

We applied GRABS (Figure 3C, D) to identify modulators of cell stiffness across the *E. coli* genome by screening 3,844 deletion mutants of non-essential genes from the Keio collection (15). To quantify changes in cell stiffness, we simultaneously measured the growth of 48 strains in a 1% agarose gel and liquid LB on each plate to control for variability in growth across 96-well plates (Figure 3C). While factors in addition to changes in cell stiffness could potentially affect the growth of embedded cells, we previously demonstrated that differences in the diffusion of nutrients, small molecules, or ions in agarose compared to liquid, changes in cell turgor due to osmolarity, and the secretion of enzymes that could alter the structure of the gel did not influence our microscopy-based measurements of *E. coli*'s Young's modulus using agarose-embedded

cells (8). Additionally, agarose-embedded growth did not induce the SOS stress response (Figure 5) or cause noticeable alterations in cell shape (Figure 6A), also suggesting that information from GRABS assays pertained to changes in cell stiffness per se.

To simplify growth curves to a scalar representation of the effects of agarose embedding on growing cells, we calculated the percent change in OD of each mutant (in agarose relative to liquid) compared to wildtype after 8 h (Figure 1). We refer to this metric as the GRABS score (Extended Experimental Procedures), where a negative score indicates that the mutant exhibits less growth in agarose than expected based on its growth in liquid. By calculating GRABS scores across the Keio collection, we identified dozens of mutants that had a large decrease in growth rate in agarose and no significant change in growth rate in liquid relative to wildtype (Figure 3D, 7A), indicating a specific effect of the agarose on growth rate that is consistent with a reduction in cell stiffness. Interestingly, we also identified mutants that grew slowly in liquid, yet displayed growth rates in agarose that were comparable to the rate of wild-type cells. These mutants thus had a positive GRABS score (Figure 3D, 7A), although the large changes in liquid growth rate complicate the interpretation of these mutations as affecting cell stiffness alone.

Cell-stiffness modulators span a wide range of functions. To exclude the possibility that kanamycin (the selective marker of the Keio collection) was directly responsible for changes in embedded growth, we rescreened ~25% of the Keio collection in the absence of kanamycin, focusing on mutants with the largest GRABS scores. Kanamycin had little effect on growth rates in liquid (Figure S5A), but growth rates in 1% agarose were slightly higher in the absence of kanamycin (Figure 8B). From this second screen, we identified 41 mutants (~1% of the genome) with a GRABS score < -0.15 and 5 mutants with a score > 0.3 (Figure 7C). We classified these hits using the Clusters of Orthologous Groups (COG) nomenclature (27) and found that they represent a diverse set of functions (Figure 7B, 7C; Tables 3, 4). As anticipated, cell-wall and membrane biogenesis genes (nine mutants) constituted the largest subset of hits; these mutations likely affect cell stiffness by creating defects in the cell envelope through changes in peptidoglycan architecture or membrane structure. A mutant lacking *mrcB*, the gene encoding the bifunctional protein PBP1b, was the mutant with the largest negative GRABS score (Figure 7C). However, not all cell envelope-related deletions exhibited phenotypes, indicating that cell-wall synthesis activities can differentially impact mechanically confined growth. Moreover, 40/46 hits were from other functional categories (Tables 3, 4); in addition to the 37 mutants not related to cell-envelope assembly, 3/9 cell-wall and membrane biogenesis genes had multiple assigned COG classifications), with the next-largest groups represented by energy production and

conversion (eight mutants), replication/recombination and repair (six mutants), and amino-acid transport and metabolism (four mutants; Figure 7B, 7C). Cell-wall perturbations often result in changes in cell shape, which can affect the spatial distribution of stresses across the cell envelope (stresses are proportional to the radius in a idealized cylindrical thin shell under constant turgor pressure); however, we determined that all Keio mutants except D*rodZ* are rod-shaped (data not shown) and that GRABS scores did not correlate with average cell width or length (Figure 9), indicating that mechanical changes identified in our screen could not be due to changes in cell geometry alone.

Cell stiffness also decreased in strains harboring deletions of genes involved in homologous recombination (Figure 7B, 7C; Tables 3, 4), which is consistent with a recent report that these genes exhibit higher cell lysis/decreased cell envelope integrity (13) that could arise from defects in cell stiffness. Another interesting hit was the deletion of *hfq* (Figure 7C), which encodes the abundant small-RNA regulator Hfq (28). Hfq regulates the functions of 30 small RNAs in *E. coli*, and in turn these small RNAs have hundreds of putative direct or indirect target genes (29). These targets are associated with several of the functions we identified in our screen, including nucleotide transport and metabolism, cell motility, replication, and recombination and repair (Figure 7B, 7C; Tables 3, 4). Several mutants with decreased cell stiffness contained deletions of genes of unknown function, including *yecT*, *yedN,* and *yhfZ*

(Figure 7C). *yecT* was previously found to display increased sensitivity to aztreonam, the antibiotic inhibitor of the division-specific peptidoglycan transpeptidase PBP3, as well as the outer membrane disruptor polymyxin B (14). *yedN* was not included in a previous chemical genomics screen of the Keio collection (14), so the reduced GRABS score defined here is the first known phenotype for this gene.

To confirm that our GRABS measurements were due to a specific gene deletion and not to polar effects or gene replication during strain construction (15), we carried out complementation studies with four genes that yielded large decreases in GRABS score (*mrcB*, *lpoB*, *hfq*, and *hscA*) and two genes that produced essentially no stiffness change (*mrcA* and *lpoA*). We used a low-copy plasmid to express the gene of interest in *trans*, and observed 80-100% recovery of cell growth in agarose at 8 h for *mrcB*, *lpoB*, *hfq*, and *hscA* and no changes in the wild-type-like growth of *mrcA* and *lpoA* mutants (Figure 10A). Difficulties in fully complementing the *in vivo* function of Hfq using recombinant plasmids have been previously noted, as overexpression is toxic (30). Our data, along with the lack of mechanical phenotypes in deletions of genes downstream of *hfq* in the operon containing *hfq* (Figure 10B), indicate that the stiffness phenotype we observe is unlikely to be due to polar effects. To further confirm the GRABS effects of these deletions, we constructed clean deletions in the well-characterized *E. coli* strain MG1655 (Extended Experimental Procedures). The phenotypes for *E. coli* MG1655 cells grown in agarose quantitatively matched the phenotypes of corresponding BW25113

mutants (Figure 10C), indicating that the role of these proteins in maintaining cellular mechanical properties is conserved in these *E. coli* strains.

GRABS scores are highly correlated with measurements of Young's modulus. To determine whether our GRABS measurements reflect changes in cell stiffness, we directly measured Young's modulus using two complementary microscopy-based methodologies: 1) a microfluidic-based bending assay (19), and 2) our previously developed single-cell assay of embedded growth (8). In the bending assay, a shear fluid force is applied to filamentous cells (Figure 11A) and flexural (bending) rigidity is estimated by fitting the deflection (Figure 12) of the cell body to a mechanical model (Extended Experimental Procedures); elastic-shell theory predicts that the magnitude of deflection of the cell tip under flow is proportional to l^4, where l is the cell length exposed to flow (19).

For a set of 13 mutants reflecting a broad range of cellular processes and spanning the complete range of GRABS scores, we induced filamentation through the production of SulA (Extended Experimental Procedures), which inhibits polymerization of the key division protein FtsZ (31) and abolishes the recruitment of the division-specific cell-wall machinery to the division site (32). We obtained flexural rigidities of 8.9×10^{-20} N m^2 for wild-type cells and 3.5×10^{-20} N m^2 for Δ*mrcB* cells, the mutant with the largest magnitude GRABS score. Using an estimate of 3 nm for the thickness of the

E. coli cell wall (33), we estimated the Young's modulus of wild-type cells to be 28 MPa (Figure 11B, left; Extended Experimental Procedures), similar to previous studies (8, 34). By contrast, the Young's modulus of Δ*mrcB* cells was 12 MPa (Figure 11B); the ~2-fold decrease relative to wild-type cells is in good agreement with our GRABS scores (Figure 7C), validating the importance of PBP1b for cell-stiffness determination. The additional 11 mutants had both positive and negative GRABS scores and displayed Young's moduli in agreement with the GRABS scores (Figure 7C; Pearson correlation coefficient $R = 0.83$, Student's t-test: $p < 0.00025$). We even observed a higher Young's modulus in Δ*recA* cells (Figure 11B, left), which had a positive GRABS score (Figure 7C) by virtue of the only slight defect in agarose-embedded growth relative to the substantial decrease in liquid growth (Figure 13). Interestingly, the Δ*hscA* mutant, which had a large, negative GRABS score (Figure 7C), had a Young's modulus close to that of wild-type cells (Figure 11B, left). Since HscA plays a role in cell division by affecting FtsZ localization at the division plane (35), we hypothesized that the discrepancy between the Young's modulus and the GRABS score for this mutant was due to inducing filamentation via SulA. To test this idea, we filamented Δ*hscA* cells using aztreonam, an inhibitor of the division-specific transpeptidase PBP3 (36). Under aztreonam treatment, Δ*hscA* cells had a lower Young's modulus than wild-type cells (Figure 11B, right), in agreement with our GRABS data (Figure 7C), indicating that the proper localization of

FtsZ or division-specific cell-wall machinery is important for the cell stiffness decrease in Δ*hscA* cells.

To complement our microfluidics-based measure of radial cell stiffness, we also compared GRABS to our previous microscopy-based approach (8), which measures longitudinal cell stiffness. We measured the elongation of wild-type (MG1655), Δ*mrcB*, Δ*lpoB*, Δ*hfq*, Δ*hscA*, Δ*mrcA*, and Δ*lpoA* cells embedded in agarose gels of variable stiffness (Figure 14). Our single-cell data was consistent with our GRABS scores, with wild-type, Δ*mrcA*, and Δ*lpoA* cells showing similar growth in gels from 1-4% agarose and Δ*mrcB*, Δ*lpoB*, Δ*hfq*, and Δ*hscA* cells showing relatively less growth (Figure 14). Using ultra performance liquid chromatography (Extended Experimental Procedures), we ascertained that the peptidoglycan composition in each of these mutants was similar to that in wild-type cells (Figure 15). We also measured cell viability within the gel using fluorescence microscopy (Extended Experimental Procedures) of wild-type cells and nine mutants in liquid and embedded in 1% agarose. There was no obvious difference in cell viability for wild-type cells or most of the mutants embedded in agarose (Figure 16A). A few Δ*mrcB* and Δ*lpoB* cells were dead after 4 h, which is approximately the period of most rapid growth in 1% agarose (Figure 16A); this level of cell death is insufficient to account for the decrease in embedded growth. Taken together, our results confirm that decreased cell stiffness is a major cause of the

increased growth inhibition of mutant cells embedded in agarose, and validates GRABS as a methodology for identifying changes in Young's modulus in bacterial cells.

Differential embedded growth among cell-wall synthesis mutants indicates a potential mechanism for reduced cell stiffness. Given that cell-wall assembly is of paramount importance for the mechanical integrity of bacterial cells and yet deletion of key enzymes had variable mechanical impacts in our experiments, as a case study, we sought to interrogate how genetic perturbations to the biochemical activities of two of these enzymes affected cell stiffness. A major fraction of cell-wall synthesis in *E. coli* is carried out by the high molecular weight PBPs 1a and 1b (10), which are encoded by the genes *mrcA* and *mrcB*, respectively. PBP1a and PBP1b are bifunctional enzymes that contain both glycosyltransferase and transpeptidase activities for glycan-strand polymerization and peptide crosslinking, respectively. The prevailing hypothesis for the functions of these proteins based on their spatial localization is that PBP1a is primarily responsible for peptidoglycan construction along the elongating peripheral cell wall and PBP1b controls peptidoglycan assembly at the division site (37). Δ*mrcA* Δ*mrcB* double mutants are synthetically lethal (38, 39), but deletion of *mrcA* or *mrcB* alone does not substantially affect growth (Figure 6B) or cell shape (Figure 6C, 6D), indicating partial compensation for each other's *in vivo* activities (40). However, the two enzymes are not biochemically identical (41, 42), and thus it remains unclear to what

extent their functions are redundant *in vivo*. For example, in contrast to Δ*mrcA* cells, Δ*mrcB* cells are outcompeted by wild-type cells in stationary phase (43), have increased sensitivity to β-lactam antibiotics (38, 44, 45), and cannot revert into walled rods from spheroplasts due to their inability to divide (46). In our GRABS screen (Figure 7C) and bending measurements (Figure 11B), Δ*mrcB* was the mutant with the strongest phenotype, while Δ*mrcA* was phenotypically wildtype (Figure 6E), demonstrating that PBP1a and PBP1b make dramatically different contributions to cell stiffness.

PBP1b contains a glycosyltransferase domain, a transpeptidase domain, and a UB2H domain (Figure 17A). To determine which domains and biochemical function(s) of PBP1b were responsible for the decrease in GRABS score (Figure 7C) and bending stiffness (Figure 11B), we complemented Δ*mrcB* cells with mutant forms of *mrcB* expressed in *trans* from a plasmid and measured cell growth in liquid (Figure 18) and embedded in 1% agarose. Inactivation of the glycosyltransferase domain via the mutation E233Q (47, 48) resulted in a decrease in the OD of agarose-embedded cells that was similar to that of Δ*mrcB* (Figure 17B), indicating that glycosyltransferase activity is necessary for the modulation of cell stiffness by PBP1b. By contrast, a mutant with inactivated transpeptidase activity (S510A) (47, 48) (Figure 17A) partially restored the decrease in OD of embedded Δ*mrcB* cells (Figure 17B).

The lipoprotein cofactor LpoB is important for the activation and enhancement of the transpeptidase and glycosyltransferase activities of PBP1b through the UB2H

domain over an extended interface (49, 50). It was previously shown that the D163A/E166A double mutation (Figure 17A) resulted in two-fold lower binding affinity of the PBP1b UB2H domain to LpoB *in vitro* (49); however, this mutation did not noticeably affect embedded OD relative to wild-type cells (Figure 4B). Although the R190D mutation decreased activation by LpoB ~16-fold (49), we observed only a slight decrease (~6%) in the ability of PBP1b^{R190D} to fully complement embedded cell growth (Figure 4B). A PBP1b mutant with six amino-acid substitutions in the UB2H domain (6UB2H) displayed a 50-fold decrease in binding to LpoB (49); in our GRABS assay, this mutant exhibited a substantial decrease in OD when grown in agarose that was intermediate between the decreases in OD for BW25113 and Δ*mrcB* (Figure 17B). To confirm whether the 6UB2H mutant lost all interaction with LpoB, we compared its growth curve for embedded growth to that of the Δ*lpoB* mutant. The two curves did not qualitatively match (Figure 17C), indicating that there may be a minor interaction between LpoB and the UB2H domain that persists in the 6UB2H mutant.

The quantitative difference between the Δ*mrcB* and Δ*lpoB* phenotypes suggests a basal level of PBP1b functionality in the absence of LpoB. Interestingly, the growth curve of the embedded Δ*lpoB* mutant was qualitatively similar to that of an S510A transpeptidase mutant (Figure 17C), illustrating that *in vivo* activation of PBP1b's glycosyltransferase domain may be independent of its interaction with LpoB. It is possible that these mutations may alter the stability or expression of PBP1b. Regardless,

using the GRABS assay, we were able to disentangle nuances of the biochemical activities of PBP1b and its activator LpoB and link transglycosylase activity to changes in *E. coli* cell stiffness, thereby translating *in vitro* measurements to *in vivo* phenotypes; this strategy could be used to dissect the biochemical mechanism by which any protein modulates cell stiffness.

Carbonyl cyanide m-chlorophenyl hydrazone (CCCP) increases cell stiffness. The genomic scale of our stiffness measurements empowered the use of statistical correlations to identify chemicals that generally affect cell stiffness across the strains in the Keio collection. We correlated our GRABS scores in the presence of kanamycin with a previously published chemical-genomics dataset of colony growth under hundreds of conditions (14). The 20 conditions with the largest positive Pearson correlation coefficient, indicating that reductions in GRABS score coincide with negative S-score (reduced growth), included known envelope perturbations that are expected to disrupt cell mechanics (Table 5), such as the detergents sodium dodecyl sulfate and Triton X-100, the small molecule A22 (which inhibits the MreB cytoskeleton) (12), and the antibiotic cefsulodin (which targets PBP1a and PBP1b) (51). Intriguingly, there were also conditions associated with a negative correlation of a similar magnitude to the highest positive correlations in Table 5, indicating conditions in which GRABS score

generally increased in strains with negative S-scores (Table 6). Thus, we hypothesized that some of these conditions may result in a general increase in cell stiffness.

We focused on the proton ionophore CCCP, which rapidly eliminates membrane potential by dissipating the proton motive force (52); CCCP treatment at multiple concentrations had a significant negative correlation with GRABS scores (Table 6). We performed GRABS on wild-type cells and on 40 strains with the largest reduction in GRABS scores in the presence of 2 μg/mL CCCP. As expected, CCCP reduced growth rates in liquid (Figure 19A). However, embedded growth rates were reduced to a lesser extent (Figure 19B), and GRABS scores generally increased as predicted (Figure 20). Thus, our assay can be used to reveal conditions that modulate cell stiffness in both directions and to predict chemicals that will display synergy or antagonism with genetic perturbations that affect cell stiffness.

Discussion

Here, we report a straightforward, high-throughput technology for rapid characterization of bacterial stiffness that should be widely applicable to the discovery of the mechanical effects of genetic or chemical perturbations to cellular functions. GRABS requires only standard lab equipment. Since absorbance-based optical measurements are sufficient for identifying genes connected to cell stiffness, as demonstrated here, GRABS is the first mechanical measurement technology that can be applied to genome-scale libraries. Because GRABS is based on a direct readout of proliferation, it can be easily applied to bacteria that display a variety of morphological phenotypes, such as filamentation, rounding, or branching. Embedding cells in an agarose hydrogel confines them and introduces a defined and tunable force that opposes growth while ensuring a constant supply of nutrients by diffusion. We previously demonstrated that agarose does not significantly alter the diffusion of growth factors, nor does it trigger contact-dependent phenotypes (8). To normalize measurements of growth on agarose to growth in liquid, we also generated growth curves for Keio mutants in liquid LB (Table 7), a data-mining resource for the microbiology community. The GRABS score is correlated with the maximal growth rate obtained from fitting agarose growth curves with a Gompertz relation (Figure 21), potentially further simplifying future screens of cell mechanics. The GRABS score used here does not necessarily directly translate to quantitation of Young's modulus, a

standard measure of cellular stiffness. Nonetheless, GRABS scores were generally consistent with Young's moduli determined from microfluidic-based bending assays (Figure 11) and single-cell embedded growth measurements (Figure 14), suggesting that GRABS enables rapid screening of genomic-scale mutant collections for changes in cell stiffness (Figure 7). When computing Young's modulus, we assumed a common value for wall thickness in all mutants; changes to this parameter would affect our modulus estimates. Cases such as Δ*hscA*, in which GRABS and other mechanical measurements appear to make conflicting estimates of cell stiffness (Figure 11B), can in fact reveal subtle feedback between biochemical functions of the affecting protein and cellular stiffness. Regardless, our identification of stiffness modulators related to numerous functions in *E. coli* (Figure 7B, 7C) indicates that cell mechanics is a global property connected to many intracellular pathways.

Our screen identified many new factors that affect the mechanical properties of cells. These factors span diverse gene classes (Figure 7B, 7C); even for envelope-biogenesis genes that may be more intuitively connected with cell stiffness, our assay revealed qualitative differences between the high molecular weight PBPs that are partially redundant (Figures 7C, 11B, 14). Our demonstration that a wide range of cellular processes affects stiffness highlights the potential for insights gleaned through combinations of genetic and chemical perturbations (as used here) and establishes that perturbing processes that are not directly linked to cell-envelope construction can alter

cell stiffness. An excellent example is the protonophore CCCP, which eliminates the proton-motive force. Although it remains to be clarified how CCCP increases cell stiffness (Figure 20), the increase in Young's modulus of Δ*recA* cells demonstrates (Figure 11B, left) that stiffness can be modulated up and down. It is possible that imbalances in growth resulting from CCCP exposure affect the crosslinking of the cell wall or alter the composition of the outer membrane by inducing the expression of porins. Regardless, cell stiffness is an important factor when assaying the efficacy of any chemical inhibitor of growth, particularly since many bacteria reside in natural environments that resemble the mechanical constraints of agarose gels (such as the mucosal lining of the intestinal epithelium) more than liquid.

This investigation demonstrates that GRABS can reveal connections among genetic, biochemical, and mechanical perturbations and cellular physiology. GRABS enabled us to characterize the drastic difference in cell stiffness between PBP1a and PBP1b deletion mutants *in vivo* (Figure 7C, 11B, 6), and GRABS was sensitive enough to identify small changes in the growth in agarose of PBP1b mutants that were connected with their known effects on its biochemical activities (Figure 17B, 17C). We confirmed that the glycosyltransferase domain of PBP1b is a major contributor to *E. coli* cell stiffness (Figure 17B). Our results provide further support for the model that LpoB interacts with the UB2H domain and thereby enhances transpeptidase activity (49, 50). However, the growth curve of the Δ*lpoB* mutant qualitatively matched that of a PBP1b

transpeptidase mutant (Figure 17C), indicating that PBP1b's interaction with LpoB may not drastically affect its glycosyltransferase function *in vivo*. Mutation of the UB2H domain may prevent LpoB from binding to and/or activating PBP1b, by affecting structural changes required for enhanced transpeptidase activity. Variability in the expression, stability, or toxicity of mutant PBP1b proteins may be responsible for incomplete recovery of growth in agarose. Overall, our observations of the links between mutations and mechanical phenotypes emphasize that GRABS is a powerful, high-throughput tool for screening targeted libraries of specific mutants in proteins of interest.

Future agarose growth-based studies of cells and mutants with morphological perturbations will be empowered by modeling the effects of mechanical perturbations on cellular dimensions and viability to disentangle changes in shape from changes in intrinsic mechanical properties. Changes in the anisotropy in the wall (53) or the cell's propensity for lysis can also alter cell mechanics. Although intractable for genome-scale libraries, our previously described, microscopy-based approach (8) provides a methodology to deconvolve some of these factors by simultaneously quantifying cell morphology, lysis, and agarose-mediated inhibition of elongation. For example, application of our previous, microscopy-based approach revealed that Δ*mrcB* cells exhibit both elongation inhibition in gels (Figure 14) and increased lysis (Figure 16B) in a 4% agarose gel.

GRABS also enables secondary screens for genetic and chemical discovery, for example the identification of small molecules that affect cell stiffness individually or in combination with non-essential genes. *E. coli* cells can survive during elongation with a 50% reduction in peptidoglycan density (54); however, alterations to normal peptidoglycan composition may alter cell stiffness (55), thereby sensitizing cells to small molecules or to environmental changes such as osmotic shifts. A recent study demonstrated that many *E. coli* genes increase the permeability of the cell envelope in responses to changes in temperature and salt concentration (among other conditions), which was sometimes accompanied by morphological changes (13). Investigating the effects of these environmental variables through growth in agarose may reveal genes that act synergistically or antagonistically with changes in the cell envelope.

GRABS is well suited to mechanical-genomics studies of any single-celled organism with a cell wall, including a wide range of pathogens (bacterial and fungal), and may also be applicable to eukaryotic cells surrounded by an extracellular matrix such as those within a tumor. The embedded-growth framework of this method is also relevant for a wide variety of environmental contexts such as when cells grow surrounded by mucus or other extracellular polymers or within a tissue (56). Using this technique to explore the growing number of genome-wide gene deletion libraries (57, 58) will enable the discovery of conserved mechanisms of mechanical modulation, as well as generate new opportunities for rewiring cellular mechanical properties and

studying cellular adaptation, survival, and novel mechanisms for antibiotic chemotherapeutics.

Acknowledgements

The authors thank the Huang and Weibel labs for useful discussions, Andrew Gray, Carol Gross, and Waldemar Vollmer for helpful feedback, and Suresh Kannan and Kevin Young for strains. This work was supported by NIH Director's New Innovator Awards DP2OD006466 (to K.C.H.) and DP2OD008735 (to D.W.), NSF CAREER Award MCB-1149328 (to K.C.H.), NSF Award DMR-1121288 (to U. Wisconsin at Madison), the Stanford Systems Biology Center funded by NIH grant P50 GM107615 (to K.C.H.), and a Wisconsin Alumni Research Foundation Distinguished Graduate Fellowship (to M.R.). This work was also supported in part by the National Science Foundation under Grant PHYS-1066293 and the hospitality of the Aspen Center for Physics.

Figure 1. Distributions of GRABS scores over time for all Keio strains. GRABS scores were calculated as described in the Extended Experimental Procedures, but with the time point of the final OD measurement varied from t = 3 h to t = 14 h. Curves are shown with variable shifts along the y-axis for visual clarity. The largest range of GRABS scores occurred after ~8 h of growth. Kan, kanamycin.

(A) Distribution of GRABS scores.

(B) Distribution of OD values for agarose-embedded growth.

(C) Distribution of OD values for liquid growth.

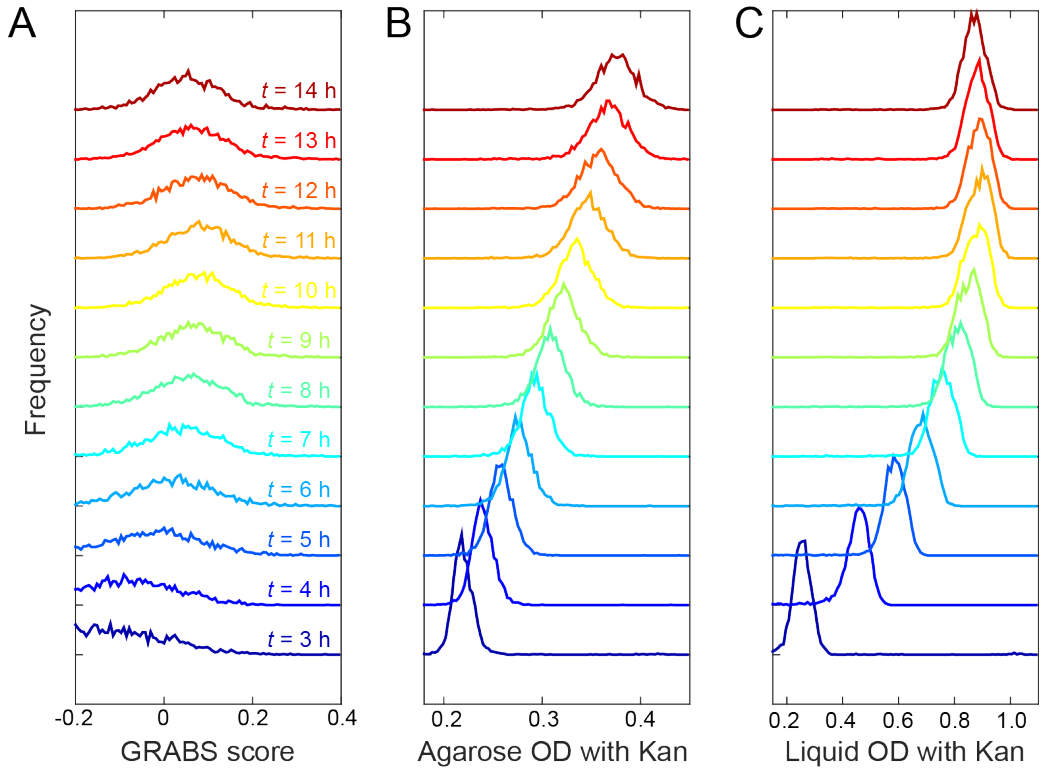
A
B
C
Frequency
t = 14 h
t = 13 h
t = 12 h
t = 11 h
t = 10 h
t = 9 h
t = 8 h
t = 7 h
t = 6 h
t = 5 h
t = 4 h
t = 3 h
-0.2
0
0.2
0.4
GRABS score
0.2
0.3
0.4
Agarose OD with Kan
0.2
0.4
0.6
0.8
1.0
Liquid OD with Kan

Figure 1

Figure 2. GRABS scores are not correlated with cellular dimensions ($n \geq 100$ cells for each strain).

A) GRABS score was not significantly correlated with average cell width (Experimental Methods; $p = 0.075$)

GRABS score was not significantly correlated with average cell length ($p = 0.68$).

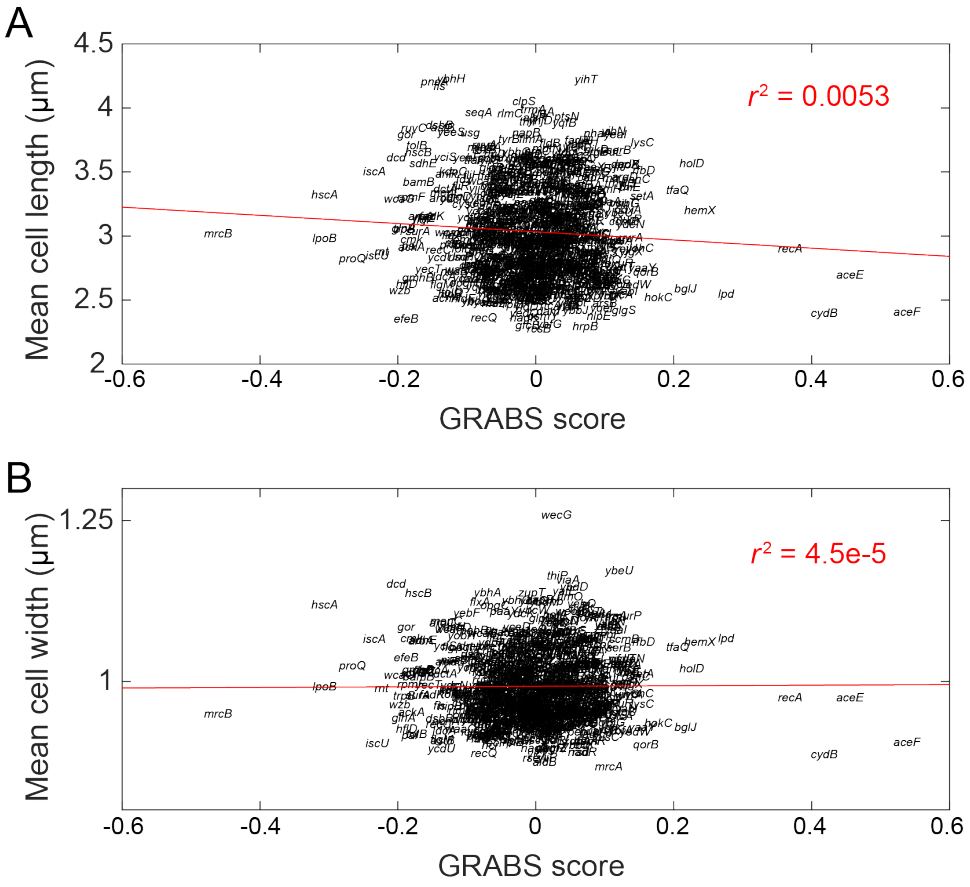
A
Mean cell length (μm)
4.5
4
3.5
3
2.5
2
r^2 = 0.0053
-0.6
-0.4
-0.2
0
0.2
0.4
0.6
GRABS score
B
Mean cell width (μm)
1.25
1
r^2 = 4.5e-5
-0.6
-0.4
-0.2
0
0.2
0.4
0.6
GRABS score

Figure 2

Figure 3. GRABS methodology enables high-throughput measurements of cellular mechanical properties.

A) Growth curves of *E. coli* BW25113 embedded in 0.25%-5% agarose gels and liquid medium (n = 3) monitored with a plate reader; cell growth diminishes as gel stiffness increases. Solid lines and shaded areas represent the smoothed average and one standard deviation, respectively. Inset: schematic of a bacterial cell growing in agarose. Of the forces acting on the cell, F_{gel} is proportional to the stiffness of the agarose gel, F_{cw} is proportional to the composite stiffness of the cell envelope including the membranes and peptidoglycan layer, and F_{turgor} represents the turgor pressure across the cell membrane.

B) Maximal growth rate of an embedded *E. coli* culture and gel Young's modulus (8) as a function of gel stiffness. Solid lines and shaded areas represent the average and one standard deviation ($n \geq 3$ for each concentration), respectively.

C) Schematic of the GRABS assay. A microwell is filled with 1% agarose or liquid medium, cells are pipetted into the well, and cells are mixed using a magnetic stirrer until homogenously dispersed. The stirrer is then removed and the agarose is left to solidify. In the 96-well microplate, wells in columns 1-6 are filled with 150 mL of 1% agarose and columns 7-12 are filled with liquid medium. Grey circles in columns 1-6 represent magnetic stirrers.

D) Example growth curves for wild-type *E. coli* BW25113 (black) and mutants with GRABS score = 0 (wildtype-like, green), > 0 (increased stiffness, red), and < 0 (decreased stiffness, blue). Wildtype growth curves in liquid are represented by dotted lines, and growth curves of cells in agarose are represented by dashed lines. Many mutants with a GRABS score < 0 have the same growth rate as wild-type cells in liquid and a reduced

growth rate in 1% agarose. A GRABS score > 0 typically occurs when a mutant has a decreased growth rate in liquid and a growth rate similar to that of wild-type cells in agarose.

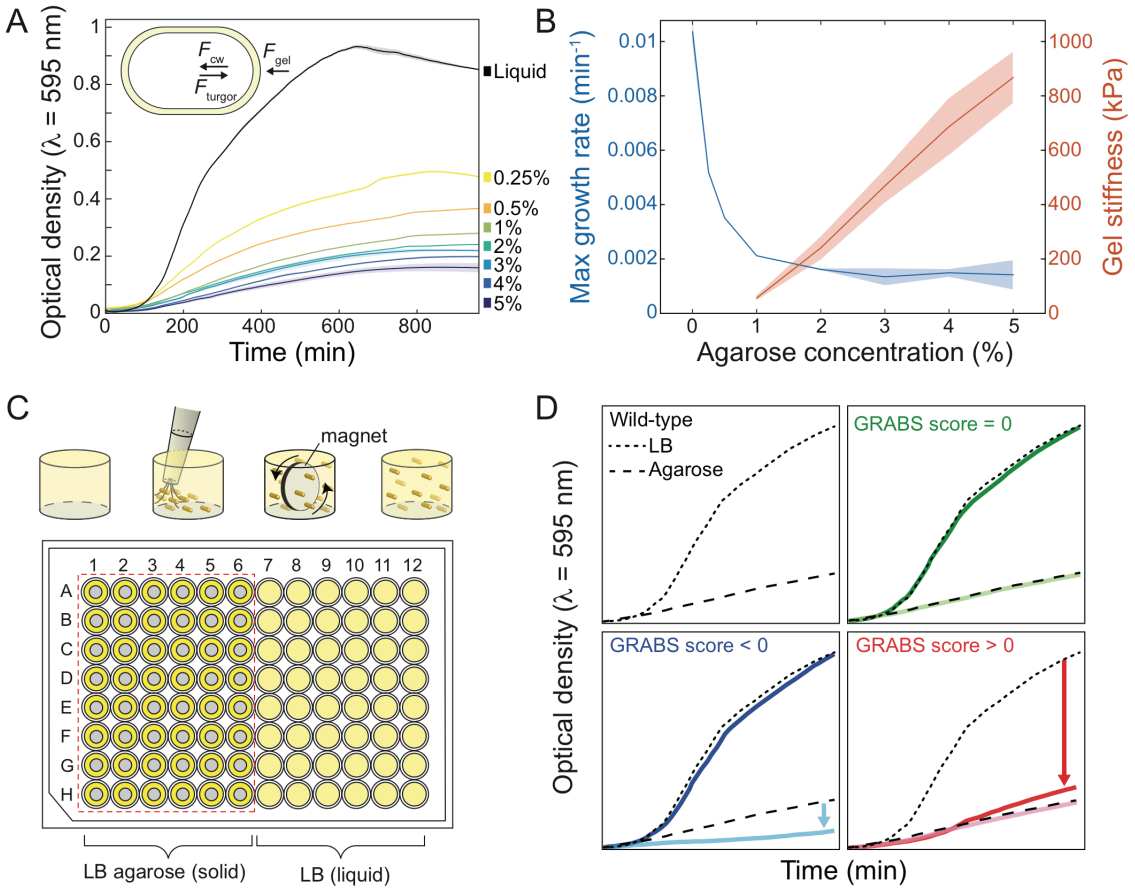
A
Optical density (λ = 595 nm)
Time (min)
Liquid
0.25%
0.5%
1%
2%
3%
4%
5%
B
Max growth rate (min-1)
Gel stiffness (kPa)
Agarose concentration (%)
C
magnet
LB agarose (solid)
LB (liquid)
D
Wild-type
LB
Agarose
GRABS score = 0
GRABS score < 0
GRABS score > 0
Optical density (λ = 595 nm)
Time (min)

Figure 3

Figure 4. Optical density of *E. coli* BW25113 cells embedded in 1% agarose exhibits an approximately linear increase with increasing cell density. Shaded region represents one standard deviation above and below mean growth curves (n = 3 curves).

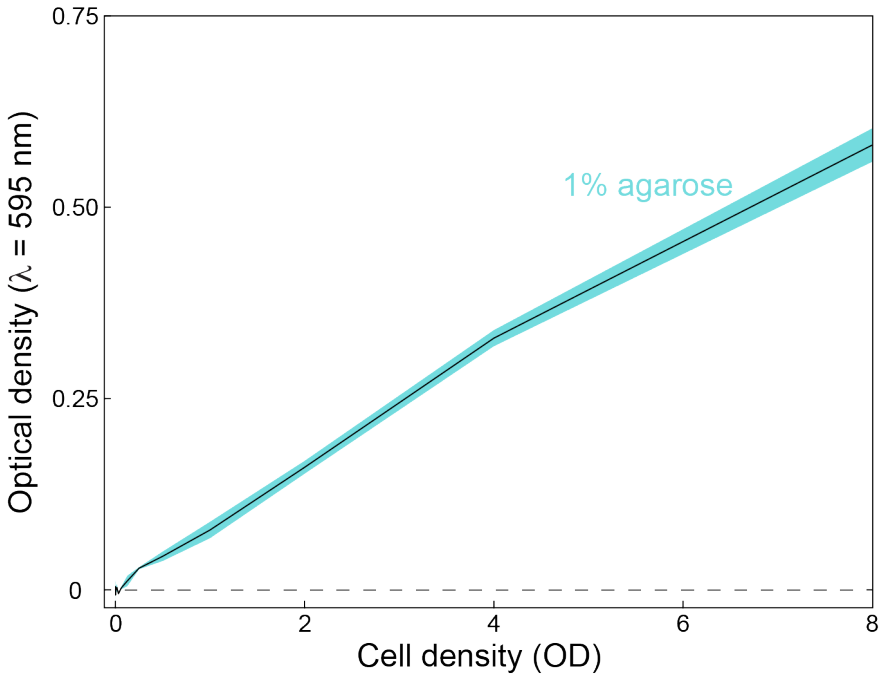
0.75
0.50
0.25
0
Optical density (λ = 595 nm)
1% agarose
0
2
4
6
8
Cell density (OD)

Figure 4

Figure 5. Embedded growth in 1% agarose does not induce the SOS response. Cells with a *sulA* promoter fusion to GFP were grown in wells of a 96-well plate and fluorescence (λ_{ex} = 485 nm, λ_{em} = 515 nm) was quantified using a plate reader. To normalize fluorescence signal to cell density, the optical density was monitored at λ = 595 nm. Shaded regions represent one standard deviation above and below mean growth curves (n = 3 biological replicates). A.U., arbitrary units.

(A) In *E. coli* BW25113 cells, we observed induction of the SOS response in both liquid and agarose when cells were treated with norfloxacin at three times the minimum inhibitory concentration (MIC).

(B-H) By contrast, SOS induction was negligible in both liquid and agarose for wild-type cells and six mutants with large-magnitude GRABS scores.

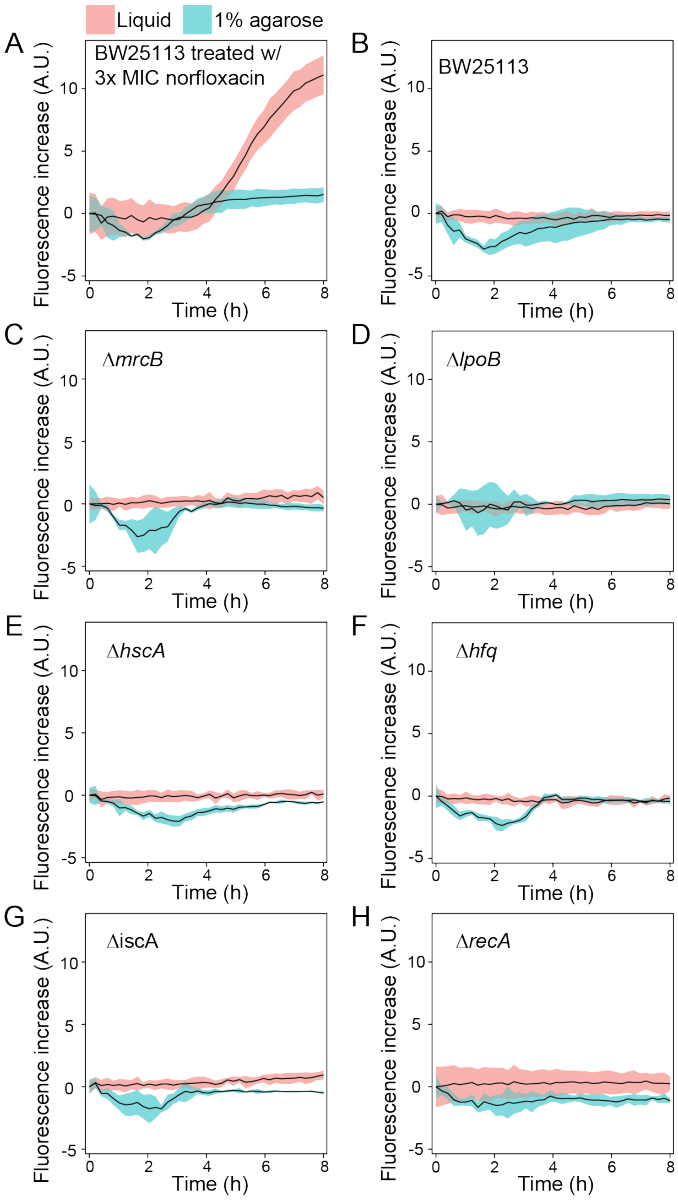
Liquid
1% agarose
A
BW25113 treated w/
3x MIC norfloxacin
B
BW25113
C
ΔmrcB
D
ΔlpoB
E
ΔhscA
F
Δhfq
G
ΔiscA
H
ΔrecA
Fluorescence increase (A.U.)
Time (h)

Figure 5

Figure 6. Δ*mrcA* and Δ*mrcB* cells have distinct mechanical properties, yet their growth rates in liquid and cell morphology in liquid and agarose are similar to each other.

A) Δ*mrcA* and Δ*mrcB* cells do not exhibit substantial changes in cell size or shape after 8 h of growth embedded in 1% agarose. Blue is a false color of the phase-contrast image. Green is a false color of the fluorescence channel from FM4-64 membrane stain. Scale bar: 10 mm.

B) Δ*mrcA* and Δ*mrcB* cells have similar growth rates, with slight growth-rate deficiencies relative to wild-type, in liquid LB. Growth curves were measured by monitoring optical absorbance. Solid lines represent the mean over $n = 3$ curves. Shaded regions represent one standard deviation away from the mean. Maximum growth rates, obtained by fitting to a Gompertz relation: (BW25113, 0.01 min^{-1}; Δ*mrcA*, 0.0072 min^{-1}; Δ*mrcB*, 0.0077 min^{-1}).

C) Phase-contrast images of *E. coli* BW25113, Δ*mrcA*, and Δ*mrcB* cells grown in liquid LB. Scale bar: 5 mm.

D) Δ*mrcA* and Δ*mrcB* cells have similar cellular dimensions as wild-type cells ($n \geq 217$ cells for each strain). Error bars represent one standard deviation from the mean.

E) Δ*mrcA* cells have a GRABS score indicating that their stiffness is similar to wild-type cells. By definition, wild-type cells have a GRABS score of zero because all measurements are normalized to the wells containing wild-type cells. Error bars are one standard deviation away from the mean ($n = 4$).

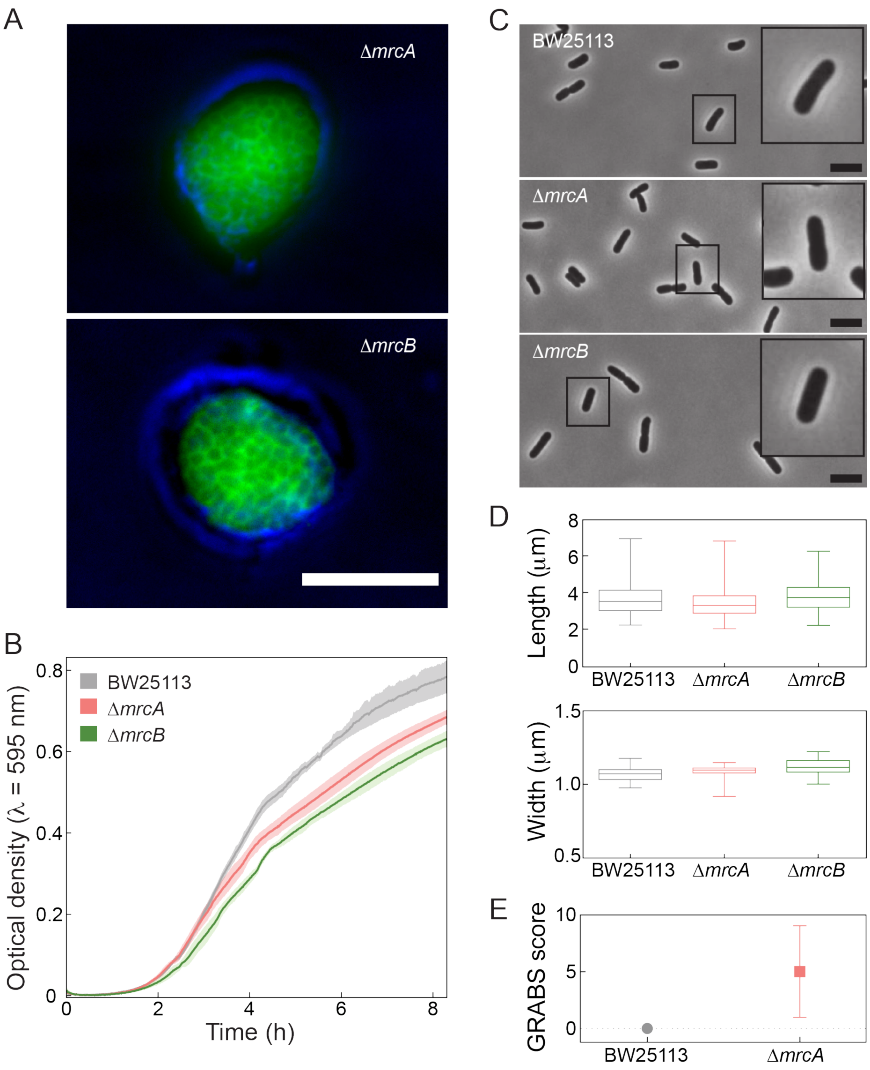
A
ΔmrcA
ΔmrcB
B
Optical density (λ = 595 nm)
Time (h)
BW25113
ΔmrcA
ΔmrcB
C
BW25113
ΔmrcA
ΔmrcB
D
Length (μm)
Width (μm)
BW25113
ΔmrcA
ΔmrcB
E
GRABS score
BW25113
ΔmrcA

Figure 6

Figure 7. Cell-stiffness modulators encompass a large range of cellular functions.

A) Maximal growth rates in liquid and agarose. Blue and red ovals represent the mean growth rates ± one standard deviation for BW25113 and Δ*mrcB*, respectively ($n \geq 5$ independent experiments); the gray oval represents the distribution of values for the Keio collection.

B) The 46 genes with GRABS score < -0.15 ($n = 41$) or > 0.3 ($n = 5$) come from 18 Clusters of Orthologous Groups (COGs). Several genes (Δ*recA,* Δ*tolR,* Δ*tolB,* ΔwcaG, Δ*fliA*) are assigned to two or more orthologous groups, which gives rise to $n = 53$ total assignments.

C) Top: distribution of GRABS scores. Bottom: GRABS hits in (B). The average GRABS score and standard deviation across ≥ 6 replicates from multiple independent experiments are shown. Genes are colored according to their COG assignment. Genes with ≥ 2 COG assignments are colored accordingly. *E. coli* BW25113 has a GRABS score of 0 by definition.

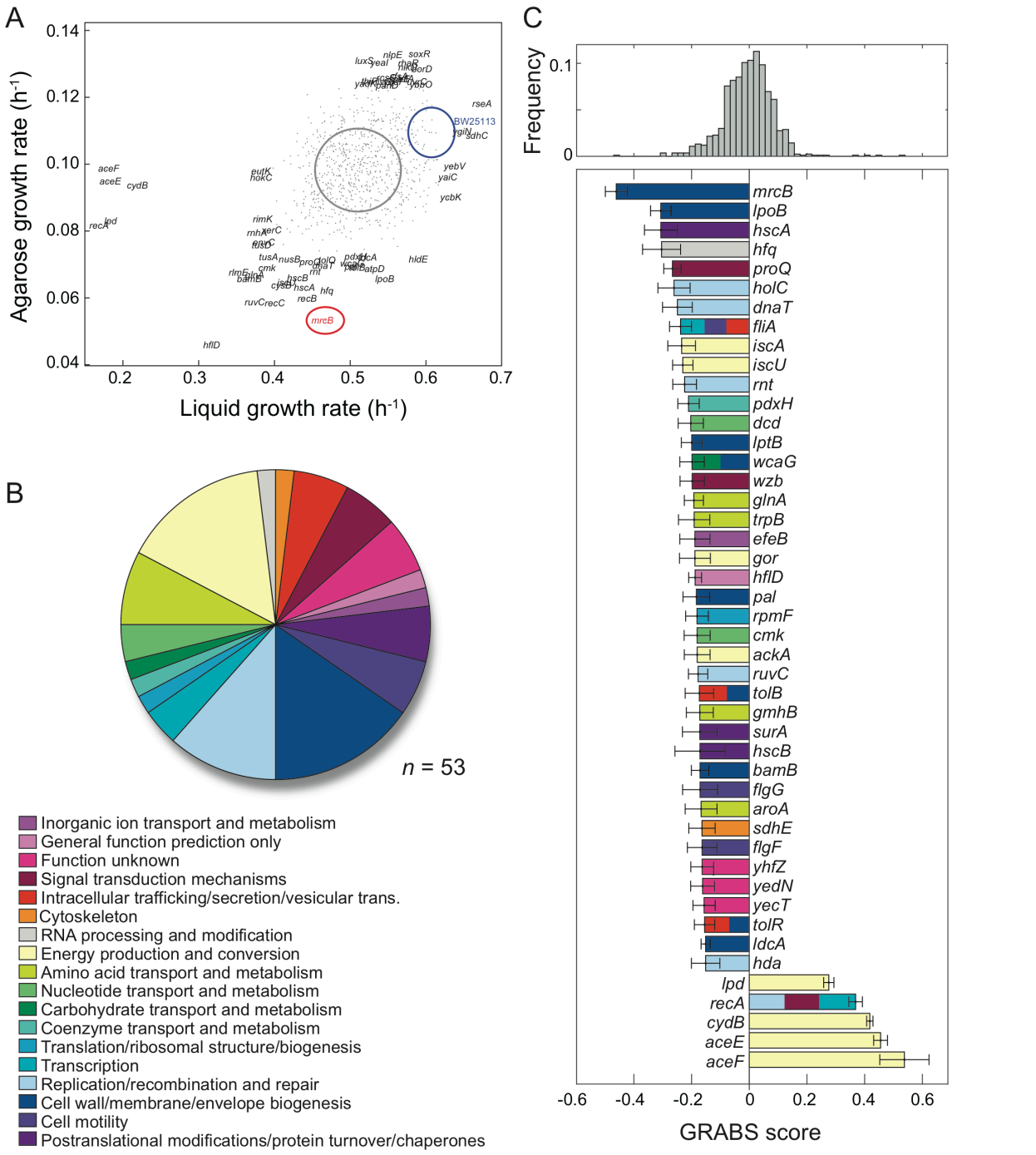
A
Agarose growth rate (h-1)
Liquid growth rate (h-1)
0.14
0.12
0.10
0.08
0.06
0.04
0.2
0.3
0.4
0.5
0.6
0.7
BW25113
mrcB
B
n = 53
Inorganic ion transport and metabolism
General function prediction only
Function unknown
Signal transduction mechanisms
Intracellular trafficking/secretion/vesicular trans.
Cytoskeleton
RNA processing and modification
Energy production and conversion
Amino acid transport and metabolism
Nucleotide transport and metabolism
Carbohydrate transport and metabolism
Coenzyme transport and metabolism
Translation/ribosomal structure/biogenesis
Transcription
Replication/recombination and repair
Cell wall/membrane/envelope biogenesis
Cell motility
Postranslational modifications/protein turnover/chaperones
C
Frequency
0.1
0
mrcB
lpoB
hscA
hfq
proQ
holC
dnaT
fliA
iscA
iscU
rnt
pdxH
dcd
lptB
wcaG
wzb
glnA
trpB
efeB
gor
hflD
pal
rpmF
cmk
ackA
ruvC
tolB
gmhB
surA
hscB
bamB
flgG
aroA
sdhE
flgF
yhfZ
yedN
yecT
tolR
ldcA
hda
lpd
recA
cydB
aceE
aceF
-0.6
-0.4
-0.2
0
0.2
0.4
0.6
GRABS score

Figure 7

Figure 8. Kanamycin (Kan) has little effect on growth rates in liquid, but growth inhibition in agarose is enhanced by kanamycin treatment. Blue lines are $y = x$.

A) Mean growth rates ($n = 4$) of Keio mutants in liquid is unaffected by the presence or absence of Kan.

B) Growth inhibition during encapsulation in 1% agarose is enhanced by Kan ($n = 4$).

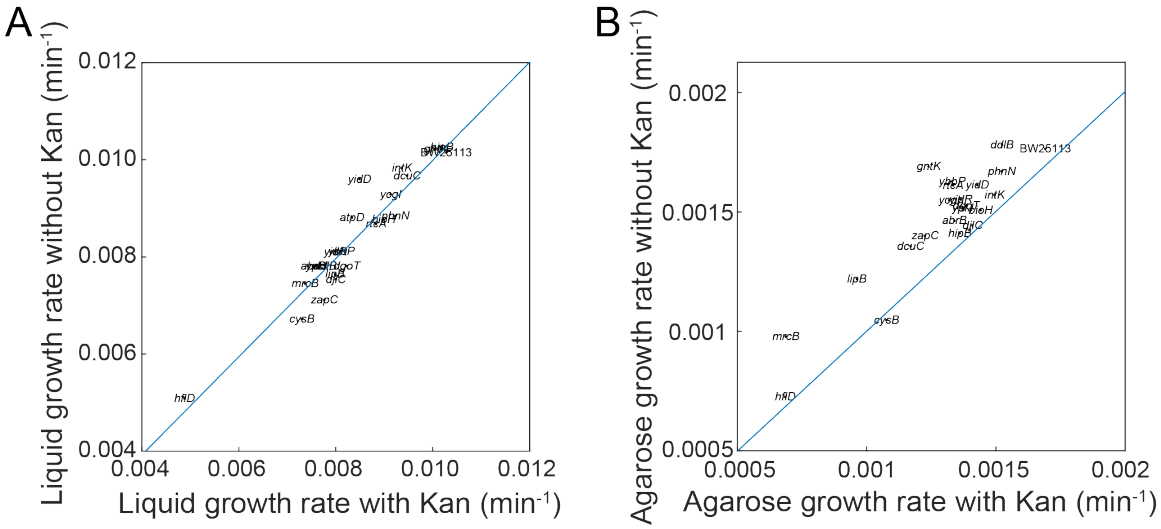
A
Liquid growth rate without Kan (min-1)
Liquid growth rate with Kan (min-1)
0.004
0.006
0.008
0.010
0.012
B
Agarose growth rate without Kan (min-1)
Agarose growth rate with Kan (min-1)
0.0005
0.001
0.0015
0.002
BW26113
ddlB
gntK
phnN
yieD
intK
dcuC
zapC
lipB
cysB
mrcB
hflD

Figure 8

Figure 9. GRABS scores are not correlated with cellular dimensions ($n \geq 100$ cells for each strain).

A) GRABS score was not significantly correlated with average cell width (Extended Experimental Methods; $p = 0.075$)
B) GRABS score was not significantly correlated with average cell length ($p = 0.68$).

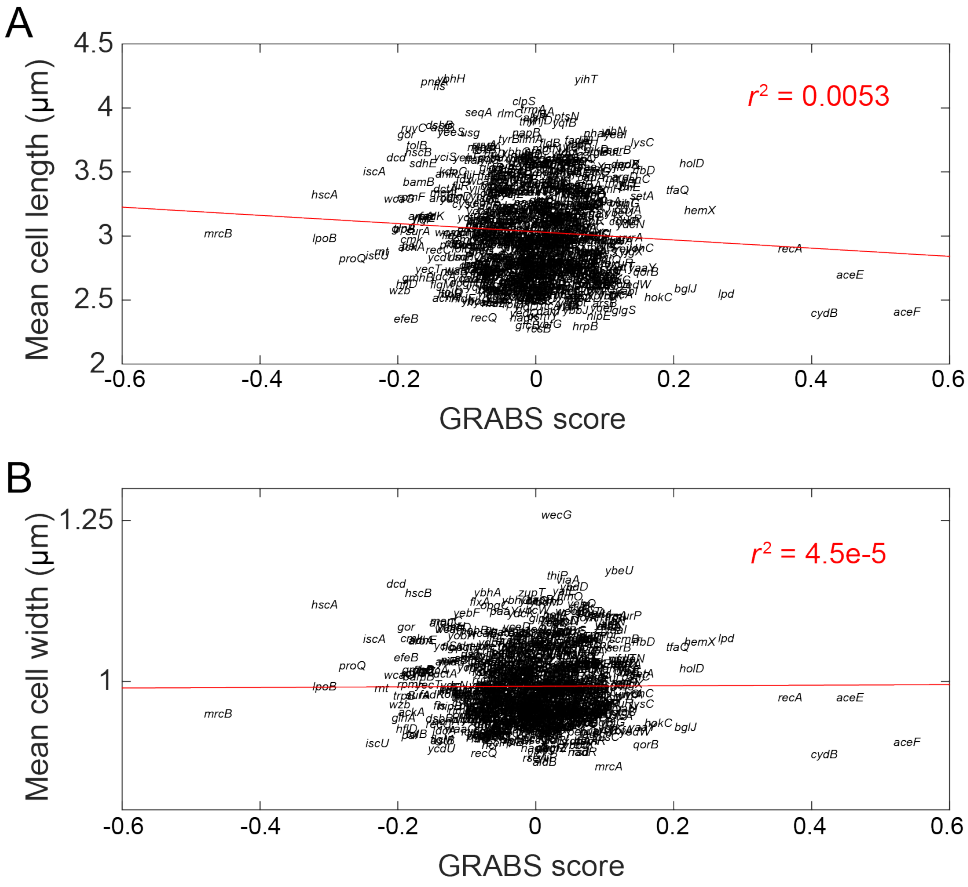
A
Mean cell length (μm)
4.5
4
3.5
3
2.5
2
-0.6
-0.4
-0.2
0
0.2
0.4
0.6
GRABS score
r^2 = 0.0053
B
Mean cell width (μm)
1.25
1
GRABS score
r^2 = 4.5e-5

Figure 9

Figure 10. Clean deletions in *E. coli* MG1655 and complementation studies validate GRABS measurements of Keio strains.

A) Complementation of four genes that yielded large decreases in GRABS score (*mrcB*, *lpoB*, *hfq*, and *hscA*) and two genes that produced essentially no stiffness change (*mrcA* and *lpoA*) resulted in recovery of mechanical defects when the cells were embedded in 1% agarose. Average growth curves (solid lines) of agarose-embedded *E. coli* BW25113 cells with an empty vector (green) compared to growth curves of Keio BW25113 mutants complemented in *trans* indicate 80-100% recovery after 8 h in Δ*mrcB*, Δ*lpoB*, Δ*hfq*, and Δ*hscA* and no change in Δ*mrcA* and Δ*lpoA*. Shaded regions represent one standard deviation above and below mean growth curves (n = 6).

B) We detected no mechanical phenotypes in deletions of genes downstream of *hfq* in the operon containing *hfq*. *tsaE* is not included in the Keio collection and therefore we did not test it.

C) The phenotypes of *E. coli* MG1655 mutants embedded in agarose are quantitatively similar to those of the corresponding BW25113 mutants after 8 h. Mean agarose-embedded growth curves of *E. coli* MG1655 (green) and selected gene deletions in MG1655 (black) and BW25113 (blue). Shaded regions represent one standard deviation above and below the mean (n = 6).

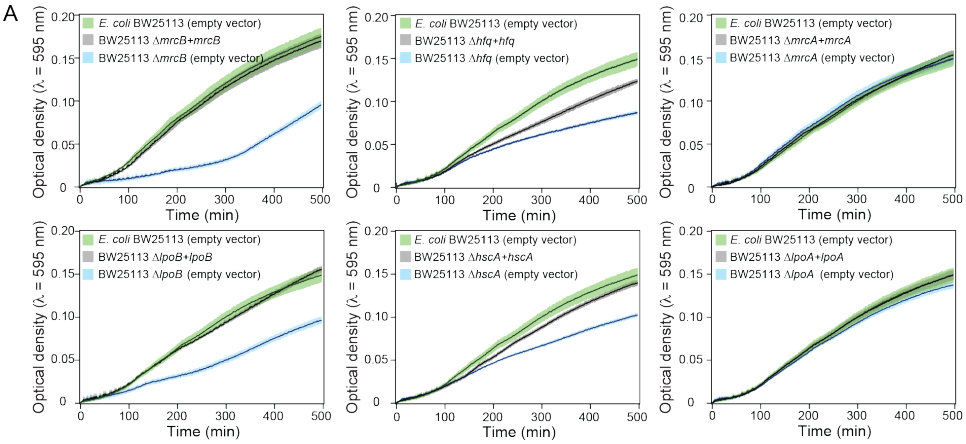

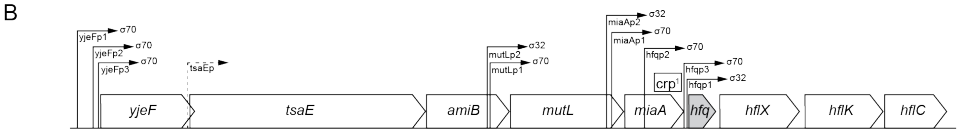

Gene name	In Keio	Essential	Location	GRABS score
yjeF	Yes	No	4,392,089 → 4,393,636	-0.057
tsaE	No	Yes	4,393,608 → 4,394,069	N/A
amiB	Yes	No	4,394,084 → 4,395,425	-0.128
mutL	Yes	No	4,395,435 → 4,397,282	-0.076
miaA	Yes	No	4,397,275 → 4,398,225	-0.086
hfq	Yes	No	4,398,311 → 4,398,619	-0.304
hflX	Yes	No	4,398,695 → 4,399,975	0.026
hflK	Yes	No	4,400,061 → 4,401,320	0.021
hflC	Yes	No	4,401,323 → 4,402,327	0.011

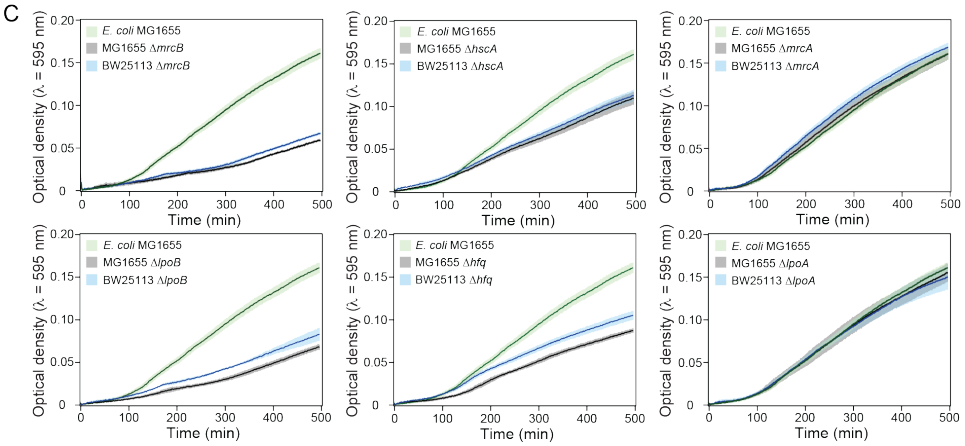

Figure 10

Figure 11. Microfluidic bending assay and elongation rate measurements of embedded cells yield relative stiffness measurements consistent with GRABS scores.

A) Representative images of filamentous wild-type cells and Δ*mrcB* cells in a microfluidic cell-bending device. Blue and black lines indicate the configuration of cells in the absence and presence of fluid flow, respectively. Deflection was measured as the difference between the position of the cell tip in the flow direction in the absence and presence of fluid flow. Scale bar: 10 μm.

B) Young's moduli for *sulA*-induced (left) and aztreonam-treated (right) cells were determined by fitting deflection data (Extended Experimental Procedures) from a microfluidic-based bending assay. Error bars indicate 95% confidence interval to the fit (Extended Experimental Procedures). Data are colored according to each gene's assignment to Clusters of Orthologous Groups, as in Figure 2B ($n \geq$ 130 cells, two independent experiments).

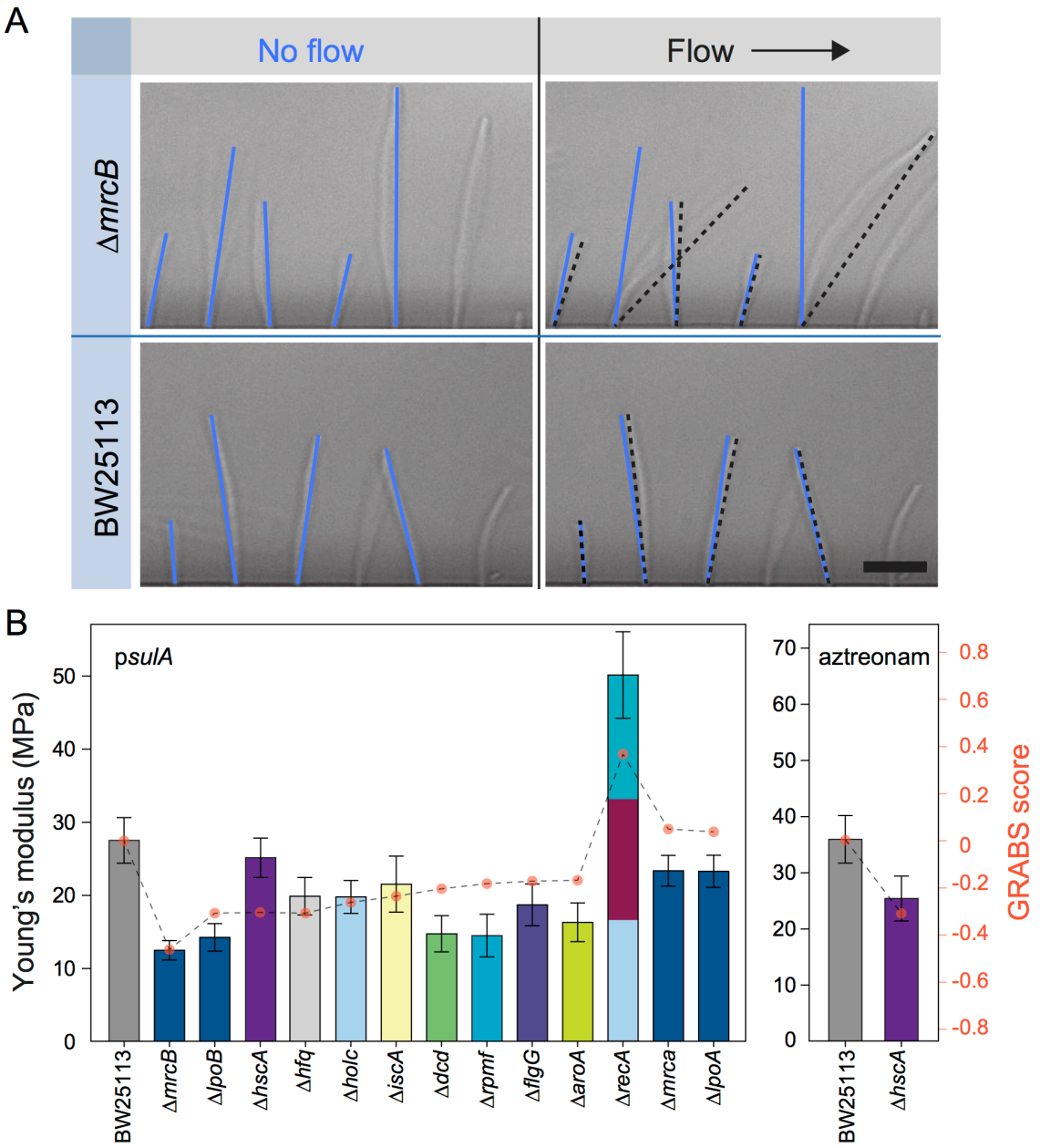
A
No flow
Flow
ΔmrcB
BW25113
B
psulA
Young's modulus (MPa)
GRABS score
aztreonam
BW25113
ΔmrcB
ΔlpoB
ΔhscA
Δhfq
Δholc
ΔiscA
Δdcd
Δrpmf
ΔflgG
ΔaroA
ΔrecA
Δmrca
ΔlpoA

Figure 11

Figure 12. Deflection of *E. coli* BW25113 and Δ*mrcB* cells upon flow-induced bending during stiffness measurements in microfluidic devices. Circles represent deflection values along the flow direction for individual cells. Greater deflection of Δ*mrcB* cells relative to wild-type cells of the same length indicates a decrease in cell stiffness ($n > 200$ cells, two independent experiments).

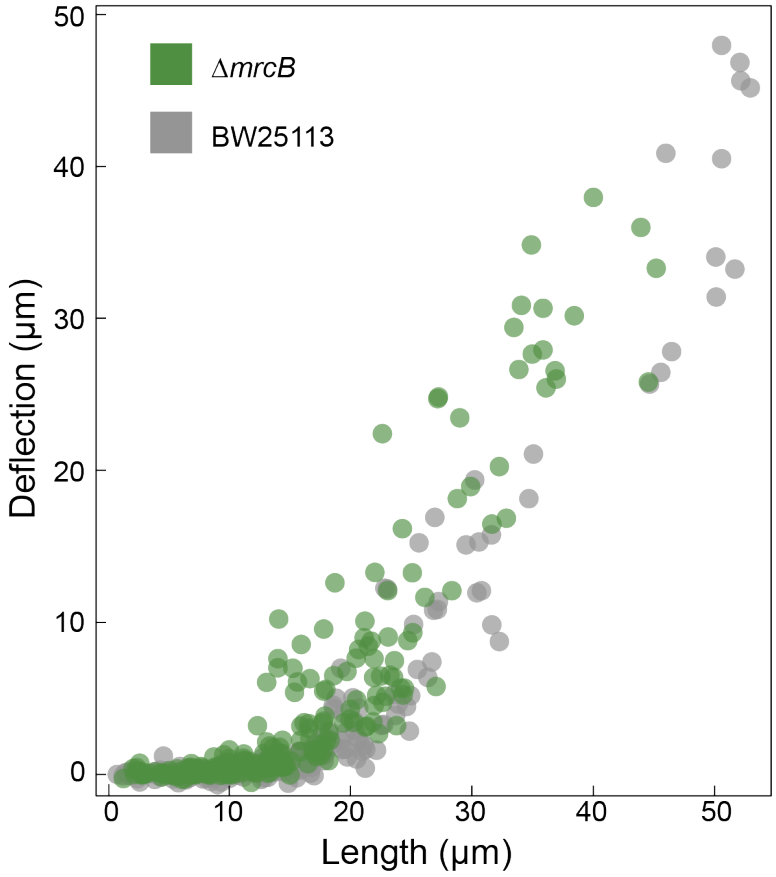

Figure 12

Figure 13. Δ*recA* cells exhibit much slower growth in liquid than wild-type BW25113 cells (A), while growth in agarose is only affected to a small degree (B). Solid lines are means of $n = 3$ growth curves; shaded regions represent one standard deviation about the mean.

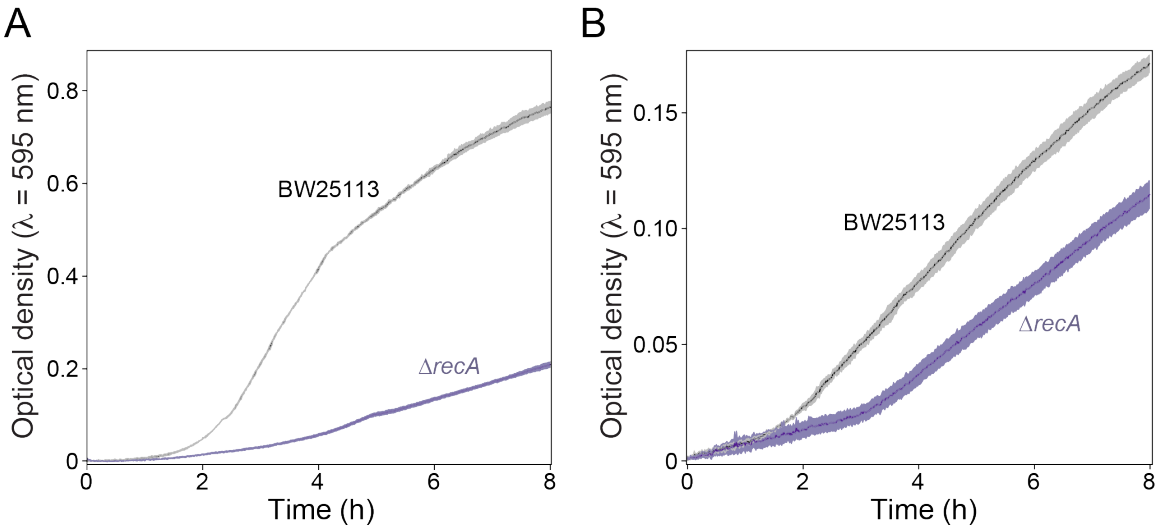
A
B
Optical density (λ = 595 nm)
Time (h)
BW25113
ΔrecA
0
0.2
0.4
0.6
0.8
0.05
0.10
0.15
2
4
6
8

Figure 13

Figure 14. Single-cell, microscopy-based measurements of elongation inhibition agree with GRABS data. Average fractional elongation curves while embedded in 1-4% agarose gels for wild-type and six deletion strains of *E. coli* MG1655. The Δ*mrcB*, Δ*lpoB*, Δ*hfq*, Δ*hscA* mutants consistently display increased inhibition of elongation compared to wild-type, Δ*mrcA*, and Δ*lpoA* cells, as predicted by GRABS scores. L_0, initial cell length; Δ*L*, the change in length between time points. Curves are averages over single-cell trajectories and were smoothed over a 5-min window. The number of cells measured decreases over the course of the experiment as some cell trajectories become difficult to track; the initial number of trajectories for a given mutant and agarose concentration ranged from 26-79 across experiments.

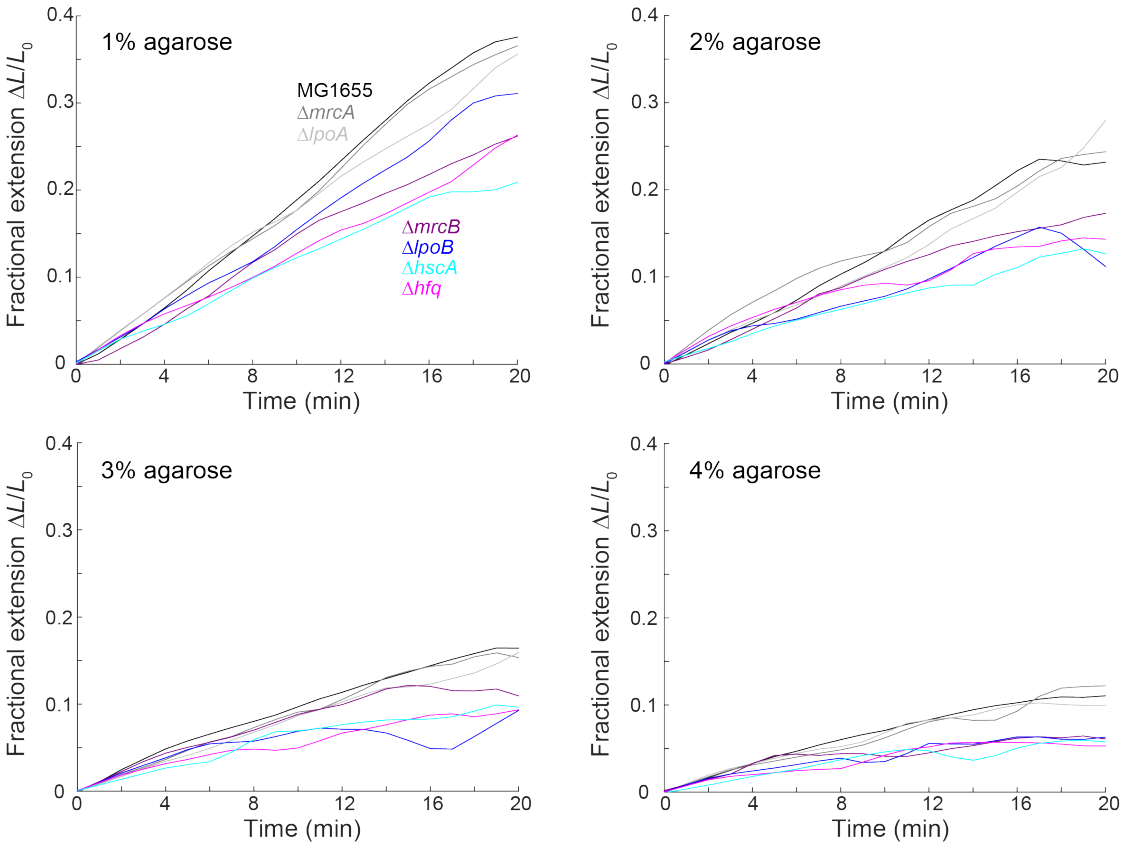
1% agarose
2% agarose
3% agarose
4% agarose
MG1655
ΔmrcA
ΔlpoA
ΔmrcB
ΔlpoB
ΔhscA
Δhfq
Fractional extension ΔL/L0
Time (min)
0
0.1
0.2
0.3
0.4
0
4
8
12
16
20

Figure 14

Figure 15. UPLC analysis of mutants shows no striking differences in peptidoglycan composition between wildtype and several mutants with most negative GRABS scores.

(A) Chromatograms of purified cell walls from *E. coli* MG1655, BW25113, and six Keio mutants, including four with large, negative GRABS scores (Δ*mrcB*, Δ*hscA*, Δ*lpoB*, and Δ*hfq*) and two with GRABS scores close to zero (Δ*mrcA* and Δ*lpoA*). Cell walls were purified and digested, and samples were analyzed using UPLC (Extended Experimental Procedures). Chromatograms were normalized to have the same integrated total absorbance and overlaid with baselines staggered for easier comparison. No substantial differences among the chromatograms were evident.

(B) Molar fractions of monomers, dimers, trimers, pentapeptides, and anhydro peaks, as well as the glycan strand length computed from total anhydro fraction, were quantified. The low abundance of anhydro species typically leads to greater variability in the calculation of average strand length.

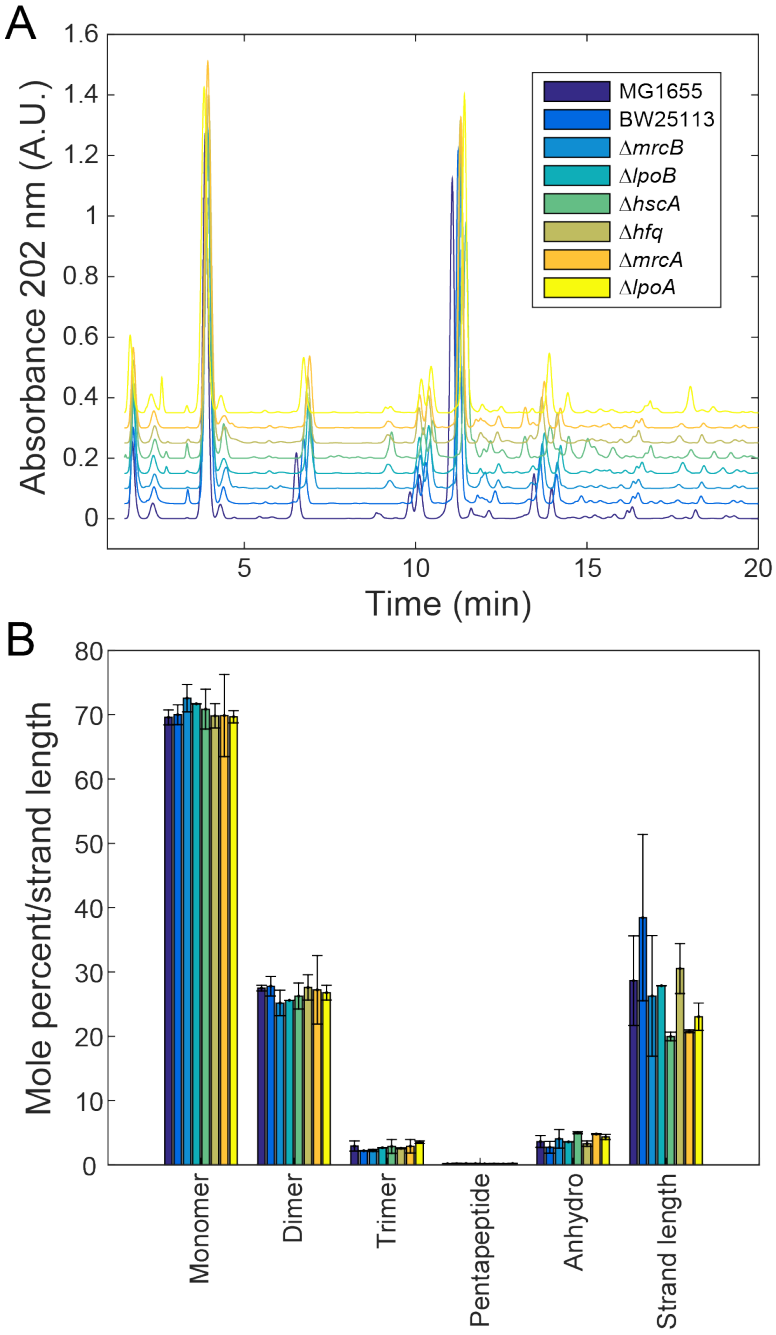
A
Absorbance 202 nm (A.U.)
Time (min)
MG1655
BW25113
ΔmrcB
ΔlpoB
ΔhscA
Δhfq
ΔmrcA
ΔlpoA
B
Mole percent/strand length
Monomer
Dimer
Trimer
Pentapeptide
Anhydro
Strand length

Figure 15

Figure 16. Occurences of cell death in GRABS assay.

A) Survival of wildtype *E. coli* BW25113 and Keio mutants embedded in 1% agarose gel after 4 h (left) and 8 h (right), monitored using a LIVE/DEAD stain (Extended Experimental Procedures). There is a similar level of survival for wildtype and most mutants at 8 h. Δ*mrcB* and Δ*lpoB* show little death at 4 h, which is the period of most rapid growth in 1% agarose, and a small degree of death at 4 h that is not sufficient to explain the large reduction in cell stiffness. Cells were labeled with Syto-9 (live cells, green) and propidium iodide (dead cells, red). Scale bar: 10 μm.

B) Phase-contrast microscopy illustrating lysis of Δ*mrcB* cells in a 4% agarose gel. Cells that undergo lysis are highlighted in green dashed circles (alive at t = 0 min) and red dashed circles (dead at t = 38 min). Scale bar: 5 μm.

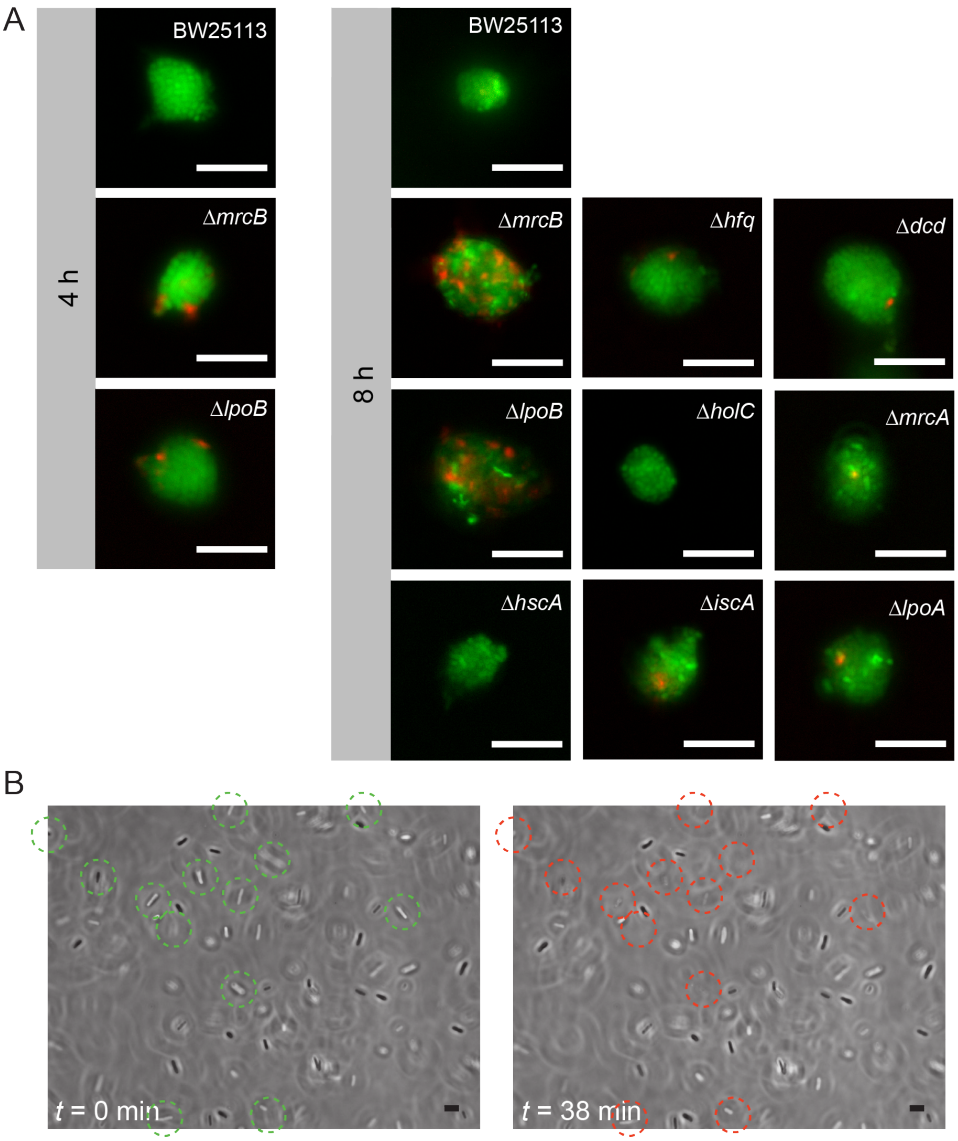
A
4 h
BW25113
ΔmrcB
ΔlpoB
8 h
BW25113
ΔmrcB
Δhfq
Δdcd
ΔlpoB
ΔholC
ΔmrcA
ΔhscA
ΔiscA
ΔlpoA
B
t = 0 min
t = 38 min

Figure 16

Figure 17. GRABS analysis of cell-wall synthesis mutants relates biochemical activities *in vitro* to changes in embedded growth *in vivo*.

A) Crystal structure of PBP1b (PDB ID: 3VMA) highlighting residues used for mutational analysis via GRABS. N-terminal trans-membrane α-helix, residues 64-87 (orange); UvrB Domain 2 Homolog (UB2H) domain, residues 109-200 (gold); glycosyltransferase (GT) domain, residues 203-367 (green); transpeptidase (TP) domain, residues 444-736 (pink). Other residues are colored in black. Inset: mutated residues in the UB2H domain.

B) OD at t = 8 h of agarose-embedded *E. coli* BW25113 cells and Δ*mrcB* cells expressing various *mrcB* alleles in *trans*. WT, wild-type. Error bars represent one standard deviation above and below the mean. ∗ indicates a point mutation in the corresponding domain of PBP1b (UB2H, glycosyltransferase (GT), and transpeptidase (TP)). $n \geq 5$ independent experiments.

C) Growth curves of agarose-embedded Δ*lpoB* cells and cells harboring mutations in the 6UB2H domain, E233Q (glycosyltransferase), and S510A (transpeptidase) of *mrcB*. Shaded regions represent one standard deviation above and below mean growth curves. ∗ indicates a point mutation in the corresponding domain of *mrcB*. $n \geq 5$ independent experiments.

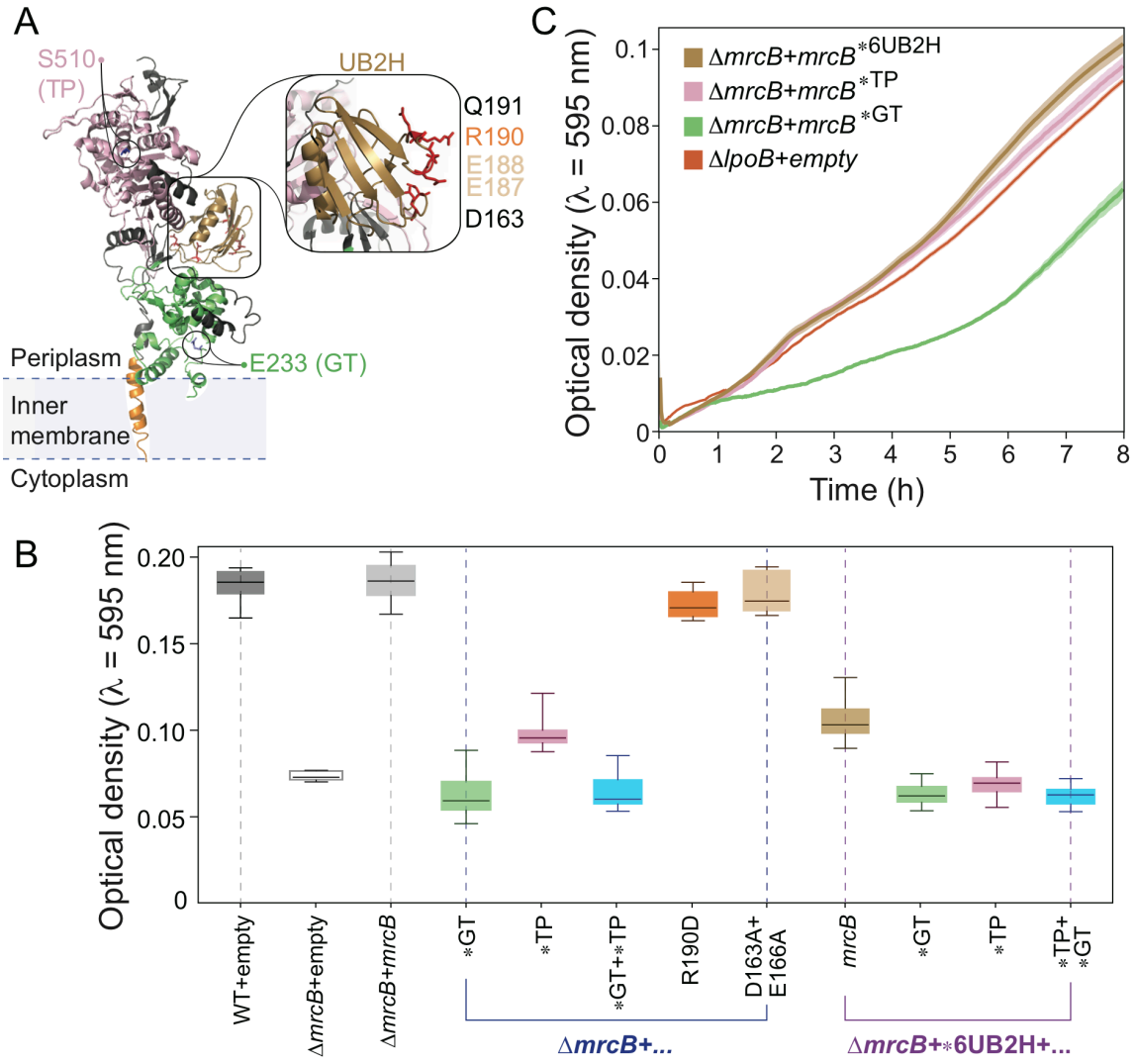
A
S510
(TP)
UB2H
Q191
R190
E188
E187
D163
Periplasm
E233 (GT)
Inner
membrane
Cytoplasm
C
ΔmrcB+mrcB*6UB2H
ΔmrcB+mrcB*TP
ΔmrcB+mrcB*GT
ΔlpoB+empty
Optical density (λ = 595 nm)
Time (h)
B
Optical density (λ = 595 nm)
WT+empty
ΔmrcB+empty
ΔmrcB+mrcB
*GT
*TP
*GT+*TP
R190D
D163A+
E166A
mrcB
*GT
*TP
*TP+
*GT
ΔmrcB+...
ΔmrcB+*6UB2H+...

Figure 17

Figure 18. Liquid LB growth curves of Δ*mrcB* strains complemented with *mrcB* point mutants. Plots are ordered according to the OD for each strain at 8 h. The shaded regions represent one standard deviation above and below the mean growth curves ($n \geq 5$ independent experiments). Unless otherwise indicated, all mutations were performed in a Δ*mrcB* background. ***** indicates a point mutation in the corresponding domains (UB2H, glycosyltransferase (GT), and transpeptidase (TP)) of *mrcB*.

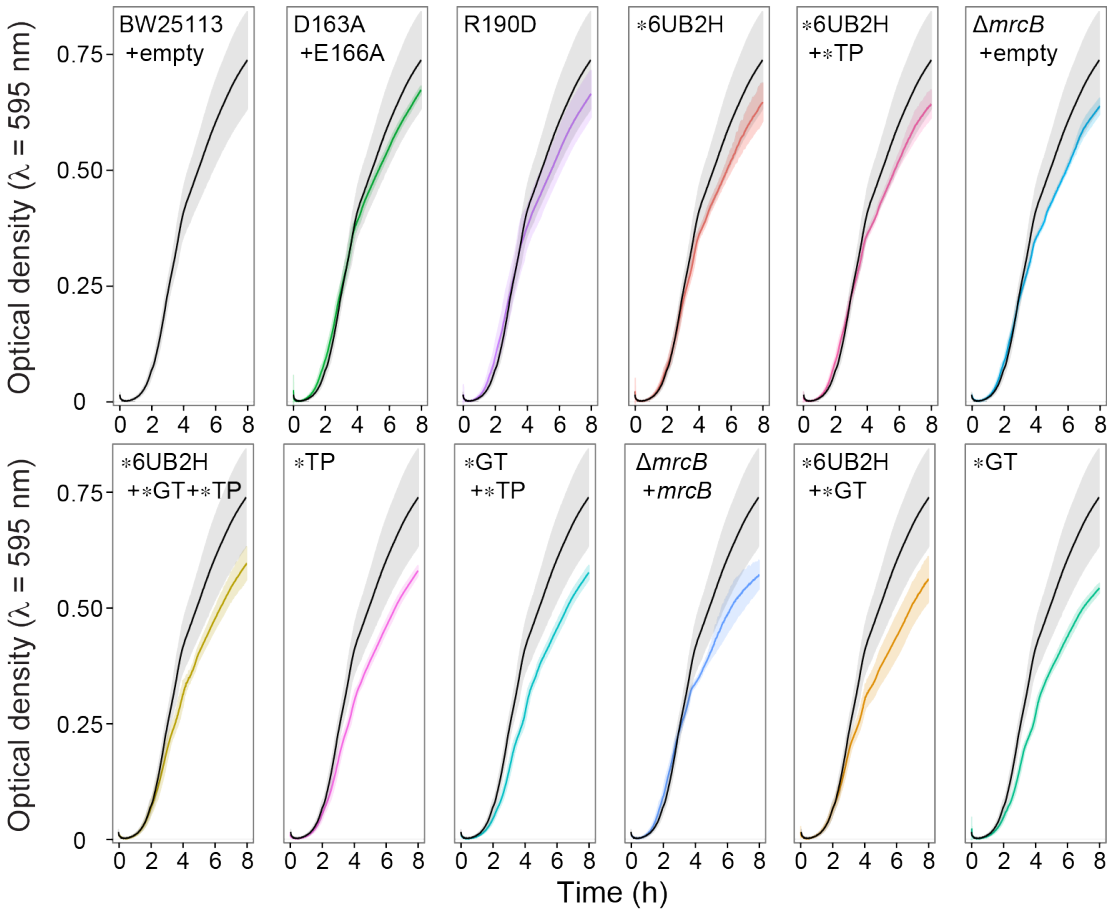
BW25113 +empty
D163A +E166A
R190D
∗6UB2H
∗6UB2H +∗TP
ΔmrcB +empty
∗6UB2H +∗GT+∗TP
∗TP
∗GT +∗TP
ΔmrcB +mrcB
∗6UB2H +∗GT
∗GT
Optical density (λ = 595 nm)
Time (h)
0
0.25
0.50
0.75
0 2 4 6 8

Figure 18

Figure 19. Carbonyl cyanide *m*-chlorophenyl hydrazone (CCCP) generally reduces growth rates. However, the fractional growth-rate reduction is stronger in liquid (A) than in agarose (B), as evidenced by the difference in slopes. DMSO, dimethyl sulfoxide.

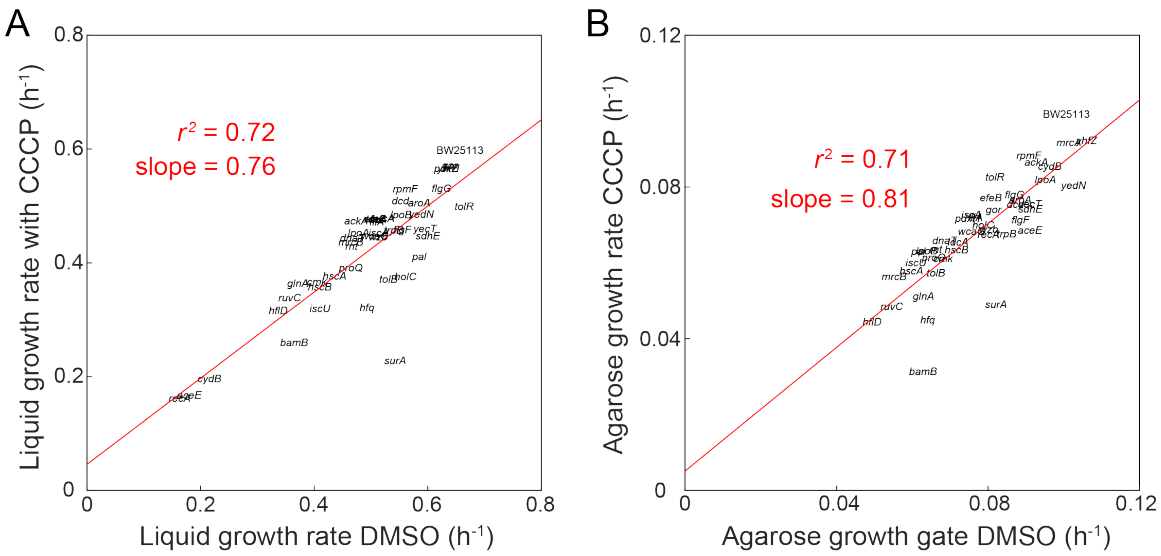
A
r^2 = 0.72
slope = 0.76
Liquid growth rate with CCCP (h^{-1})
Liquid growth rate DMSO (h^{-1})
0
0.2
0.4
0.6
0.8
BW25113
rpmF
flgG
tolR
pal
proQ
tolB
tolC
ruvC
hflD
iscU
hfq
bamB
surA
cydB
B
r^2 = 0.71
slope = 0.81
Agarose growth rate CCCP (h^{-1})
Agarose growth gate DMSO (h^{-1})
0
0.04
0.08
0.12
BW25113
rpmF
tolR
yedN
aceE
glnA
ruvC
hfq
surA
bamB

Figure 19

Figure 20. GRABS score generally increases under CCCP treatment.

GRABS score with and without CCCP, a proton ionophore that reduces membrane potential. Solid circles, representing GRABS score for the dimethyl sulfoxide (DMSO) control, are generally at lower values than the open circles, which represent GRABS score in the presence of 2 μg/mL CCCP. Genes are colored according to their assignment to Clusters of Orthologous Groups. Solid lines and shaded areas represent the average and 95% confidence interval to a linear fit, respectively, of $n \geq 4$ independent experiments.

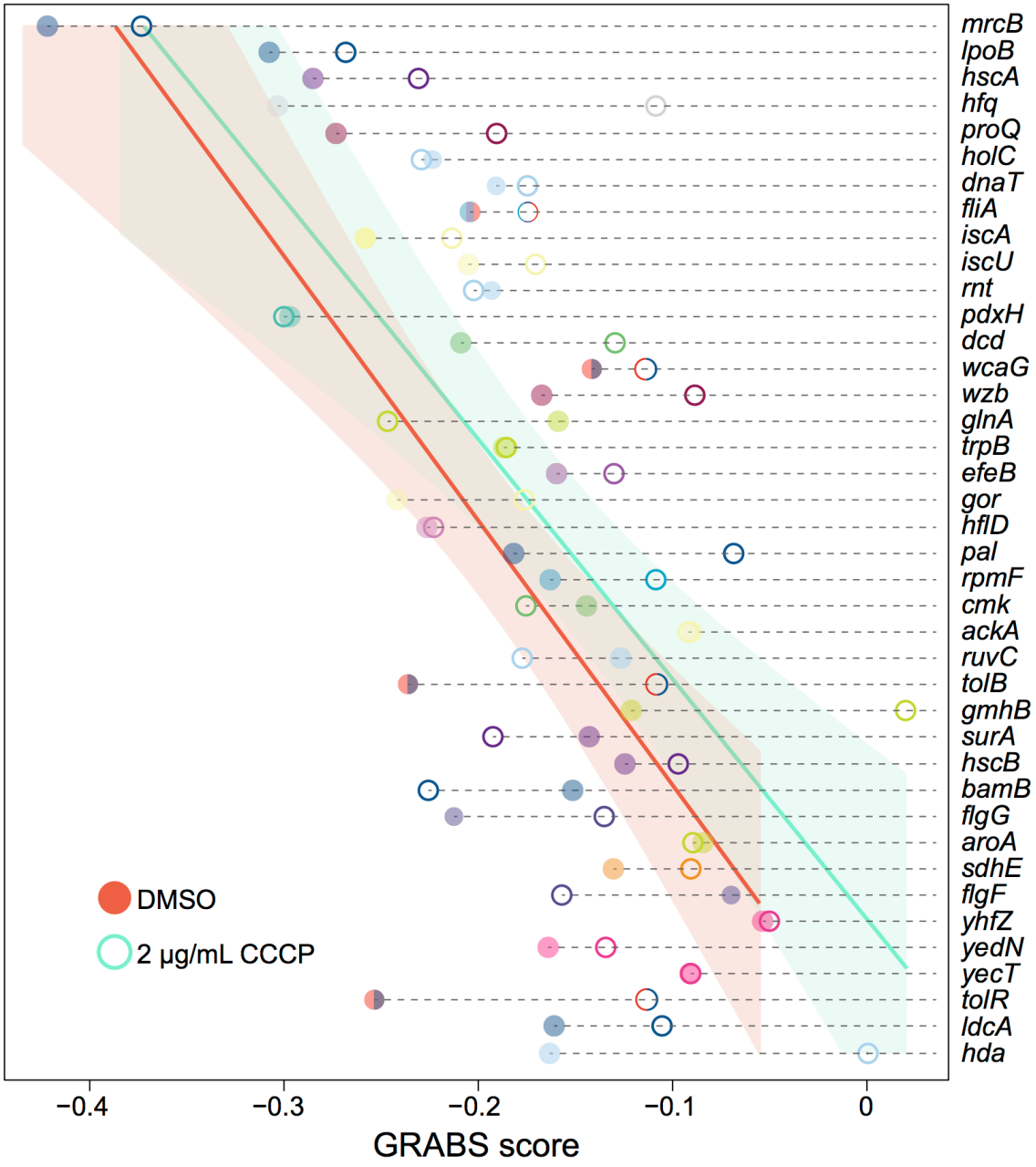
mrcB
lpoB
hscA
hfq
proQ
holC
dnaT
fliA
iscA
iscU
rnt
pdxH
dcd
wcaG
wzb
glnA
trpB
efeB
gor
hflD
pal
rpmF
cmk
ackA
ruvC
tolB
gmhB
surA
hscB
bamB
flgG
aroA
sdhE
flgF
yhfZ
yedN
yecT
tolR
ldcA
hda
DMSO
2 µg/mL CCCP
−0.4
−0.3
−0.2
−0.1
0
GRABS score

Figure 20

Figure 21. GRABS scores are correlated with maximal growth rates in agarose. Growth rates were obtained by fitting growth curves for encapsulated cells with a Gompertz relation. The highly significant correlation ($p < 10^{-81}$) indicates that agarose growth rate is a reasonable proxy for GRABS score, potentially simplifying experimental design and analysis, although this simplification is less accurate for some mutants.

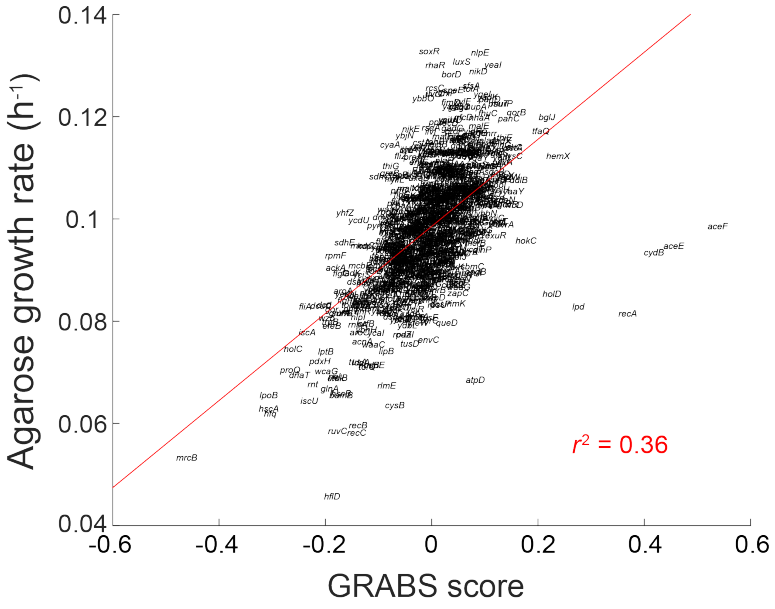
Agarose growth rate (h-1)
GRABS score
r2 = 0.36
0.14
0.12
0.1
0.08
0.06
0.04
-0.6
-0.4
-0.2
0
0.2
0.4
0.6

Figure 21

Table 1. Strains and plasmids used in this study.

Strain	Description	Reference/source
MG1655	*E. coli* K-12 wildtype	CGSC #6300
BW25113	*E. coli* (Keio collection parent)	(Baba *et al*., 2006a)
Keio collection	Single deletion mutants (numbered JW####)	(Baba *et al*., 2006a)
DH5α	F−*endA*1 *glnV*44 *thi*-1 *recA*1 *relA*1 *gyrA*96 *deoR nupG* Φ80d*lacZ*ΔM15 Δ(*lacZYA-argF*)U169, *hsdR*17(rK− mK+)	Invitrogen
DH5α(λpir)	F−*endA*1 *glnV*44 *thi*-1 *recA*1 *relA*1 *gyr*A96 *deoR nupG* Φ80d*lacZ*ΔM15 Δ(*lacZYA-argF*)U169, *hsdR*17(rK− mK+) λ::pir	Invitrogen
MFDpir	MG1655, RP4-2-Tc::[ΔMu1::*aac*(3)IV-Δ*aphA* Δ*nic*35 ΔMu2::*zeo*] Δ*dapA*::(*erm*-pir) Δ*recA*	(Ferrieres *et al*., 2010)
HTC1	MG1655 Δ*mrcB*	This study
HTC2	MG1655 Δ*lpoB*	This study
HTC3	MG1655 Δ*mrcA*	This study
HTC4	MG1655 Δ*lpoA*	This study
HTC5	MG1655 Δ*hscA*	This study
HTC6	MG1655 Δ*hfq*	This study
BW25113-E1	BW25113 pBAD33 c280	This study
JW3359-E1	BW25113 *mrcA* : kan pBAD33c280	This study
JW3116-E1	BW25113 *lpoA* : kan pBAD33c280	This study
JW5157-E1	BW25113 *lpoB* : kan pBAD33c280	This study
JW2510-E1	BW25113 *hscA* : kan pBAD33c280	This study
JW4130-E1	BW25113 *hfq* : kan pBAD33c280	This study
JW3359-C	BW25113 *mrcA* : kan pBAD33c280-*mrcA*	This study
JW3116-C	BW25113 *lpoA* : kan pBAD33c280-lpoA	This study
JW5157-C	BW25113 *lpoB* : kan pBAD33c280-lpoB	This study
JW2510-C	BW25113 *hscA* : kan pBAD33c280-	This study

	hscA	
JW4130-C	BW25113 *hfq* : kan pBAD33c280-*hfq*	This study
BW25113-E2	BW25113 pAM238	This study
JW0145-E2	BW25113 *mrcB* : kan pAM238	This study
JW5157-E2	BW25113 *lpoB* : kan pAM238	This study
JW1045-C	JW0145 psK12	This study
HTC7	JW0145 psK12-R190D	This study
HTC8	JW0145 psK12-D163A/E166A	This study
HTC9	JW0145 psK12-E233Q (∗GT)	This study
HTC10	JW0145 psK12-S510A (∗TP)	This study
HTC11	JW0145 psK12-D163A/E166A/E187A/ N188A/R190A/Q191A (6UB2H)	This study
HTC12	JW0145 psK12-(∗TP/∗GT)	This study
HTC13	JW0145 psK12-(∗6UB2H/∗TP)	This study
HTC14	JW0145 psK12-(∗6UB2H/∗GT)	This study
HTC15	JW0145 psK12-(∗6UB2H/∗TP/∗GT)	This study
BW25113-sulA	BW25113 pDB192	This study
JW3359-sulA	BW25113 *mrcA* : kan pDB192	This study
JW3116-sulA	BW25113 *lpoA* : kan pDB192	This study
JW1045-sulA	BW25113 *mrcB* : kan pDB192	This study
JW5157-sulA	BW25113 *lpoB* : kan pDB192	This study
JW2510-sulA	BW25113 *hscA* : kan pDB192	This study
JW4130-sulA	BW25113 *hfq* : kan pDB192	This study
JW4216-sulA	BW25113 *holC* : kan pDB192	This study
JW2512-sulA	BW25113 *iscA* : kan pDB192	This study
JW2050-sulA	BW25113 *dcd* : kan pDB192	This study
JW1075-sulA	BW25113 *rpmF* : kan pDB192	This study
JW1065-sulA	BW25113 *flgG* : kan pDB192	This study
JW0891-sulA	BW25113 *aro*A : kan pDB192	This study
JW2669-sulA	BW25113 *recA* : kan pDB192	This study
BW25113-E3	BW25113 PUA66	This study
JW1045-E3	BW25113 *mrcB* : frt pUA66	This study
JW5157-E3	BW25113 *lpoB* : frt pUA66	This study
JW2510-E3	BW25113 *hscA* : frt pUA66	This study
JW4130-E3	BW25113 *hfq* : frt pUA66	This study

JW2512-E3	BW25113 *iscA* : frt pUA66	This study
JW2669-E3	BW25113 *recA* : frt pUA66	This study
BW25113-sulA-R	BW25113 PUA66-*sulA*-GFP	This study
JW1045-sulA-R	BW25113 *mrcB* : frt pUA66-*sulA*-GFP	This study
JW5157-sulA-R	BW25113 *lpoB* : frt pUA66-*sulA*-GFP	This study
JW2510-sulA-R	BW25113 *hscA* : frt pUA66-*sulA*-GFP	This study
JW4130-sulA-R	BW25113 *hfq* : frt pUA66-*sulA*-GFP	This study
JW2512-sulA-R	BW25113 *iscA* : frt pUA66-*sulA*-GFP	This study
JW2669-sulA-R	BW25113 *recA* : frt pUA66-*sulA*-GFP	This study
Plasmid	Description	Reference/source
pDS132	R6K ori, *sacB*, MCS, *cat*, CmR	(Phillipe *et al*., 2004)
pBAD33 c280	pACYC ori, pBAD promoter, MCS, *cat*, CmR	(Lee *et al*., 2007)
pAM238	pSC101 ori, pLac, SpecR	(Gonzalez *et al*., 2010)
pSK12	pAM238-*mrcB*	(Ranjit and Young, 2013)
pDB192	*sulA*, pLac, SpecR	(Amir *et al*., 2014)
pUA66	gfpmut2, KanR	GE Dharmacon
pUA66-*sulA*-GFP	*sulA* promoter, *sulA-gfpmut2*	GE Dharmacon

Table 2. Primers used in this study (5′ to 3′).

Primer (pBAD33 c280)	Sequence
mrcA_C-Fwd	CATGTCTAGATTACGCCAGACGCGGGTTAA
mrcA_C-Rev	CATGTCTAGAGTGAAGTTCGTAAAGTATTTTT
lpoA_C-Fwd	CATGTCTAGAATGGTACCCTCAACATTTTCTCG
lpoA_C-Rev	CATGTCTAGATTAACTGACGGGGACTACCTGA
lpoB_C-Fwd	CATGTCTAGAATGACAAAAATGAGTCGCTACGC
lpoB_C-Rev	CATGTCTAGATTATTGCTGCGAAACGGCACCT
hscA_C-Fwd	CATGTCTAGAATGGCCTTATTACAAATTAGTGAACCT
hscA_C-Rev	CATGTCTAGATTAAACCTCGTCCACGGAATG
hfq_C-Fwd	CATGTCTAGAATGGCTAAGGGGCAATCTTTACA
hfq_C-Rev	CATGTCTAGATTATTCGGTTTCTTCGCTGTCCT
Primer (pSK12)	Sequence
mrcB_R190D_Fwd	CGTCAATATGGAGAACAACGATCAGTTCGGTTTCTTCCG
mrcB_R190D_Rev	CGGAAGAAACCGAACTGATCGTTGTTCTCCATATTGACG
mrcB_D163A/E166A_Fwd	CCGTTTGATTTCCCGGCCAGTAAAGCAGGACAGGTGCGCGCG
mrcB_D163A/E166A_Rev	CGCGCGCACCTGTCCTGCTTTACTGGCCGGGAAATCAAACGG
mrcB_R190A/Q191A_Fwd	CGTCAATATGGCGGCCAACGCTGCGTTCGGTTTCTTCCG
mrcB_R190A/Q191A_Rev	CGGAAGAAACCGAACGCAGCGTTGGCCGCCATATTGACG
mrcB_E187A/N188A_Fwd	CGTCAATATGGCGGCCAACCGTCAGTTCGGTTTCTTCCG
mrcB_E187A/N188A_Rev	CGGAAGAAACCGAACTGACGGTTGGCCGCCATATTGACG
mrcB_S510A_Fwd	GCGTCGTTCGATTGGTGCCCTTGCAAAACCAGCG
mrcB_S510A_Rev	CGCTGGTTTTGCAAGGGCACCAATCGAACGACGC
mrcB_E233Q_Fwd	GGATACTTTGCTGGCGACACAAGACCGTCATTTTTACG

mrcB_E233Q_Rev	CGTAAAAATGACGGTCTTGTGTCGCCAGCAAAGTATCC
Primer (pDS132)	Sequence
lpoA_Del_N_term_Fwd	GCATGCAGCGCATCACGGCGGCCT
lpoA_Del_N_term_Rev	TGGTACTCTAGCCATAATGTATCCAGTGATATTTTTTTACGCAATGCTCAATATTAAATCGGC
lpoA_Del_C_term_Fwd	ATCACTGGATACATTATGGCTACAGTACCAACAAG
lpoA_Del_C_term_Rev	ATTGAGCAGAGACTGAAC
lpoB_Del_N_term_Fwd	TTGCCGAAGATGGCTATC
lpoB_Del_N_term_Rev	GCTGCGAAACGGCACCAAGATTCACCCCTTACAAATATAG
lpoB_Del_C_term_Fwd	AAGGGGTGAATCTTGGTGCCGTTTCGCAGCAAT
lpoB_Del_C_term_Rev	CTGACGCGCTATGCACTAAATTTC
mrcA_Del_N_term_Fwd	AGTAAGCAGCGTTGCCAG
mrcA_Del_N_term_Rev	GAAGCGCCT TTTTAATGGAAATTTCCCATTTAGTTTCATTTG
mrcA_Del_C_term_Fwd	AATGGGAAATTTCCATTAAAAAGGCGCTTCGGC
mrcA_Del_C_term_Rev	ATCCTGATCCGCGAATAC
mrcB_Del_N_term_Fwd	AAATCACTCGACATTTATCAGG
mrcB_Del_N_term_Rev	TTTCACGCTTAGATGGCTTTTTCTCCGCAATATTC
mrcB_Del_C_term_Fwd	TTGCGGAGAAAAAGCCATCTAAGCGTGAAATACCG
mrcB_Del_C_term_Rev	TCAGGTGGTCATAGGTGTTG
hscA_Del_N_term_Fwd	ATGGATTACTTCACCCTC
hscA_Del_N_term_Rev	ACAATCTTTGGCATAGTTTAGCTTCCAGAAATTAAAAATC
hscA_Del_C_term_Fwd	TTCTGGAAGCTAAACTATGCCAAAGATTGTTATTTTGCCTCATCAGG
hscA_Del_C_term_Rev	GCCAACGCATCTGCGGCG
hfq_Del_N_term_Fwd	CTTCAGGAGGTAGATCCG
hfq_Del_N_term_Rev	AAACAGCCCGAAACCTCTCTCTTTTCCTTATATGCTTATTTG
hfq_Del_C_term_Fwd	TAAGGAAAAGAGAGAGGTTTCGGGCTGTTTTTTTAC
hfq_Del_C_term_Rev	CATGCGTACGCCTTTCTGTCTTTCAAGGTG

Table 3. Gene Ontology (GO) enrichment of GRABS hits.

GO Term	Counts	Definition
GO:0016226	3	iron-sulfur cluster assembly
GO:0009242	2	colanic acid biosynthetic process
GO:0043165	2	Gram-negative-bacterium-type cell outer membrane assembly
GO:0006457	3	protein folding
GO:0043213	2	bacteriocin transport
GO:0006260	3	DNA replication
GO:0015949	2	nucleobase-containing small molecule interconversion
GO:0000162	1	tryptophan biosynthetic process
GO:0006082	1	organic acid metabolic process
GO:0006083	1	acetate metabolic process
GO:0006085	1	acetyl-CoA biosynthetic process
GO:0006105	1	succinate metabolic process
GO:0006220	1	pyrimidine nucleotide metabolic process
GO:0006226	1	dUMP biosynthetic process
GO:0006229	1	dUTP biosynthetic process
GO:0006267	1	pre-replicative complex assembly involved in nuclear cell cycle DNA replication
GO:0006542	1	glutamine biosynthetic process
GO:0006568	1	tryptophan metabolic process
GO:0006749	1	glutathione metabolic process
GO:0007059	1	chromosome segregation
GO:0009220	1	pyrimidine ribonucleotide biosynthetic process
GO:0009399	1	nitrogen fixation
GO:0009443	1	pyridoxal 5'-phosphate salvage
GO:0010608	1	posttranscriptional regulation of gene expression
GO:0015740	1	C4-dicarboxylate transport
GO:0017013	1	protein flavinylation
GO:0019395	1	fatty acid oxidation
GO:0019413	1	acetate biosynthetic process
GO:0019542	1	propionate biosynthetic process
GO:0019676	1	ammonia assimilation cycle
GO:0032298	1	positive regulation of DNA-dependent DNA replication initiation

GO:0033212	1	iron assimilation
GO:0040033	1	negative regulation of translation, ncRNA-mediated
GO:0042351	1	'de novo' GDP-L-fucose biosynthetic process
GO:0042780	1	tRNA 3'-end processing
GO:0042816	1	vitamin B6 metabolic process
GO:0044092	1	negative regulation of molecular function
GO:0045975	1	positive regulation of translation, ncRNA-mediated
GO:0046080	1	dUTP metabolic process
GO:0051050	1	positive regulation of transport
GO:0051085	1	chaperone mediated protein folding requiring cofactor
GO:0051259	1	protein oligomerization
GO:0060274	1	maintenance of stationary phase
GO:0071932	1	replication fork reversal
GO:0009073	2	aromatic amino acid family biosynthetic process
GO:0009252	2	peptidoglycan biosynthetic process
GO:0000271	1	polysaccharide biosynthetic process
GO:0000725	1	recombinational repair
GO:0006259	1	DNA metabolic process
GO:0006269	1	DNA replication, synthesis of RNA primer
GO:0008156	1	negative regulation of DNA replication
GO:0015684	1	ferrous iron transport
GO:0015920	1	lipopolysaccharide transport
GO:0019740	1	nitrogen utilization
GO:0032297	1	negative regulation of DNA-dependent DNA replication initiation
GO:0044237	1	cellular metabolic process
GO:0050821	1	protein stabilization
GO:0051205	1	protein insertion into membrane
GO:0070417	1	cellular response to cold
GO:0097171	1	ADP-L-glycero-beta-D-manno-heptose biosynthetic process
GO:0008360	2	regulation of cell shape
GO:0042710	2	biofilm formation
GO:0015031	2	protein transport
GO:0001123	1	transcription initiation from bacterial-type RNA polymerase promoter
GO:0006261	1	DNA-dependent DNA replication

GO:0006807	1	nitrogen compound metabolic process
GO:0009117	1	nucleotide metabolic process
GO:0017038	1	protein import
GO:0044781	1	bacterial-type flagellum organization
GO:0071973	2	bacterial-type flagellum-dependent cell motility
GO:0006352	1	DNA-templated transcription, initiation
GO:0008615	1	pyridoxine biosynthetic process
GO:0006631	1	fatty acid metabolic process
GO:0010468	1	regulation of gene expression
GO:0006396	1	RNA processing
GO:0006928	1	movement of cell or subcellular component
GO:0045454	1	cell redox homeostasis
GO:0009423	1	chorismate biosynthetic process
GO:0006629	1	lipid metabolic process
GO:0009244	1	lipopolysaccharide core region biosynthetic process
GO:0008033	1	tRNA processing
GO:0006508	1	proteolysis
GO:0006310	1	DNA recombination
GO:0006412	1	translation
GO:0009408	1	response to heat
GO:0008652	2	cellular amino acid biosynthetic process
GO:0046677	1	response to antibiotic
GO:0016310	2	phosphorylation
GO:0006281	1	DNA repair
GO:0009103	1	lipopolysaccharide biosynthetic process
GO:0006974	3	cellular response to DNA damage stimulus
GO:0005975	1	carbohydrate metabolic process
GO:0008152	3	metabolic process
GO:0055114	4	oxidation-reduction process
GO:0006355	2	regulation of transcription, DNA-templated
GO:0006810	4	transport
GO:0006351	1	transcription, DNA-templated
GO:0000018	0	regulation of DNA recombination
GO:0000027	0	ribosomal large subunit assembly
GO:0000028	0	ribosomal small subunit assembly

Table 4. Clusters of Orthologous Groups (COGs) for GRABS hits.

COG code	Counts	Definition
A	1	RNA processing and modification
C	8	Energy production and conversion
E	4	Amino acid transport and metabolism
F	2	Nucleotide transport and metabolism
G	1	Carbohydrate transport and metabolism
H	1	Coenzyme transport and metabolism
J	1	Translation, ribosomal structure, and biogenesis
K	2	Transcription
L	6	Replication, recombination, and repair
M	9	Cell wall, membrane, and envelope biogenesis
N	3	Cell motility
O	3	Posttranslational modification and metabolism
P	1	Inorganic ion transport and metabolism
R	1	General function prediction only
S	3	Function unknown
T	3	Signal transduction mechanisms
U	3	Intracellular trafficking, secretion, and vesicular transport
V	1	Cytoskeleton

Table 5. Chemical-genomics conditions with the largest-magnitude positive Pearson correlation coefficients with stiffness scores. GRABS scores were correlated with S-scores from the chemical genomics dataset in (14). SDS, sodium dodecyl sulfate.

Condition	Correlation coefficient
Chloropromazine, 12.0 μg/mL	0.092
Calcofluor	0.079
Chloropromazine, 3.0 μg/mL	0.079
Ceftazidime, 0.05 μg/mL	0.078
Cefsulodin, 12.0 μg/mL	0.076
SDS, 3.0%	0.075
Cefsulodin, 6.0 μg/mL	0.075
Cefoxitin, 1.0 μg/mL	0.07
Chloropromazine, 6.0 μg/mL	0.07
Trimethoprim, 0.4 μg/mL	0.068
Dibucaine, 0.8 μg/mL	0.068
Cefaclor, 2.0 μg/mL	0.068
Nigericin, 0.1 μg/mL	0.065
Ampicillin, 8.0 μg/mL	0.065
SDS, 2.0%	0.064
Doxorubicin, 1.0 μg/mL	0.063
Bacitracin, 300 μg/mL	0.063
Ultraviolet light, 18 s	0.061
Cefoxitin, 0.75 μg/mL	0.059
pH 4	0.059

Table 6. Chemical-genomics conditions with the largest-magnitude negative Pearson correlation coefficients with stiffness scores. GRABS scores were correlated with S-scores from the chemical genomics dataset in (14). MMS, methyl methanesulfonate; CCCP, carbonyl cyanide *m*-chlorophenyl hydrazone.

Condition	Correlation coefficient
Amoxicillin, 0.5 μg/mL	-0.081
Amoxicillin, 0.25 μg/mL	-0.069
Thiolactomycin, 5.0 μg/mL	-0.062
MMS, 0.05%	-0.060
Tetracycline, 1.0 μg/mL	-0.057
Gentamycin, 0.1 μg/mL	-0.056
Tetracycline, 0.75 μg/mL	-0.056
Thiolactomycin, 1.0 μg/mL	-0.053
CCCP, 0.5 μg/mL	-0.053
CHIR-090, 0.02 μg/mL	-0.053
Nitrofurantoin, 0.5 μg/mL	-0.052
Oxacillin, 5.0 μg/mL	-0.051
Theophylline, 100.0 μg/mL	-0.051
Oxacillin, 0.5 μg/mL	-0.050
High nickel, 0.1 μg/mL	-0.050
Norfloxacin, 0.01 μg/mL	-0.049
Nitrofurantoin, 1.0 μg/mL	-0.048
CCCP, 2.0 μg/mL	-0.046
CCCP, 0.1 μg/mL	-0.046
High nickel, 1.0 μg/mL	-0.046

Table 7. Liquid growth-curve data for Keio strains in the absence of kanamycin.

Optical density (l = 595 nm) was measured as a function of time. Growth data are included as a separate text file.

References

1. Holtje JV (1998) Growth of the stress-bearing and shape-maintaining murein sacculus of *Escherichia coli*. *Microbiol Mol Biol Rev* 62(1):181-203.

2. Mille Y, Beney L, & Gervais P (2002) Viability of *Escherichia coli* after combined osmotic and thermal treatment: a plasma membrane implication. *Biochim Biophys Acta* 1567(1-2):41-48.

3. Riley M, *et al.* (2006) *Escherichia coli* K-12: a cooperatively developed annotation snapshot--2005. *Nucleic Acids Res* 34(1):1-9.

4. Kitano H (2004) Biological robustness. *Nat Rev Genet* 5(11):826-837.

5. Dufrene YF (2014) Atomic force microscopy in microbiology: new structural and functional insights into the microbial cell surface. *MBio* 5(4):e01363-01314.

6. Thwaites JJ & Mendelson NH (1989) Mechanical properties of peptidoglycan as determined from bacterial thread. *Int J Biol Macromol* 11(4):201-206.

7. Wang S, Arellano-Santoyo H, Combs PA, & Shaevitz JW (2010) Actin-like cytoskeleton filaments contribute to cell mechanics in bacteria. *Proc Natl Acad Sci USA* 107(20):9182-9185.

8. Tuson HH, *et al.* (2012) Measuring the stiffness of bacterial cells from growth rates in hydrogels of tunable elasticity. *Mol Microbiol* 84(5):874-891.

9. Birdsell DC & Cota-Robles EH (1967) Production and ultrastructure of lysozyme and ethylenediaminetetraacetate-lysozyme spheroplasts of *Escherichia coli*. *J Bacteriol* 93(1):427-437.

10. Scheffers DJ & Pinho MG (2005) Bacterial cell wall synthesis: new insights from localization studies. *Microbiol Mol Biol Rev* 69(4):585-607.

11. Lee TK, *et al.* (2014) A dynamically assembled cell wall synthesis machinery buffers cell growth. *Proc Natl Acad Sci USA* 111(12):4554-4559.

12. Gitai Z, Dye NA, Reisenauer A, Wachi M, & Shapiro L (2005) MreB actin-mediated segregation of a specific region of a bacterial chromosome. *Cell* 120(3):329-341.

13. Paradis-Bleau C, Kritikos G, Orlova K, Typas A, & Bernhardt TG (2014) A genome-wide screen for bacterial envelope biogenesis mutants identifies a novel factor involved in cell wall precursor metabolism. *PLoS genetics* 10(1):e1004056.

14. Nichols RJ, *et al.* (2011) Phenotypic landscape of a bacterial cell. *Cell* 144(1):143-156.

15. Baba T, *et al.* (2006) Construction of *Escherichia coli* K-12 in-frame, single-gene knockout mutants: the Keio collection. *Mol Syst Biol* 2:2006 0008.

16. Philippe N, Alcaraz JP, Coursange E, Geiselmann J, & Schneider D (2004) Improvement of pCVD442, a suicide plasmid for gene allele exchange in bacteria. *Plasmid* 51(3):246-255.

17. Ursell TS, *et al.* (2014) Rod-like bacterial shape is maintained by feedback between cell curvature and cytoskeletal localization. *Proc Natl Acad Sci USA* 111(11):E1025-1034.

18. Sliusarenko O, Heinritz J, Emonet T, & Jacobs-Wagner C (2011) High-throughput, subpixel precision analysis of bacterial morphogenesis and intracellular spatio-temporal dynamics. *Mol Microbiol* 80(3):612-627.

19. Amir A, Babaeipour F, McIntosh DB, Nelson DR, & Jun S (2014) Bending forces plastically deform growing bacterial cell walls. *Proc Natl Acad Sci USA* 111(16):5778-5783.

20. Edelstein A, Amodaj N, Hoover K, Vale R, & Stuurman N (2010) Computer control of microscopes using microManager. *Curr Protoc Mol Biol* Chapter 14:Unit14 20.

21. Brown PJ, *et al.* (2012) Polar growth in the Alphaproteobacterial order Rhizobiales. *Proc Natl Acad Sci USA* 109(5):1697-1701.

22. Desmarais SM, Cava F, de Pedro MA, & Huang KC (2014) Isolation and preparation of bacterial cell walls for compositional analysis by ultra performance liquid chromatography. *J Vis Exp* (83):e51183.

23. Desmarais SM, *et al.* (2015) High-throughput, highly sensitive analyses of bacterial morphogenesis using ultra performance liquid chromatography. *J Biol Chem* 290(52):31090-31100.

24. Ottolenghi AC, Caparros M, & de Pedro MA (1993) Peptidoglycan tripeptide content and cross-linking are altered in *Enterobacter cloacae* induced to produce AmpC beta-lactamase by glycine and D-amino acids. *J Bacteriol* 175(5):1537-1542.

25. Pisabarro AG, de Pedro MA, & Vazquez D (1985) Structural modifications in the peptidoglycan of *Escherichia coli* associated with changes in the state of growth of the culture. *J Bacteriol* 161(1):238-242.

26. Narayanan J, Xiong JY, & Liu XY (2006) Determination of agarose gel pore size: Absorbance measurements vis a vis other techniques. *J Phys Conf Ser* 28:83-86.

27. Galperin MY, Makarova KS, Wolf YI, & Koonin EV (2015) Expanded microbial genome coverage and improved protein family annotation in the COG database. *Nucleic Acids Res* 43(Database issue):D261-269.

28. De Lay N, Schu DJ, & Gottesman S (2013) Bacterial small RNA-based negative regulation: Hfq and its accomplices. *J Biol Chem* 288(12):7996-8003.

29. Modi SR, Camacho DM, Kohanski MA, Walker GC, & Collins JJ (2011) Functional characterization of bacterial sRNAs using a network biology approach. *Proc Natl Acad Sci USA* 108(37):15522-15527.

30. Tsui HC, Leung HC, & Winkler ME (1994) Characterization of broadly pleiotropic phenotypes caused by an hfq insertion mutation in *Escherichia coli* K-12. *Mol Microbiol* 13(1):35-49.

31. Mukherjee A, Cao C, & Lutkenhaus J (1998) Inhibition of FtsZ polymerization by SulA, an inhibitor of septation in *Escherichia coli*. *Proc Natl Acad Sci USA* 95(6):2885-2890.

32. Chung HS, *et al.* (2009) Rapid beta-lactam-induced lysis requires successful assembly of the cell division machinery. *Proc Natl Acad Sci USA* 106(51):21872-21877.

33. Gan L, Chen S, & Jensen GJ (2008) Molecular organization of Gram-negative peptidoglycan. *Proc Natl Acad Sci U S A* 105(48):18953-18957.

34. Yao X, Jericho M, Pink D, & Beveridge T (1999) Thickness and elasticity of gram-negative murein sacculi measured by atomic force microscopy. *J Bacteriol* 181(22):6865-6875.

35. Uehara T, Matsuzawa H, & Nishimura A (2001) HscA is involved in the dynamics of FtsZ-ring formation *in Escherichia coli* K12. *Genes Cells* 6(9):803-814.

36. Arends SJ & Weiss DS (2004) Inhibiting cell division in *Escherichia coli* has little if any effect on gene expression. *J Bacteriol* 186(3):880-884.

37. Typas A, Banzhaf M, Gross CA, & Vollmer W (2012) From the regulation of peptidoglycan synthesis to bacterial growth and morphology. *Nat Rev Microbiol* 10(2):123-136.

38. Yousif SY, Broome-Smith JK, & Spratt BG (1985) Lysis of *Escherichia coli* by beta-lactam antibiotics: deletion analysis of the role of penicillin-binding proteins 1A and 1B. *J Gen Microbiol* 131(10):2839-2845.

39. Kato J, Suzuki H, & Hirota Y (1985) Dispensability of either penicillin-binding protein-1a or -1b involved in the essential process for cell elongation in Escherichia coli. *Mol Gen Genet : MGG* 200(2):272-277.

40. Paradis-Bleau C*, et al.* (2010) Lipoprotein cofactors located in the outer membrane activate bacterial cell wall polymerases. *Cell* 143(7):1110-1120.

41. Bertsche U, Breukink E, Kast T, & Vollmer W (2005) In vitro murein peptidoglycan synthesis by dimers of the bifunctional transglycosylase-transpeptidase PBP1B from Escherichia coli. *J Biol Chem* 280(45):38096-38101.

42. Born P, Breukink E, & Vollmer W (2006) In vitro synthesis of cross-linked murein and its attachment to sacculi by PBP1A from *Escherichia coli*. *J Biol Chem* 281(37):26985-26993.

43. Pepper ED, Farrell MJ, & Finkel SE (2006) Role of penicillin-binding protein 1b in competitive stationary-phase survival of *Escherichia coli*. *FEMS Microbiol Lett* 263(1):61-67.

44. Schmidt LS, Botta G, & Park JT (1981) Effects of furazlocillin, a beta-lactam antibiotic which binds selectively to penicillin-binding protein 3, on *Escherichia*

coli mutants deficient in other penicillin-binding proteins. *J Bacteriol* 145(1):632-637.

45. Garcia del Portillo F & de Pedro MA (1990) Differential effect of mutational impairment of penicillin-binding proteins 1A and 1B on *Escherichia coli* strains harboring thermosensitive mutations in the cell division genes ftsA, ftsQ, ftsZ, and pbpB. *J Bacteriol* 172(10):5863-5870.

46. Ranjit DK & Young KD (2013) The Rcs stress response and accessory envelope proteins are required for de novo generation of cell shape in *Escherichia coli*. *J Bacteriol* 195(11):2452-2462.

47. Meisel U, Holtje JV, & Vollmer W (2003) Overproduction of inactive variants of the murein synthase PBP1B causes lysis in *Escherichia coli*. *J Bacteriol* 185(18):5342-5348.

48. Terrak M, *et al.* (1999) The catalytic, glycosyl transferase and acyl transferase modules of the cell wall peptidoglycan-polymerizing penicillin-binding protein 1b of *Escherichia coli*. *Mol Microbiol* 34(2):350-364.

49. Egan AJ, *et al.* (2014) Outer-membrane lipoprotein LpoB spans the periplasm to stimulate the peptidoglycan synthase PBP1B. *Proc Natl Acad Sci USA* 111(22):8197-8202.

50. Lupoli TJ, *et al.* (2014) Lipoprotein activators stimulate *Escherichia coli* penicillin-binding proteins by different mechanisms. *J Am Chem Soc* 136(1):52-55.

51. Curtis NA, Orr D, Ross GW, & Boulton MG (1979) Affinities of penicillins and cephalosporins for the penicillin-binding proteins of *Escherichia coli* K-12 and their antibacterial activity. *Antimicrob Agents Chemother* 16(5):533-539.

52. Strahl H, Burmann F, & Hamoen LW (2014) The actin homologue MreB organizes the bacterial cell membrane. *Nat Commun* 5:3442.

53. Tropini C, *et al.* (2014) Principles of bacterial cell-size determination revealed by cell-wall synthesis perturbations. *Cell Rep* 9(4):1520-1527.

54. Prats R & de Pedro MA (1989) Normal growth and division of *Escherichia coli* with a reduced amount of murein. *J Bacteriol* 171(7):3740-3745.

55. Francius G, Domenech O, Mingeot-Leclercq MP, & Dufrene YF (2008) Direct observation of *Staphylococcus aureus* cell wall digestion by lysostaphin. *J Bacteriol* 190(24):7904-7909.

56. McGuckin MA, Linden SK, Sutton P, & Florin TH (2011) Mucin dynamics and enteric pathogens. *Nat Rev Microbiol* 9(4):265-278.

57. Porwollik S, *et al.* (2014) Defined single-gene and multi-gene deletion mutant collections in *Salmonella enterica* sv Typhimurium. *PloS one* 9(7):e99820.

58. Noble SM, French S, Kohn LA, Chen V, & Johnson AD (2010) Systematic screens of a Candida albicans homozygous deletion library decouple morphogenetic switching and pathogenicity. *Nat Genet* 42(7):590-598.

Chapter 4

Altered cell mechanics increases the susceptibility of *Proteus mirabilis* and *Vibrio parahaemolyticus* swarmer cells to β-lactam antibiotics

Adapted from

George K. Auer, Piercen M. Oliver, Manohary Rajendram, Qing Yao, Grant J. Jensen, Douglas B. Weibel, *Manuscript in preparation*

G.K.A, P.M.O., M.R., Q.Y., G.J.J., and D.B.W designed the research; P.M.O designed model and associated analysis tools; G.K.A, P.M.O., M.R., and Q.Y. performed the research; G.K.A, P.M.O., M.R., Q.Y., G.J.J., and D.B.W contributed new reagents/analytic tools; G.K.A, P.M.O., M.R., and Q.Y. analyzed data; G.K.A, P.M.O., M.R., Q.Y., G.J.J., and D.B.W. wrote the paper.

Abstract

Swarmer cells of the gram-negative pathogenic bacteria *Proteus mirabilis* and *Vibrio parahaemolyticus* become long (>10-100 μm) and multinucleate during motility on surfaces. Here, we demonstrate that the length of these swarmer cells is compensated by a large increase in flexibility, enabling them to pack into multicellular structures and coordinate their motility across surfaces. Using a microfluidic assay to measure single-cell mechanics, we identified large differences in the stiffness of swarmer cells (bending rigidity of *P. mirabilis*, 9.64×10^{-22} N m^2; *V. parahaemolyticus*, 9.75×10^{-23} N m^2) compared to vegetative cells (1.43×10^{-20} N m^2 and 3.22×10^{-22} N m^2, respectively). The reduction in bending rigidity (~3-15 fold) was not due to significant changes in peptide crosslinking density or polysaccharide chain lengths in peptidoglycan. Electron cryotomography and atomic force microscopy revealed that peptidoglycan thickness in *P. mirabilis* decreased from 1.54 nm (vegetative) to 1.07 nm (swarmer), which increased the susceptibility of swarmer cells to osmotic pressure and cell wall-modifying antibiotics. *P. mirabilis* and *V. parahaemolyticus* swarmer cells were ~30% more likely to die after 3 h of treatment with a minimum inhibitory concentrations of the β-lactams cephalexin and penicillin G compared to vegetative cells. Thus, in these pathogenic bacteria, the adaptive cost of swarmer surface motility is offset by a fitness cost—cells are more susceptible to physical and chemical changes in their environment—that could guide the design of antibiotic regimens to treat infections.

Introduction

Bacteria have evolved a variety of mechanisms to adapt to their physical environment. For example, in response to fluctuating environmental conditions, changes in biochemistry and gene regulation can alter bacterial shape and increase cell fitness. Cell filamentation is one commonly observed change in bacterial cell shape (1, 2); it has been described as a mechanism that enables bacteria to evade predation by the innate immune system during host infections (1).

In close proximity to the surface of materials, many bacteria alter their extracellular environment and morphology and leverage cell-cell physical contact to move collectively to access new sources of nutrients and growth factors (3, 4). This process, swarming, is common among motile bacteria, has been connected to bacterial pathogenesis and infections, and is an example of adaptive behavior (3, 4). Swarmer cells of *Salmonella enterica*, *Pseudomonas aeruginosa*, *Serratia marcescens*, and *Bacillus subtilis* have reduced susceptibility—compared to vegetative cells—to a variety of antibiotics that target protein translation, DNA transcription, and the bacterial cell membrane and cell wall (5-8). The specific biochemical and biophysical mechanisms underlying these observations are unknown.

Here we investigated the physical changes in swarmer cells of the gram-negative pathogenic bacteria *Proteus mirabilis* and *Vibrio parahaemolyticus*, changes that *increase* their susceptibility to cell wall-targeting clinical antibiotics. For example, we found that

large changes in the cell length of *P. mirabilis* and *V. parahaemolyticus* swarmer cells are accompanied by an increase in flexibility that enables long cells to pack together tightly and to form cell-cell interactions; these interactions have been demonstrated previously to promote surface motility (9). Using biophysical, biochemical, and structural techniques, we quantified changes in the structure and composition of the *P. mirabilis* and *V. parahaemolyticus* cell wall in swarmer versus vegetative cells and characterized the resulting susceptibility of these cells to osmotic changes and cell wall-modifying antibiotics. Our results indicate that morphological changes that enable these bacteria to adapt to new physical environments come at a significant fitness cost: cells become more susceptible to changes in their chemical environment. These results suggest reconsidering the use of cell wall-modifying antibiotics for infections of *P. mirabilis* and *V. parahaemolyticus* in which swarming is implicated (e.g., in urinary tract infections).

Materials and Methods

Bacterial Strains and Cell Culture. *P. mirabilis* strain HI4320, *V. parahaemolyticus* LM5674, *Escherichia coli* MG1655, and *E. coli* SJ286 (10) were used for experiments described in this paper. *P. mirabilis* was grown in PLB nutrient medium consisting of 1% peptone (weight/volume), 0.5% yeast extract (w/v), and 1% NaCl (w/v). *V. parahaemolyticus* was grown in nutrient medium (HI medium) consisting of 2.5% heart infusion (w/v) and 2.5% NaCl (w/v). *E. coli* was grown in lysogeny broth (LB) consisting of 1% tryptone (w/v), 0.5% yeast extract (w/v), and 1% NaCl (w/v). All strains were grown at 30 °C with shaking at 200 rpm.

Filamentation of Vegetative Bacteria. To create filamentous vegetative bacterial cells for investigations of cell mechanics (osmotic shock and bending rigidity), we diluted an overnight culture of cells 1:200 into fresh medium as indicated above. We grew cultures at 30 °C with shaking for 1 h, added aztreonam or IPTG (the latter for *E. coli* MG1655-p*sulA*, in which SulA expression is induced by IPTG) to a final concentration of 10 μg/mL or 1 mM, respectively, and grew cells for an additional 70 min.

Harvesting Swarming Bacterial Cells. To isolate swarming bacteria, we used 1.5% Difco agar (w/v) containing PLB medium for *P. mirabilis* and 1.4% Difco agar (w/v) containing HI medium for *V. parahaemolyticus.* We used HI-containing agar plates

within 3 h after their preparation, and PLB-containing plates within 3 days of their preparation. We isolated *P. mirabilis* swarmer cells from agar plates as described previously (11). To isolate *V. parahaemolyticus* swarmers, we pipetted 4 μL of a fresh overnight culture on the agar surface, 5 cm from the edge of the plate, and incubated the plate overnight at 30 °C. We collected the outer 1-cm region of the colony using a 1-μL calibrated inoculation loop (220215, Becton, Dickinson) and transferred *V. parahaemolyticus* swarmers to HI liquid medium.

Imaging Swarmer Cells in Motile Colonies. To visualize individual swarmer cells in actively swarming colonies, we used a scalpel to remove a 20 mm x 20 mm square of agar containing swarmer cells on the surface and positioned the agar between two pieces of cover glass (#1, 35 mm x 50 mm). We collected images using a TE2000-E inverted microscope (Nikon, Tokyo, Japan) equipped with a Perfect Focus System (Nikon), a CoolSNAP DV2 camera (Photometrics, Munich, Germany), a Nikon PlanApo 60x oil objective, an objective heater (Bioptechs, Butler, PA, USA), and a heated stage (Tokai hit, Fujinomiya, Japan) at 30 °C.

Fabrication of Microfluidic Devices for Measuring Cell Bending and Cell Growth. Masters for microfluidics devices—for measuring cell bending rigidity and for constructing the cell growth/osmotic shock device—were fabricated on separate 3"

silicon wafers using SU8 photoresist, patterned using a Heidelberg μPG101 mask writer (Heidelberg Instruments, Heidelberg, Germany), and developed using solvent. The cell bending rigidity microfluidic device (Figure 1) consisted of two layers. The first SU8 layer contained channels 1 μm in height and width for capturing bacterial cells. After fabricating this layer, we coated it with a second SU8 layer (25 μm in height) that formed a central flow channel (100 μm in width). The other microfluidic device consisted of a flow chamber for imaging cell growth, division, and physical response to osmotic shock. This device had a single channel (volume, ~10 μL) that was 10 mm in length, 5 mm in width, and 50 μm in height. We used the masters for the two devices to emboss layers of poly(dimethylsiloxane) (PDMS), punched holes for inlets and outlets, cleaned the surfaces with tape, and treated them with oxygen plasma. We immediately sealed each PDMS layer against a plasma-treated #1.5 cover glass (24 x 50 mm Fisherbrand 12-544-E) to form a permanent bond.

Calculating Vegetative and Swarmer Cell Division Times. We prepared vegetative cells by diluting an overnight culture 1:200 in fresh medium and grew the cells at 30 °C with shaking at 200 rpm to an optical density (OD; λ=600 nm) of 0.6. We prepared swarmer cells as described previously (11). We monitored the growth of *P. mirabilis*, *V. parahaemolyticus*, and *E. coli* vegetative cells for 120 min at 30 °C in the microfluidic growth chamber device. We performed a similar experiment with *P. mirabilis* and *V.*

parahaemolyticus swarmers for 65 min at 30 °C to determine the amount of time elapsed before cells divided. We collected images of cells at 1-min intervals and determined the division time for a maximum of 10 generations (for vegetative cells) and four division events (for swarmer cells).

Immunostaining Flagella on *E. coli* Cells to Determine Flagella Surface Density. As a control to determine the influence of the surface density of bacterial flagella on measurements of bending rigidity, we imaged two *E. coli* MG1655 strains with different flagella densities using a polyclonal flagellin antibody and an immunostaining procedure for flagella visualization (11).

Measuring the Sensitivity of Cells to Osmotic Shock in a Microfluidic Device. We prepared filamentous vegetative cells and swarmer cells of *P. mirabilis* and *V. parahaemolyticus* as described above. To maximize the number of cells attached to a surface in the microfluidic device, we concentrated cells to an OD_{600} of 8 in 100 μL of liquid nutrient medium.

We prepared the microfluidic device by flowing 10 μL of undiluted Cell-Tak into the device and incubated it for 10 min at 25 °C. Next, we flowed 20 μL of a suspension of cells (OD_{600}=8) through the device, then repeated with another 20 μL aliquot of cell suspension. To aid the adherence of the highly motile swarmer cells to the Cell-Tak-

coated surface, we centrifuged the device for 5 min at 300 x *g* in a centrifuge equipped with a swimming bucket rotor.

For osmotic shock experiments, we filled separate 1-mL syringes with a solution of UltraPure distilled water (Invitrogen) or 1 M of a NaCl solution prepared in ddH_2O and connected the syringes using a three-way valve. We mounted the microfluidic device on the TE2000-E inverted microscope (described above) and imaged at cells in the chamber at 25 °C to minimize growth and cell division. Prior to osmotic shock, we flowed 200 μL of fresh medium (PLB for *P. mirabilis*, LB for *E. coli*, and HI for *V. parahaemolyticus*) through the device to remove cells that were not adhered to the channel surface. While imaging, we flowed a 1 M NaCl solution through the channel and observed cell plasmolysis, immediately after which we flowed ddH_2O through the channel and observed cells elongating. We collected images of single cells after each of the three conditions: 1) isotonic culture (PLB, LB, HI); 2) hypertonic shock (1 M NaCl); and 3) hypotonic shock (ddH_2O).

To determine changes in cell size and width, we extracted individual cell contours from the images taken for each treatment using MATLAB 2014a (MathWorks, Inc., Natick, MA, USA) and used MicrobeTracker (12) to determine cell lengths (L) and widths (W). From these measurements we calculated ΔL ($L_{hypotonic} - L_{hypertonic}$) and ΔW ($W_{hypotonic} - W_{hypertonic}$) for vegetative and swarmer cells of *P. mirabilis* and *V. parahaemolyticus*.

Determining the Minimum Inhibitory Concentration (MIC) of Vegetative Cells of *P. mirabilis* and *V. parahaemolyticus.* We used the micro-dilution protocol to determine the MIC of cephalexin in accordance with National Committee for Clinical Laboratory Standards guidelines (13). Briefly, we added 400 μg/mL of cephalexin or penicillin G to the first well of a 96-well microplate and diluted these antibiotics 2-fold across adjacent wells (wells #1-11); well 12 was a no-drug control. We determined the MIC after 16 h of growth at 30 °C with shaking by identifying the lowest concentration of cephalexin and penicillin G that inhibited cell growth by visual inspection. The MIC was determined from three replicate plates. We determined the MIC of cephalexin against *E. coli* MG1655 (1X MIC = 6.25 μg/mL, 32X MIC = 200 μg/mL), *P. mirabilis* (100 μg/mL), and *V. parahaemolyticus* (50 μg/mL). The MIC of penicillin G against *P. mirabilis* was 12.5 μg/mL.

Antibiotic Treatment of Vegetative and Swarmer Cells and Measurement of Their Growth in a Microfluidic Device. We prepared vegetative and swarmer cells of *P. mirabilis* and *V. parahaemolyticus* as described previously. Prior to use, we diluted cells 1:100 in fresh medium to a cell density that enabled us to image many individual cells simultaneously in the microfluidic device.

To prepare the microfluidic device for monitoring growth, we applied a 250 μm-thick layer of PDMS prepolymer to the surface of 35 x 50 mm #1 glass cover slips

(Fisherfinest) using a spincoater (Laurell Technology Corporation, North Wales, PA, USA) and polymerized the polymer overnight at 60 °C. We subsequently removed a 6 mm x 4 mm rectangle of PDMS from the center of the cover glass using a scalpel. We applied transparent tape to both sides of this rectangular well and pipetted 100 μL of medium containing 2% (w/v) molten agarose (UltraPure Agarose, Invitrogen) into the well. We placed a 22 x 30 mm #1.5 glass cover slip on top of the molten agarose (to flatten the agarose surface), pressed the cover slip against the transparent tape, and solidified the agarose at 25 °C. Next, we removed the #1.5 cover glass, tape, and any residual agarose from the PDMS surface. We pipetted 2 μL of cells onto the agarose pad surface, waited until the excess liquid had evaporated or been absorbed by the agarose, carefully removed the agarose layer, inverted it, and placed it back into the well such that the cells were positioned between the agarose surface and the glass cover slip. We placed the PDMS flow chamber used in the construction of the osmotic shock microfluidic device on the PDMS-coated glass cover slip and aligned it such that the agarose pad was centered in the flow channel (Figure 2).

For antibiotic treatment of cells in the microfluidic cell growth device, we filled a 6-mL syringe with cephalexin or penicillin G at a concentration corresponding to 1X MIC dissolved in nutrient medium. We supplied a constant flow of 20 μL/min to the device using a syringe pump and monitored the growth of individual cells during

antibiotic exposure using a TE2000-E inverted microscope. The stage and objective heater were maintained at 30 °C. Images were collected every 1 min for 3 h.

Due to the aberrant shape of cells treated with cephalexin and penicillin G, we were unable to use MicrobeTracker to determine cell death. Instead, we visually determined the time of death for individual cells when they exhibited three phenotypes that collectively indicate cell death: blebbing (membrane swelling), lysis (bleb rupture), and disappearance of cells in phase contrast microscopy (loss of cytoplasmic material).

Determining Cell Growth Rate in the Presence of Antibiotics. We prepared vegetative and swarmer cells of *P. mirabilis* and *V. parahaemolyticus* as described above. We monitored individual cell growth at 30 °C in the presence of 1X MIC of cephalexin and pencillin G in our microfluidic growth device by collecting an image every 1 min for 15 min. To calculate the growth rate, we first extracted individual cell contours at each time point using MicrobeTracker and determined cell length. To take into account the differences in starting length between *P. mirabilis* and *V. parahaemolyticus* cells, we normalized the change in length to the initial cell length ($\Delta L/L_0$) at each time point. To determine the growth rate for individual cells, we fit their relative length over time to an exponential function using GraphPad Prism version 6.0 (GraphPad Software Inc., La Jolla, CA, USA).

Measuring Cell Envelope Architecture and Peptidoglycan Thickness Using Electron Cryotomography. We prepared vegetative and swarmer cells of *P. mirabilis* and *V. parahaemolyticus* and concentrated them to an OD_{600}=10. For ECT, we mixed vegetative and swarmer cells with bovine serum albumin-treated 10-nm diameter gold particles that served as fiducial markers, applied them to electron microscopy grids, and plunge-froze them in a mixture of liquid ethane and propane, as described previously (14). Grids were stored in liquid nitrogen until imaging.

We acquired images on a 300 KeV Polara transmission electron microscope (FEI) with a GIF energy filter (Gatan) and a K2 Summit direct detector (Gatan). We collected tilt series from -60° to +60° with 1° increments using UCSFtomo software with a defocus of -10 μm and a total dosage of 190 $e^-/Å^2$ (15) at a magnification of 27500×. Tomograms were calculated using IMOD software (16).

For sub-tomogram averaging, smooth and flat membrane regions were chosen by eye; a volume of 40 × 70 × 12 voxels (62 nm × 109 nm × 19 nm) was centered using the outer membrane and extracted. We aligned 38 extracted "membrane fragments" from four *P. mirabilis* vegetative cells and 42 fragments from nine *P. mirabilis* swarmer cells and averaged them in PEET (17). The densities from two averaged membranes were scaled to match each other using IMOD (16), cross-averaged density profiles were measured using ImageJ (18), and figures were generated in OriginPro (OriginLab).

Determining the Thickness of *P. mirabilis* and *V. parahaemolyticus* Sacculi (Isolated Peptidoglycan) via Atomic Force Microscopy (AFM) Under Ambient Conditions. We isolated *P. mirabilis* and *V. parahaemolyticus* swarmer cells, concentrated them at 800 x *g* for 10 min, removed the supernatant, flash froze the cell pellet in liquid nitrogen, and stored it at -80 °C. Swarmer cell pellets were thawed at 4 °C and pooled for isolation of sacculi (intact peptidoglycan). To increase the efficiency of cell lysis prior to isolating sacculi, we resuspended vegetative and swarmer cell pellets in 3 mL of cold 1X phosphate-buffered saline, then lysed cells with a tip sonicator (Qsonica, Newton, CT) for ~10 s at a power setting of 75%. We confirmed cell lysis via optical microscopy. We isolated sonicated cells, resuspended sacculi in 20 (*V. parahaemolyticus* swarmers) or 200 μL of ddH_2O (all other cells), immediately flash froze the sacculi in liquid nitrogen, and stored them at -80 °C**.**

To prepare sacculi for AFM, we transferred 10 μL of sacculi thawed at 4 °C to a new microcentrifuge tube placed in a bath sonicator (Branson 2510) that was cooled with ice for 10 min to aid in the dispersal of sacculi without affecting sacculus architecture (19). After sonication, we pipetted 10 μL of the sacculi onto freshly cleaved mica, dried the mica under nitrogen gas, washed it 3x with 1 mL of ddH_2O (filtered through a 0.2 μm-diameter pore filter), dried the sacculi under nitrogen gas, and imaged immediately after preparation.

We performed AFM using a Catalyst AFM (Bruker) operating in tapping mode in ambient conditions (air) with an aluminum reflex-coated silicon AFM probe (Ted Pella, Inc.; k = 40 N/m). Before imaging, AFM probes were auto-tuned using Nanoscope 8.15 (Bruker). We collected all images at high resolution (512 x 512 pixels) with a scan speed of 1 Hz and analyzed images using NanoScope Analysis 1.4 (Bruker). Prior to determining sacculi thickness, we flattened (0^{th} order) all images to remove variations in surface thickness. Thickness was determined perpendicular to the long axis; we avoided surface debris, folds in the sacculi, and trapped material in sacculi (Figure 3).

Measuring the Bending Rigidity of *P. mirabilis*, *V. paramaemolyticus*, and *E. coli* Cells. We used streak velocimetry to determine the profile of fluid flow rates in the central channel of the microfluidic device driven by gravity flow. We added fluorescently labeled microspheres (Polysciences Catalog # 24050, 0.22 μm) diluted ~1:10000 in deionized H_2O containing 0.01% Brij-35 to the microfluidic channel and collected videos of the fluorescent beads moving through the channel at focal planes 2 μm apart. We analyzed the movies with custom-written code in Igor Pro 6. Briefly, we applied a Gaussian blur and threshold to each frame and used the thresholded image to establish a region that was fit to a function based on a 2D Gaussian. We used the image exposure time and length of the streaks—taking into account the size of the microspheres—to calculate microsphere velocity. We mapped the velocity profile

within the channel by analyzing several hundred microspheres. We binned the velocity data into a 3D matrix and fit it to a Poiseuille function, letting the velocity coefficient, height, and width float. The velocity coefficient was used as an input to the cell bending fitting function.

The system for gravity flow pumping (Figure 4) consisted of two 6-mL syringes, one 60-mL syringe, one 1-mL syringe, a ruler, and a VC-6 channel valve controller (Warner Instruments) connected to a VC-8 mini-valve system (Warner Instruments) that drives a three-way solenoid valve (Lee Co). Syringe #1 (6 mL) was mounted to an immobile post, positioned 16" above the table surface; this syringe was used to load cells. Syringe #2 (6 mL) was positioned 30" above the table surface, was connected to a stage that could be raised and lowered vertically, and was used to apply flow force in the device. Syringe #3 (60 mL) was mounted to an immobile post, positioned 30" above the surface of the table, and was used to apply an opposing flow force at the device outlet and to collect spent media/cells. We attached two-way valves, a blunt-end needle, and tubing to each syringe, including syringe #4 (1 mL). We joined the two 6-mL syringes using a Y-junction connector that led to the VC-8-mini-valve system inlet. The outlet of the valve system was connected to the microfluidic system. A ruler on an immobile post indicated the '0 position' (no pressure).

For cell bending experiments, we prepared filamentous vegetative cells and swarmer cells of *P. mirabilis* and *V. paramaemolyticus*; the cells were normalized to an

OD_{600}=1. Prior to starting a measurement, syringes 1 and 2 were flushed with ddH_2O and fresh medium. Syringe 2 was filled with 4 mL of medium, syringe 3 was filled with 30 mL of ddH_2O, and syringe 4 was filled with 0.8 mL of ddH_2O. We added cells to syringe 1 and flowed them through the tubing until they reached the device outlet. To load the cells into the side channels of the device (from the central channel), we applied a suction force using the 1-mL syringe. After the side channels were loaded with cells, we adjusted the height of syringe 2 until no flow occurred in the device. Syringe 2 was then raised 7 cm from the no-flow position (a height of 0 cm). We collected images of cells in the channel when syringe 2 was at positions 0 cm and 7 cm using a Zeiss Axiovert 100 inverted microscope equipped with an iXon3 CCD (Andor), a 63X Plan-APOCHROMAT oil objective, and Micro-Manager version 1.4.16. After collecting cell-bending deflections for all loaded cells, we expelled cells from the side channels, flowed liquid through the device for 15 s, and reloaded the side channels with new cells.

We analyzed images to determine cell deflection under flow using custom image-analysis software written in Igor Pro 6.37 (Wavemetrics, Inc.). The cell-bending model (Supplementary Information) is a differential equation that lacks an analytical solution and thus requires calculation of a numerical solution. To determine the bending rigidity of cells, we wrote custom code in Igor Pro 6.37 that uses a variety of input parameters, including channel dimensions, fluid velocity, flexural rigidity of the cell, cell radius, and cell length. The function numerically calculates the maximum

deflection based on our model. This function is integrated into a fitting algorithm to find a least-squares solution to a dataset of maximum deflections versus cell lengths with flexural rigidity as the fitting parameter.

Our model for bending a cell under flow is based on the mechanics model of a suspended rod or cantilever bending under its own weight. Our experimental system was similar to that of Amir et al. (10). Although laminar flow is perpendicular to the long axis of cells in this system, the lateral deformations of cells that we measured were substantially larger (in our case, as large as 10 μm; compared to <1 μm in Amir et al. (10)). For this reason, many of the assumptions of the model presented by Amir et al. are not valid for our dataset. The model we developed to extract the flexural rigidity of the bacterium takes into account the shape of the laminar flow profile, the angle of the cell against the flow profile, and the arc length of the cell (longer cells tend to fold over and do not penetrate as deeply into the flow profile). Our only major assumption is that the force of the bending moment at a particular point along a cell is not applied as an integration to the end of the cell, but is rather applied exactly one-half the distance (arc length) to the end of the cell. We found that models that take into account the full integration of the bending moment are computationally time-consuming and do not provide a substantial change in the calculated cell shape (data not shown). A detailed derivation of the model is presented in the Supplementary Information.

Determining the Composition of Peptidoglycan in *P. mirabilis* and *V. parahaemolyticus* Vegetative and Swarmer Cells using Ultra High Performance Liquid Chromatography/Mass Spectrometry (UPLC/MS). To purify peptidoglycan for UPLC/MS, we carried out a previously reported isolation technique for Gram-negative bacteria (20) with the following modifications. Briefly, after trypsin inactivation (Sigma), we incubated the sacculi in 1 M HCl for 4 h at 37 °C to remove any O-acetylation from the peptidoglycan, which is present in *P. mirabilis* (21). Then, the sacculi were washed three times in ddH_2O, resuspended in 500 mM boric acid [pH 9] to OD_{600}=3, and mixed with 1/10 the volume of mutanolysin (Sigma). The sample was incubated 16 h at 37 °C with 200 rpm shaking. The next day, the samples were centrifuged for 10 min at 9500 x *g*, pelleting the remaining insoluble material. The supernatant was removed and put into a glass vial. To reduce the isolated muropeptide fragments, we added 50 μL of 20 μg/mL sodium borohydride in 500 mM boric acid [pH 9] and incubated the mixture for 30 min at room temperature. We adjusted the pH of the solution to 2-3 by adding 50% phosphoric acid, then filtered the muropeptide solution through a Durapore polyvinylidine fluoride filter (0.22-μm pores; Millex) into a clean vial. Vials were immediately stored at -80 °C until use within 1 week of muropeptide isolation.

For UPLC/MS, we injected 7.5 μL of purified muropeptides on a Cortecs 2.1 x 100 mm C18 column packed with 1.6 μM-diameter particles and equipped with a Cortecs C18 guard column. The column temperature maintained at 52 °C using an Acquity

standard flow UPLC system equipped with an inline photodiode array (Waters Corp., Milford MA). For muropeptide separation by UPLC, we used solvent A (Optima LCMS-grade water with 0.05% trifluoroacetic acid) and solvent B (30% (v/v) Optima LCMS-grade methanol in Optima LCMS-grade water with 0.05% trifluoroacetic acid) (Fisher Scientific, Pittsburgh PA). Muropeptides were eluted from the column with a gradient of increasing solvent B (1 min hold at 1% B, to 99% B at 60 min, hold 99% B 5 min, to 1% B at 65.5 min, 4.5 min hold at 1% B) at a flow rate of 0.2 mL/min. We analyzed the eluent from the column using a Bruker MaXis Ultra-High Resolution time-of-flight 4G mass spectrometer (Bruker Daltonic, Billerica MA) with either an MS method or a data-dependent, top 3 MS/MS method. For both methods, the capillary voltage was set to 4100 V, the nebulizer pressure was 2.0 bar, and the drying gas was set to 6.0 L/m at 220 °C. Muropeptides were detected at λ=205 nm and via MS.

We determined the peptidoglycan composition of *E. coli*, *P. mirabilis*, and *V. parahaemolyticus* vegetative and swarmer cells by comparing MS/MS fragmentation patterns using DataAnalysis version 4.2 (Bruker) (Figure 5). Muropeptides were identified according to mass values using DataAnalysis version 4.2. We calculated muropeptide masses using ChemDraw 14.0 (Table 1). We quantified the corresponding UV (λ=205) absorbing peaks (Figure 6) identified via MS (Bruker), from which we calculated peptidoglycan cross-linking density and strand length (22) for each species.

Results

The Flexibility of *P. mirabilis* and *V. parahaemolyticus* Cells Increases Significantly During Swarming. During surface motility, *P. mirabilis* and *V. parahaemolyticus* cells grow into swarmers that are characteristically long (10-100 μm) and display a high surface density of flagella (3, 11). We found that these swarmer cells display an unusual phenotype that is rarely observed among gram-negative bacteria: cells become remarkably flexible and their shape is altered by adjacent cell motion and collisions (Figure 7). The ability of *P. mirabilis* swarmer cells to form cell-cell contacts plays a role in their cooperative motility (11), leading us to hypothesize that increasing flexibility enables these long cells to optimize packing into multicellular structures that move cooperatively across surfaces. Bacterial cell mechanics is generally attributed to the peptidoglycan layer of the cell wall (23), which has a thickness of 3~50 nm and surrounds the cytoplasmic membrane (24). Very little is known about mechanical regulation in bacteria (25-29) and we are unaware of studies connecting swarming to changes in cell mechanics.

We quantified changes in swarmer-cell stiffness using cell-bending assays in a reloadable microfluidic-based device (Figure 8, 1) that is related to a method developed previously (10). We used bending rigidity as a parameter to quantify *P. mirabilis* and *V. parahaemolyticus* cell stiffness rather than Young's modulus, as the latter metric of the intrinsic mechanical properties of materials requires a quantitative understanding of

cell-wall thickness, which we found changes during swarming (described below). In the bending assay, a shear fluid force is applied to multiple filamentous cells, resulting in horizontal deflection of their cell tips (Figure 8); fitting the deflection data to a mechanical model provides an estimate of the (flexural) bending rigidity of cells (Figure 9). Introducing a reloadable approach for performing these assays enabled us to perform rapid measurements of the deflection of *P. mirabilis* and *V. parahaemolyticus* swarmer cells after isolating them from swarm plates and before they began to divide (Figure 10B). As a point of comparison, we filamented vegetative cells of *P. mirabilis* and *V. parahaemolyticus* using aztreonam—an inhibitor of the division specific transpeptidase PBP3 (30)—and compared their bending rigidity values to swarmer cells. As a control we measured the bending rigidity of *Escherichia coli* strain MG1655 to be 9.75×10^{-23} N m^2 (Figure 11); using a value for the thickness of the peptidoglycan of 4 nm (31), this measurement corresponds to a Young's modulus of 26 MPa, which is close to values that have been reported previously (10, 25). We found a significant decrease in the stiffness of both *P. mirabilis* (~15-fold) and *V. parahaemolyticus* (3-fold) swarmer bacteria versus vegetative cells (Figure 11). *V. parahaemolyticus* vegetative cells were remarkably flexible and were ~134-fold more flexible than *E. coli* cells and ~3-fold more flexible than *P. mirabilis* swarmer cells (Figure 11).

As PBP3 inhibition may change the cross-linking density of peptidoglycan at the division plane and alter cell mechanics, we compared bending rigidity values of cells

treated with aztreonam and cells filamented by overexpressing SulA, a protein that inhibits polymerization of the division protein FtsZ. Both mechanisms of *E. coli* filamentation produced similar bending rigidity values: 4.02 x 10^{-20} N m^2 and 4.18 x 10^{-20} N m^2, respectively (Figure 12A). To account for the high surface density of flagella on swarmer cells, which may influence cell drag in fluid flow and bias measurements, we performed bending rigidity measurements on two K-12-derived strains of *E. coli* with substantially different flagella densities (Figure 12C) and observed no appreciable change in values (bending rigidity 4.01 x 10^{-20} N m^2 at high flagella density and 4.18 x 10^{-23} N m^2 at low flagella density; Figure 12B).

Overexpressing FlhDC, the heterohexameric activator that is important for swarming, produces a phenotype that replicates many of the characteristics of swarmer cells, including increased cell length and flagella density (32). However, the connection of this protein to cell mechanics has not been reported to date. To test whether FlhDC is connected to changes in swarmer cell stiffness, we overexpressed the protein from the plasmid-encoded genes *pFlhDC* in *P. mirabilis* filamentous cells and measured bending rigidity. We detected a ~1.5-fold difference in bending rigidity between wildtype (1.43 x 10^{-20} N m^2) and *pFlhDC*-containing *P. mirabilis* vegetative cells (9.26 x 10^{-21} N m^2), and no difference versus *pFlhDC*-containing *P. mirabilis* swarmer cells (Figure 10). These results indicate that a non-FlhDC-regulated pathway produces the observed mechanical phenotype.

Changes in Peptidoglycan Composition of *P. mirabilis* and *V. parahaemolyticus* Swarmers. Peptidoglycan consists of the disaccharide building block β-(1,4)-N-acetylmuramic acid/N-acetyl-glucosamine (MurNAc-GlcNAc) containing a pentapeptide attached to each 4'-OH group on MurNAc. Crosslinking between adjacent pentapeptides creates a polymeric layer in many bacterial cells, and altering its structure and composition affects cell-mechanical properties (27-29). To determine whether the peptidoglycan composition of *P. mirabilis* and *V. parahaemolyticus* changes during swarming, we used ultra performance liquid chromatography-mass spectrometry (UPLC-MS) to compare vegetative and swarmer cells (Figure 6). As the peptidoglycan composition of *V. parahaemolyticus* was previously unknown, we characterized the muropeptide stem peptide using UPLC-MS/MS (Figure 5, Table 1). Similar to *E. coli* (33) and *P. mirabilis* (21), *V. parahaemolyticus* has a peptidoglycan structure that is similar to other gram-negative bacteria, in which the peptide stem consists of L-Ala-D-Glu-*meso*-diaminopimelic acid (*meso*-DAP)-D-Ala-D-Ala (Figure 5) (34).

Compared to vegetative cells, *P. mirabilis* swarmer cells contained fewer monomers (MurNAc-GlcNAc), more dimers, and more anhydrous-containing saccharides that indicate glycan-strand termination (Figure 13A) (24). We were unable to detect differences in the relative abundance of trimers between swarmer and

vegetative cells of *P. mirabilis* (Figure 13A). The observed higher levels of dimers and anhydrous-containing saccharides in swarmer cells may indicate a shorter strand length (Figure 13B), a characteristic that has been reported in the peptidoglycan composition of the stiff gram-positive bacterium *Staphylococcus aureus* (35, 36), as well as a higher degree of crosslinking (Figure 13C). A comparison of the peptidoglycan composition of *V. parahaemolyticus* vegetative and swarmer cells revealed consistent differences, with the exception of an increase in anhydrous-containing saccharides in swarmers (Figure 13A). The composition of *V. parahaemolyticus* peptidoglycan exhibited two characteristics consistent with an increase in flexibility compared to *E. coli* and *P. mirabilis*: a relatively high concentration of monomers (Figure 13A) and lower cross-linking density (Figure 13C).

Swarmer Cells Have a Thinner Peptidoglycan Layer than Vegetative Cells and Display Membrane Defects. Unable to explain how the lower swarmer cell stiffness was related to differences in peptidoglycan composition, we explored an alternative hypothesis: that the thickness of the peptidoglycan layer is reduced or the organization of the cell envelope changes during swarming. To identify changes in the peptidoglycan thickness of swarmer cells, we isolated the intact layer of peptidoglycan (sacculi) from *P. mirabilis* vegetative and swarmer cells and measured the thickness of dried sacculi using tapping-mode atomic force microscopy (AFM) (Figure 14A). Although differences

in the nanoscopic appearance of the sacculi of different cells were not obvious through AFM (Figure 3), these changes may be indistinguishable once the peptidoglycan is isolated, turgor pressure is removed, and the sacculus relaxes to its equilibrium structure (19). Isolated, dry *P. mirabilis* swarmer cell sacculi were ~1.5-fold less thick (1.08 ± 0.20 μm) than vegetative cells (1.55 ± 0.27 μm) (Figure 6A). *V. parahaemolyticus* swarmer cells (0.68 ± 0.11 μm) exhibited a similar ~1.2 fold decrease in thickness compared to vegetative cells (0.84 ± 0.21 μm). A comparison of peptidoglycan thickness and cell bending rigidity suggested that the relationship between these data is approximately linear (Figure 14B).

To complement AFM, we performed electron cryotomography (ECT) on intact vegetative and swarmer cells with native peptidoglycan architecture (Figure 14C,D, 15, 16). Sub-tomogram-averaged ECT volumes of the cell wall (Figure 14C) confirmed that the native peptidoglycan was less thick in *P. mirabilis* swarmer cells than in vegetative cells (Figure 14C, D). We also detected a substantial change in the membrane architecture of *P. mirabili*s swarmer cells (Figure 15E, F): instead of the smooth membrane observed in vegetative cells (Figure 15A, B), swarmer cells had an undulating outer membrane suggestive of altered membrane properties (Figure 15E, F). Although *V. parahaemolyticus* vegetative cells contained a smooth membrane (Figure 15A, B), we observed two phenotypically distinct morphologies for swarmer cells. The first morphology was indistinguishable from that of vegetative cells (Figure 16C). The

second morphology displayed severe cell-envelope defects, including variable cell diameter (Figures 16E, F), membrane budding (Figure 16D), and membrane vesicles (Figure 16E). We observed excessive deformation of *V. parahaemolyticus* cells during cryo-EM sample preparation (Figure 16D, E, F), suggesting that these membrane deformations are artifacts of preparation and supporting the low values of cell stiffness that we measured.

***P. mirabilis* and *V. parahaemolyticus* Swarmer cells Are More Sensitive to Osmotic Stress than Vegetative Cells.** To complement our measurements of cell stiffness and peptidoglycan organization and thickness, we investigated swarmer and vegetative filamented cell mechanics using osmotic stress to shrink (in hypotonic liquid such as H_2O) and swell (in hypertonic liquid such as NaCl) cells (Figure 17). We filamented *P. mirabilis*, *V. parahaemolyticus*, and *E. coli* cells (the last as a control) by treating them with aztreonam to create a range of cell lengths that matched the lengths of *P. mirabilis* and *V. parahaemolyticus* swarmer cells. We expected that low values of bending rigidity and compositional changes in peptidoglycan (e.g., changes in glycan strand length, cross-linking, or thickness) would cause cells to elongate upon exposure to large changes in turgor. The extension of *P. mirabilis* and *V. parahaemolyticus* swarmer cells under osmotic shock conditions was substantially different from that of vegetative filamented cells (Figure 18). To circumvent the cellular production of osmolytes to protect against the

large changes in osmotic pressure during shock (typically produced over < 1 min) (37, 38), we used a microfluidic-based device to rapidly switch between hypo-osmotic and hyper-osmotic media and measured changes in cell length before the cells could adapt (Figure 17).

We found that osmotic shifts produced small changes in the length (Figure 18A) and width of vegetative filamented *P. mirabilis* cells (Figure 18C) that were similar to those of *E. coli* cells (Figure 18A, C). In contrast, *V. parahaemolyticus* vegetative cells substantially increased in cell length (Figure 18B) and displayed a small change in cell width (Figure 18D) compared to *E. coli* cells. *P. mirabilis* and *V. parahaemolyticus* swarmer cells dramatically increased in cell length (Figure 18A, B) and *P. mirabilis* swarmers displayed an increase in cell width (Figure 18C) during osmotic jumps. These results suggest that swarmer cells of *P. mirabilis* and *V. parahaemolyticus* are more susceptible to osmotic shifts as a result of changes in cell mechanics, consistent with our observations of membrane deformations in these cells (Figure 15E-F, 16D-F).

Susceptibility of *P. mirabilis* and *V. parahaemolyticus* Swarmers to the Cell Wall-targeting Antibiotics Cephalexin and Penicillin G. Although high-density swarming colonies of bacteria display resistance to a wide range of antibiotics (5), our characterization of cell mechanics and changes in peptidoglycan structure suggest that *P. mirabilis* and *V. parahaemolyticus* swarmers may be more susceptible to cell wall-

targeting antibiotics. The traditional measurement of antibiotic susceptibility involves determining the minimum inhibitory concentration (MIC) of drugs against cells using growth-based assays that are unsuitable for swarmer cells, due to their change in phenotype within hours after removal from surfaces. To determine the sensitivity of *P. mirabilis* and *V. parahaemolyticus* swarmers to the cell wall-targeting antibiotics cephalexin (inhibits PBP3 and 4) (39) and penicillin G (inhibits PBP3, 4, and 6) (40), we isolated cells from agar plates and determined their division profiles over time (Figure 10A). We measured swarmer single-cell growth in a microfluidic device (Figure 2, 20) for 3 h in the presence of 1X MIC cephalexin, a previous report (41) indicated that treating cells with cephalexin for 3 h was sufficient to kill ~100% of a population of *E. coli* cells growing in bulk liquid culture.

Our microfluidic device enabled us to supply cells with fresh medium to ensure exponential cell growth and a constant concentration of antibiotics. It also provided us with an advantage over another method (E-strips, (5, 6)) used to measure antibiotic susceptibility in swarming bacteria, in which exposing bacteria to sub-MIC concentrations of drug can accelerate the frequency of antibiotic resistance, provide inaccurate susceptibility data, and yield information on cell adaptability instead of MIC. We found that the survival of *P. mirabilis* (66%) and *V. parahaemolyticus* (64%) vegetative cells treated with 1X MIC cephalexin was similar and slightly higher than of similarly treated *E. coli* (55%) (Figure 19A, 20). Treating *P. mirabilis* and *V. parahaemolyticus*

swarmer cells with 1X MIC cephalexin reduced their survival to 37% and 19%, respectively (Figure 19A, 20). Related experiments using penicillin G led to similar rates of survival (Figure 19A). Cells were considered to be alive until they displayed membrane blebbing, cell lysis, and loss of phase contrast on phase-contrast microscopy.

Cell wall-targeting antibiotics are most effective against actively growing cells and therefore mechanisms that increase growth will reduce cell survival and may explain our experimental observations. After normalizing for cell length, we detected no change in the growth rate of swarmer cells when they were treated with either antibiotic (Figure 21). We measured the mean survival time of cells (the amount of time elapsed after treatment with drugs before cell death) for *P. mirabilis* and *V. parahaemolyticus* swarmer cells treated with cephalexin and pencillin G (Figure 19B). We found that the survival time for these swarmer cells was lower than that for vegetative cells (Figure 19B), and hypothesized that the difference was due to an increase in these compounds entering cells and binding their target PBPs. To test this hypothesis, we treated *E. coli* cells with 32X MIC and observed that while the percentage of cells surviving decreased (5.1%), survival time did not decrease substantially (Figure 19B), indicating that decreased survival time is a direct result of decreased peptidoglycan thickness.

Discussion

P. mirabilis is commonly associated with complicated urinary tract infections, and are known to be linked to a higher rate of mortality in cases of bacteremia (42). Our findings indicate that the physiological changes associated with *P. mirabilis* swarmer cells come a fitness cost, due to a decrease in bacterial cell wall thickness (Figure 14). Changes in the thickness of the peptidoglycan layer are rarely witnessed. One of the few instances that we aware of is the increase in peptidoglycan thickness, in *Staphylococcus aureus*, that is associated with resistance to the drug vancomycin (43). This is a nice contrast to our finding that indicate a decrease in the thickness of the peptidoglycan layer increase the sensitivity of *P. mirabilis* and *V. parahaemolyticus* to cell wall targeting antibiotics.

Our work was enabled by the development of an updated tool for the measurement of bacterial cell mechanics. By developing a reloadable microfluidic device (Figure 8) we could rapidly determine the bending rigidity of swarming bacteria, a phenotype that is highly transient. We believe that this device will be incredibly enabling to the field of bacterial cell mechanics due to its low cost and ease of use, two factors that may have limited the study of bacterial cell mechanics to this point. One of the short-comings of this method is its inability to determine the mechanical properties of cells that do not undergo filamentous rod growth such as *S. aureus*.

We believe that these studies have shed further light onto the highly plastic nature of bacteria, when adapting to different lifestyles and environments. We believe that the changes we witnessed in *P. mirabilis* and *V. parahaemolyticus* are not rare in the environment and more likely are used as a way to combat physical and chemical environmental stresses, in addition to facilitating transient changes in bacterial lifestyles.

Figure 1. Reloadable microfluidic device design.

Bottom design is of the entire device including inlet, outlet, and vacuum inlet and the central bending chamber. Loading Channels inset: image of the central bending chamber, cells are loading into the 1st tier of channels, by vacuum force. Pillars (Vacuum Chamber) inset: pillars located in the vacuum chamber, to ensure that there is no collapse of chamber when vacuum is applied. Color green indicates 1st layer of device (1 μm thick). Color black indicates 2nd layer of device (25 μm thick).

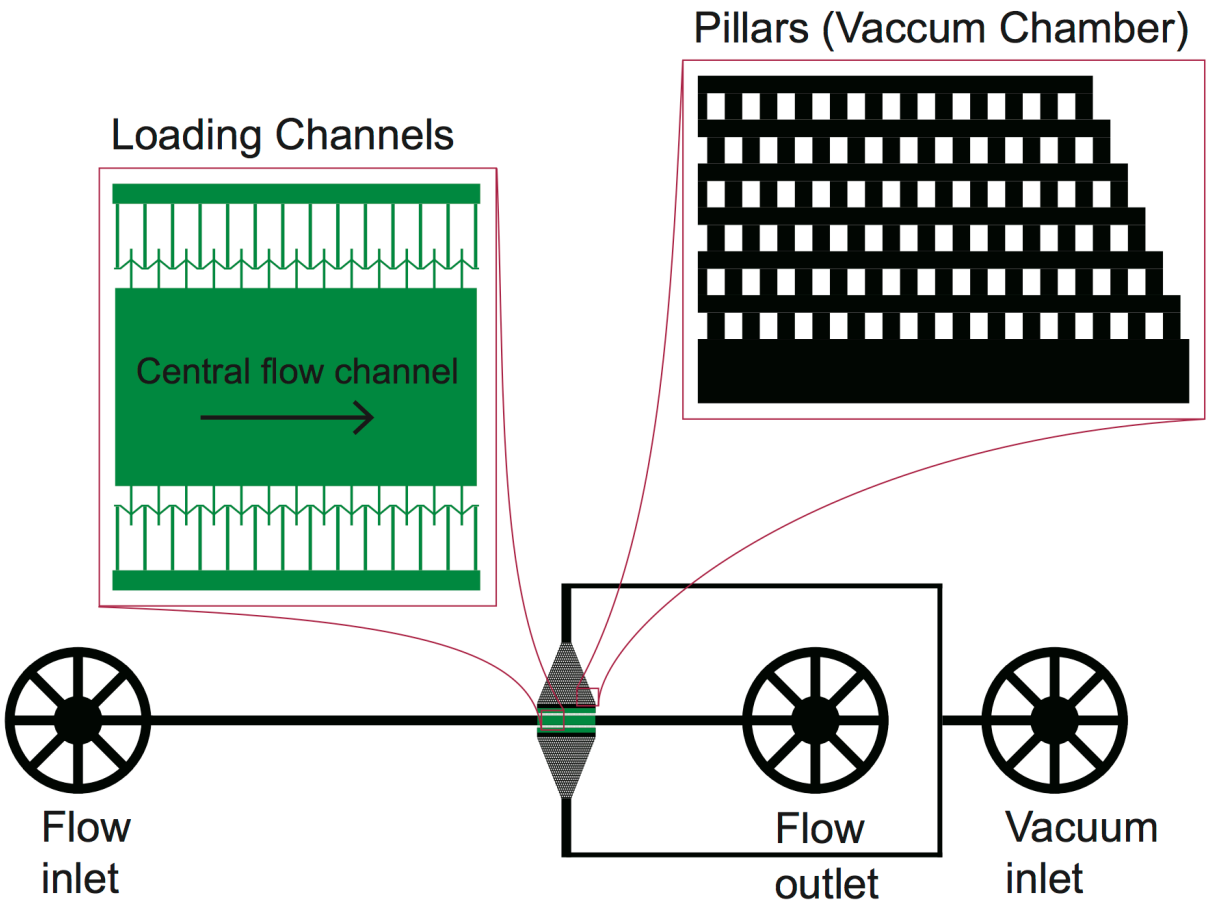
Pillars (Vaccum Chamber)
Loading Channels
Central flow channel
Flow
inlet
Flow
outlet
Vacuum
inlet

Figure 1

Figure 2. Assembly of microfluidic flow device.

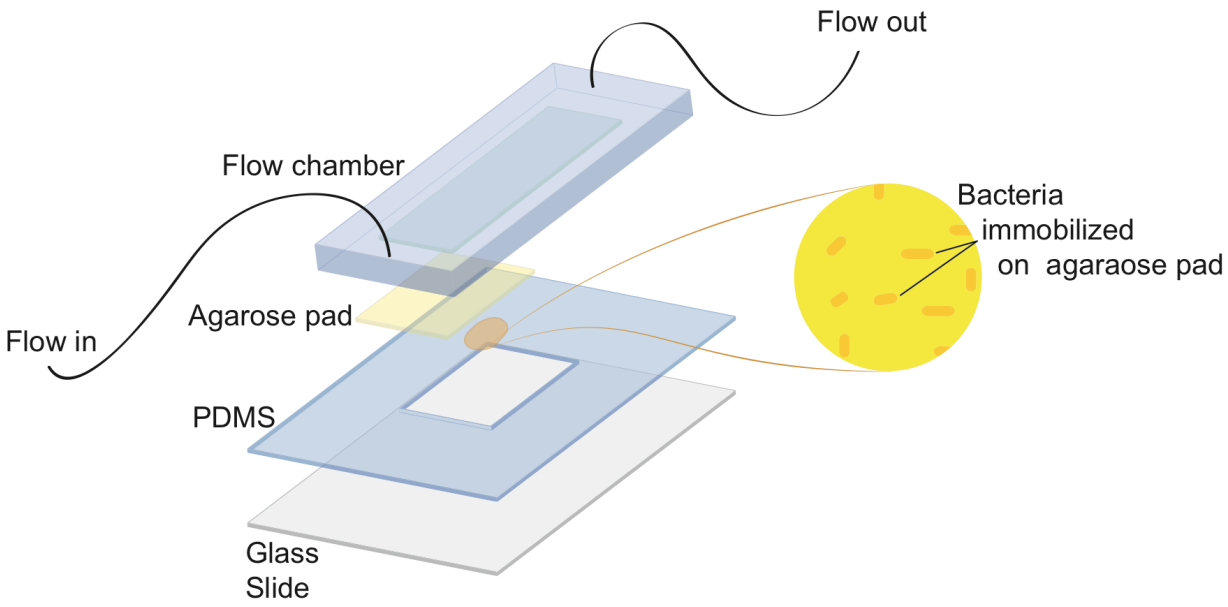
Flow out
Flow chamber
Bacteria
immobilized
on agaraose pad
Agarose pad
Flow in
PDMS
Glass
Slide

Figure 2

Figure 3. AFM images of *E.coli*, *P. mirabilis*, and *V. parahaemolyticus* sacculi. Field of view for sacculi imaged under ambient conditions. (A) *E. coli* vegetative, (B) *P. mirabilis* vegetative, (C) *P. mirabilis* swarmer, (D) *V. parahaemolyticus* vegetative, (E) *V. parahaemolyticus* swarmer. Scale bar = 1 μm.

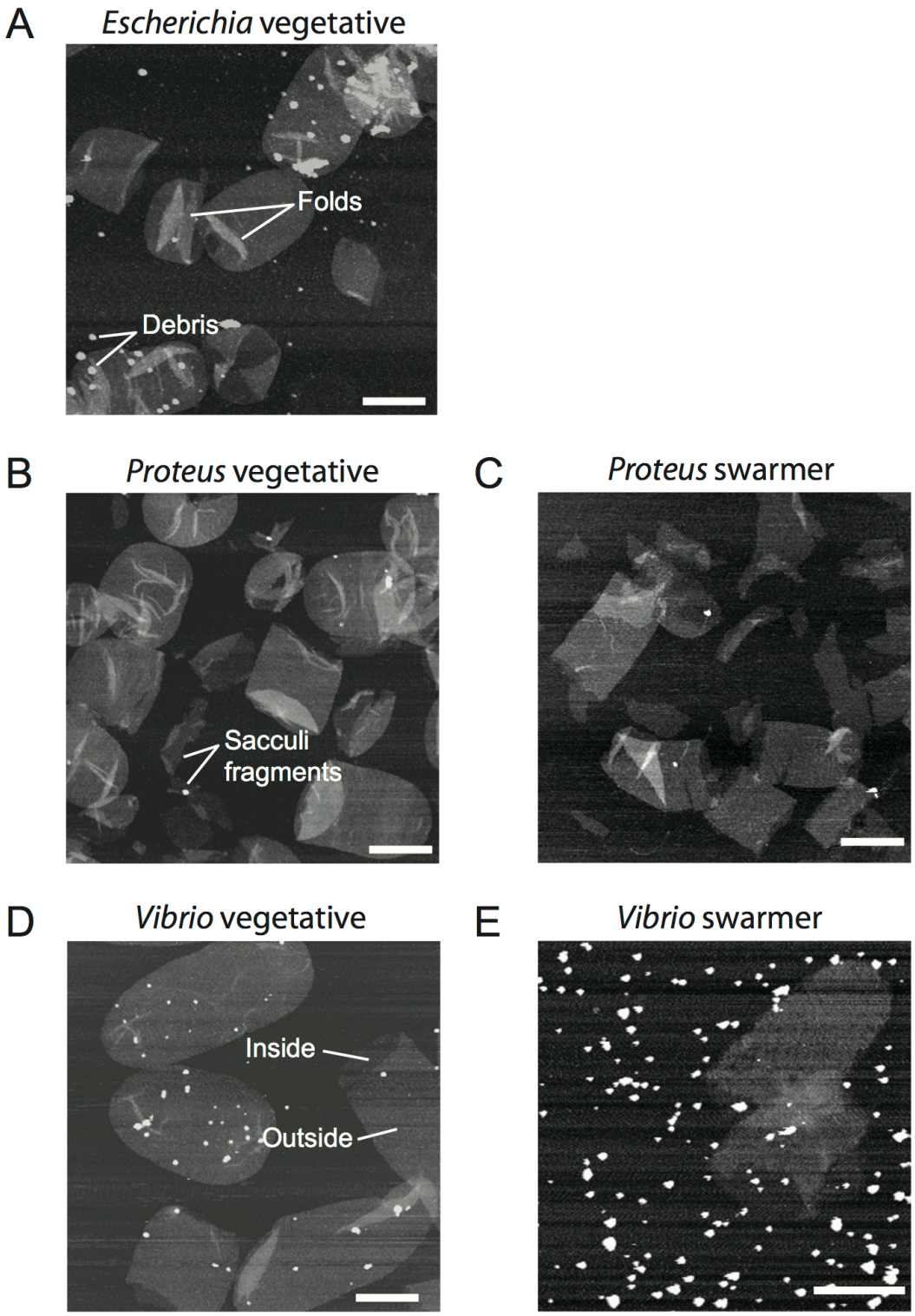
A
Escherichia vegetative
Folds
Debris
B
Proteus vegetative
Sacculi fragments
C
Proteus swarmer
D
Vibrio vegetative
Inside
Outside
E
Vibrio swarmer

Figure 3

Figure 4. Gravity flow setup used with reloadable bending microfluidics device.

Image of gravity flow set up assembled next to inverted microscope. VC-6 Channel valve controller is located outside of image. See methods for operation.

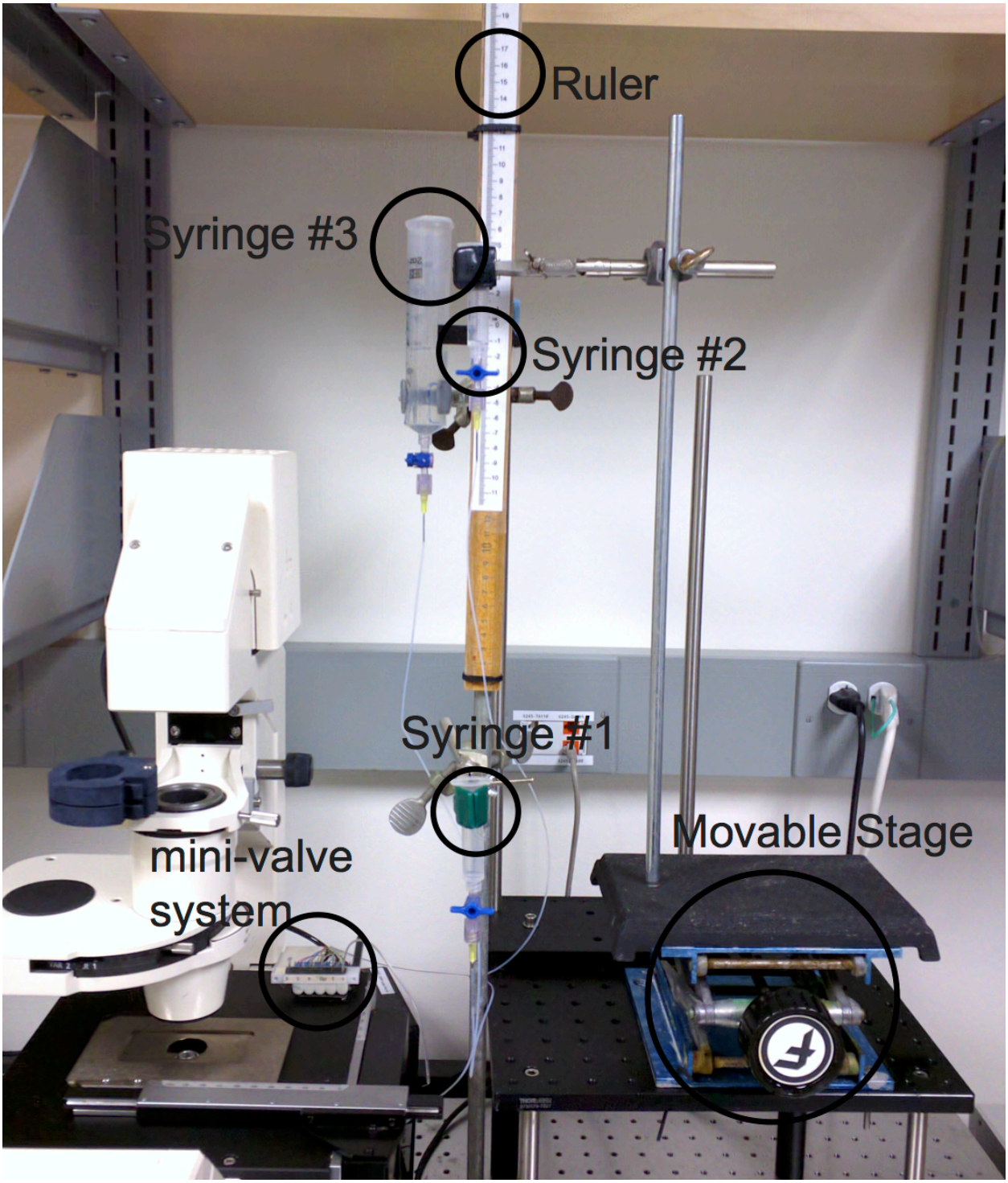
Ruler
Syringe #3
Syringe #2
Syringe #1
Movable Stage
mini-valve
system

Figure 4

Figure 5. Determination of the muropeptide stem by MS/MS. Interrogation of tetra peak (observed - 942.4036 m/z, calculated – 942.4155 m/z) by MS/MS of parent ion. MS/MS confirmed that *E. coli*, *P. mirabilis*, and *V. parahaemolyticus* muropeptide compositions are identical.

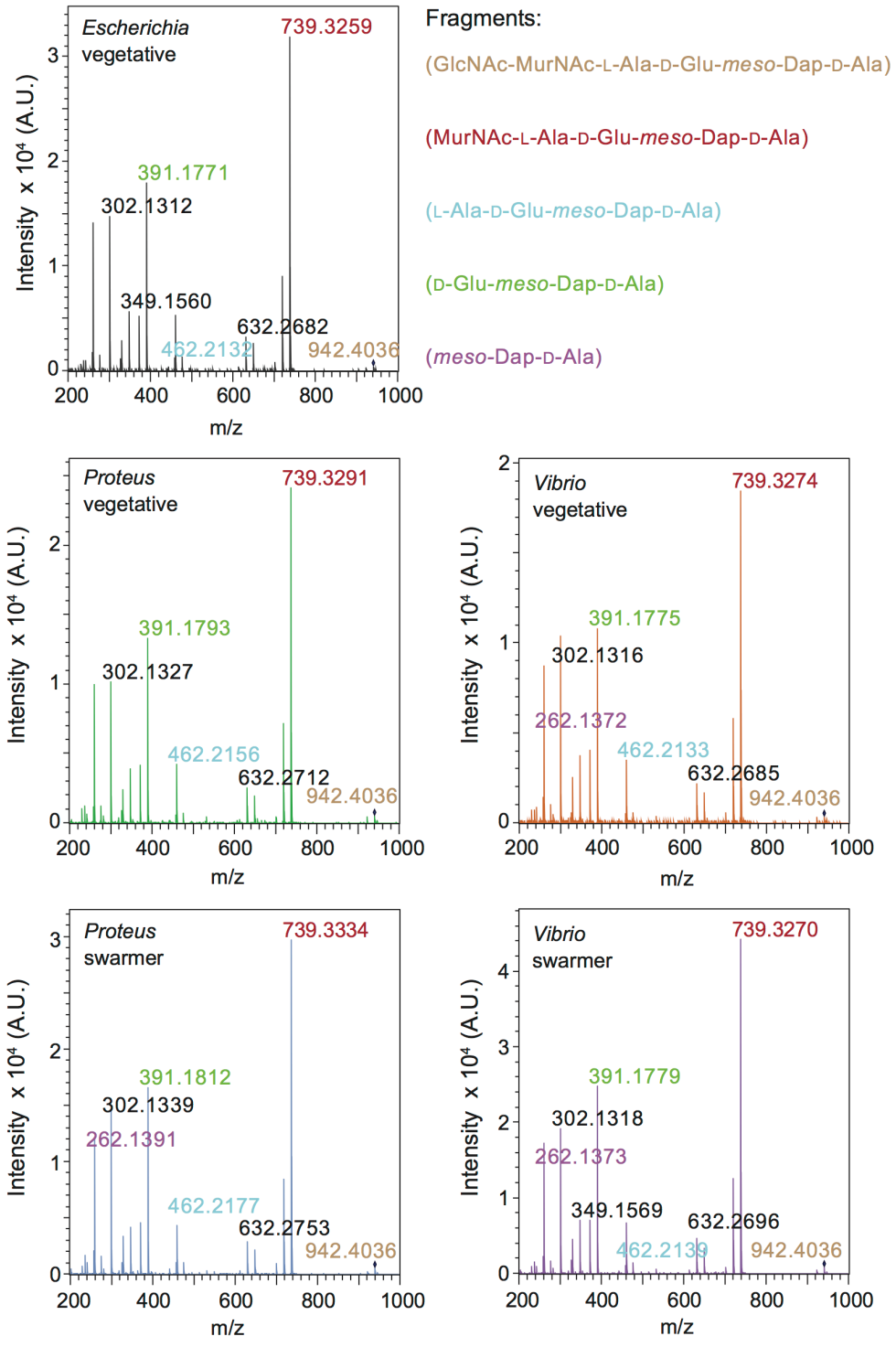
Escherichia
vegetative
739.3259
391.1771
302.1312
349.1560
632.2682
462.2132
942.4036
Fragments:
(GlcNAc-MurNAc-L-Ala-D-Glu-meso-Dap-D-Ala)
(MurNAc-L-Ala-D-Glu-meso-Dap-D-Ala)
(L-Ala-D-Glu-meso-Dap-D-Ala)
(D-Glu-meso-Dap-D-Ala)
(meso-Dap-D-Ala)
Proteus
vegetative
739.3291
391.1793
302.1327
462.2156
632.2712
942.4036
Vibrio
vegetative
739.3274
391.1775
302.1316
262.1372
462.2133
632.2685
942.4036
Proteus
swarmer
739.3334
391.1812
302.1339
262.1391
462.2177
632.2753
942.4036
Vibrio
swarmer
739.3270
391.1779
302.1318
262.1373
349.1569
632.2696
462.2139
942.4036
Intensity x 10⁴ (A.U.)
m/z

Figure 5

Figure 6. UPLC/MS of muropeptides for vegetative and swarmer cells.

Chromatograms of purified cell wall from *E. coli, P. mirabilis, V. parahaemolyticus* vegetative cells; and *P. mirabilis*, *V. parahaemolyticus* swarmer cells. Cell walls were purified and digested and analyzed by UPLC/MS. Identified peaks provided in Table 1. Quantification of peaks is shown in Figure 6.

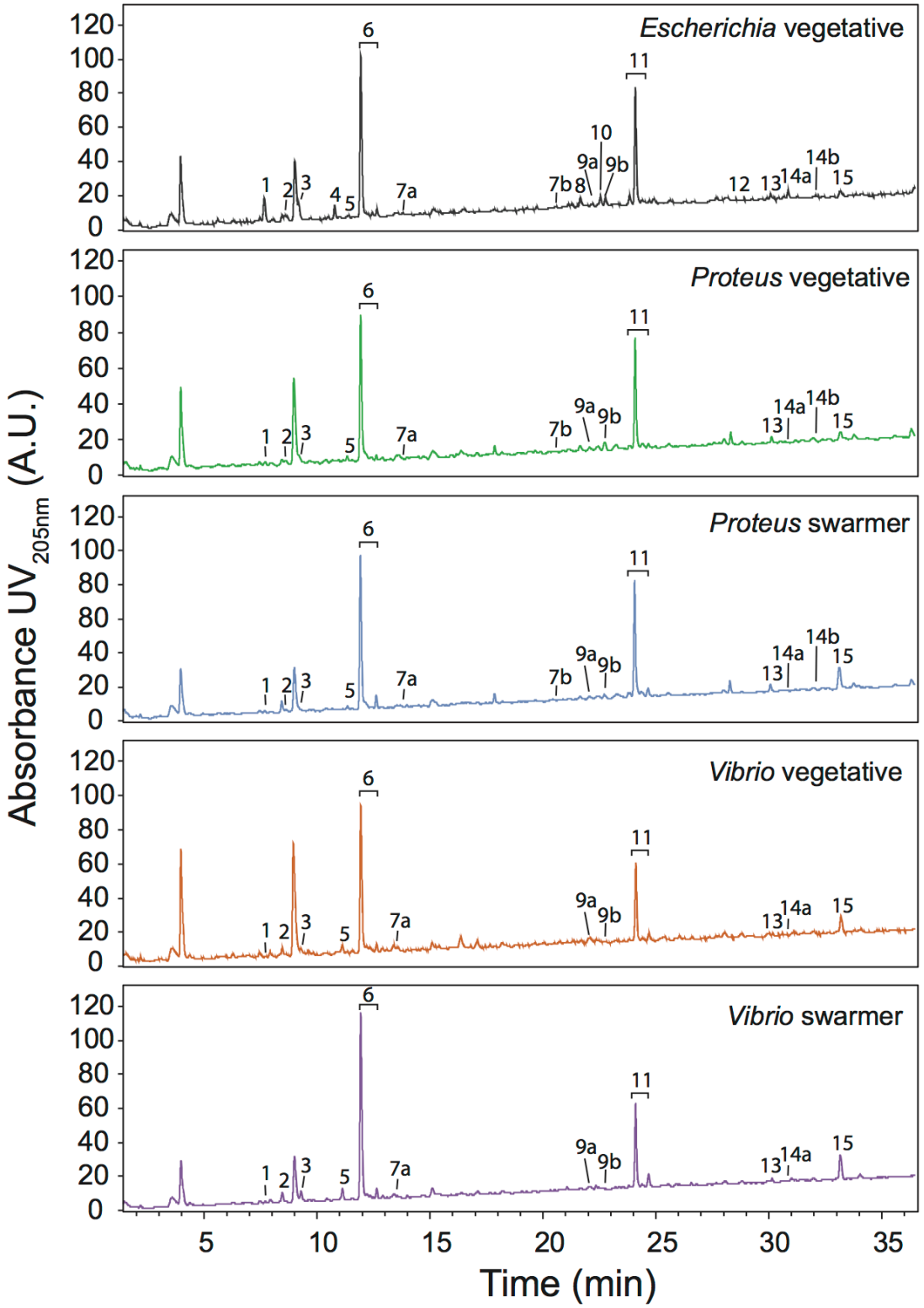
Escherichia vegetative
Proteus vegetative
Proteus swarmer
Vibrio vegetative
Vibrio swarmer
Absorbance UV205nm (A.U.)
Time (min)
1
2
3
4
5
6
7a
7b
8
9a
9b
10
11
12
13
14a
14b
15

Figure 6

Figure 7. *P. mirabilis* and *V. parahaemolyticus* swarmer cell flexibility.

A) Time-series of *P. mirabilis* swarmer cells in a colony actively moving across the surface of a 1.5% agarose gel. A representative cell, false colored green, is relatively linear at t=0 s, and is bent in half at t=1.46 s. Most of the cells in this frame are bending during this imaging sequence.

B) A time-series of *V. parahaemolyticus* swarmer cells in a colony actively moving across the surface of a 1.4% agarose gel. A representative cell (false colored purple) is approximately linear at t=0 s and is bent in half at t=6.02 s.

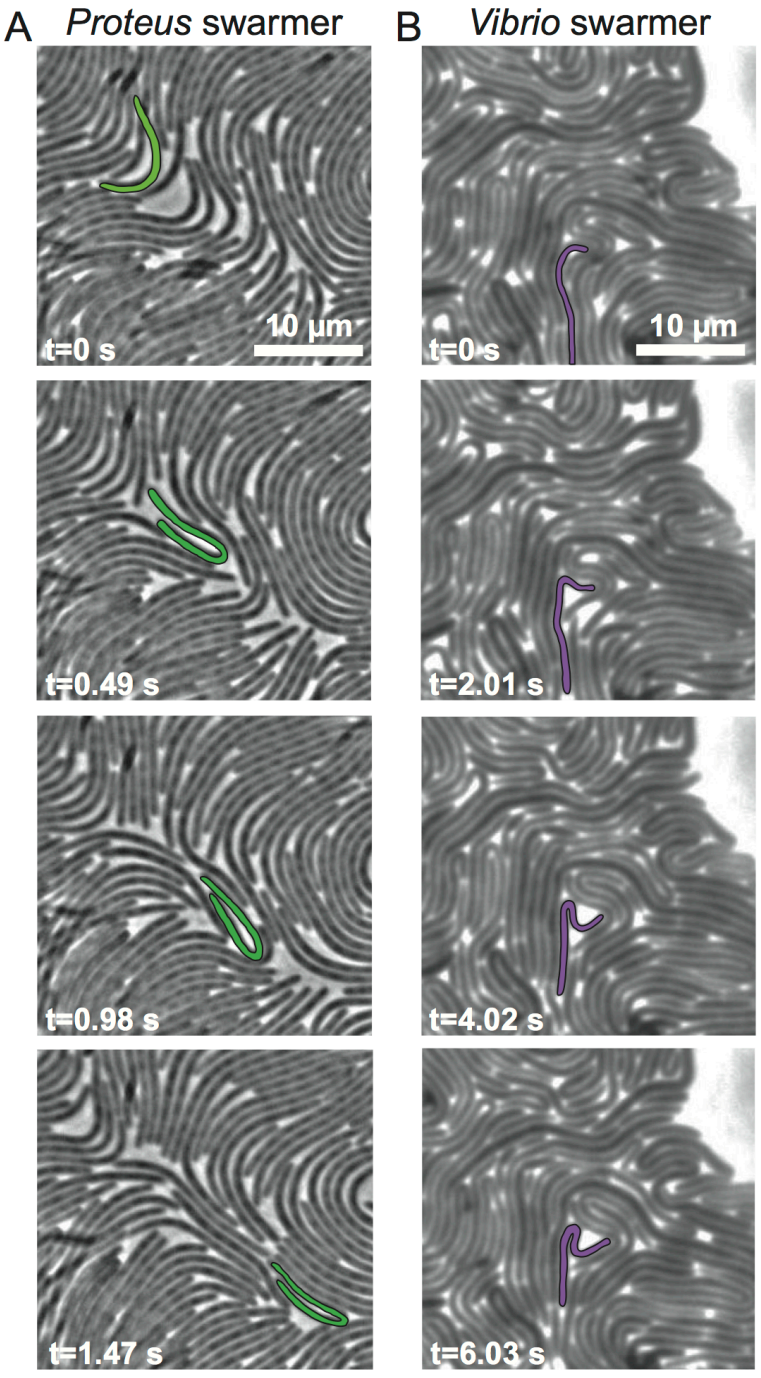
A Proteus swarmer
B Vibrio swarmer
10 µm
t=0 s
10 µm
t=0 s
t=0.49 s
t=2.01 s
t=0.98 s
t=4.02 s
t=1.47 s
t=6.03 s

Figure 7

Figure 8. Reloadable microfluidic-based assay to determine bacterial cell stiffness.

A) Schematic of the microfluidic channel used to apply a user-defined shear force to bend filamentous cells. Single-sided green arrows depict the flow of fluid through the central channel; the parabolic flow profile of the fluid is shown. Double-sided green arrows mark the vacuum chamber used to load cells into side channels and to empty the device.

B) Cartoon of a flexible bacterium (left) and a stiff bacterium (right) under flow force (V_{flow}). X_{max} indicates the deflection of cells in the flow; 2r = cell diameter; L = cell length in contact with the flow force.

C) Representative images of filamentous cells of *P. mirabilis* in no flow (left) and flow (right) conditions (top) and *P. mirabilis* swarmers (bottom). Purple dashed lines indicate the position of a cell tip under no flow conditions and black dashed lines illustrate the position after flow is applied using a gravity-fed mechanism. The arrow indicates the direction of fluid flow in the channel.

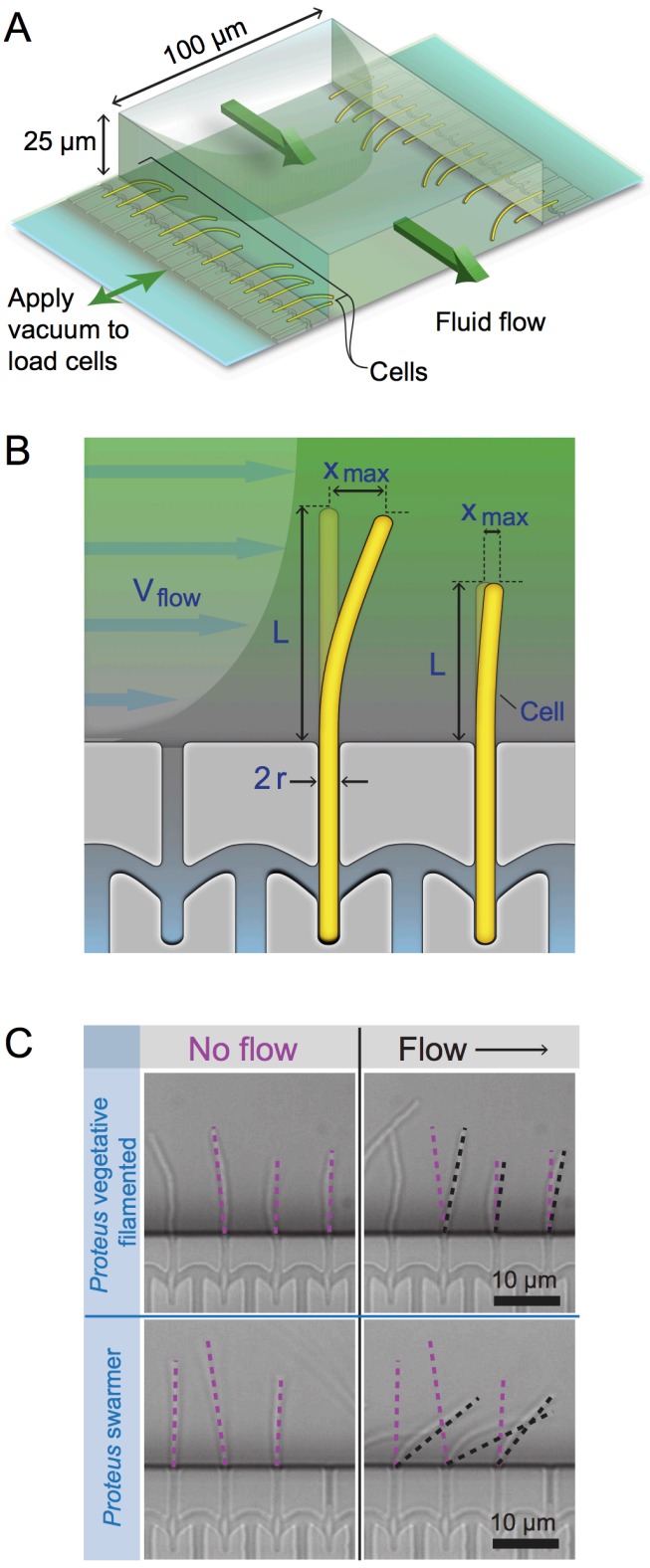
A
100 µm
25 µm
Apply
vacuum to
load cells
Cells
Fluid flow
B
x max
x max
V flow
L
L
Cell
2 r
C
No flow
Flow
Proteus vegetative
filamented
Proteus swarmer
10 µm
10 µm

Figure 8

Figure 9. Deflection of vegetative filamented and swarmer cells immediately after flow-induced bending in microfluidic device.

Circles represent the deflection value of individual cells under flow. (A) *E. coli* vegetative, (B) *P. mirabilis* vegetative, (C) *P. mirabilis* swarmer, (D) *V. parahaemolyticus* vegetative, (E) *V. parahaemolyticus* swarmer. Greater deflections, (Figure S6C, E) indicate a decrease in cell stiffness. Black line represents fit of our model (see methods) to the data, in order to determine the flexural rigidity. $n > 200$ cells, from at least 2 independent experiments).

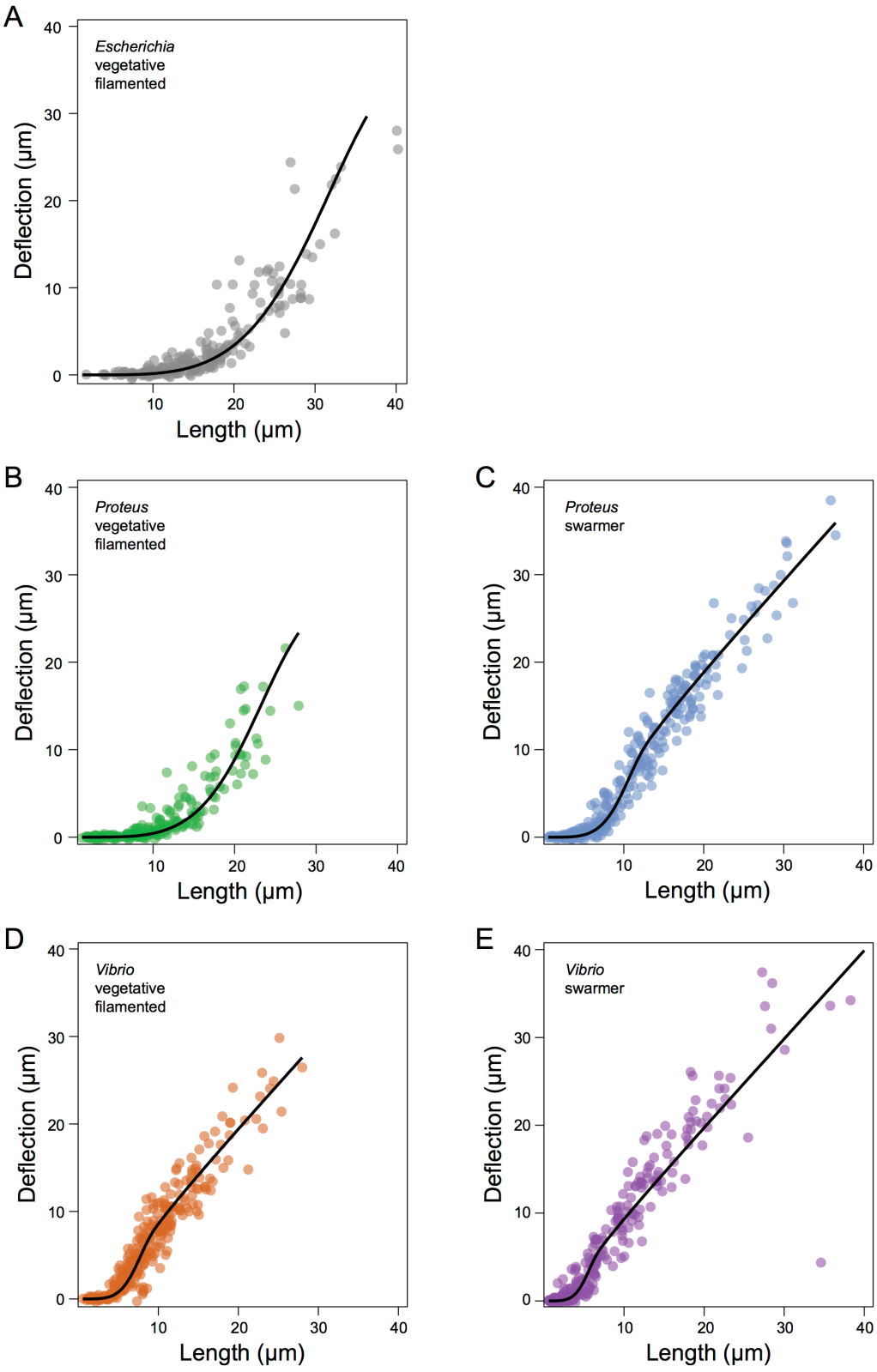
A
Escherichia
vegetative
filamented
B
Proteus
vegetative
filamented
C
Proteus
swarmer
D
Vibrio
vegetative
filamented
E
Vibrio
swarmer
Deflection (µm)
Length (µm)
0
10
20
30
40

Figure 9

Figure 10. Division time for vegetative and swarmer cells grown at 30°C.

A) *V. parahaemolyticus* vegetative cells have a faster division time compared to *E.coli* and *P. mirabilis*. The division time of vegetative cells. $n > 100$ cells, from at least 3 independent experiments. Points represent the division time of single cells. Box plot is representative of media, 1st and 3rd quartiles ("hinges"), and the 95% confidence interval of the median ("notches").

B) The onset of division in *P. mirabilis* swarmer cells is slower than *V. parahaemolyticus* cells, but the time between division (division time interval) is lesser. Multiple division sites could be present on a single swarmer cell, and simultaneous division at 2 sites did occur. If simultaneous division occurred at two sites; one division time interval was designated as 0 min. The 2nd, 3rd, and 4th division time interval was calculated as (2nd Division = 1st division time - 2nd division time). $n >100$ cells at time of 1st division. Points represent the division time of single cells. Box plot is representative of media, 1st and 3rd quartiles ("hinges"), and the 95% confidence interval of the median ("notches").

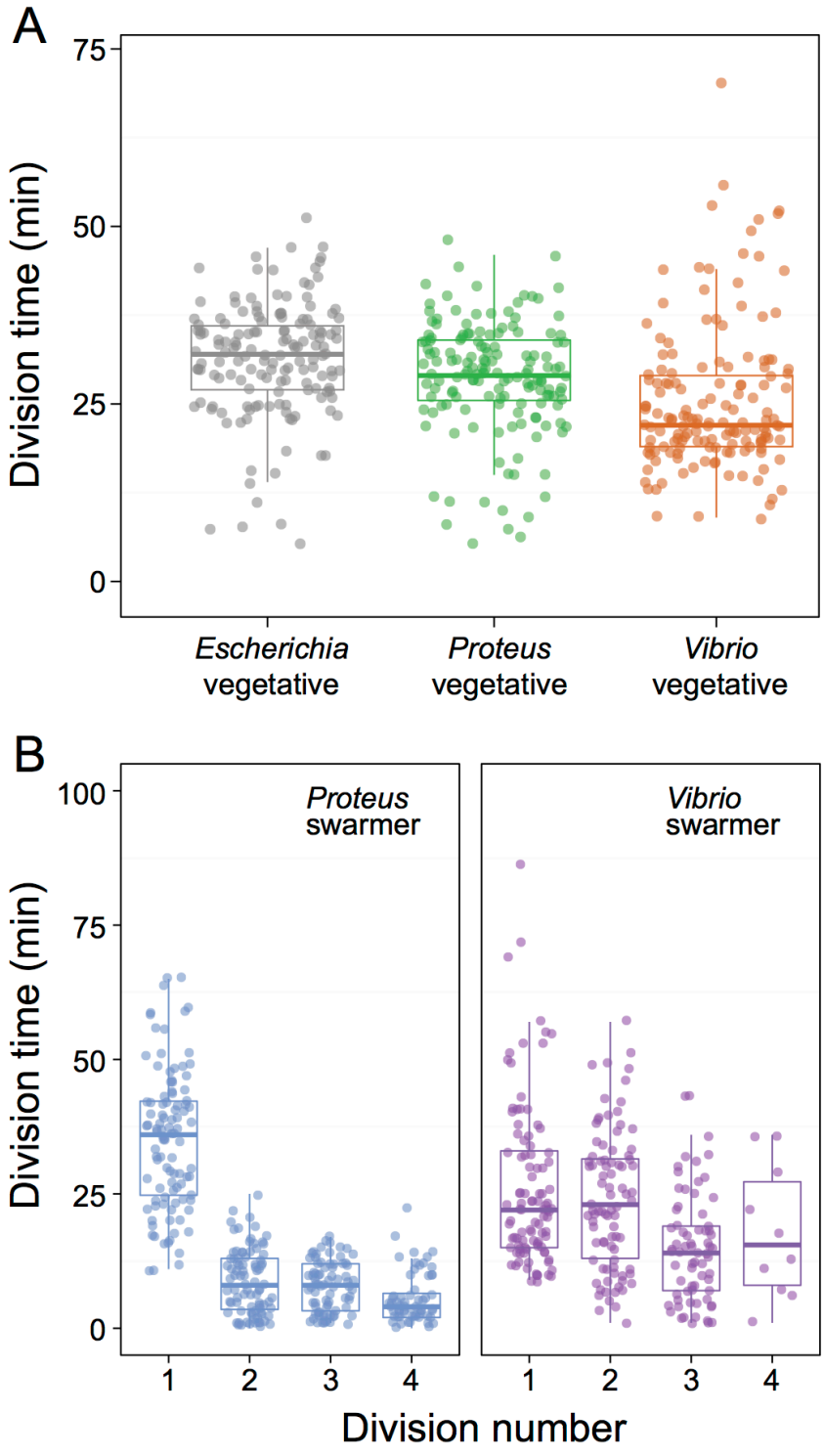
A
Division time (min)
75
50
25
0
Escherichia vegetative
Proteus vegetative
Vibrio vegetative
B
Division time (min)
100
75
50
25
0
Proteus swarmer
Vibrio swarmer
1
2
3
4
Division number

Figure 10

Figure 11. *P. mirabilis* and *V. parahaemolyticus* swarmer cells have less bending rigidity than vegetative cells.

We measured the bending rigidity of *P. mirabilis* and *V. parahaemolyticus* swarmer cells and filamentous vegetative cells in a microfluidic flow assay and included measurements of vegetative *E. coli* cells as a control. *P. mirabilis* swarmers exhibited 15-fold less bending rigidity than vegetative cells; *V. parahaemolyticus* swarmers were 3-fold less rigid than vegetative cells. Overexpression of FlhDC (from the plasmid-encoded element *pflhDC*) had little effect on the stiffness of *P. mirabilis* vegetative and swarmer cells. Error bars represent the 95% confidence interval of a fit to data. $n > 100$ cells, from at least three independent experiments.

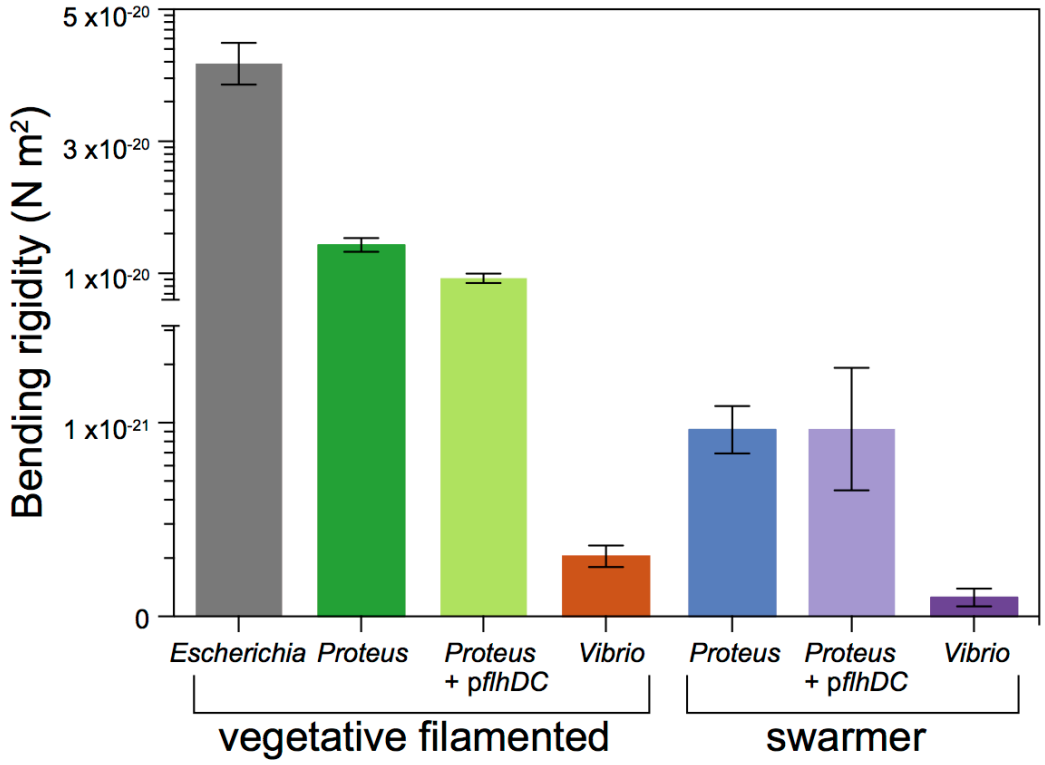
5 x10-20
3 x10-20
1 x10-20
1 x10-21
0
Bending rigidity (N m2)
Escherichia
Proteus
Proteus + pflhDC
Vibrio
Proteus
Proteus + pflhDC
Vibrio
vegetative filamented
swarmer

Figure 11

Figure 12. Flexural rigidity of *E. coli* is unaffected by treatment aztreonam or by increases in flagella density.

A) Bending rigidity isn't affected by filamentation with aztreonam. Flexural rigidity of wild-type *E. coli* MG1655 cells filamented by expression of *SulA* (green) or treatment with aztreonam (gray). Flexural rigidity of cells was determined by fitting deflection data (Methods) from microfluidic-based bending assay.

B) Bending rigidity isn't affected by an increase in number of flagella on the cell body. Flexural rigidity of cells filamented with aztreonam. Wild-type *E. coli* MG1655 (gray) and isolated *E.* coli MG1655 that exhibit increased flagella density (red), see Fig S6C. Flexural rigidity of cells was determined by fitting deflection data (Methods) from microfluidic-based bending assay. For all measurements, we performed $n > 100$ cells. Error bars represent 95% confidence interval.

C) Immunofluorescence image of wild-type *E. coli* MG1655 (top panel) and isolated *E. coli* MG1655 with increased flagella density (bottom panel) filamented with aztreonam. Flagella were labeled with anti-FliC primary antibody and an Alexa Fluor 488 conjugated secondary antibody. Scale bar = 10 μm

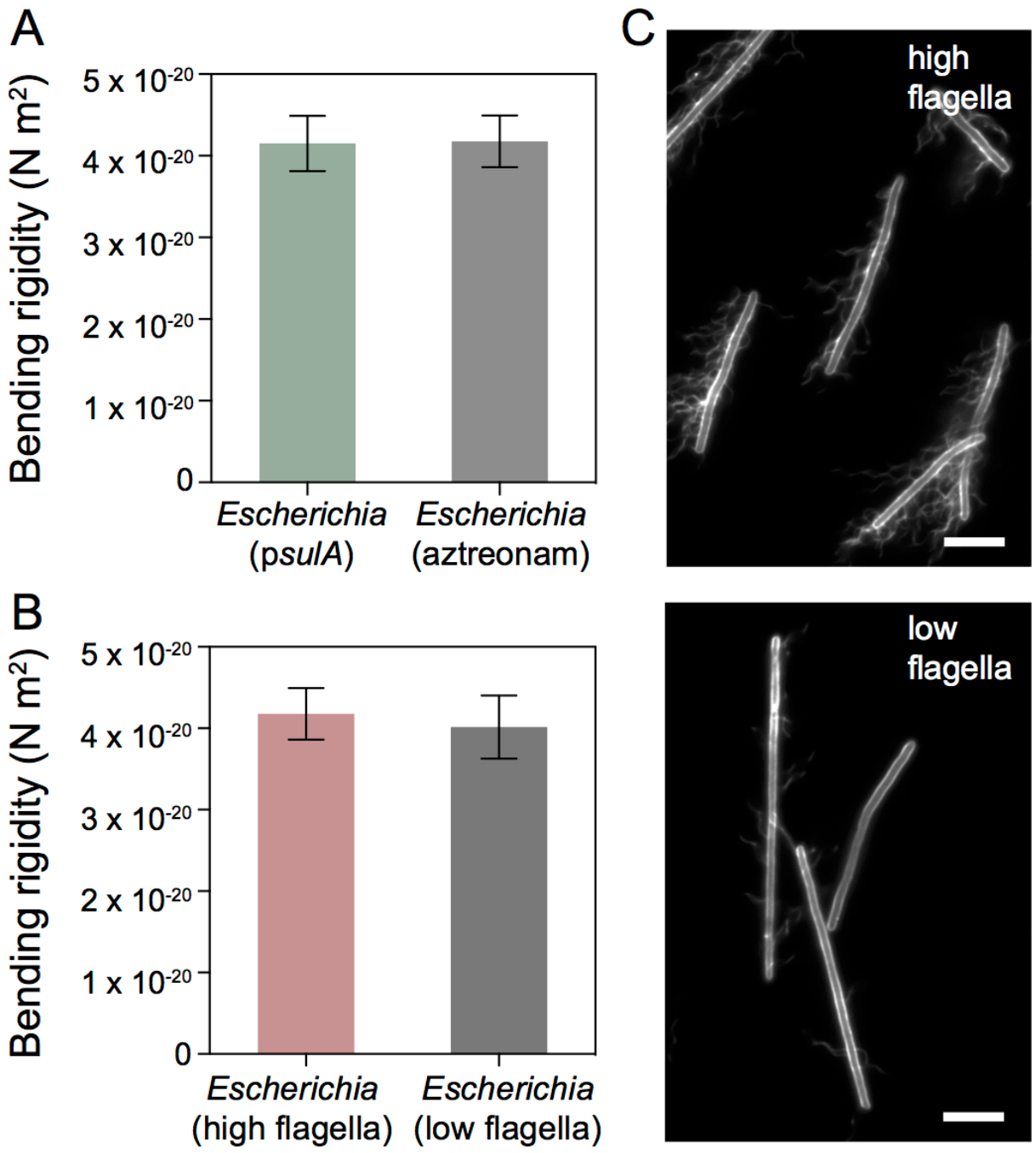
A
Bending rigidity (N m²)
5 x 10-20
4 x 10-20
3 x 10-20
2 x 10-20
1 x 10-20
0
Escherichia (psulA)
Escherichia (aztreonam)
B
Bending rigidity (N m²)
5 x 10-20
4 x 10-20
3 x 10-20
2 x 10-20
1 x 10-20
0
Escherichia (high flagella)
Escherichia (low flagella)
C
high flagella
low flagella

Figure 12

Figure 13. Differences in the peptidoglycan muropeptide composition of *P. mirabilis* and *V. parahaemolyticus* vegetative and swarmer cells.

A) UPLC-MS data reveal that the muropeptide composition of *P. mirabilis* and *V. parahaemolyticus* vegetative and swarmer cells differs slightly in the abundance of monomer, dimer, and anhydrous-terminated saccharides. Significance was determined via two-way analysis of variance: *P ≤ 0.05, **P ≤ 0.01, ***P ≤ 0.001, ****P ≤ 0.0001, ns = not significant (P > 0.05).

B) We observed that the relative increase in the amount of anhydrous-containing saccharides in swarmers produces a decrease in the polysaccharide strand length. Significance was determined via one-way analysis of variance and defined as in (*A*).

C) There was no change in peptidoglycan cross-linking of *P. mirabilis* and *V. parahaemolyticus* vegetative and swarmer cells, although *V. parahaemolyticus* does display a lower level of cross-linking. Significance was determined via one-way analysis of variance and defined as in (*A*). For all measurements, we performed $n = 3$ biological replicates. Error bars represent the standard deviation of the mean.

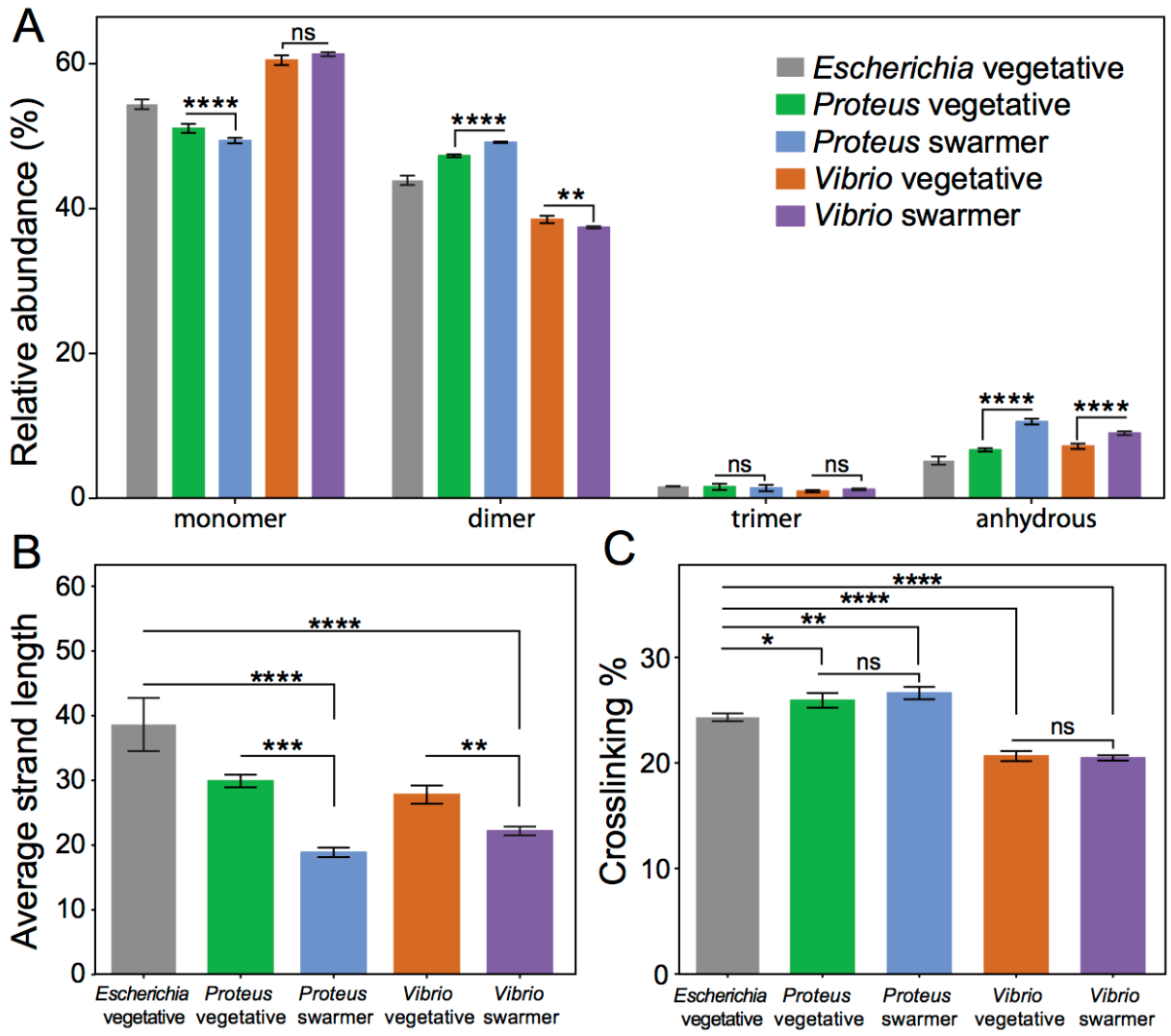
A
Relative abundance (%)
60
40
20
0
ns
****
****
**
ns
ns
****
****
monomer
dimer
trimer
anhydrous
Escherichia vegetative
Proteus vegetative
Proteus swarmer
Vibrio vegetative
Vibrio swarmer
B
Average strand length
60
50
40
30
20
10
0
****
****
***
**
Escherichia vegetative
Proteus vegetative
Proteus swarmer
Vibrio vegetative
Vibrio swarmer
C
Crosslinking %
30
20
10
0
****
****
**
*
ns
ns
Escherichia vegetative
Proteus vegetative
Proteus swarmer
Vibrio vegetative
Vibrio swarmer

Figure 13

Figure 14. AFM and ECT reveal that the peptidoglycan layer of *P. mirabilis* and *V. parahaemolyticus* swarmer cells is thinner than that of vegetative cells

A) Sacculi were isolated from cells and imaged via AFM. Sacculi from swarmer cells had lower peptidoglycan thickness, which correlates with cell bending rigidity measurements. We analyzed $n > 65$ vegetative cells of *E. coli*, *P. mirabilis*, and *V. parahaemolyticus*, $n > 65$ *P. mirabilis* swarmer cells, and $n = 7$ *V. parahaemolyticus* swarmer cells. Error bars represent the standard deviation of the mean.

B) Bending rigidity and cell-wall thickness display an approximately linear relationship.

C) Sub-tomogram-averaged ECT volume images of the *P. mirabilis* vegetative (left) and swarmer (right) cell wall. Two central slices of sub-tomogram average volume images with normalized image densities are shown. Yellow dashed line indicates the orientation used for gray-value measurement. ES, extracellular space; OM, outer membrane; PG, peptidoglycan; IM, inner membrane; CP, cytoplasm.

D) The density profile of sub-tomogram-averaged cryo-EM volume images reveals that swarmer cells have less thick peptidoglycan layers. The vertical axis is the normalized gray value with the darkest value equal to 0 and the lightest value equal to 1. The red dashed line denotes the average gray value of the extracellular space and serves as a reference for the background; the blue shaded area indicates the thickness of the peptidoglycan layer.

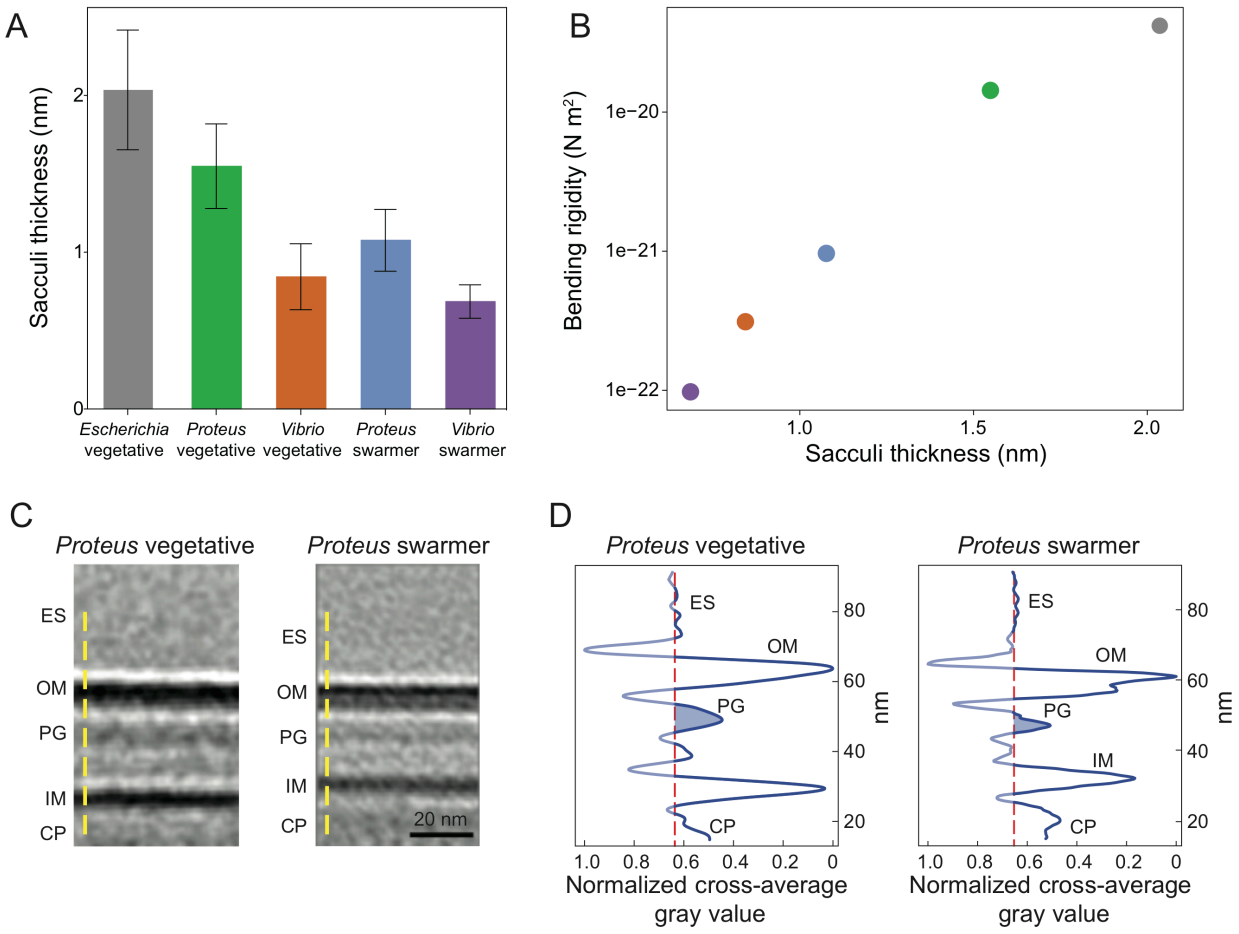
A
Sacculi thickness (nm)
2
1
0
Escherichia vegetative
Proteus vegetative
Vibrio vegetative
Proteus swarmer
Vibrio swarmer
B
Bending rigidity (N m²)
1e−20
1e−21
1e−22
1.0
1.5
2.0
Sacculi thickness (nm)
C
Proteus vegetative
Proteus swarmer
ES
OM
PG
IM
CP
20 nm
D
Proteus vegetative
Proteus swarmer
ES
OM
PG
IM
CP
80
60
40
20
nm
1.0 0.8 0.6 0.4 0.2 0
Normalized cross-average gray value

Figure 14

Figure 15. Cryo-EM of *P. mirablis* vegetative and swarmer cells reveals decreased membrane stability. *P. mirabilis* vegetative cells (A, B) have a smooth outer membrane, but display an increase in the distance between the inner and outer membrane, including a drastically increased membrane distance at the poles (polar endcap). Swarmer cells (C-F) display a smooth lateral wall membrane (C, D) and a ruffled outer membrane near the pole (E, F) indicating a decrease in the membrane stability; there were no polar endcaps observed. Representative features are indicated in the figure.

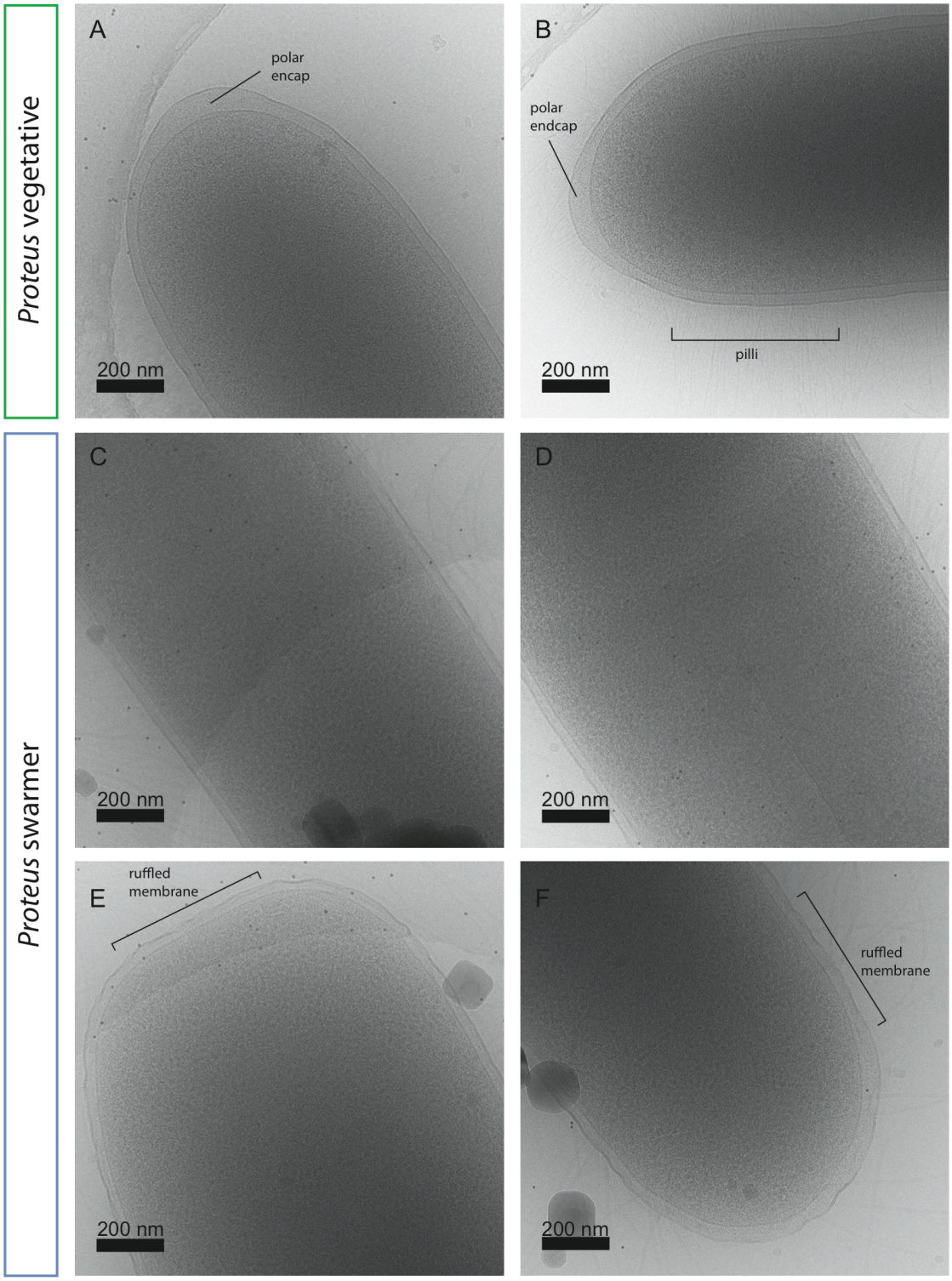
Proteus vegetative
Proteus swarmer
A
polar
encap
200 nm
B
polar
endcap
pilli
200 nm
C
200 nm
D
200 nm
E
ruffled
membrane
200 nm
F
ruffled
membrane
200 nm

Figure 15

Figure 16. Cryo-EM of *V. parahaemolyticus* vegetative and swarmer cells reveals possible changes in cell stability. *V. parahaemolyticus* vegetative cells (A, B) have a smooth outer membrane. While *V. parahaemolyticus* swarmer cells (C-F) also displayed smooth outer membrane (C) there were cells within the population that showed drastic changes membrane integrity (D-F) including membrane budding and vesicle formation. Ruptures in the cell wall (C) and variable cell diameter (E, F) were also observed. It could not be determined if the features observed for *V. parahaemolyticus* swarmer cells were the result of sensitivity to blotting pressures used when preparing the grids (D-F). Representative features are indicated in the image.

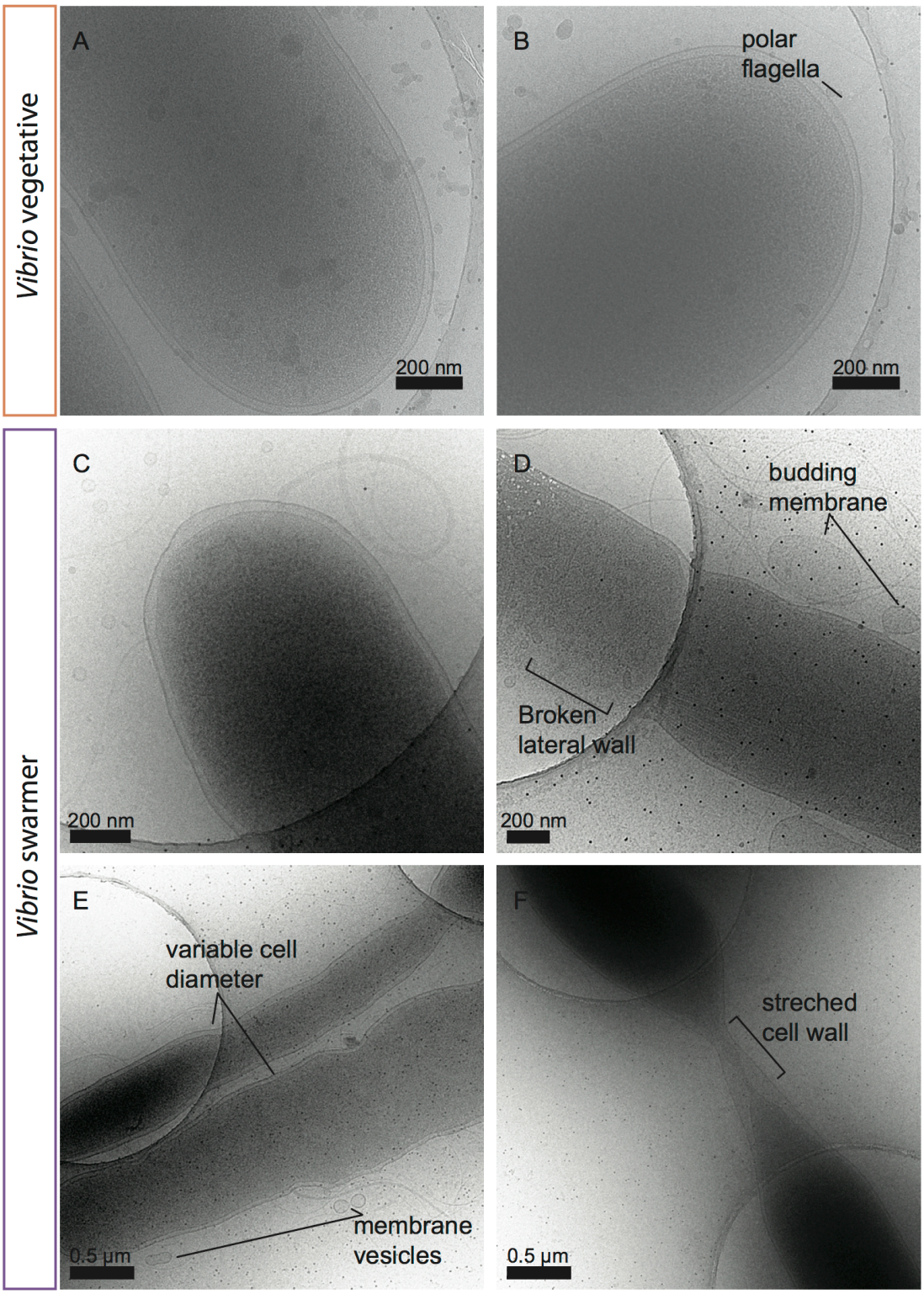
Vibrio vegetative
A
200 nm
B
polar
flagella
200 nm
Vibrio swarmer
C
200 nm
D
budding
membrane
Broken
lateral wall
200 nm
E
variable cell
diameter
membrane
vesicles
0.5 µm
F
streched
cell wall
0.5 µm

Figure 16

Figure 17. Vegetative filamented and swarmer cells elongation pressured by osmotic shock.

A) Vegetative filamented cells and swarmer cells exposed to hypotonic (pure ddH_2O) and hypertonic (1M NaCl) conditions to induce changes in cell elongation by increasing and decreasing turgor pressure, respectively. Scale bar = 10 μm.

B) Idealized response of cells under osmotic shock to facilitate changes in cell length, arrows indicate direction of turgor pressure in the cell.

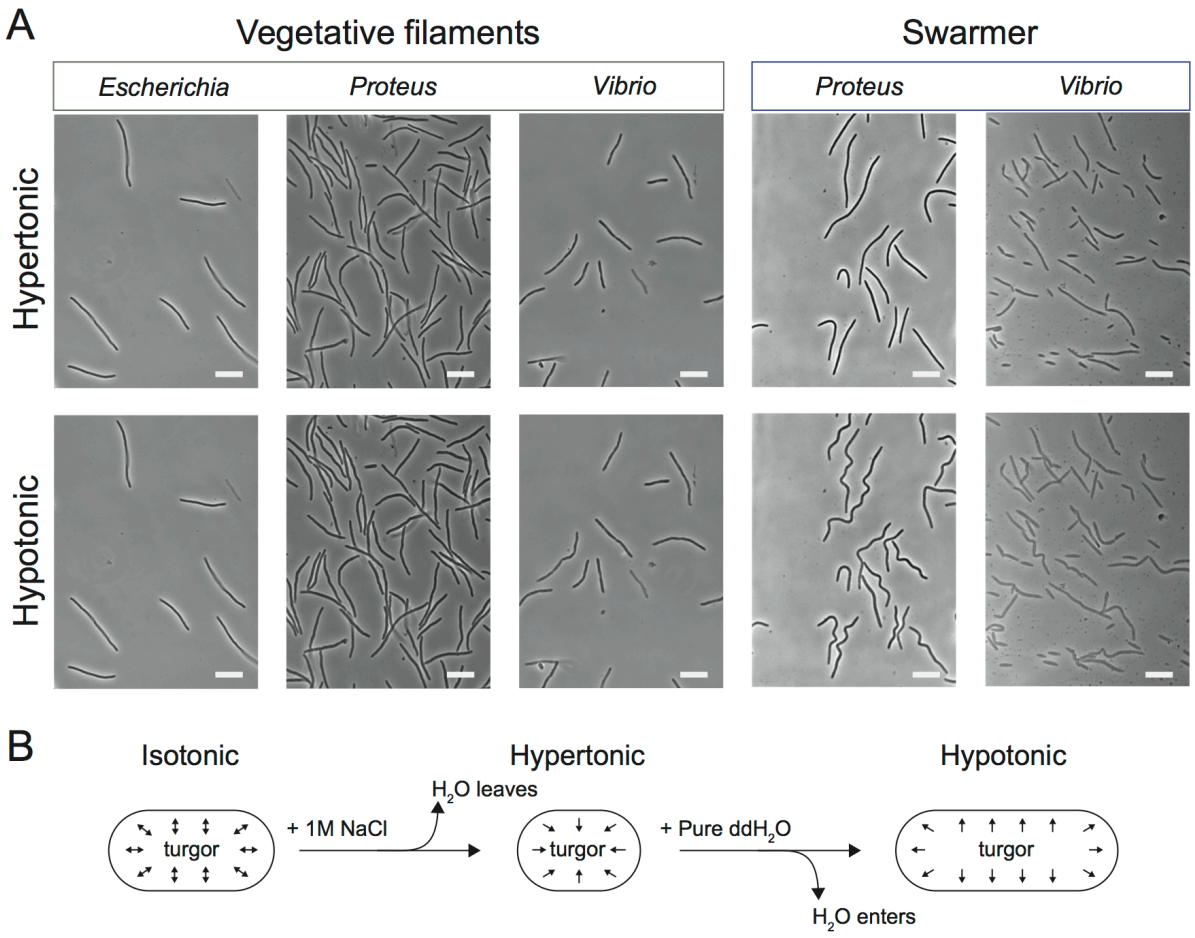
A
Vegetative filaments
Swarmer
Escherichia
Proteus
Vibrio
Proteus
Vibrio
Hypertonic
Hypotonic
B
Isotonic
Hypertonic
Hypotonic
turgor
+ 1M NaCl
H2O leaves
turgor
+ Pure ddH2O
H2O enters
turgor

Figure 17

Figure 18. Swarmer cells increase in cell extension during osmotic shock.

We calculated ΔL as (cell length in water – cell length in 1 M NaCl) and performed a similar calculation for ΔW, substituting cell width. Cell length indicates length prior to osmotic shock. We filamented all vegetative cells using aztreonam to grow them to lengths that were comparable with those of *P. mirabilis* and *V. parahaemolyticus* swarmers. Lines indicate linear fits to single-cell measurements (circles) of $n > 100$ cells from at least three independent experiments.

A) *P. mirabilis* swarmer cells have an increase in extension (ΔL) under osmotic shock compared to *E. coli* and *P. mirabilis* vegetative cells.

B) *V. parahaemolyticus* vegetative and swarmer cells have an increase in extension (ΔL) under osmotic shock compared to *E. coli*.

C) *P. mirabilis* swarmer cells have an increase in ΔW compared to *E. coli; P. mirabilis* vegetative cells display a slight decrease in width and increased cell length.

D) The ΔW of *V. parahaemolyticus* swarmer and vegetative cells changes with increased cell length.

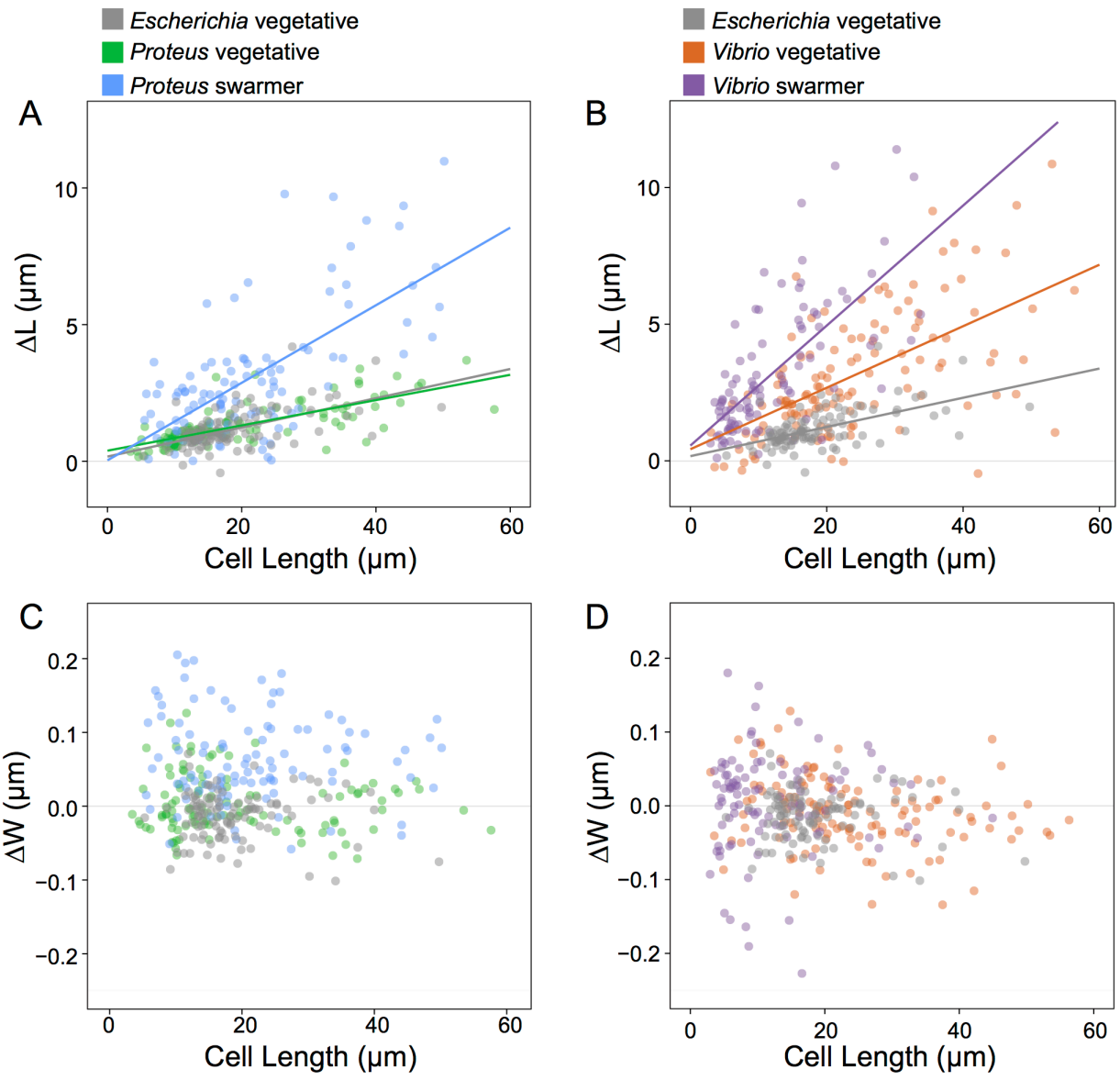
Escherichia vegetative
Proteus vegetative
Proteus swarmer
A
ΔL (μm)
Cell Length (μm)
Escherichia vegetative
Vibrio vegetative
Vibrio swarmer
B
ΔL (μm)
Cell Length (μm)
C
ΔW (μm)
Cell Length (μm)
D
ΔW (μm)
Cell Length (μm)

Figure 18

Figure 19. Swarmer cells are more susceptible to antibiotics that target the cell wall than are vegetative cells.

A) Survival of cells treated with 1X MIC of cephalexin after 3 h of incubation. We define percent survival as (cell $count_{no\ lysis}$ / cell $count_{total}$) x 100. *P. mirabilis* and *V. parahaemolyticus* swarmer cells exhibit decreased levels (~30%) of survival compared to vegetative cells; $n \geq 90$ cells from at least two independent experiments. A similar decrease occurred when *P. mirabilis* was treated with penicillin G; $n \geq 77$ cells from at least two independent experiments).

B) After exposure to cephalexin or penicillin G, the survival time of *P. mirabilis* and *V. parahaemolyticus* swarmers was 2~3 fold lower than that of vegetative cells. Survival time was determined for cells that lysed; $n \geq 49$ cells, from at least two independent experiments.

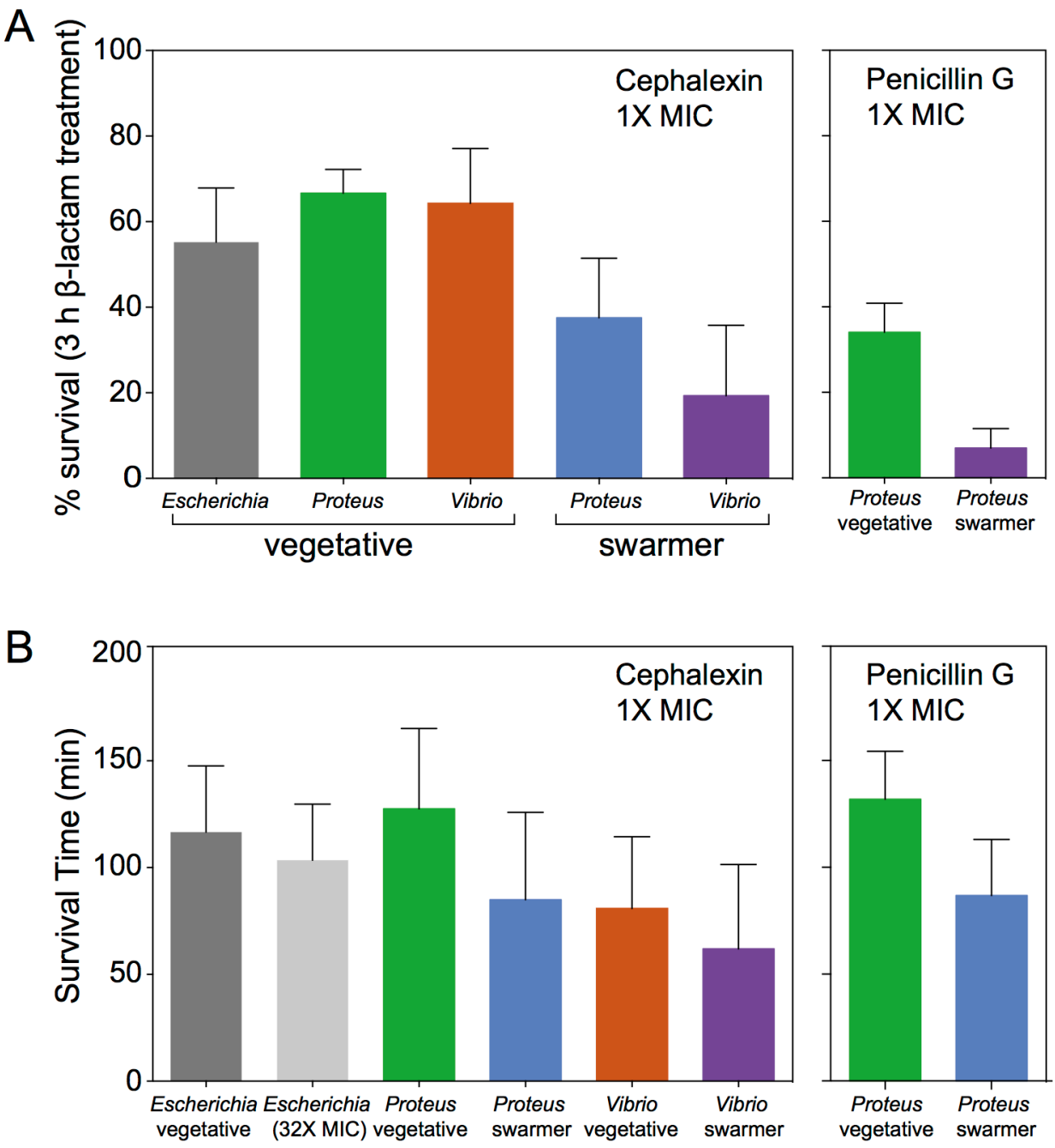
A
% survival (3 h β-lactam treatment)
100
80
60
40
20
0
Cephalexin
1X MIC
Penicillin G
1X MIC
Escherichia
Proteus
Vibrio
Proteus
Vibrio
vegetative
swarmer
Proteus
vegetative
Proteus
swarmer
B
Survival Time (min)
200
150
100
50
0
Cephalexin
1X MIC
Penicillin G
1X MIC
Escherichia
vegetative
Escherichia
(32X MIC)
Proteus
vegetative
Proteus
swarmer
Vibrio
vegetative
Vibrio
swarmer
Proteus
vegetative
Proteus
swarmer

Figure 19

Figure 20. Treatment of cells with 1x MIC cephalexin.

A) Field of *P. mirabilis* and *V. parahaemolyticus* cells treated with 1X MIC cephalexin in microfluidic device. Time = 0 min, cells immediately after the introduction of 1X MIC cephalexin. Time = 180 min, there is greater lysis of swarmer cells compared to vegetative cells. Dead cells are phase transparent. Membrane blebbing and filamentation are the direct result of cephalexin treatment. Scale bar = 10 μm.

B) Cartoon time course of cells treated with cephalexin. Time progresses from left to right. The ring structure represents the division protein FtsZ.

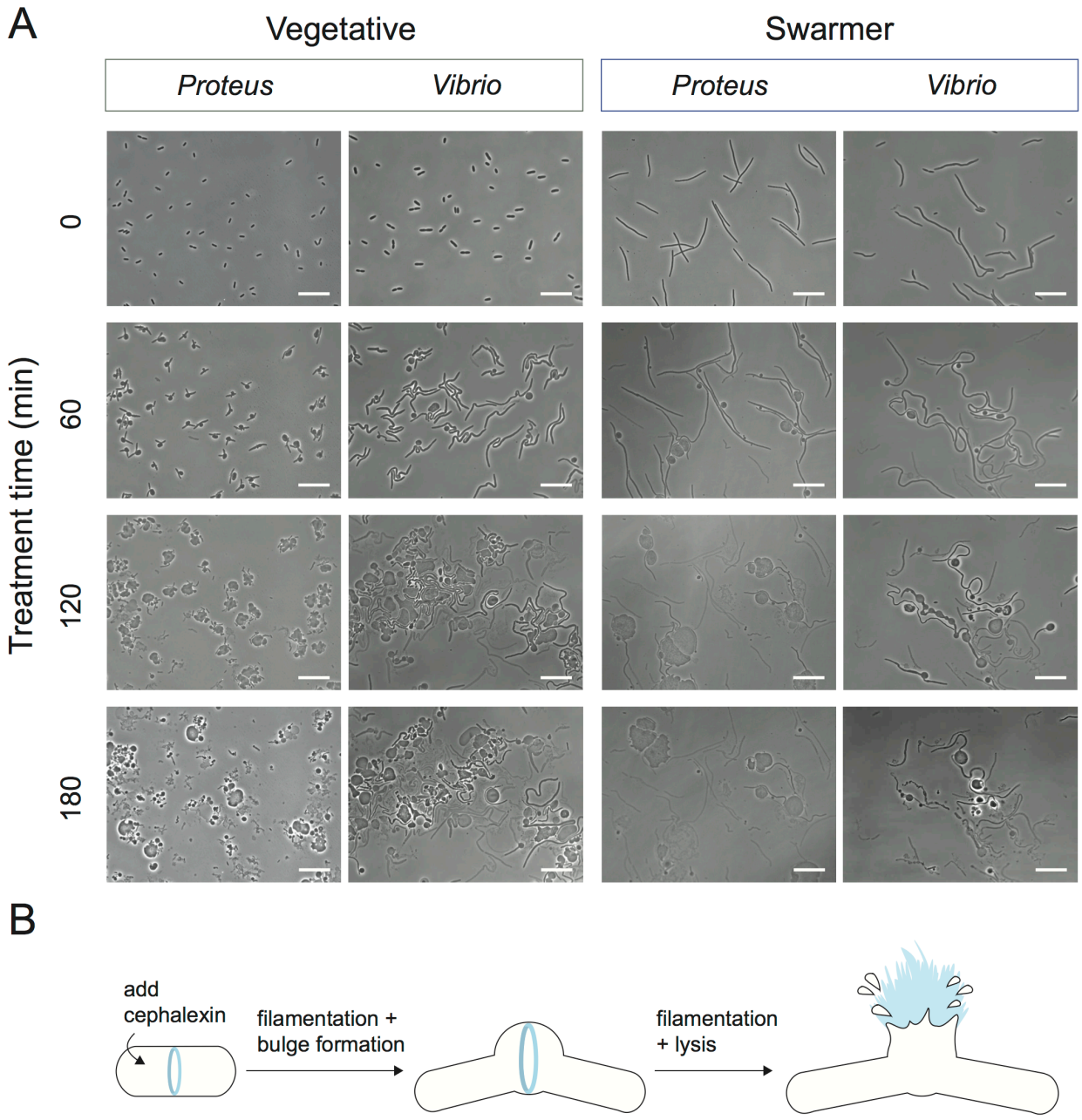
A
Vegetative
Swarmer
Proteus
Vibrio
Proteus
Vibrio
Treatment time (min)
0
60
120
180
B
add
cephalexin
filamentation +
bulge formation
filamentation
+ lysis

Figure 20

Figure 21. There is no significant change in the growth rate of cells under β-lactam treatment.

Vegetative and swarmer cells don't show significant changes in growth rate. The growth rate of vegetative exponential phase cells and swarmer cells were monitored for 15 minutes in microfluidic growth device (See methods).

A) Growth in the presence of 1X MIC cephalexin,

B) Growth in the presence of 1X MIC Penicillin G. For all measurements, we performed $n > 40$ cells, from at least 2 independent experiments. Box plot is representative of media, 1st and 3rd quartiles ("hinges"), and the 95% confidence interval of the median ("notches"). Black dots represent outliers in data.

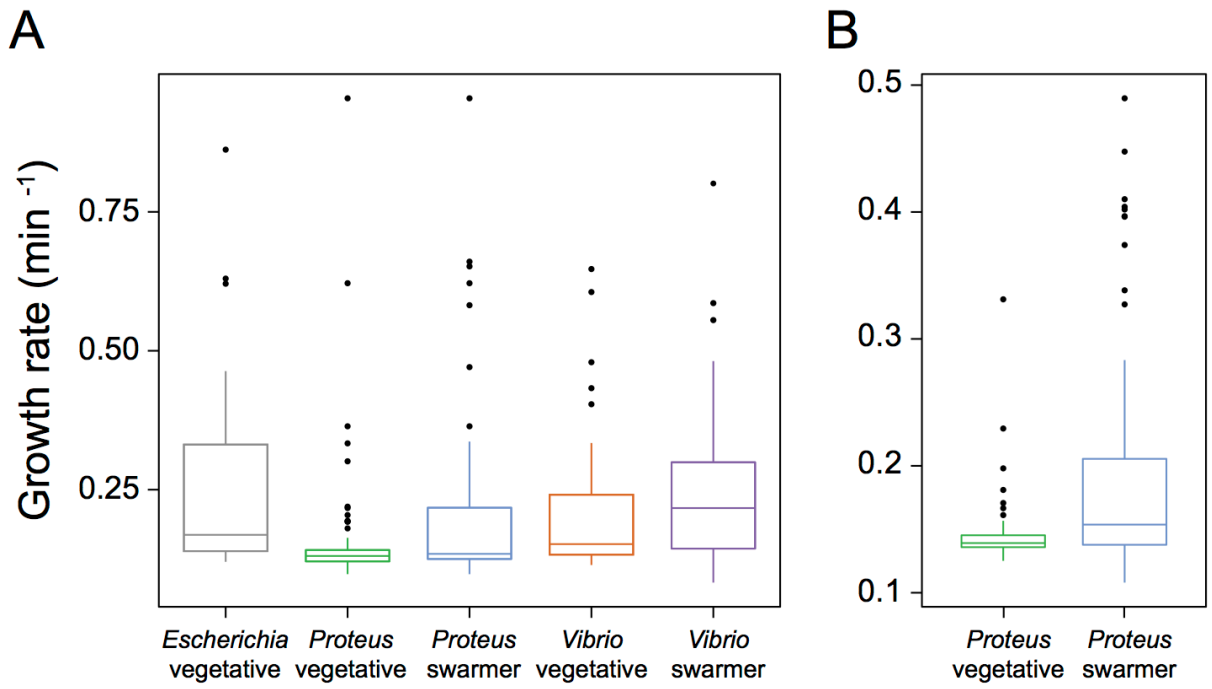
A
Growth rate (min -1)
0.75
0.50
0.25
Escherichia vegetative
Proteus vegetative
Proteus swarmer
Vibrio vegetative
Vibrio swarmer
B
0.5
0.4
0.3
0.2
0.1
Proteus vegetative
Proteus swarmer

Figure 21

Table 1. Muropeptides analyzed by UPLC-MS in positive ion mode. Identification of muropeptides by MS. Muropeptides were identified within (± 0.01 m/z) of the calculated muropeptide mass values. Identified peaks corresponded to mass values with following adducts (H^+, H^{2+}, H^{3+}). MS peaks were used to identify and quantify area under curve of UPLC UV_{205nm} peaks (Figure. S8).

Peak	Retention time (min)	Calculated mass (m/z)			Length of stem peptides
		H+	2+	3+	
1	7.7	871.3784	436.1892	291.1261	Tri
2	8.6	928.3999	464.6999	310.1333	Tetra-Gly(4)
3	9.2	699.2936	350.1468	233.7645	Di
4	10.8	999.4370	500.2185	333.8123	Penta-Gly (4)
5	11.6	1243.5202	622.2601	415.5067	Tri-Tri (-DS)
6	12	942.4155	471.7078	314.8052	Tetra
7a	13.6	1723.7102	862.3551	575.2367	Tri-Tri
7b	20.6	1723.7102	862.3551	575.2367	Tri-Tri
8	21.3	1851.7970	926.3985	617.9323	Tetra-Tetra-Gly(4)
9a	21.7	1794.7756	897.8878	598.9252	Tetra-Tri
10	22.6	1922.8341	961.9171	641.6114	Tetra-Tetra-Gly (5)
9b	22.8	1794.7756	897.8878	598.9252	Tetra-Tri
11	24.1	1865.8127	933.4063	622.6042	Tetra-Tetra
12	28.6	2846.2313	1423.6156	949.4104	Penta-Gly(5)-Tetra-Tetra
13	30.1	2789.2098	1395.1049	930.4033	Tetra-Tetra-Tetra
14a	30.7	1774.7402	887.8701	592.2467	anhydro Tetra-Tri
14b	32.1	1774.7402	887.8701	592.2467	anhydro Tetra-Tri
15	33.2	1845.7865	923.3932	615.9288	anhydro Tetra-Tetra

References

1. Justice SS, Hunstad DA, Cegelski L, & Hultgren SJ (2008) Morphological plasticity as a bacterial survival strategy. *Nat Rev Microbiol* 6(2):162-168.

2. Rajendram M, *et al.* (2015) Anionic phospholipids stabilize RecA filament bundles in *Escherichia coli*. *Mol Cell* 60(3):374-384.

3. Copeland MF & Weibel DB (2009) Bacterial Swarming: A Model System for Studying Dynamic Self-assembly. *Soft Matter* 5(6):1174-1187.

4. Kearns DB (2010) A field guide to bacterial swarming motility. *Nat Rev Microbiol* 8(9):634-644.

5. Butler MT, Wang Q, & Harshey RM (2010) Cell density and mobility protect swarming bacteria against antibiotics. *Proc Natl Acad Sci U S A* 107(8):3776-3781.

6. Kim W & Surette MG (2003) Swarming populations of Salmonella represent a unique physiological state coupled to multiple mechanisms of antibiotic resistance. *Biol Proced Online* 5:189-196.

7. Overhage J, Bains M, Brazas MD, & Hancock RE (2008) Swarming of *Pseudomonas aeruginosa* is a complex adaptation leading to increased production of virulence factors and antibiotic resistance. *J Bacteriol* 190(8):2671-2679.

8. Lai S, Tremblay J, & Deziel E (2009) Swarming motility: a multicellular behaviour conferring antimicrobial resistance. *Environ Microbiol* 11(1):126-136.

9. Hay NA, Tipper DJ, Gygi D, & Hughes C (1999) A novel membrane protein influencing cell shape and multicellular swarming of *Proteus mirabilis*. *J Bacteriol* 181(7):2008-2016.

10. Amir A, Babaeipour F, McIntosh DB, Nelson DR, & Jun S (2014) Bending forces plastically deform growing bacterial cell walls. *Proc Natl Acad Sci U S A* 111(16):5778-5783.

11. Tuson HH, Copeland MF, Carey S, Sacotte R, & Weibel DB (2013) Flagellum density regulates *Proteus mirabilis* swarmer cell motility in viscous environments. *J Bacteriol* 195(2):368-377.

12. Sliusarenko O, Heinritz J, Emonet T, & Jacobs-Wagner C (2011) High-throughput, subpixel precision analysis of bacterial morphogenesis and intracellular spatio-temporal dynamics. *Mol Microbiol* 80(3):612-627.

13. CLSI (2000) *Methods for Dilution Antimicrobial Susceptibility Tests for Bacteria That Grow Aerobically; Approved Standard* (Clinical and Laboratory Standards Institute, Wayne, PA) Fifth Ed.

14. Tivol WF, Briegel A, & Jensen GJ (2008) An improved cryogen for plunge freezing. *Microscopy and microanalysis : the official journal of Microscopy Society of America, Microbeam Analysis Society, Microscopical Society of Canada* 14(5):375-379.

15. Zheng SQ, *et al.* (2007) UCSF tomography: an integrated software suite for real-time electron microscopic tomographic data collection, alignment, and reconstruction. *J Struct Biol* 157(1):138-147.

16. Kremer JR, Mastronarde DN, & McIntosh JR (1996) Computer visualization of three-dimensional image data using IMOD. *J Struct Biol* 116(1):71-76.

17. Nicastro D, *et al.* (2006) The molecular architecture of axonemes revealed by cryoelectron tomography. *Science* 313(5789):944-948.

18. Collins TJ (2007) ImageJ for microscopy. *Biotechniques* 43(1 Suppl):25-30.

19. Turner RD, Hurd AF, Cadby A, Hobbs JK, & Foster SJ (2013) Cell wall elongation mode in Gram-negative bacteria is determined by peptidoglycan architecture. *Nat Commun* 4:1496.

20. Kuhner D, Stahl M, Demircioglu DD, & Bertsche U (2014) From cells to muropeptide structures in 24 h: peptidoglycan mapping by UPLC-MS. *Sci Rep* 4:7494.

21. Strating H, Vandenende C, & Clarke AJ (2012) Changes in peptidoglycan structure and metabolism during differentiation of *Proteus mirabilis* into swarmer cells. *Can J Microbiol* 58(10):1183-1194.

22. Glauner B (1988) Separation and quantification of muropeptides with high-performance liquid chromatography. *Anal Biochem* 172(2):451-464.

23. Holtje JV (1998) Growth of the stress-bearing and shape-maintaining murein sacculus of *Escherichia coli*. *Microbiol Mol Biol Rev* 62(1):181-203.

24. Vollmer W & Seligman SJ (2010) Architecture of peptidoglycan: more data and more models. *Trends Microbiol* 18(2):59-66.

25. Wang S, Arellano-Santoyo H, Combs PA, & Shaevitz JW (2010) Actin-like cytoskeleton filaments contribute to cell mechanics in bacteria. *Proc Natl Acad Sci U S A* 107(20):9182-9185.

26. Tuson HH, *et al.* (2012) Measuring the stiffness of bacterial cells from growth rates in hydrogels of tunable elasticity. *Mol Microbiol* 84(5):874-891.

27. Wheeler R, *et al.* (2015) Bacterial cell enlargement requires control of cell wall stiffness mediated by peptidoglycan hydrolases. *MBio* 6(4):e00660.

28. Loskill P, *et al.* (2014) Reduction of the peptidoglycan crosslinking causes a decrease in stiffness of the *Staphylococcus aureus* cell envelope. *Biophys J* 107(5):1082-1089.

29. Francius G, Domenech O, Mingeot-Leclercq MP, & Dufrene YF (2008) Direct observation of *Staphylococcus aureus* cell wall digestion by lysostaphin. *J Bacteriol* 190(24):7904-7909.

30. Arends SJR & Weiss DS (2004) Inhibiting cell division in *Escherichia coli* has little if any effect on gene expression. *J Bacteriol* 186(3):880-884.

31. Gan L, Chen S, & Jensen GJ (2008) Molecular organization of Gram-negative peptidoglycan. *Proc Natl Acad Sci U S A* 105(48):18953-18957.

32. Patrick JE & Kearns DB (2012) Swarming motility and the control of master regulators of flagellar biosynthesis. *Mol Microbiol* 83(1):14-23.

33. Desmarais SM, *et al.* (2015) High-throughput, highly sensitive analyses of bacterial morphogenesis using ultra performance liquid chromatography. *J Biol Chem* 290(52):31090-31100.

34. Vollmer W & Bertsche U (2008) Murein (peptidoglycan) structure, architecture and biosynthesis in *Escherichia coli*. *Biochim Biophys Acta* 1778(9):1714-1734.

35. Boneca IG, Huang ZH, Gage DA, & Tomasz A (2000) Characterization of *Staphylococcus aureus* cell wall glycan strands, evidence for a new beta-N-acetylglucosaminidase activity. *J Biol Chem* 275(14):9910-9918.

36. Dejonge BLM, Chang YS, Gage D, & Tomasz A (1992) Peptidoglycan composition of a highly methicillin-resistant *Staphylococcus aureus* strain. The role of penicillin binding protein 2A. *J Biol Chem* 267(16):11248-11254.

37. McLaggan D, Naprstek J, Buurman ET, & Epstein W (1994) Interdependence of K+ and glutamate accumulation during osmotic adaptation *of Escherichia coli*. *J Biol Chem* 269(3):1911-1917.

38. Tsatskis Y, *et al.* (2008) Core residue replacements cause coiled-coil orientation switching in vitro and in vivo: structure-function correlations for osmosensory transporter ProP. *Biochemistry-Us* 47(1):60-72.

39. Eberhardt C, Kuerschner L, & Weiss DS (2003) Probing the catalytic activity of a cell division-specific transpeptidase in vivo with beta-lactams. *J Bacteriol* 185(13):3726-3734.

40. Sun S, Selmer M, & Andersson DI (2014) Resistance to beta-lactam antibiotics conferred by point mutations in penicillin-binding proteins PBP3, PBP4 and PBP6 in *Salmonella enterica*. *PloS one* 9(5):e97202.

41. Chung HS, *et al.* (2009) Rapid beta-lactam-induced lysis requires successful assembly of the cell division machinery. *Proc Natl Acad Sci U S A* 106(51):21872-21877.

42. Chen CY, *et al.* (2012) *Proteus mirabilis* urinary tract infection and bacteremia: risk factors, clinical presentation, and outcomes. *J Microbiol Immunol Infect* 45(3):228-236.

43. Cui L, *et al.* (2003) Cell wall thickening is a common feature of vancomycin resistance in *Staphylococcus aureus*. *J Clin Microbiol* 41(1):5-14.

Chapter 5

Conclusions and Significance

Conclusions and Significance

When Hans Christian Joachin Gram developed a staining procedure in 1884 to enable the visualization of bacteria, he inadvertently stumbled on a surprising observation. His staining procedure revealed the presence of either purple bacteria (Gram–positive) or bacteria that did not retain the stain (Gram–negative). This led to the classification of bacteria into two simple categories based on the apparent thickness of the peptidoglycan, which is a component of the bacterial cell wall. Gram–positive bacteria have 3–layers (wall teichoic and lipoteichoic acids, a thick peptidoglycan layer, and a lipid membrane), and Gram–negative bacteria have 4–layers (lipopolysaccharides, the outer lipid membrane, a thin peptidoglycan layer, and an inner lipid membrane).

Out of these layers the large macromolecular structure, peptidoglycan, is currently believed to be most important for mechanical properties of bacteria. It counteracts the high osmotic pressure differential (1) and when it is structurally compromised, bacteria lyse (1, 2) . Due to its important mechanical role in bacteria, its mechanical properties have been determined using a variety of methodologies (3-5). However, measurements of the mechanical properties have been plagued by high variability where reported values can vary by orders of magnitude, even for identical species (6).

In Chapter 2, our studies of the mechanical properties of the cell wall are discussed. We developed CLAMP (Cell Length Analysis of Mechanical Properties), a

new methodology that can be used to measure the Young's modulus of both Gram–negative and Gram–positive rod shaped bacteria. When developing CLAMP, we kept in mind the materials and equipment available in a typical microbiology lab, therefore ensuring that our method could be performed anywhere. CLAMP involves embedding bacterial cells in agarose hydrogels with tunable stiffness, monitoring cell growth over time using phase contrast microscopy, and fitting the bacterial growth data to three-dimensional finite-element simulations to extract a Young's modulus value. We used CLAMP to measure the Young's modulus of three different bacteria, *Escherichia coli* MG1655 (50-150 MPa), *Pseudomonas aeruginosa* PAO1 (100-200 MPa), and *Bacillus subtilis* BB11 (100-200 MPa). Despite the different cell wall thickness of each organism, our results show their Young's moduli are relatively the same, indicating that they may all share common peptidoglycan architecture. Additionally, we discovered that upon depolymerization of the bacterial actin homolog, MreB, there were no measurable changes in the longitudinal stiffness of *E. coli*. Previously, it had been shown that MreB has a stiffen affect when cells are examined under bending stress (7), contributing 30% to the bending rigidity of *E. coli*. We attribute the notable impact of MreB on bending rigidity but not on longitudinal stiffness to the fast association/disassociation of MreB filaments from the cell wall, to affect our measured longitudinal stiffness MreB would have to stay bound to the wall for longer timescales. This application highlights the

capabilities of CLAMP to not only identify small molecules that affect cell stiffness, but can also shed light on cellular mechanisms.

In chapter 3, we described GRABS (General Regulators Affecting Bacterial Stiffness), a high-throughput screening method that allowed us to characterize the mechanical contribution of all non-essential genes in *E. coli* using a pre-existing collection of mutants, the Keio collection. Similar to CLAMP, we tried to keep in mind the capabilities and equipment that is accessible in a typical microbiology lab. GRABS uses absorbance based measurements, in a 96-well microplate, to monitor changes in growth of bacterial mutants embedded in 1% agarose and in liquid nutrient broth. By embedding bacteria in agarose we are able to apply a sufficient amount of force to inhibit the growth of mutants that exhibit stiffness defects, while simultaneously monitoring liquid culture to account for any growth based defect inherent to the genetic mutant. Our results demonstrate that the mechanical properties of the cell are modulated by a highly diverse set of genes. We identified 46 mutants (~1% of the genome) that had a significant impact on stiffness, either increasing or decreasing stiffness. We found in agreement with our current understanding of bacterial mechanics that genes involved in cell wall and membrane biogenesis account for the highest number of mechanical modulators (9 mutants). The next-largest groups were energy production and conversion (eight mutants), and replication/recombination and repair (6 mutants). We further validated 13 mutants using a previously developed microfluidic

bending assay (4) to determine the Young's modulus. We found a high correlation between our GRABS results and the bending measurements, confirming that our methodology could accurately identify mutants with mechanical defects, and effectively increasing the number of proteins (7) with a direct mechanical contribution by 13 fold. Furthermore, our GRABS data identified a curious discrepancy between the mechanical importance of cell wall enzymes PBP1a and PBP1b. Although these proteins are thought to be functionally redundant (8) we determined that only PBP1b causes a significant decrease in cell wall mechanical properties. We further identified the importance of the glycosyltransferase domain for it mechanical role; inactivation of this domain is already know to abolish all enzymatic abilities (transpeptidation and transglycosylation) of PBP1b (9). Finally, we show that by correlating our data with an existing chemical screen, that we can identify new/unknown functions for existing small molecules, antibiotics, and environmental conditions in modulating cell stiffness.

In Chapter 4, the change in bending rigidity of *Proteus mirabilis* and *Vibrio parahaemolyticus*, opportunistic pathogens associated with urinary tract infections and food poisoning, is described. These two bacteria undergo a specialized type of surface motility known as swarming (10). During swarming, cells increase in length, become highly filamented, are multinucleated, and show resistance to many antibiotics due to their high surface densities (11). We found while swarming, these bacteria are extremely flexible, and further study of their mechanical properties using our custom reloadable

microfluidic device revealed a decrease in the bending rigidity of swarmer cells. And while the composition of peptidoglycan in swarmer cells was unchanged there was a consistent decrease in peptidoglycan thickness that would account for the measured decrease in bending rigidity. We investigated the fitness costs that are associated with this change in peptidoglycan thickness. Primarily, we determined that swarming bacteria are more sensitive to cell wall targeting antibiotics, exhibiting a higher amount and rate of cell lysis. These findings demonstrate a previously unknown cost of swarming and suggest changes in antibiotic dosing regimens may optimize treating infections of these bacteria.

Together these studies provide additional insight into the physical, chemical and genetically induced changes that underlie the 'altered' mechanical properties of model bacteria *E. coli*. It also stresses the importance of unbiased screening in order to get a true representation of all genes that contribute to a global characteristic, such as mechanical stiffness. Finally, we hope that by developing more accessible tools for the study of bacterial mechanical properties that it will continue to drive the field onwards and upwards.

References

1. Holtje JV (1998) Growth of the stress-bearing and shape-maintaining murein sacculus of *Escherichia coli*. *Microbiol Mol Biol Rev* 62(1):181-203.

2. Mille Y, Beney L, & Gervais P (2002) Viability of *Escherichia coli* after combined osmotic and thermal treatment: a plasma membrane implication. *Biochim Biophys Acta* 1567(1-2):41-48.

3. Abu-Lail NI & Camesano TA (2006) The effect of solvent polarity on the molecular surface properties and adhesion of Escherichia coli. *Colloids Surf B Biointerfaces* 51(1):62-70.

4. Amir A, Babaeipour F, McIntosh DB, Nelson DR, & Jun S (2014) Bending forces plastically deform growing bacterial cell walls. *Proc Natl Acad Sci U S A* 111(16):5778-5783.

5. Thwaites JJ & Mendelson NH (1989) Mechanical properties of peptidoglycan as determined from bacterial thread. *Int J Biol Macromol* 11(4):201-206.

6. Tuson HH, *et al.* (2012) Measuring the stiffness of bacterial cells from growth rates in hydrogels of tunable elasticity. *Mol Microbiol* 84(5):874-891.

7. Wang S, Arellano-Santoyo H, Combs PA, & Shaevitz JW (2010) Actin-like cytoskeleton filaments contribute to cell mechanics in bacteria. *Proc Natl Acad Sci U S A* 107(20):9182-9185.

8. Paradis-Bleau C, *et al.* (2010) Lipoprotein cofactors located in the outer membrane activate bacterial cell wall polymerases. *Cell* 143(7):1110-1120.

9. Terrak M, *et al.* (1999) The catalytic, glycosyl transferase and acyl transferase modules of the cell wall peptidoglycan-polymerizing penicillin-binding protein 1b of *Escherichia coli*. *Mol Microbiol* 34(2):350-364.

10. Copeland MF & Weibel DB (2009) Bacterial Swarming: A Model System for Studying Dynamic Self-assembly. *Soft Matter* 5(6):1174-1187.

11. Butler MT, Wang Q, & Harshey RM (2010) Cell density and mobility protect swarming bacteria against antibiotics. *Proc Natl Acad Sci U S A* 107(8):3776-3781.

Appendix

Future Directions

During the course of the research described in this dissertation we have made several interesting observations that could provide some avenues for further study. I discuss these observations below:

Changes in the membrane composition of swarming bacteria

It has been previously suggested that there are changes in the membrane composition between *Proteus mirabilis* swarmer and vegetative cells. Specifically, Infared Microspectroscopy revealed variations in the lipid membrane and lipopolysaccharide (LPS) composition (1) confirming previous reports that the LPS O–antigen is increased in swarmer cells (2). Additional studies have shown *P. mirabilis* swarmer cells have higher rates of pentose (2–fold) and amino acid (3–fold) leakage, a decrease in the active transport of nutrients from the environment, and are more susceptible to surfactant treatment, which indicates increases in membrane permeability (3). During the course of our experiments we made several observations that give further credence to this hypothesis. While investigating the single cell response of swarming bacteria to cell wall modifying antibiotics we also investigated the effects to sodium dodecyl sulfate (SDS) treatment, a detergent that causes dissolution of the membrane (4). With the addition of SDS at 1x minimum inhibitory concentration (MIC), all swarmer cells became phase transparent within 2 mins of treatment as observed by

phase contrast microscopy. The effect of SDS treatment on vegetative cells was not as drastic (~50% phase transparent after 20 min). The loss of contrast as evidenced by phase microscopy could indicate either cell death or a change in the refractive index of the cells, due to the refractive index of the cell approximating that of the surrounding media The increased sensitivity of swarmers to SDS treatment could indicate that there is a better accessibility of SDS to the lipid membrane, and therefore it is more potent disruptor. Additionally, we noticed while performing Cryo-EM of *P. mirabilis* swarmer and vegetative cells that swarmer cells exhibited wavy outer membrane architecture, a sign of membrane instability (Chapter 4, Figure S8E,F) (5).

We believe there are several experiments that could be performed to understand the fundamental differences in the membrane structure of *P. mirabilis*. To understand the physical changes in the membranes of *P. mirabilis* vegetative and swarmer cells, we could determine the effect that disruption of the membrane has on bending rigidity of the cells. First, we consider the membrane to be a composite of the outer lipid membrane and LPS layer. Due to the importance of divalent cations in the stability of the LPS layer (6) we first suggest using ethylenediaminetetraacetic acid (EDTA), a chelator of divalent cations, to destabilize the LPS layer. Second, to investigate differences in the lipid membrane composition of *P. mirabilis* vegetative and swarmer cells we suggest using quantitative mass spectrometry (7). We believe it plausible that the cell modifies the length or saturation of the acyl chains thereby changing the

physical properties of the membrane, such as rigidity. We have done some preliminary lipid mass spectrometry, using *P. mirabilis* vegetative cells and were able to resolve ~40 different lipid species.

Changes in the construction of the peptidoglycan layer

It is accepted that there is typically no turnover of peptidoglycan at the polar regions of rod shaped cells (8), and currently there are no known peptidoglycan related proteins that localize to the poles of the cell. While investigating bacterial swarming we observed cells, set back from the swarm front, which exhibited blebbing at one or both cell poles. Furthermore, we noticed when spinning cells down at speeds > 9000 x *g* in a microcentrifuge, that some of the swarming cells would again develop a large polar bleb. Finally, when we observed the cell wall of *P. mirabilis* vegetative and swarmer cells by Cryo-EM we noticed abnormal polar features in both cell types. Vegetative cells exhibited a region near the pole with an enlarged periplasmic space (~140 nm) (Chapter 4, Figure S8A, B) and swarmer cells had altered membrane integrity that appeared highest at the poles of the cell (Chapter 4, Figure S9E, F).

We have previously determined certain osmolarity media that can elicit membrane blebbing at the poles. By flowing these buffers through our microfluidic device (Chapter 4, Figure S11) we can monitor the integrity of the peptidoglycan layer upon the initiation of a bleb in the membrane. To visualize the peptidoglycan layer and

its turnover in *P. mirabilis* we could use a fluorescent D-amino acid, which has been previously shown to incorporate into the peptide stem of the peptidoglycan and is sufficient for time-lapse imaging (9). Furthermore, we could use 3D Structured Illumination Microscopy to collect high-resolution images of the peptidoglycan layer (10) in combination with the membrane dye FM 4-64. Additional studies could also be performed investigating the localization of cell wall related proteins using fluorescent protein tags (11).

Determining the role of the chromosome in the stiffness of the bacterial cell

In a previous study using Atomic Force Microscopy, high-resolution images of *E. coli* surface stiffness were collected, identifying two distinct regions of the cell that showed increased stiffness, the authors theorized that these regions could be a complex of the chromosome and chromosome associated proteins (nucleoid) (12). From our screen for stiffness modulators in *E. coli* we identified 2 mutants that might indicate the nucleoid is able to influence the stiffness of bacteria; A Δ*recA* mutant exhibited an increase in stiffness, while a Δ*holC* mutant exhibited a decrease in stiffness. It has been shown previously that HolC mutants exhibit diffuse nucleoid architecture indicating low packing, but upon deletion of RecA the nucleoids reform, increasing packing (13).

We have previously confirmed an increase and decrease in the Young's modulus of Δ*recA* and Δ*holC* mutants, respectively, using our microfluidic-bending assay

(Chapter 3, Figure 4B). To determine whether the nucleoid can contribute to cell stiffness, the bending rigidity of bacteria with altered nucleoid packing could be probed. To alter nucleoid packing, it is possible to use already identified temperature sensitive mutants that exhibit aberrant nucleoid packing when grown at a nonpermissive temperature (14). In order to obtain quantitative data about the packing of the nucleoid in these mutants, the expansion rate of nucleoid could be monitored in vitro using a microfluidic device (15). Briefly, cells are loaded into individual channels of a microfluidic device, treated with lysozyme to remove the cell wall, and then lysed to release the chromosome. Using a fluorescent fusion of a highly abundant nucleoid-associated protein, HupA, it is possible to visualize the chromosome using fluorescence microscopy (15). This method would enable us to quantitatively relate our measurements of bending rigidity to nucleoid packing in order to understand the impact of nucleoid structure on bacterial mechanics.

References

1. Keirsse J, *et al.* (2006) Mapping bacterial surface population physiology in real-time: infrared spectroscopy of *Proteus mirabilis* swarm colonies. *Appl Spectrosc* 60(6):584-591.

2. Armitage JP, Smith DG, & Rowbury RJ (1979) Alterations in the cell envelope composition of *Proteus mirabilis* during the development of swarmer cells. *Biochim Biophys Acta* 584(3):389-397.

3. Armitage JP, Rowbury RJ, & Smith DG (1975) Indirect evidence for cell-wall and membrane differences between filamentous swarming cells and short non-swarming cells of *Proteus mirabilis*. *J Gen Microbiol* 89(Jul):199-202.

4. Woldringh CL & van Iterson W (1972) Effects of treatment with sodium dodecyl sulfate on the ultrastructure of *Escherichia coli*. *J Bacteriol* 111(3):801-813.

5. Cascales E, Bernadac A, Gavioli M, Lazzaroni JC, & Lloubes R (2002) Pal lipoprotein of *Escherichia coli* plays a major role in outer membrane integrity. *J Bacteriol* 184(3):754-759.

6. Amro NA, *et al.* (2000) High-resolution atomic force microscopy studies of the Escherichia coli outer membrane: Structural basis for permeability. *Langmuir* 16(6):2789-2796.

7. Oliver PM, *et al.* (2014) Localization of anionic phospholipids in *Escherichia coli* cells. *J Bacteriol* 196(19):3386-3398.

8. Park JT & Uehara T (2008) How bacteria consume their own exoskeletons (turnover and recycling of cell wall peptidoglycan). *Microbiol Mol Biol Rev* 72(2):211-227, table of contents.

9. Kuru E, *et al.* (2012) In Situ probing of newly synthesized peptidoglycan in live bacteria with fluorescent D-amino acids. *Angew Chem Int Ed Engl* 51(50):12519-12523.

10. Zhou X, *et al.* (2015) Bacterial division. Mechanical crack propagation drives millisecond daughter cell separation in *Staphylococcus aureus*. *Science* 348(6234):574-578.

11. Lee TK, *et al.* (2014) A dynamically assembled cell wall synthesis machinery buffers cell growth. *Proc Natl Acad Sci U S A* 111(12):4554-4559.

12. Longo G, *et al.* (2013) Antibiotic-induced modifications of the stiffness of bacterial membranes. *J Microbiol Methods* 93(2):80-84.

13. Marceau AH, *et al.* (2011) Structure of the SSB-DNA polymerase III interface and its role in DNA replication. *Embo J* 30(20):4236-4247.

14. Sun Q & Margolin W (2004) Effects of perturbing nucleoid structure on nucleoid occlusion-mediated toporegulation of FtsZ ring assembly. *J Bacteriol* 186(12):3951-3959.

15. Pelletier J, *et al.* (2012) Physical manipulation of the *Escherichia coli* chromosome reveals its soft nature. *Proc Natl Acad Sci U S A* 109(40):E2649-2656.